Investigation of heat transfer near the critical point of R134a

Zur Erlangung des akademischen Grades eines
DOKTORS DER INGENIEURWISSENSCHAFTEN (Dr.-Ing.)

von der KIT-Fakultät für Maschinenbau des
Karlsruher Institut für Technologie (KIT)

genehmigte
DISSERTATION

von

Dipl.-Ing. Florian Feuerstein

aus Spaichingen

Tag der mündlichen Prüfung: 12.04.2019

Hauptreferent: Prof. Dr.-Ing. Xu Cheng

Korreferent: Prof. Dr.-Ing Thomas Schulenberg

Declaration

Ich versichere wahrheitsgemäß, die Arbeit selbstständig angefertigt, alle benutzten Hilfsmittel vollständig und genau angegeben und alles kenntlich gemacht zu haben, was aus Arbeiten anderer unverändert oder mit Abänderungen entnommen wurde.

Karlsruhe, 25.07.2019

. . . .
        (**Florian Feuerstein**)

Acknowledgements

My family deserves special thanks because the fundamental studies and the conduction of this study would not have been possible without the support and encouragement of my parents.

I want to acknowledge the unconditional patience and support from my fiancée Klaudia throughout my studies as well as her valuable support in writing the thesis.

Kurzfassung

Neue Kraftwerkskonzepte, wie zum Beispiel der sogenannte Supercritical Water Cooled Reactor (SCWR), nutzen überkritisches Wasser als Kühlmittel. Mit überkritischem Wasser ist ein vereinfachtes und kompaktes Kraftwerk mit einer enormen Steigerung des thermischen Wirkungsgrades möglich. Eine zuverlässige und genaue Vorhersage der Wärmeübertragung ist unerlässlich, um diese Kraftwerke zu entwerfen und sicher zu betreiben. Flüssigkeiten weisen bei einem Druck nahe dem kritischen Punkt starke Änderungen der thermophysikalischen Eigenschaften auf. Diese Änderungen können die Turbulenz reduzieren und somit den Wärmeübergang beeinträchtigen. Experimente sind notwendig, um diese Phänomene zu verstehen, Modelle für die Wärmeübertragungsvorhersage zu entwickeln und zu validieren. Experimente mit überkritischem Wasser erfordern Testeinrichtungen, die sehr kostspielig und komplex im Aufbau, Wartung und Betrieb sind. Daher werden die Experimente mit einem Modellfluid durchgeführt. Dies bedeutet jedoch, dass die Ergebnisse des Modellfluids auf Wasser übertragen werden müssen.

Ziel dieser Studie ist es, Wärmeübergangsphänomene in der Nähe des kritischen Punktes zu untersuchen und Fluid-zu-Fluid-Skalierungsmodelle für den Wärmeübergang bei überkritischen Bedingungen zu bewerten. Zwei umfangreiche Versuchsreihen zum Wärmeübergang bei überkritischen Bedingungen für das Fluid R134a und CO_2 werden durchgeführt. Der Einfluss von Druck, Eingangstemperatur, Massenstrom und Wärmestrom auf den Wärmeübergang werden im Detail untersucht. Darauffolgend werden die Effekte des Auftriebs und der thermisch induzierten Beschleunigung der Strömung auf den Wärmeübergang im Detail diskutiert. Die Entdeckung von neuen Phänomenen, wie dem Einfluss der Eintrittstemperatur, verbessert das Verständnis des Wärmeübergangs bei überkritischen Bedingungen. Zusätzlich werden Strömungsinstabilitäten mit unerwartetem Einfluss auf den Wärmeübergang beobachtet und diskutiert. Weitere Gründe für die hohe Abweichungen zu Daten aus der Literatur und die schwierige Reproduzierbarkeit nahe dem pseudokritischen Punkt werden identifiziert. Basierend auf den durchgeführten Experimenten dieser Studie werden zwei zuverlässige Datenbanken für R134a und CO2 vorgeschlagen. Diese werden verwendet, um Wärmeübertragungskorrelationen der Literatur zu bewerten, wobei die Korrelation von Chen und Fang die Daten am Besten reproduziert. Mit einer zusätzlichen Datenbank für Wasser werden die Datenbanken für die direkte Validierung von Fluid-to-Fluid-Skalierungsmodellen genutzt. Zu diesem Zweck wird eine neue und zuverlässige Methode für den Vergleich der skalierten Daten mit bestehenden experimentellen Daten entwickelt. Die Auswertung zeigt, dass die bisher entwickelten Modelle nur bestimmte Fluidkombinationen oder bestimmte beeinflusste Daten zuverlässig skalieren können. Die vorhandenen Datenbanken werden verwendet, um die Modelle von Cheng et al. und Tian et al. an die Fluidkombination R134a-Wasser und CO2-Wasser anzupassen. Zusätzlich werden Experimente zum kritischen Wärmestrom bei hohem unterkritischem Druck mit R134a durchgeführt. Die Einflüsse von Druck, Unterkühlung am Eingang und Massenstrom werden diskutiert. Die Daten werden zur Beurteilung von Korrelationen verwendet und mit einem Modell, das auf dem Modell von Ahmad basiert, zu Wasser skaliert. Die skalierten Daten sind gut mit der CHF-Look-up-Tabelle von Groeneveld et al. reproduzierbar. Die Korrelationen von Katto und Ohno sowie Shah sind in der Lage, den kritischen Wärmestrom selbst bei Druck nahe dem kritischen Punkt genau vorherzusagen.

Abstract

New power plant concepts, which are currently being investigated, use water at supercritical conditions as coolant like the Supercritical Water cooled Reactor (SCWR). With supercritical water, a compact and simplified power plant with an enormous increase of the thermal efficiency is possible. A reliable and accurate prediction of the heat transfer is essential to design and safely operate these power plants. Fluids at pressure close to the critical point exhibit strong variations of the thermal-physical properties. Those changes can lead to a reduced turbulence production and thus to a impairment of the heat transfer. Experiments are necessary to understand these phenomena in order to develop and validate models for the heat transfer prediction. Caused by the high critical point of water, these experiments require test facilities which are very expensive and complex to construct, maintain and operate. Therefore, the experiments are conducted with a model fluid as coolant. This means, however, that the data of the model fluid must be scaled to water conditions.

The purpose of this study is to investigate heat transfer phenomena nearby the critical point and to validate the fluid-to-fluid scaling models for heat transfer at supercritical conditions and for critical heat flux. Two extensive sets of experimental investigations for the heat transfer at supercritical conditions are conducted for the fluid R134a and CO_2. The influence of pressure, inlet temperature, mass flux and heat flux on the heat transfer are investigated in detail. The effect of buoyancy and thermal-induced bulk flow acceleration on the heat transfer are discussed in detail. The discovery of new phenomena like the influence of the inlet temperature improves the understanding of the heat transfer at supercritical conditions. Reasons for high deviations between data of the literature and the difficult reproducibility close to the pseudo-critical point are identified. Additionally, flow instabilities with unexpected influence on the heat transfer are observed and discussed. Based on the conducted experiments of this study, two reliable databases are proposed for R134a and CO_2, respectively. The databases are used to assess heat transfer correlations of the literature. Overall, the correlation of Chen and Fang predicts the data at best. An additional database for water is proposed. The databases are used to directly validate and modify fluid-to-fluid scaling models for heat transfer at supercritical conditions. For this purpose, a new and reliable method for the comparison of the scaled data with existing experimental data is developed. An evaluation shows that the models developed so far are only able to reliably scale a certain fluid combination or certain influenced data. The existing databases are used to fit the models of Cheng et al. and Tian et al. to the fluid-combination R134a-water and CO_2-water. Additionally, critical heat flux (CHF) experiments are conducted with R134a as coolant. The influences of pressure, inlet subcooling and mass flux are discussed for an improved understanding of the critical heat flux at high pressures. The data are used to asses correlations and are scaled to water using a model based on Ahmad's model. The scaled data show a good comparison with the CHF look-up table of Groeneveld et al.. The correlations of Katto and Ohno as well as Shah are able to predict the CHF well, even at pressures close to the critical point.

Contents

Nomenclature

Latin Symbols

Symbol	Dimensions	Description
A	m^2	Area
Ac	–	Acceleration number
Bu	–	Buoyancy number
c_p	$\frac{J}{kgK}$	Specific heat capacity
d	m	Diameter
e	m	Eccentricity
E	–	Eckert number
f	–	Friction factor
g	$\frac{m}{s^2}$	Gravitational constant
G	$\frac{kg}{m^2 s}$	Mass flux
Gr	–	Grashof number
h	$\frac{J}{kg}$	Specific enthalpy
α	$\frac{W}{m^2 K}$	Heat transfer coefficient
I	A	Current
l	m	Position along the tube
L	m	Length
M	$\frac{kg}{mol}$	Molar mass
$\dot{m}$	$\frac{kg}{s}$	Mass flow rate
Nu	–	Nusselt number
P	Pa	Pressure
Pe	–	Peclet Number
Pr	–	Prandtl Number
q or $\dot{q}$	$\frac{W}{m^2}$	Heat flux
$\dot{Q}$	W	Rate of heat flow
r	m	Radius
R	Ω	Electric resistance
Ra	μm	Mean roughness
Re	–	Reynolds Number

Rz	μm	Averaged maximum peak to valley roughness
s	m	Wall thickness
t	s	Time
T	$^{\circ}C$	Temperature
u	$\frac{m}{s}$	Velocity
U	V	Voltage
We	$-$	Weber number
x	$-$	Vapor quality
y	m	Distance from wall
y^+	$-$	Dimensionless distance from the wall

Greek Symbols

Symbol	Dimensions	Description
α	$\frac{W}{m^2 K}$	Heat transfer coefficient
β	$\frac{1}{K}$	Thermal expansion coefficient
ϵ	$\frac{m^2}{s^3}$	Dissipation of turbulent energy
η	$\frac{m^2}{s}$	Kinematic viscosity
κ	$\frac{m^2}{s}$	Thermal diffusivity
λ	$\frac{W}{mK}$	Thermal conductivity
μ	$\frac{Pa}{s}$	Dynamic viscosity
π	$-$	Mathematical constant π
π_A	$-$	Acceleration number of Cheng [Cheng et al., 2009b]
ρ	$\frac{kg}{m^3}$	Density (specific resistivity in eq.3.2)
τ	$\frac{N}{m^2}$	Shear stress
σ	$\frac{kg}{s^2}$	Surface tension
ϕ	$-$	Dimensionless mass flux of Ahmad

Subscripts

Symbol	Description
0	Mean
b	Bulk
c	Critical
cor	Correlation
D	Determined neighbor
DB	Dittus-Boelter correlation
env	Environment
f	Friction
g	Gas
h	Heated
HTD	Heat transfer deterioration
i	Inside
in	Inlet
l	Liquid
$loss$	Loss
m	Mean

M	Modeling fluid
n	Part n of tube
o	Outside
pc	Pseudo-critical
s	Scaled
sub	Subcooled
t	Transformed
tot	Total
un	Unheated
v	Volume
vap	Vaporization
w	Wall
W	Water

Superscripts

Symbol	Description
'	State of saturated liquid
–	Mean

Abbreviations

Abbreviation	Long form
ANN	Artificial neural network
BWR	Boiling Water Reactor
CO_2	Carbon dioxide
CHF	Critical heat flux
dev	Deviation
DNB	Departure from nucleate boiling
DNS	Direct numerical simulation
exp	Experimental
HTC	Heat transfer coefficient
IATF	Institute for Applied Thermofluidics
HPLWR	High Performance Light Water Reactor
HTD	Heat transfer deterioration
HTE	Heat transfer enhancement
KIMOF	KIT Model Fluid Facility
KIT	Karlsruhe Institute of Technology
LUL	Look-up list
LUT	Look-up table
MD	Mean deviation
MAD	Mean absolute deviation
NHT	Normal heat transfer
NIST	National Institute of Standardization
PDO	Post-dryout
PWR	Pressurized Water Reactor
RANS	Reynold averaged Navier-Stokes equations
SCUOL	Supercritical University of Ottawa Loop
SCWR	Supercritical Water Cooled Reactor
SJTU	Shanghai Jiao Tong University
STD	Standard deviation

1. Introduction

The human population is rising and so is the worldwide electrical power consumption. The main part of the power is produced by fossil sources, which emits carbon dioxide (CO_2). IEA data for 2017 show that global coal combustion was responsible for one third of the worldwide CO_2 emissions [Olivier et al., 2017]. The high CO_2 emission is most likely one cause for the climate change. The 16 hottest years since the records began in 1880 have been in the years 1998 - 2017 with the hottest one in 2016 [Olivier et al., 2017]. Energy sources for a reliable and ecologically power supply are highly demanded for a sustainable development of human society. Renewable energies and nuclear power fit this demands really well. Nuclear power plants are important to ensure the stability of the grid. This is getting more and more important in energy mixes with a high part of renewable energies.

However, 30 nations had operating nuclear power plants in the year 2016 because the nuclear power is an economical energy source. In total 448 reactors with a net capacity of 391 GW produced 2476 TWh in 2016 [International Atomic Energy Agency, 2017]. In some countries the nuclear energy provides more than 50 % of the total electrical power. Hereby, France is leading with 72.3 % of its total produced electric energy. 61 reactors have been under construction in 2016 with 5 new member states [International Atomic Energy Agency, 2017] and 80 more reactors known as planned. Therefore, the nuclear power will play an important role in the future.

In 2001, a group of nations initiated the Generation IV International Forum to collaboratively develop the next generation (Generation IV) nuclear energy systems. Six nuclear reactor technologies are selected for further research and development with four primary goals including the improvements in sustainability, economics, safety and reliability as well as proliferation resistance [DoE, 2002]. The reactors are based on three basic systems which are the gas, the water and the liquid metal cooled reactor. In Germany the research is focused on the Supercritical Water Cooled Reactor (SCWR) with a huge project of the European Union ended in 2012 with Prof. Schulenberg as coordinator. In the second phase, the group developed the concept of the High Performance Light Water Reactor (HPLWR) [Schulenberg & Starflinger, 2012] which is the background of this thesis.

1.1. Supercritical Water Cooled Reactor

The SCWR is the only type of Generation IV using light water as coolant, making it the most similar to existing power reactor concepts. The SCWR operates above the thermodynamic critical point of water (374 °C, 22.1 MPa) that enables a thermal efficiency of 44 % or more. This is much higher compared to the 34 % efficiency for current light water reactors. The higher (supercritical) steam enthalpy can enable a direct, once through steam cycle as seen in the schematic concept in figure 1.1 (a). Here, the steam generated in the core passes directly into the turbine without further processing. Therefore, neither steam generators nor steam separators, steam dryers and recirculation pumps are required [DoE, 2002]. Moreover, steam turbines and reheaters could be significantly smaller than today. Due to smaller volume flow and friction losses, the feedwater

pumps could be smaller and consume less electric power. All these factors decrease capital and operational costs and hence decrease electrical energy costs [Pioro & Duffey, 2007]. As supercritical water doesn't undergo a phase change, a boiling crisis would physically be excluded. Due to the considerable reduction in water density and mass in the reactor core, it might be possible to develop fast SCWRs with a conversion factor of more than one for a self-sustaining fuel cycle [Pioro & Duffey, 2007]. The SCWR concept combines the design and operation experiences gained from existing light water cooled reactors and supercritical fossil fuel plants. The research mainly needs to be focused on the heat transfer in and on the reactor itself [Schulenberg & Starflinger, 2012].

(a) Concept of SCWR from Generation IV roadmap [DoE, 2002]

(b) Concept of three pass core of HPLWR [Schulenberg & Starflinger, 2012]
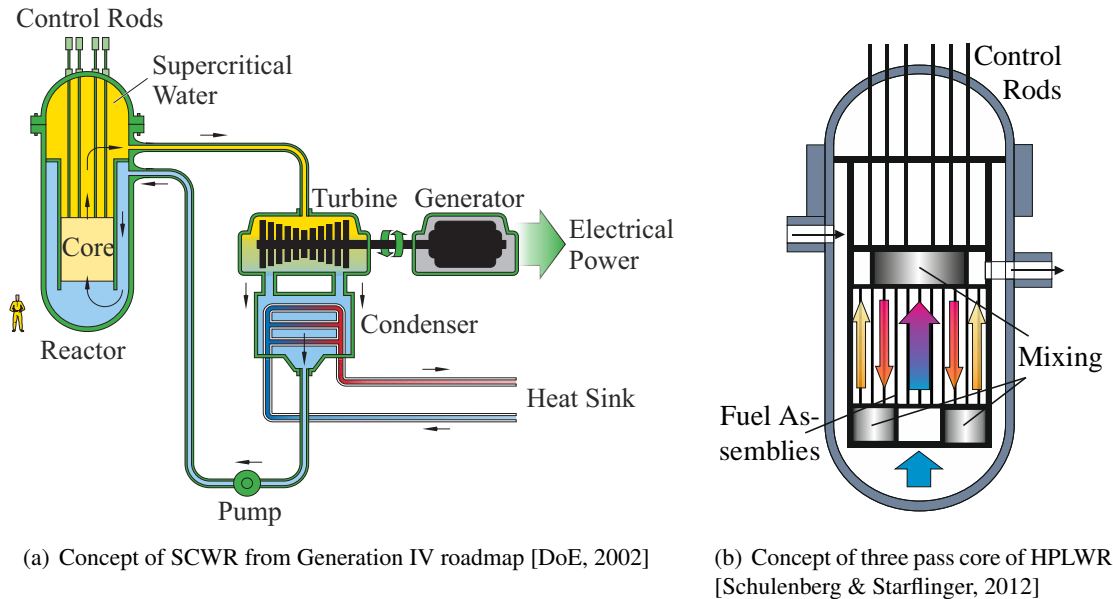
Figure 1.1.: Concept of SCWR with three pass core of HPLWR

The HPLWR is a three pass core as shown in figure 1.1 (b). Here, the coolant is entering the center fuel assemblies of the core from the bottom. The second heat-up step is in a downward flow in the fuel assemblies around the center. The third step is finally provided by an upward flow in the core periphery. The advantage of a multi pass core is the reduced hot channel factor achieved by the mixing after each heat up. This eliminates the hot streak and the next heat up is starting from a homogeneous mixture. Without exceeding coolant temperatures of $600\,°C$, an average core outlet temperature of $500\,°C$ could be achieved. [Schulenberg & Starflinger, 2012]. With this core outlet temperature, a net plant efficiency of $43.5\,\%$ and a net electrical output of 1 GW could be reached.

The core outlet temperature and the maximum of the transferred energy from the fuel to the coolant is effectively limited by the allowed temperature of the fuel cladding. For the latest version of the HPLWR, the wall temperature shouldn't exceed $650\,°C$ [Schulenberg & Starflinger, 2012]. Strong changes in thermo-physical properties of fluids passing the (pseudo-) critical point, as shown in chapter 2.1 figure 2.1, are causing an abnormal behavior in heat transfer when compared with conventional fluids. Due to high temperature peaks, the wall temperatures can exceed material limits which could led to hazardous reactor conditions. The reliable prediction of the heat transfer in every reactor conditions is a key factor for a safe and solid core design and is thereby the topic of this thesis.

1.2. Objective

Experiments are necessary to understand these heat transfer phenomena in order to develop and validate models for the heat transfer prediction. Experiments with water as coolant require test facilities which are very expensive and complex to construct, maintain and operate. Therefore, experiments are conducted with a model fluid as coolant to reduce pressure, temperature and conducting time. This means, however, that the data of the model fluid must be scaled to water conditions to satisfy the original task. From this, two main topics can be derived for this study. The first one is the investigation of heat transfer at supercritical conditions and critical heat flux (CHF) at high pressure up to the critical point with R134a and CO_2. The evaluation and possible modification of fluid-to-fluid scaling models with the produced data and available water data is the second main focus of this study. The thesis is structured as follows.

A brief introduction of the heat transfer at supercritical conditions will be given in chapter 2 with a review about conducted experiments and studies in this field. Methods for predicting the heat transfer will be introduced. Additionally, experiments and studies on critical heat flux at high pressures will be reviewed including methods for prediction. The state of the art of fluid-to-fluid scaling for data of heat transfer at supercritical conditions and CHF will be described. At the end of chapter 2, the lack of experiments in the literature will be identified which are needed for a better understanding of the heat transfer phenomena and for the assessment of the fluid-to-fluid scaling models.

In chapter 3, the setup for the measurements of the heat transfer at supercritical conditions of R134a and CO_2 and the critical heat flux in R134a will be described. The measurement procedures and the determination of parameters and heat transfer coefficient will be introduced. The measurement systems will be verified and checked using subcritical correlations and the heat balance method. A detailed investigation on the error propagation on all calculated parameters will be done.

In chapter 4, the regimes for the heat transfer at supercritical heat transfer will be defined. Issues in conducting and reproducibility of the data will be addressed. As a result, the data will be evaluated and selected for the further analysis.

The analysis of the measurements of the heat transfer at supercritical conditions will be presented in chapter 5. The observed phenomena will be discussed extensively. The produced data will be used to assess the prediction capability of 48 correlations. Difficulties of reproducibility and comparison with data from the literature will be shown and discussed.

The fluid-to-fluid scaling models for heat transfer at supercritical conditions will be assessed in chapter 6. For that purpose, the generated data from CO_2 and R134a will be scaled to water and compared with the existing water database. Reasons for deviations are investigated and discussed. An improved fluid-to-fluid scaling model will be introduced and assessed. For the assessment, a new method for interpolating the heat transfer coefficient (HTC) from a database will be introduced.

In chapter 7, the results of the experimental investigations of the critical heat flux at high pressures will be presented. The data will be used for the assessment of correlations developed for high pressures. Further, the fluid-to-fluid scaling law derived from Ahmad will be assessed using the 2006 CHF look-up table from Groeneveld et al. [Ahmad, 1973, Groeneveld et al., 2007].

The last chapter will summarize the results of this study. An outlook for further investigations and improvements for the understanding and prediction of the heat transfer near the critical point will be given. At the end a conclusion will be refereed to the motivation of this study.

2. Literature Review

In this chapter, the thermodynamic features of supercritical fluids and the heat transfer at supercritical conditions are explained. It is shown how the strong changes of the thermal-physical properties of the fluid influence the heat transfer at these conditions. The research progress work in the past focusing on experimental and theoretical work at this topic and on CHF is reviewed. Methods for predicting the heat transfer at supercritical conditions and the CHF are introduced. For both heat transfer topics, fluid-to-fluid scaling models are reviewed. The modeling fluids R134a and CO_2 are introduced and their properties are compared to water. Flow instabilities and their consequences on the heat transfer are discussed. At the end of this chapter, it is identified which researches are needed for an improved understanding of the topics.

2.1. Supercritical fluids

As the fluid is heated from subcritical to supercritical temperatures, it remains in a single phase because of the supercritical pressure. Therefore, the boiling crisis is physical eliminated. Although there is no phase change, the thermal-physical properties of water still undergo continuous but drastic variations in the vicinity of pseudo-critical temperature. Figure 2.1 shows the thermal-physical properties versus temperature at a pressure of 25 MPa for water.
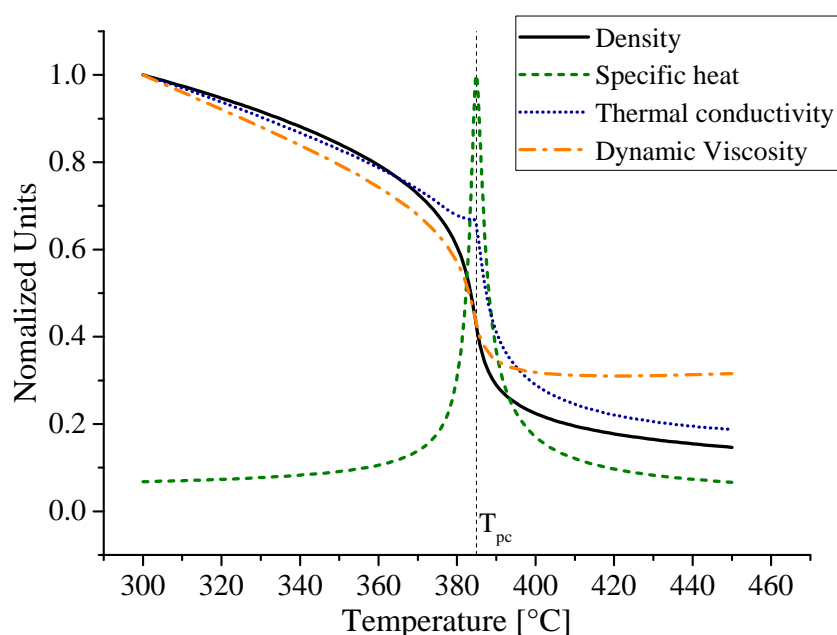
Figure 2.1.: Normalized properties around the pseudo-critical point of water at 25 MPa; data from REFPROP of NIST [Lemmon et al., 2007]

It can be seen that the density, thermal conductivity, and dynamic viscosity decrease dramatically when approaching the pseudo-critical point (384.9 °C at 25 MPa). For the thermal conductivity, there exists a small local maximum near the pseudo-critical point. This peak is getting smaller for increasing pressure until it vanishes. At the pseudo-critical temperature, the specific heat capacity reaches its maximum, which can be 10 times higher than at subcritical conditions. Density, thermal conductivity and dynamic viscosity are decreased by a factor of 3 to 5 from 350 °C to 410 °C.

(a) Change of specific heat capacity
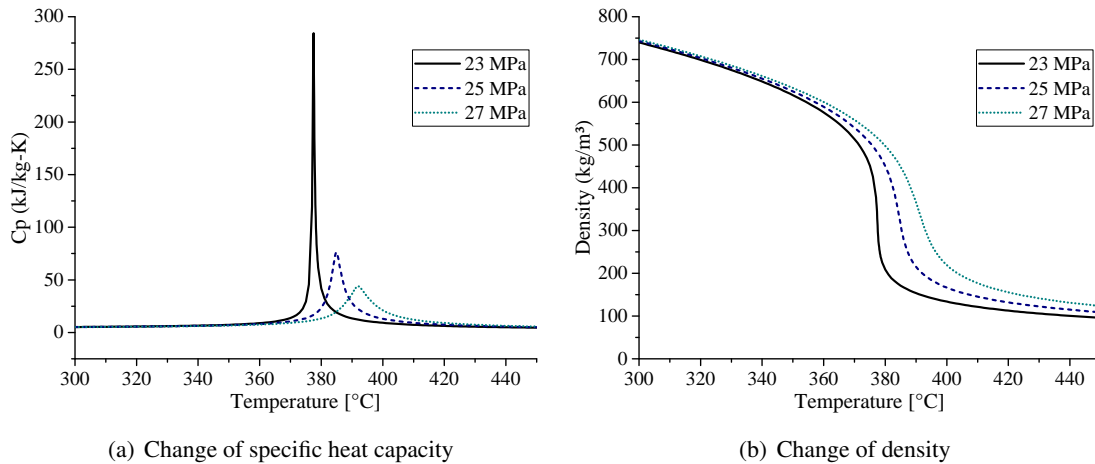
(b) Change of density

Figure 2.2.: Change of specific heat capacity and density of water at 23 MPa, 25 MPa, and 27 MPa versus temperature; data from REFPROP of NIST [Lemmon et al., 2007]

Figure 2.2 shows the influence of pressure on the variations of specific heat capacity (a) and density (b) overgoing the pseudo-critical temperature. As it can be seen in the figure 2.2, the gradients and maximum values increase as the pressure approaches the critical point. Additionally, the gradients and maximums are shifted to higher temperatures with increasing pressures. The maximums of the specific heat capacity define the pseudo-critical line. The maximum gradient of the density occurs at the pseudo-critical temperature. Viscosity and thermal conductivity are undergoing the same behavior as the density and are hence not shown. This means, the pseudo-critical line separates the supercritical region into a high density and a low density region, which are called "liquid-like" and "gas-like", respectively. The line and the regions are shown in figure 2.3.

As mentioned in chapter 1.1, the water in the reactor of a SCWR is at pressures above the critical point. The temperature increase of the HPLWR is shown in figure 2.3 plus the range of a Pressurized Water Reactor (PWR) and a Boiling Water Reactor (BWR). In the supercritical region, temperature and pressure of the water are above the critical point of 373.95 °C and 22.064 MPa.

The main usage of heat transfer with supercritical fluids was and still is as coolant in supercritical coal fired power plants, mostly motivated by the higher efficiency and thus lower power production costs. There are more application fields for supercritical fluids, which emphases the research at this field. Latest research fields of supercritical fluids are:

- supercritical steam generators with increasing efficiency

- nuclear rector concepts cooled with supercritical water

- fusion reactor cooled with supercritical water

- supercritical carbon dioxide as working fluid for cooling machines and air conditioning

- power production of geothermal energy with supercritical Organic Rankine Cycle

- waste heat recovery technology with supercritical Organic Rankine Cycle
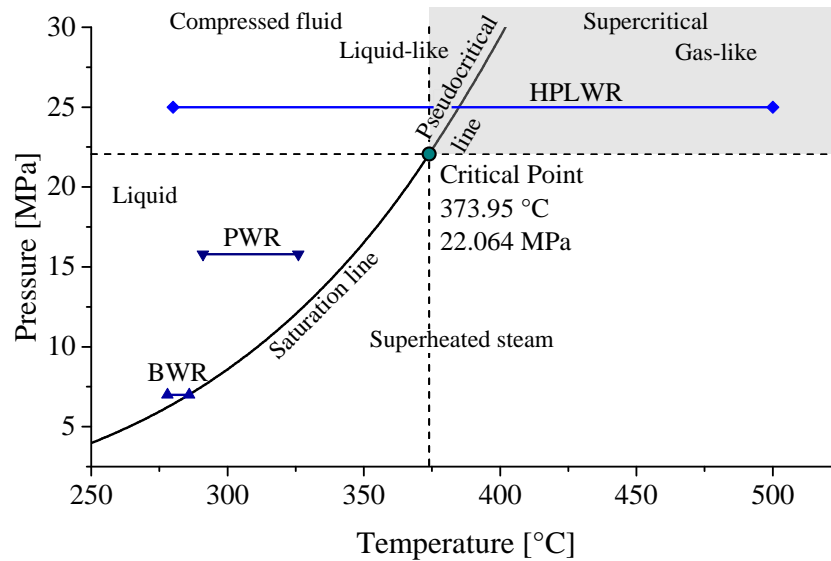
Figure 2.3.: Temperature and pressure conditions for light water reactors [Schulenberg & Starflinger, 2012]

- supercritical hydrocarbon fuel for advanced gas turbine engines, rocket engines and supersonic combustion ramjet

- supercritical helium as coolant for accelerator magnet cryostats and superconductors

- usage of supercritical fluids in the chemical and pharmaceutical industries

2.2. Heat transfer at supercritical conditions

First investigations about the heat transfer at supercritical conditions were performed in the late 1940s for example by Schmidt [Schmidt et al., 1946]. More investigations and experiments were conducted in the 1950s by Bringer and Dickinson et al. [Bringer & Smith, 1957, Dickinson & Welch, 1958]. In the 1960s more value and knowledge gaining studies at the heat transfer characteristics at supercritical conditions were published [Bishop et al., 1965, Hess & Kunz, 1965, Swenson et al., 1965, Hall et al., 1967, Herkenrath et al., 1967]. Highlighted must be the measurement of the velocity and density distribution in radial direction from Wood and Bourke [Wood & Smith, 1964, Bourke & Pulling, 1970] and the resulting influence of buoyancy at the heat transfer by Hall and Jackson [Hall & Jackson, 1969]. Further work was done by many other authors, which is discussed and summarized in this section.

2.2.1. Definitions for and distinction of heat transfer

Before discussing about heat transfer at supercritical conditions, a few definitions are needed and the exact kind of heat transfer must be clarified. Heat can be transfered via conduction, convection and radiation. In power system, as in a nuclear power plant, all three types of heat transfer exist. This study is focusing on convection with a fluid at supercritical conditions. Before describing the heat transfer in complex geometries, as the rod bundle for example, the occurring basic phenomena must be understood first. Therefore, simple geometries are used to investigate heat transfer phenomena. Since the heat transfer at supercritical conditions is not fully understood, this study focuses on the heat transfer of a fluid flowing upward in a tube at supercritical conditions.

Convection is the transport of heat by fluid motion. Displaced fluid molecules carry their inner energy from one place to another. The driving force of fluid motion can be a pressure gradient, surface tension or differences in density in combination with gravity (buoyancy). In general, there

are three types of convective flows: the forced convection, the natural or free convection and the mixed convection.

Forced convection is driven by an externally imposed force, which is often a pressure difference. Heat transfer coefficient and friction factor for such flows strongly depend on the Reynolds number Re and the Prandtl number Pr. The Reynolds number is the dimensionless ratio of inertial forces to viscous forces and is used to describe the flow pattern. The Prandtl number is the dimensionless ratio of momentum diffusivity to thermal diffusivity. It describes which type of heat transfer overweights in a fluid: convection or conduction. The Reynold and Prandtl number are defined with the diameter of the tube as characteristic length in equation 2.1 and 2.2 with the density ρ, the velocity u, the dynamic viscosity μ, the specific heat capacity c_p and the thermal conductivity λ.

$$Re = \frac{\rho u d}{\mu} = \frac{Gd}{\mu} \qquad (2.1)$$

$$Pr = \frac{c_p \mu}{\lambda} \qquad (2.2)$$

Natural or free convection is driven by the local buoyancy force induced by differences in density in combination with gravity. In the same fluid, density differences are determined by temperature differences. The characteristic governing non-dimensional parameters are the Grashof number and Prandtl number. Since there is no imposed external pressure gradient, the velocity field solution totally depends on the local density gradient caused by the temperature field. The Grashof number is the dimensionless ratio of buoyancy force to viscous force and quantifies the opposing forces. It is defined in equation 2.3 with the gravitational constant g, the thermal expansion coefficient β, the kinematic viscosity η and the temperature difference between bulk (T_b) and wall (T_w).

$$Gr = \frac{g \beta (T_w - T_b) d^3}{\eta^2} \qquad (2.3)$$

Mixed convection is a combination of an imposed flow (forced convection) and a buoyancy driven flow (natural convection). Typical governing numbers describing the heat transfer are the Reynolds number, Grashof number and Prandtl number. Throughout the literature, other important non-dimensional numbers such as the non-dimensional heat flux, buoyancy parameter, acceleration parameter, etc. are used by different authors. This will be discussed in section 2.2.2. In addition, it can be seen that forced convection and natural convection are the two extremes of the more general case of mixed convection [Verein Deutscher Ingenieure, 2013].

To describe the heat transfer from a heated wall to a flowing fluid, the heat transfer coefficient (HTC) α is defined in equation 2.4. Here, a given α and heat flux q determine the difference between wall and bulk temperature. Thus, a system with a small heat transfer coefficient induces a big temperature difference between wall and bulk to transport the same heat flux. Regarding the limitations of the wall materials, small heat transfer coefficients should be avoided at high bulk temperatures.

$$\alpha = \frac{q}{T_w - T_b} \qquad (2.4)$$

The heat flux used for the calculation of the heat transfer coefficient is calculated by equation 2.5 with the rate of heat flow $\dot{Q}$ and the area for the heat transfer A_w.

$$q = \frac{\dot{Q}}{A_w} \qquad (2.5)$$

The Nusselt number Nu is a dimensionless number to describe the convective heat transfer at a solid surface to a fluid compared to the heat conduction of the fluid at the same conditions. It is used to compare the heat transfer between different systems, geometries and fluids. Therefore, it is a key characteristic to describe the convection heat transfer. In equation 2.6, the Nu is defined with the diameter d as characteristic length.

$$Nu = \frac{\alpha d}{\lambda_b} \qquad (2.6)$$

Instead of using the mass flow rate ṁ, the mass flux G is often given for easier comparison in the literature. It is the mass flow rate divided by the flow cross section A_b, as shown in equation 2.7.

$$G = \frac{\dot{m}}{A_b} = \frac{4 \cdot \dot{m}}{\pi \cdot d^2} \qquad (2.7)$$

2.2.2. Heat transfer deviation

Heat transfer at supercritical conditions shows an abnormal behavior compared to conventional fluids. To explain the difference, the normal heat transfer (NHT) must be defined first. Normal heat transfer is characterized by heat transfer coefficients similar to those of subcritical convective heat transfer in a single-phase. This means that there is no phase change and small changes of the fluid properties occur [Pioro & Duffey, 2007]. In this case, the wall temperature increases monotonically with small changes in the gradient such as the wall temperature trend for low heat flux in figure 2.4. Many authors declare the normal heat transfer as described by equation 2.8 from Dittus and Boelter [Dittus & Boelter, 1985]. In that case, the HTC trend increases monotonically until the maximum at the pseudo-critical bulk enthalpy and decreases monotonically after. Figure 2.5 (a) shows the HTC trend of the Dittus-Boelter correlation.
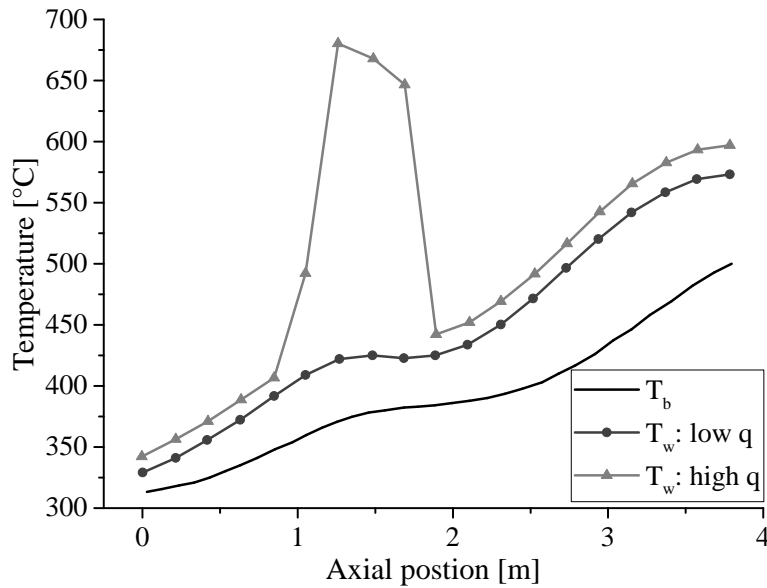
Figure 2.4.: Wall temperatures of low and high heat flux from Cheng and Schulenberg with water [Cheng & Schulenberg, 2001]

$$Nu_b = 0.023 \, Re_b^{0.8} \, Pr_b^{0.4} \qquad (2.8)$$

It is well accepted that the HTC at supercritical conditions deviates from the Dittus-Boelter correlation, especially near the pseudo-critical point. Cheng and Schulenberg [Cheng & Schulenberg,

2001] found in their literature review that the heat transfer coefficient of most experiments follow the trend of figure 2.5 (b) for low and high heat fluxes. In the literature, authors divide the heat transfer at supercritical conditions into 3 regimes: normal heat transfer (NHT), heat transfer deterioration (HTD) and heat transfer enhancement (HTE).
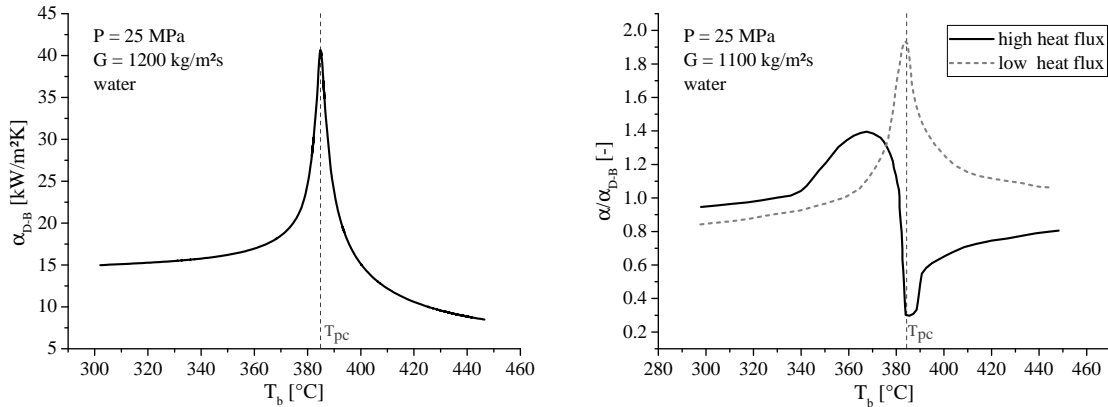
(a) Heat transfer coefficient according to the Dittus-Boelter correlation 2.8

(b) Ratio of heat transfer coefficient of experimental data to Dittus-Boelter

Figure 2.5.: Ratio and heat transfer coefficient of Dittus-Boelter correlation for water at 25 MPa [Cheng & Schulenberg, 2001]

If the HTC is higher than the one of the Dittus-Boelter equation, the regime is called HTE. This can be seen in figure 2.5 (b) for the low heat flux near the pseudo-critical bulk temperature T_{pc}. If the HTC is smaller than of the Dittus-Boelter equation, the regime is called HTD. This can be seen as a minimum of the HTC ratio, as illustrated in figure 2.5 (b) for the high heat flux. As seen in equation 2.4, a minimum in the HTC leads to a wall temperature peak. Therefore, another proposed way to identify HTD is to scan the wall temperature for these peaks. Obvious peaks, like the one seen in figure 2.4 for the high heat flux, are dedicated to the HTD. Depending on the parameters like heat flux, mass flux, pressure and inlet temperature, the deviations from the normal heat transfer appears in different ways and strength. There exists no unique definition for the onset of deterioration or enhancement. This is due to the rather smooth reduction or enhancement of the HTC compared to the boiling crisis and the missing change of heat transfer mode at supercritical conditions. Because of that, the 3 heat transfer regimes (NHT, HTD, HTE) can't be distinguished exactly.

The majority of authors have detected HTD by observing the occurrence of temperature peaks along the test section [Ackerman, 1970, Lee & Haller, 1974]. As Kline and Schatte et al. summarized, there is no established criterion for the amplitude of a peak to be classified as deteriorated [Kline, 2017, Schatte et al., 2016]. Another widely used method is from Koshizuka et al. [Koshizuka et al., 1995]. Here, the heat transfer coefficient or the Nusselt number is compared with a reference number calculated by a conventional correlation like Dittus-Boelter, which is defined in equation 2.8. Thereby, the ratio should be smaller than 1 or often smaller than 0.3 as shown in equation 2.9 [Koshizuka et al., 1995]. This definition is the most common one according to the literature review of Schatte et al. [Schatte et al., 2016].

$$\frac{\alpha}{\alpha_{DB}} < 0.3 \tag{2.9}$$

Most known are the sharp peaks of the wall temperature in the first half of the heated tube, as mentioned in almost every experimental publication. Therefore, some authors proposed that the heat transfer deterioration in the entry region of a turbulent tube flow is because of the development of the thermal boundary layer. The length of this thermal entry region decreases with increasing

Reynolds number [Miropolsky et al., 1966]. This peaks can also occur at the end of the test section as Goldman observed in his experiments [Goldmann, 1961]. Broad peaks were found, too. Yamashita et al. observed that broad peaks formed over a wide range of bulk fluid enthalpies below the pseudo-critical point and sharp peaks formed at lower flow rates [Yamashita et al., 2003]. It is also possible that the HTD spans the entire test section.

Even that the idea of the pseudo-boiling did not produce useful expressions for analogy-based models for heat transfer at supercritical conditions, the finding of Ackerman for the onset of HTD $T_b < T_{pc} < T_w$ remains true [Ackerman, 1970]. The deviations in heat transfer occur because of the drastic change of the thermal-physical properties of the coolant. Because the variations are continuous, the heat transfer mechanism can't change. Only different effects can influence the heat transfer differently strong depending on the boundary conditions.
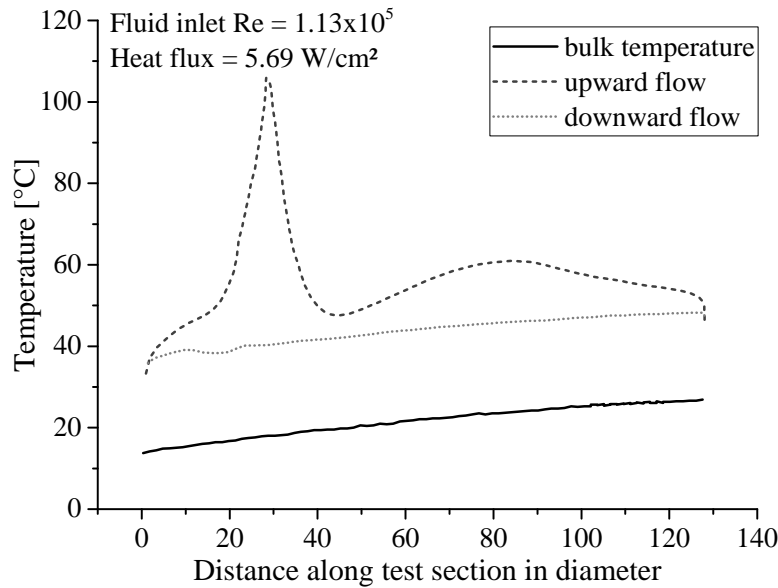
Figure 2.6.: Wall temperatures of upward and downward flow in CO_2 from Hall [Hall & Jackson, 1969]

Miropolsky et al. found that the wall temperature peaks which occurred at upward flow did not occur at downward flow [Miropolsky et al., 1966]. This is shown in figure 2.6. Thus, Shitsman [Shitsman, 1967] and Hall [Hall & Jackson, 1969] proposed explanations involving buoyancy effects on heat transfer at supercritical conditions. Experiments of Shiralkar et al. [Shiralkar & Griffith, 1968, Shiralkar & Griffith, 1970] showed also broad peaks for downward flow. The sharp peaks occur only at upward flow, but the broad peaks occur in both directions. Therefore, the sharp peaks are influenced by the buoyancy and the broad peaks by bulk flow acceleration as Jackson and Hall concluded [J.D. Jackson, W. B. Hall, 1979, Jackson, 2013a].

Kurganov et al. [Kurganov et al., 2013, Kurganov et al., 2014] found that the qualitative behavior of the HTC and wall temperature is dominated by the mass flux. The authors classified the heat transfer trends in six different groups according to their wall temperature trend appearance. Therefore, Kurganov et al. defined a new dimensionless number which is a combination of the Archimedes and Galileo number. Kurganov et al. proposed that the different qualitative behavior of the wall temperatures is due to the varying influence of the buoyancy and the bulk flow acceleration. The first 2 groups, which represent small mass fluxes approximately up to $300\,kg/m^2 s$, are dominated by buoyancy forces. At high mass fluxes from approximately $2000\,kg/m^2 s$, represented by group 5 and 6, the acceleration effects dominate the heat transfer. In group 3 and 4 both effects can lead to a heat transfer deterioration. The qualitative wall temperature trends are shown in figure 2.7.
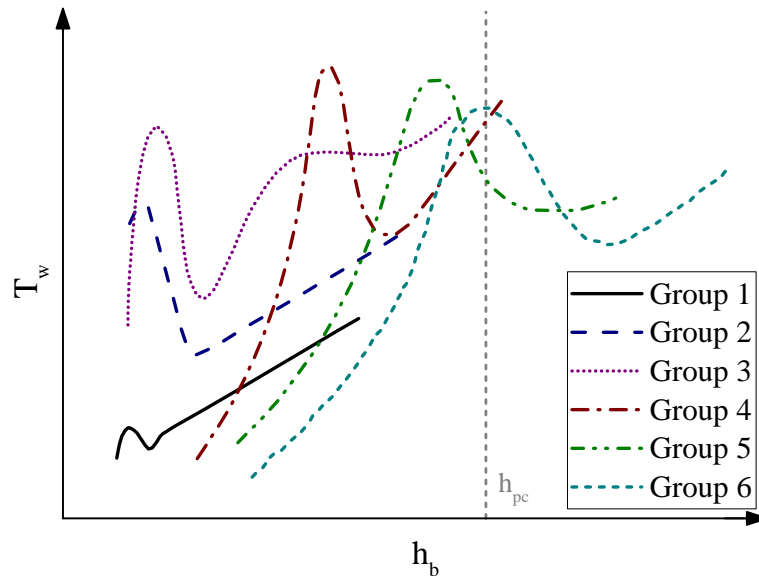
Figure 2.7.: Qualitative wall temperature trends for the six groups identified by Kurganov et al. using a derivation of the Archimedes number [Kurganov et al., 2014]

Jackson developed and improved a model for predicting the heat transfer coefficient for heat transfer at supercritical conditions over a long period. To improve the prediction capability of his model, he promoted the explanations for HTD. Thus, a lot of papers addressing this issue were published by Jackson et al. [J.D. Jackson, W. B. Hall, 1979, Jackson & Hall, 1979, Jackson et al., 1989, Jackson, 2011, Jackson, 2013b, Jackson, 2013a, Jackson, 2017]. Based on the statements of Petukhov et al. [Petukhov, 1970, Petukov et al., 1988], Jacksons states two main mechanisms for HTD: the thermally-induced bulk flow acceleration and the mixed convection mechanism (buoyancy aided flow). Both can cause a reduction in the turbulence transport of momentum and energy which leads to a laminarization of the flow near the wall. Both mechanisms will be described in detail in the following subsections as a state of the art explanation.

2.2.2.1. Enhancement

Enhancement in the heat transfer can be observed in experiments with high mass fluxes and low heat fluxes. Increasing the heat flux impairs the enhancement. This observation can be seen in the experiments of Yamagata [Yamagata et al., 1972]. The first idea was that in these cases the high specific heat spans the whole boundary layer. This results in a small temperature gradient from the wall to the bulk [Jackson & Hall, 1979]. Later, Jackson proposed the onset of enhancement by the increase of the buoyancy number beyond the range of the occurrence of the HTD [Jackson, 2011]. Enhancement and deterioration can be observed simultaneously along the test section. Often enhancement occurs downstream of local deterioration. Zhang et al. [Zhang et al., 2018] observed a different heat transfer behavior for low mass fluxes ($< 300 \, \text{kg/m}^2\text{s}$) with supercritical CO_2. The authors reported a change from HTD to HTE as the mass flux is reduced to $100 \, \text{kg/m}^2\text{s}$ and the heat transfer can be increased by the factor of 5 near the pseudo-critical point. This heat transfer transition at lower mass flux was mainly induced by the combined effects of strong buoyancy and the high heat capacity [Zhang et al., 2018].

Azih et al. [Azih et al., 2012] showed with direct numerical simulations in a zero-pressure-gradient boundary layer an enhancement in heat transfer. At certain supercritical states, the authors observed an increase of coherent vortical flow structures which results in a stronger mixing near the wall. This produces a less stable flow compared to cases of normal heat transfer and leads to HTE. This is due to the viscosity gradient imposed by the heat flux [Azih et al., 2012].

2.2.2.2. Buoyancy influenced flow

The effect of buoyancy on turbulent convective heat transfer in vertical tubes is complicated. Buoyancy requires a non-uniform density distribution in a fluid and is caused by gravity. It modifies the velocity profile of a fluid flowing in a heated tube and affects the shear stress and turbulence distribution. This can lead to HTD as described below [Petukov et al., 1988, Jackson, 2011].

The following description can be seen step by step in figure 2.8 for a deteriorated case, where the trends at the wall temperature peak are marked. Figure 2.8 shows the dimensionless numbers versus the dimensionless wall distance y^+ with y as distance from the wall and u_f as friction velocity. In a heated tube exists a low-density layer near the wall. This low-density layer grows thicker along the heated tube while the densities in the core fluid remains high (fig. 2.8 (b)). A buoyant force is generated on the low-density layer which results in a modified cross section velocity profile due to the acceleration of the layer near the wall (fig. 2.8 (c)). As the velocity gradient is reduced, the shear stress is consequently reduced, too (fig. 2.8 (d)). If the shear stress is reduced to such an extent that turbulence generation near the wall is strongly impaired, the efficiency of the heat transfer can be drastically reduced (fig. 2.8 (e)) [Jackson, 2013a].

If the low-density layer grows further, M-shape velocity profiles occur. This leads the shear stress to change the sign in the core, as observed in measurements [Wood & Smith, 1964] or numerical experiments [Cheng et al., 2017, Zhou, 2014] and described in subsection 2.2.4 or shown in figure 2.8 (c). As a result, the turbulence production increases, heat transfer recovers and sometimes transition to HTE occurs. Therefore, this theory can explain phenomena leading to HTD as well as phenomena leading to heat transfer recovery and the HTE downstream [Jackson, 2013a]. This implies that the buoyancy effect also has a direct influence on the turbulence structural effect as well as on the mean flow external effect.

Jackson and Hall [J.D. Jackson, W. B. Hall, 1979] postulated equation 2.10 to identify the influence of buoyancy on the heat transfer. The authors proposed the limit of 10^{-5}, below which the buoyancy effect is negligibly small, and claimed a good predictability with their data.

$$\frac{\overline{Gr_b}}{Re_b^{2.7}} < 10^{-5} \tag{2.10}$$

where

$$\overline{Gr_b} = \left(\frac{\rho_b - \overline{\rho}}{\rho_b}\right)\frac{gd^3}{\eta_b^2} \tag{2.11}$$

with

$$\overline{\rho} = \frac{1}{T_w - T_b}\int_{T_b}^{T_w} \rho_b\, dT \tag{2.12}$$

Later Jackson and Hall modified their criterion for the onset of buoyancy effects with introducing the buoyancy number $\overline{Bu_b}$, defined in equation 2.13, which gives good agreements with previous findings [J.D. Jackson, W. B. Hall, 1979]. Jackson further proposed that, if the wall temperature exceeds the pseudo-critical value, equation 2.10 is the corresponding criterion.

$$\overline{Bu_b} = \frac{\overline{Gr_b}}{Re_b^{2.7}Pr_b^{0.5}} \tag{2.13}$$

Based on their derivation from the shear stress influence on heat transfer, Jackson and Hall [J.D. Jackson, W. B. Hall, 1979] suggested that the reduction of the HTC is greater than 5 % at $\overline{Bu_b} \geq 10^{-5}$. This was verified by identifying HTD using the ratio of the experimental to the predicted Nusselt number: $Nu_{exp}/Nu_{pre} < 1$. Huang and Li [Huang & Li, 2018] found in their literature

review that either equation 2.10, equation 2.13 or modified versions are often used as HTD determination. Watts and Chou [Watts & Chou, 1982] confirmed the threshold of 10^{-5} by observed wall temperature peaks. Bae et al. determined the threshold of 2×10^{-5} for $\overline{Bu_b}$, above HTD was observed in their experiments.
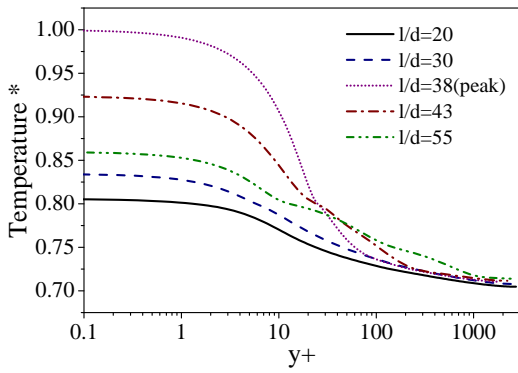
(a) Normalized temperature versus normalized distance from wall
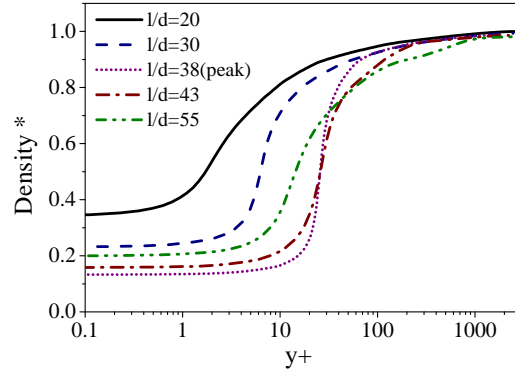
(b) Normalized density versus normalized distance from wall
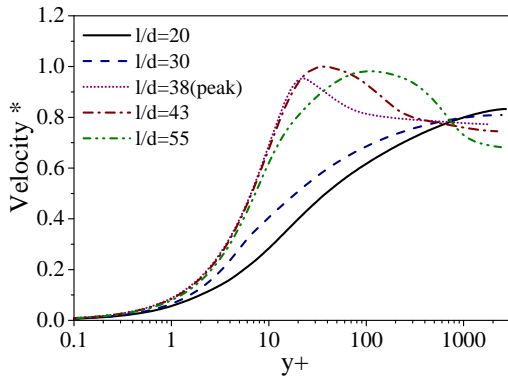
(c) Normalized velocity versus normalized distance from wall
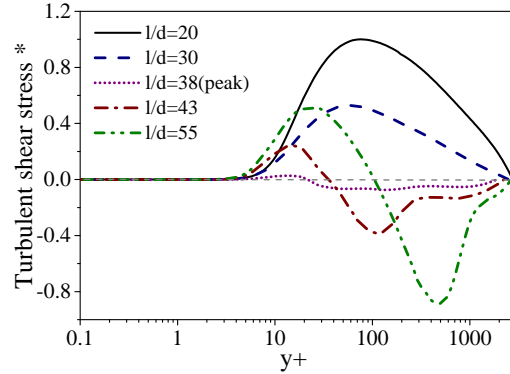
(d) Normalized shear stress versus normalized distance from wall
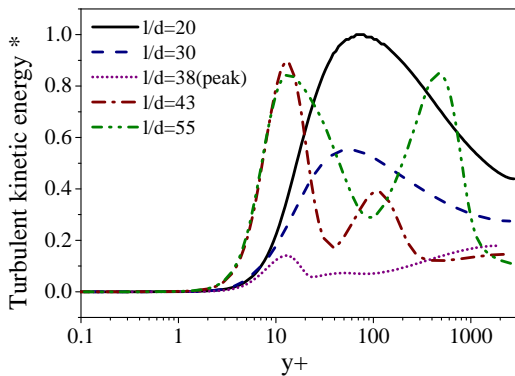
(e) Normalized turbulent kinetic energy versus normalized distance from wall
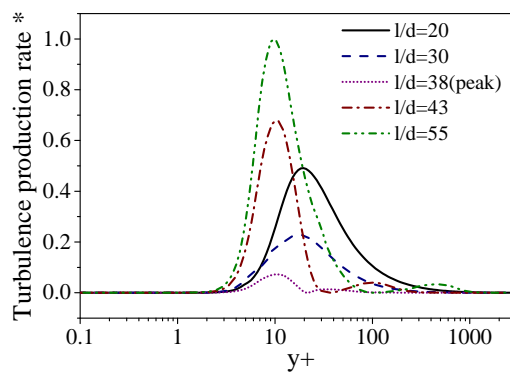
(f) Normalized turbulence production rate versus normalized distance from wall

Figure 2.8.: Properties normalized by the maximum value versus normalized distance from wall y^+ (yu_f/η) for different locations in a deteriorated heat transfer case, at P=4.59 MPa, G=508 kg/m²s, q=50 kW/m² and d=10 mm in R134a (* means that the parameters were normalized by the maximum value in each figure) from [Tian et al., 2018]

2.2.2.3. Thermally-induced bulk flow acceleration

At high mass fluxes, high heat fluxes and in tubes with relative small diameters, the thermally-induced bulk flow acceleration gets more significant than the HTD caused by buoyancy forces. As the fluid progresses in a heated tube, it gains enthalpy and its bulk temperature raises. This reduces the fluid density along the test section. At supercritical pressures, the density decreases strongly with temperature, as seen in figure 2.2. The density even varies more near the critical pressure. Consequently, the density reduction is further intensified by pressure losses due to friction along the tube, especially in small tubes. To maintain a constant mass flow rate, the flow must accelerate to compensate the density reduction [Jackson, 2011, Jackson, 2013b, Jackson, 2017].

(a) Velocity versus normalized distance from wall

(b) Turbulent kinetic energy versus normalized distance from wall
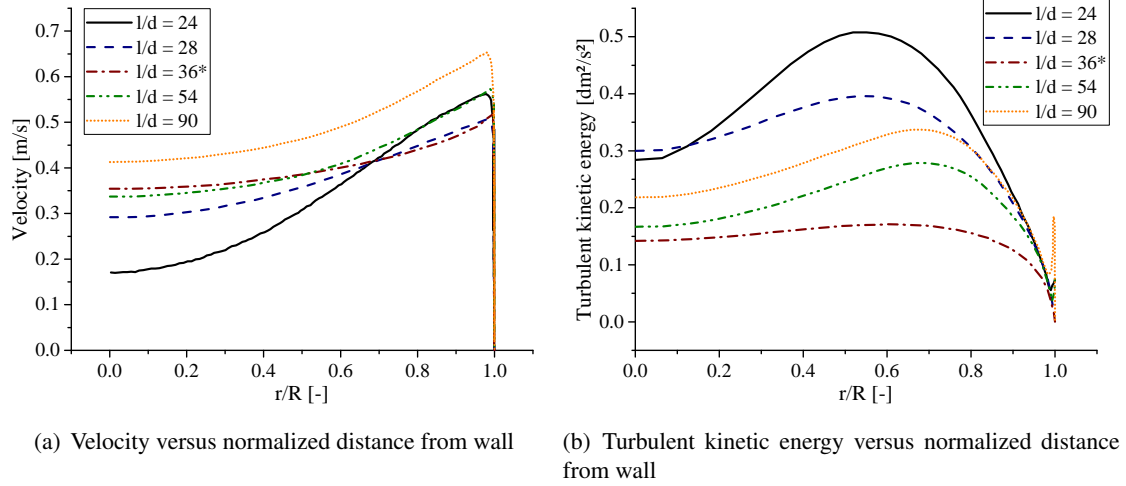
Figure 2.9.: Velocity and turbulent kinetic energy versus normalized distance from wall for a deteriorated heat transfer case, second broad peak, at P=7.44 MPa, G=311 kg/m^{2}s, q=51 kW/m^2, d=22.8 mm in CO_2 with * peak position from [Cheng et al., 2017]

This significant flow acceleration requires an additional applied axial pressure difference. However, it is well known that the fluid velocity is smaller in the boundary layer than in the core. The resulting pressure gradient near the wall is greater than needed to accelerate the flow. Thus, the shear stress across the flow has to undergo an adjustment to balance the excess pressure differences. As a result, the shear stress decreases faster with increasing radial distance from the wall than in a flow without acceleration [Cheng et al., 2017]. Due to the smaller shear stress near the wall, the turbulence production is reduced. That leads to a reduction of the heat transfer effectiveness [Jackson, 2011, Jackson, 2013b, Jackson, 2017]. This can be seen in figure 2.9, where HTD occurs at the normalized distance of 36. Unlike the buoyancy induced HTD, the HTD caused by thermally-induced bulk flow acceleration can occur in upward and downward flow.

Jackson proposed a threshold above which the effect of thermally-induced bulk flow acceleration on heat transfer could be determined. The equation for the criterion is as follows [Jackson, 2013a]:

$$Ac_b = \frac{Q_b}{Re_b^{1.625} Pr_b} \tag{2.14}$$

with

$$Q_b = \frac{q\beta_b d}{\lambda_b} \tag{2.15}$$

If $Ac_b \geq 4 \times 10^{-6}$, the effect of thermally-induced bulk flow acceleration on heat transfer is greater than 2 % [Jackson, 2013a].

2.2.2.4. Correlations for onset of HTD

For the technical design of supercritical steam generators, the knowledge of the onset of HTD is essential. The high increase of wall temperature induced by the HTD or temperature fluctuations can lead to a significant lifetime reduction. Therefore, many authors screened their or available experimental data using one or more criteria to develop a prediction method for the onset of HTD based on the input parameters like mass flux, heat flux and pressure. In the previous sections, the criteria for determination of HTD have been described. More criteria are given in the review of Huang [Huang & Li, 2018] or the studies of Kline [Kline, 2017, Kline et al., 2018].

One of the first authors to determine a correlation for the onset of HTD was Vikhrev at al. in 1967 [Vikhrev et al., 1967]. The authors proposed that the onset of HTD for the heat flux q in kW/m^2 is proportional to the mass flux G in kg/m^{2}s, as seen in equation 2.16.

$$q_{HTD} = 0.4G \tag{2.16}$$

It seems that the onset of HTD follows a power law from the form of equation 2.17 with the heat flux in kW/m^2 and the mass flux in kg/m^{2}s. In the literature the constant a, the power b were fitted and correction factors F were included for the influence of diameter or pressure. The most known and cited correlation is from Yamagata et al. [Yamagata et al., 1972] with a=0.2 and b=1.2 without a correction factor.

$$q_{HTD} = aG^b F \tag{2.17}$$

However, it should be noted that, due to the dimensional parameters, most correlations are only valid for the fluid they were fitted for. Only one correlation was found to be applicable for different fluids. Kirillov and Grabezhnaia [Kirillov & Grabezhnaia, 2006] used the ratio of the molecular weight M of a fluid to the reference value of water to determine the onset of HTD shown in equation 2.18. The authors mention that the correlation applicability was checked for water, carbon dioxide and R-12.

$$q_{HTD} = 0.6 \frac{M_{H_2O}}{M} G \tag{2.18}$$

The latest correlation for the onset of HTD in water was developed from Schatte et al. [Schatte et al., 2016]. The authors stated that their correlation performs better than any other one by using water data from the open literature for the assessment. The correlation is given in equation 2.19.

$$q_{HTD} = 1.942 \cdot 10^{-6} \cdot G^{0.795}(30 - d)^{0.339} \left(\frac{c_{p,pc}}{\beta_{pc}}\right)^{2.065} \tag{2.19}$$

Dongliang et al. [Dongliang et al., 2018] published an improved version for the heat flux of heat transfer deterioration q$_{HTD}$ (kW/m^2), which includes the mass flux G (kg/m^{2}s), diameter d (mm) and pressure P (MPa) but the inlet temperature T$_{in}$ (ÂřC) as well. The correlation shows the highest prediction accuracy with their accumulated data and is described in equation 2.20.

$$q_{HTD} = 8255.2117 \cdot G^{0.8325} d^{-0.4958} P^{-0.7486} T_{in}^{-0.8125} \tag{2.20}$$

More correlations are listed in the paper of Schatte et al. or in the thesis of Kline [Schatte et al., 2016, Kline, 2017] and are not mentioned here.

2.2.3. Previous reviews about heat transfer at supercritical conditions

In this section, the most important reviews and outcomes are discussed to give an overview about the studies in the field of heat transfer at supercritical conditions. A selected list of reviews about heat transfer at supercritical conditions is given in table 2.1.

Table 2.1.: Reviews about heat transfer at supercritical conditions

Authors	Year	Main emphases
Hall, Jackson [Hall et al., 1967]	1967	Experiments, correlations, theory
Petukhov [Petukhov, 1970]	1970	Russian experiments, correlations, theory, pressure drop, constant properties
Jackson, Hall [J.D. Jackson, W. B. Hall, 1979, Jackson & Hall, 1979]	1976	Experiments, correlations, theory, buoyancy, scaling
Jackson et al. [Jackson et al., 1989]	1989	Experiments, correlations, theory, buoyancy, HTD, simulations
Pitla et al. [Pitla et al., 1998]	1998	CO_2 only, experiments, correlations, theory and pressure drop
Kirillov [Kirillov, 2000]	2000	Russian experiments, correlations, theory, power plant concept, pressure drop, corrosion
Cheng, Schulenberg [Cheng & Schulenberg, 2001]	2001	Experiments, simulations, correlations, HTD, HPLWR, scaling
Pioro, Duffey [Pioro et al., 2004a, Pioro et al., 2004b, Pioro & Duffey, 2005, Duffey & Pioro, 2005]	2004, 2005	Experiments, correlations, theory, pressure drop, HTD
Pioro, Duffey [Pioro & Duffey, 2007]	2007	Concepts, experiments, correlations, theory, pressure drop, HTD, flow stability
Löwenberg [Löwenberg, 2007]	2007	Experiments, correlations, theory, HTD, look-up table
Oka et al. [Oka et al., 2010]	2010	Concepts, core, plant dynamics, experiments, simulations, materials
Jäger et al. [Jäger et al., 2011]	2011	Experiments, correlations, simulations, HTD
Schulenberg, Starflinger [Schulenberg & Starflinger, 2012]	2012	HPLWR, core, plant dynamics, simulations
Yoo [Yoo, 2013]	2013	Experiments, correlations, theory, simulations, DNS
IAEA-TECDOC-1746 [International Atomic Energy Agency, 2014]	2014	Concepts, experiments, correlations, theory, pressure drop, critical flow, HTD, scaling, simulations
Rahman et al. [Rahman et al., 2016]	2016	Experiments, correlations, simulations, HTD, flow between fuel rods
Cabeza et al. [Cabeza et al., 2017]	2017	CO_2 only, experiments, correlations, heat exchanger
Huang, Li [Huang & Li, 2018]	2018	Experiments, correlations for Bu and HTD

The first review about heat transfer at supercritical conditions was published by Hall and Jackson [Hall et al., 1967]. The authors found some discrepancies between experimental data made under similar conditions. Due to that, Hall mentioned the importance of knowing the heat transfer mechanism at supercritical conditions. The following reviews of Jackson and Hall [J.D. Jackson, W. B. Hall, 1979, Jackson & Hall, 1979] summarized and discussed very well the knowledge about the phenomena at heat transfer at supercritical conditions at that time. These reviews show the variations of the thermal-physical properties at supercritical pressure in detail and explain their influence on heat transfer. Jackson and Hall explained the deviation from normal heat transfer with present buoyancy forces and thermoacoustic effects. The authors developed a correlation to predict the deteriorated heat transfer triggered by buoyancy forces which is still used and shown in equation 2.10. Jackson and Hall also established the foundation for the fluid-to-fluid scaling by defining dimensionless numbers which must be satisfied for similarity between two systems. This will be shown in detail in subsection 2.4.3.

Russian studies and outcomes are collected and translated from Pethukov and Kirillov in their reviews [Petukhov, 1970, Kirillov, 2000]. This made the Russian knowledge and data accessible for the western world. Also Pioro and Duffey included Russian publications in their reviews. The authors claimed to include 282 Russian publications from total 450 references in their literature reviews [Pioro & Duffey, 2005]. Pioro and Duffey publicized many reviews regarding different topics like experiments in water [Pioro & Duffey, 2005], pressure drop [Pioro et al., 2004b], correlations [Duffey & Pioro, 2005] and experiments in CO_2 [Pioro et al., 2004a]. The book of Pioro and Duffey [Pioro & Duffey, 2007] must be highlighted. The authors gathered the most experiments, but also described the used facilities in detail. Additionally, the authors give a lot of recommendations for building a facility, test section, measurement devices and conduction the heat transfer experiments at supercritical conditions.

The studies for the HPLWR from Schulenberg and other projects at Forschungszentrum Karlsruhe from Cheng, Löwenberg and Jäger [Cheng & Schulenberg, 2001, Löwenberg, 2007, Jäger et al., 2011] form another set of reviews. The results were used in the HPLWR Design and Analysis book from Schulenberg and Starflinger [Schulenberg & Starflinger, 2012]. However, this book focuses more on the concept, core design and the power plant itself rather on thermal-physics alone. Therefore, a lot of simulations are included.

The book of Oko [Oka et al., 2010] is a huge collection of information on heat transfer at supercritical conditions as well as related findings. It is more focused on the whole power plant and its dynamic behavior in different situations like the book about the HPLWR . Many topics as core design, safety, start-up, materials and heat transfer at supercritical conditions are discussed.

There are two specific reviews about CO_2 from Pitla and Cabeza et al. [Pitla et al., 1998, Cabeza et al., 2017]. The review of Yoo [Yoo, 2013] focuses on CO_2 as well. It is obvious that CO_2 plays the second important role after water as fluid for heat transfer at supercritical conditions. This can be substantiated by the fact that most publications and experimental data are about CO_2 heat transfer. This is due to the easy access and handling of CO_2 combined with its small global warming potential and harmlessness as well as its planned use for power cycles.

The review of Huang et al. [Huang & Li, 2018] focuses only on different observations, correlations and thresholds of different authors about the effect of buoyancy. The authors concluded that there is no consensus on the buoyancy criteria. In general, the criteria of Jackson and Hall $Bu_b < 10^{-5}$ [J.D. Jackson, W. B. Hall, 1979] works well for vertical round tubes [Huang & Li, 2018].

2.2.4. Experiments about heat transfer at supercritical conditions

First experiments were conducted in 1950s and early 1960s from Dickinson [Dickinson & Welch, 1958], Goldmann [Goldmann, 1961] and Shitsman [Shitsman, 1963]. The motivation was to build a high efficient steam generator. Goldman and Shitsman observed an impairment of the heat

transfer compared to the Dittus-Boelter equation dependent on the heat flux. Goldman also stated to hear a whistle sound when the impairment occurred [Goldmann, 1961]. The heat transfer at supercritical conditions depends on mass flux, heat flux, bulk enthalpy, pressure and tube diameter [J.D. Jackson, W. B. Hall, 1979].

Many experiments about heat transfer at supercritical conditions have been conducted in the past with water and CO_2 as the most common coolants. A lot of reviews collected and evaluated this huge number of experiments. This reviews are listed in table 2.1. Pioro and Duffey [Pioro & Duffey, 2007] found more than 100 data sets for heat transfer at supercritical conditions. The problem is that only a minority of these data are available. This is due to loss, non-digital, unusable filing or limited release attributed by data classification as proprietary or commercial. Many data are only available as graphs, often done manually. Through the digitalization an unknown uncertainty is added to the data. Often the data reduction and measurement uncertainties are not specified in the publications. This limits the reliability of the accessible data further [Zhao et al., 2017].

2.2.4.1. Experiments with water, CO_2 and R134a

Experiments conducted with water as coolant, which data are available, are described by Zhao et al. [Zhao et al., 2017]. A lot of experiments were conducted with CO_2 as Krasnoshchevkov, Bourke, Fewster, Bae, Mokry, Kim, Eter, Zahlan, Kline et al. and are not discussed in detail [Krasnoshchekov et al., 1964, Bourke, P. and D. Pulling, 1971, Fewster, 1976, Kim et al., 2007a, Bae & Kim, 2009, Mokry et al., 2009, Zahlan et al., 2015a, Eter et al., 2017b, Kline et al., 2018]. Most studies focus on the buoyancy effect and the onset of the HTD. There are two reviews listed in table 2.1 focusing only on CO_2 heat transfer at supercritical conditions, which can be read for detailed information.

Experiments conducted with R134a are limited. Most comparable investigations are from Kang et al. [Kang & Chang, 2009] and Zhang et al. [Zhang et al., 2014]. Unfortunately, in the paper of Kang, only one graph is shown with data points. The main objective of Kang et al. was an applicability of a steady-state heat transfer correlation to pressure transient sequences. The usage of the data from Hong et al. [Hong et al., 2004], Li et al. [Li et al., 2017] and Cui and Wang [Cui & Wang, 2017] are limited because they were conducted in an annulus geometry or partially in a downward flow.

2.2.4.2. Development of thermal boundary layer - inlet effect

To investigate the influence of the thermal boundary layer and its development at heat transfer at supercritical conditions, Xiong et al. [Xiong et al., 2017] conducted experiments with an interrupted heating. For that, the current was bypassed at a length of 300 mm for the part without heat flux. The authors observed an enhancement of the heat transfer after the unheated part compared to the tube with continuous heat flux. For high heat fluxes, a shift of the HTD to higher bulk enthalpies was observed. It was concluded that the development of the boundary layer has a higher and longer influence in deteriorated cases compared to normal cases. Thus, the length of the boundary layer development can increase from 40 to 90 times of the tube diameter. Xiong et al. stated that the distortion of velocity is more significant for the heat transfer deterioration cases. The velocity distortion can be recovered in the unheated part, increasing the bulk enthalpy at which HTD occurs [Xiong et al., 2017]. This means that the heat transfer at supercritical conditions can only be described with local parameters after a developing length. Before that, the HTC depends also on the history of the stream, which means inlet and boundary conditions, like temperature, geometry and heat flux. This was discussed by Polyakov [Polyakov, 1991], who limited the development length to 50 diameters. In contrary, Kays et al. [Kays & Crawford, 1980] stated that for high heat fluxes the development of the boundary layer will never finish for gas-like fluids. This is due to the thermal acceleration effect, which is explained in section 2.2.2.

Experiments from Swenson et al. [Swenson et al., 1965] showed an inlet effect at a position up to 97 times of the tube diameter. The experiments of Song et al. [Song et al., 2008] showed no influence of the inlet. This is maybe due to the small heat fluxes because no HTD was observed. Shiralkar and Griffith [Shiralkar & Griffith, 1970] showed that the HTD can be eliminated due to the weakened entrance effect with a high inlet temperature. Fewster [Fewster, 1976] showed in his thesis how the HTD moves upstream with increasing inlet temperature. The wall temperatures are shown in figure 2.10 and it is not obvious or discussed if the wall temperature curves converge at higher bulk enthalpies. Unfortunately, in recent publications the influence of the developing boundary layer or inlet temperature are not discussed any more.
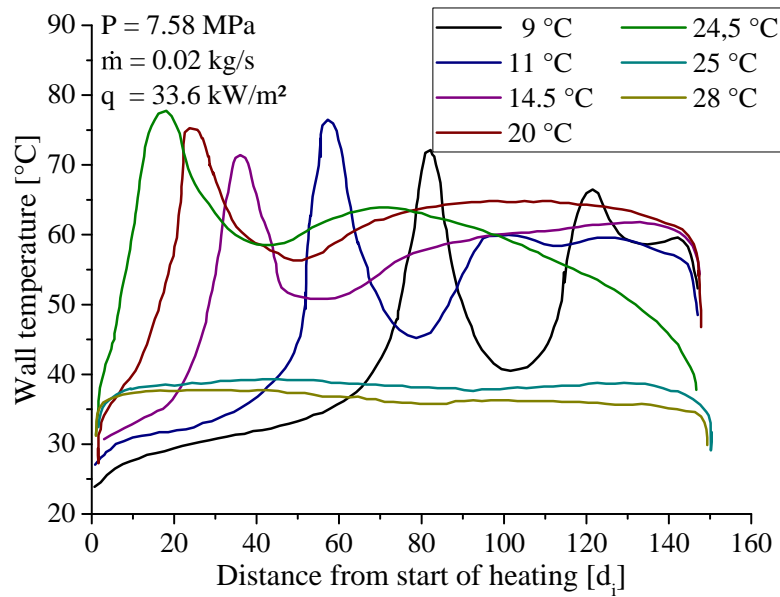
Figure 2.10.: Wall temperatures versus heated length with different inlet temperatures in CO_2 from Fewster [Fewster, 1976]

2.2.4.3. Reproducibility of experiments

Hall et al. [Hall et al., 1967] stated a discrepancy between sets of measurements made under apparently similar conditions. The authors mentioned that some relevant parameters, like the buoyancy forces, were not controlled [Hall et al., 1967]. With a deeper insight to the data, the authors concluded that no parameter set was identical. There were always little differences in heat flux, mass flux, pressure or diameter. This shows how sensitive the heat transfer at supercritical conditions can be to these parameters. Additionally, the influences of the parameters get stronger when HTD occurs.

Zahlan et al. [Zahlan et al., 2015a] reproduced some experiments from Fewster [Fewster & Jackson, 2004] and Song [Song et al., 2008] to show the reliability of their loop and measurement devices. The authors found a good agreement between similar experiments. However, discrepancies in HTC between the set of Zahlan and Song can be observed as HTD occurs [Zahlan et al., 2015a]. Huge discrepancies between different authors for the HTC for measurements at similar conditions were observed from Zhao et al. [Zhao et al., 2017]. As the authors gathered data from the literature to build a water data base for heat transfer at supercritical conditions, they could easily compare similar measurement sets from different authors. Zhao et al. found deviations up to 100 % for the HTC, especially at bulk temperatures near the pseudo-critical point [Zhao et al., 2017]. Even if the same facility was used, deviations can be observed. A reason could be unknown parameters like tube diameter, inlet conditions and surface roughness of the tube [Zhao et al., 2017].

2.2.4.4. Influence of wall thickness

Another effect on the measurement results of heat transfer experiments was described by Watts and Chou [Watts & Chou, 1982]. The authors attached their thermocouples alternating at the opposite sides of the tube. Measurements showed that the wall thickness of both sides differ. Thus, Watts and Chou included the eccentricity correction in the conduction equation when calculating the inside wall temperature [Watts & Chou, 1982]. Also other authors like Yamagata et al. [Yamagata et al., 1972] and Kim et al. [Kim et al., 2008] attached their thermocouples at different angles to the wall. In both papers it is not mentioned how or if this is treated. From their graphs it is obvious that there is some differences for the wall temperature at different sides of the tube.

Lei et al. [Lei et al., 2016], Shen et al. [Shen et al., 2017, Shen et al., 2016] and Sharma et al. [Sharma et al., 2014] measured the wall temperature with two to six thermocouples at the same cross section. No authors mentioned if differences in the measured outside wall temperature were observed at the same level. Data from Sharma et al. show differences from up to 30 K for the wall temperature measured at the same level. Lei et al. [Lei et al., 2016] calculated the inside wall temperature using a control volume method. This gives one value for the inside wall temperature, thus, deviations in outside wall temperature are smoothed. Shen et al. did not mention how they treated the multiple wall temperatures at the same level [Shen et al., 2017, Shen et al., 2016].

2.2.4.5. Influence of surface

Supercritical fluids are very corrosive, an overview about corrosion is given by Sarrade [Sarrade et al., 2017]. Corrosion increases the roughness of the heated wall, resulting in a different heat transfer than with a smooth tube. Changing the wall geometry can lead to HTE and less deteriorated heat transfer as Zhang et al. [Zhang et al., 2015a] and Wang et al. [Wang et al., 2011] reported. All authors suggest internally ribbed tubes to avoid or weaken HTD.

2.2.5. Numerical methods for heat transfer at supercritical conditions

Many simulations have been carried out to analyze or predict the heat transfer at supercritical conditions in tubes. Reviews focusing on numerical methods are listed in table 2.1. Many authors focused their simulations on HTD and tried to understand the phenomena leading to HTD. In contrast to experimental investigations, simulations can show the temperature, velocity and turbulence production distribution in the boundary layer in high spatial resolution. This enables investigations of buoyancy or acceleration effects on the velocity, shear stress, turbulence and consequently on the heat transfer behavior of mixed convection [Koshizuka et al., 1995].

For NHT Reynolds-Averaged-Navier-Stokes (RANS) simulations show good agreement with experimental measurements of the wall temperature, as discussed by Li et al. [Li et al., 2014]. However, RANS simulations may show huge differences to experiments if the heat transfer deviates from the normal case. Especially for HTD, deviations with several 100 K are observed [Tang et al., 2016]. The choice of the turbulence model is crucial to get reasonable results. As several authors [Kim et al., 2004, He et al., 2008, International Atomic Energy Agency, 2014, Pucciarelli et al., 2015] showed, the results of different turbulence models can vary strongly. Even using different software tools with the same turbulence models can lead to different results. This is due to the fact that turbulence is roughly modeled and RANS simulation cannot treat the boundary layer well for varying fluid properties, which is crucial at supercritical conditions. Therefore, the turbulence models need to be improved. Summarization of this improvements are listed in the review of Rahman [Rahman et al., 2016] and in the thesis of Kunik [Kunik, 2012]. Kunik developed an approach for a variable turbulent Prandtl model which was further improved from Tang et al. [Tang et al., 2016]. This describes the varying fluid properties closer and showed better agreement with experimental results [Tang et al., 2016].

Pandey and Laurien [Pandey & Laurien, 2015] suggested a two-layer modeling theory. It divides the wall-bounded flow into a laminar sub-layer and a turbulent layer, each of which can be modeled

separately. One set of models used wall function with correction factors for deterioration. The other model was based on the thermal resistance analogy [McEligot & Laurien, 2015]. Later Pandey et al. [Pandey et al., 2017] improved the two-layer model by implementing buoyancy and acceleration effects. The authors validated and refined their model with direct numerical simulation (DNS) results from Bae [Bae et al., 2005].

Pucciarelli et al. [Pucciarelli et al., 2015] summarized the 4-equations turbulence models and applied them to a wide set of experimental results. 4-equation turbulence models allow for adopting the improved models to the turbulent heat flux and to a more accurate study of the turbulent thermal field compared with the conventional 2-equations models. Pucciarelli [Pucciarelli et al., 2016] improved the model set with Algebraic Heat Flux Models used in the buoyancy production term of the turbulence kinetic energy. The comparison with experimental and DNS data showed a promising improvement in predicting the wall temperature.

Bypassing the uncertainties in the turbulence modeling, DNS is an attractive tool for fundamental research. Starting from Bae et al. [Bae et al., 2005] DNS has delivered plenty of statistics and improved the understanding on the deteriorated heat transfer in the supercritical fluids [Wang & He, 2015, Chu & Laurien, 2016, He et al., 2016]. However, as a result of the resolution requirement from the high Reynolds number and the high Prandtl number near the pseudo-critical point, DNS is still limited to theoretical studies far from real applications [Chu & Laurien, 2016]. Large eddy simulations (LES) are a compromise between resolution and computing time by modeling only the small sized turbulences. Therefore, LES could be a promising tool for heat transfer at supercritical conditions simulations, as it could describe the changes in the boundary layer detailed enough [Kunik, 2012].

2.2.6. Predicting methods for heat transfer at supercritical conditions

Due to the strong variations of the thermal-physical properties of the coolant and the resulting varying degree of influences, the conventional correlations fail to predict the heat transfer at supercritical conditions, especially around the pseudo-critical point. At high temperature gradients, the property changes become very strong across the flow. Therefore, the heat transfer depends also on heat flux and mass flux in this region.

No analytical model has been developed yet which gives satisfactory results for predicting the heat transfer at supercritical conditions [Zahlan, 2015]. With variable fluid properties, models are complex and result in difficulties. Mathematical difficulties mainly occur due to the coupling of heat transfer and momentum, which are nonlinear. Additionally, modulating difficulties can be attributed to the variable fluid properties and the unavailability of an analytical solution for the turbulent diffusivity [Petukhov, 1970]. To predict the heat transfer, empirical correlations, look-up tables and neural networks are used so far.

2.2.6.1. Empirical correlations

Many reviews addressed various methods of predicting the heat transfer at supercritical conditions. An overview is given in table 2.1. Reviews which focus on correlations are indicated. Highlighted should be the book of Pioro and Duffey [Pioro & Duffey, 2007] with the largest accumulation of correlations. Beside the reviews, many assessments were done in the past, which give a precious insight about the prediction capability of the used correlations. A few assessments can be found in [Pioro et al., 2004b, Kim et al., 2006, Bae et al., 2010, Bae et al., 2011, Zahlan et al., 2011, Wang & Li, 2013, Chen & Fang, 2014, International Atomic Energy Agency, 2014, Chen et al., 2015a, Churkin et al., 2015, Zhao et al., 2017]. None of the reviews gathers the results of all assessments to give a general statement about the prediction accuracy of each correlation. This is maybe due to the fact that each correlation is limited to a small range of parameters with satisfying results [Bae et al., 2011, Wang & Li, 2013]. This limitation was approved by Kurganov et al. [Kurganov et al.,

2013, Kurganov et al., 2014]. As described in section 2.2.2, the authors classified the HTD in six different groups. According to these classifications, correlations predict heat transfer differently well.

To describe the strong variations of the thermo-physical properties, conventional correlations were modified mainly with ratios of thermo-physical properties given at the wall and bulk temperature. Two conventional correlations were adapted: the Dittus-Boelter equation 2.8 and the correlation of Gnielinski [Gnielinski, 1975].

Correlation based on Dittus-Boelter

Most correlations are based on the Dittus-Boelter equation, which was originally developed for single phase water only. Sieder and Tate [Sieder & Tate, 1936] extended the Dittus-Boelter equation with a ratio of the viscosity given by the wall and bulk temperature to describe the heat transfer more precisely at high temperature gradients. In this manner many authors tried to fit the Dittus-Boelter equation to their experimental data to describe the heat transfer at supercritical conditions. The constant a, the exponentials b and c and the correction factor F_{DB} in equation 2.21 are determined empirically.

$$Nu_b = a \, Re_b^b \, Pr_b^c \, F_{DB} \qquad (2.21)$$

Density and heat capacity are the most used properties. The average heat capacity defined by equation 2.22 is mainly used instead of the heat capacity defined at the wall temperature. It is the enthalpy difference of the fluid at the wall (h_w) and the bulk (h_b) divided by the temperature difference of the wall and bulk. Petukhov showed that this definition describes the correction factor for the heat transfer more accurately [Petukhov, 1961].

$$\overline{c_p} = \frac{h_w - h_b}{T_w - T_b} \qquad (2.22)$$

For selected correlations, the modified constants, the correction factor F_{DB} and the reference for the dimensionless numbers are listed in table 2.2. Some authors developed correlations with factors depending on the heat transfer region, using parameter ranges to distinguish the region. For that, temperatures or the buoyancy number are often used. The parameter ranges are listed in table 2.2, too. All correlations mentioned in this subsection or used in this thesis are described in detail in the appendix A.

Swenson and Bishop et al. [Swenson et al., 1965, Bishop et al., 1965] were the first ones to modify the Dittus-Boelter equation using the density and heat capacity ratio. The correlations are still used in many data assessments. Yamagata [Yamagata et al., 1972] introduced 1972 the Eckert number (eq.: A.44) for the correction factor. Watts and Chou [Watts & Chou, 1982] used the Jackson criterion for buoyancy (equation 2.13) to distinguish between NHT and HTD in their correlation for mixed convective water and CO_2. Mokry et al. developed two correlations to adapt the Dittus-Boelter equation to supercritical water [Mokry et al., 2011] and CO_2 [Mokry et al., 2009].

Gupta et al. modified the correlation of Swenson et al. with an additionally viscosity ratio to gain a higher prediction ability [Gupta et al., 2013]. To address all strongly varying properties, more parameters are added to the correlations recently, which consequently complicates the understanding and applicability. In contrast, Cheng et al. proposed the need of simplifying the correlations [Cheng et al., 2009a, Cheng et al., 2009b]. The authors argued that physics and phenomena of heat transfer at supercritical conditions are not understood and more effort must be done. Additionally, Cheng et al. proposed four essential conditions that must be fulfilled by a correlation for describing heat transfer at supercritical conditions [Cheng et al., 2009b]:

- The correlation should be based on dimensionless numbers so that it can be extended and applied to various supercritical fluids.

- The correlation should contain as few parameters as possible.

- The correlation should cover both normal and HTD conditions.

- The correlation should not contain wall temperature or parameters depending on wall temperature, to avoid numerical instability problems.

For their correlation, Cheng et al. derived the dimensionless acceleration number π_A based on phenomenological assessment of heat transfer behavior with an evaluation of experimental data. The new dimensionless number, defined in equation 2.23, has a strong dependency on the correction factor F_{DB} as Zhao et al. have shown [Zhao et al., 2014, Zhao et al., 2017]. Zhang et al. included π_A in a new correlation evaluated with R134a data [Zhang et al., 2014, Zhang et al., 2015b].

$$\pi_A = \frac{\beta\, q}{c_p\, G} \tag{2.23}$$

Table 2.2.: Selected correlations in form of Dittus-Boelter

Authors	Fluid	Ref.	a	b	c	F_{DB}	Cond.
Bae et al. (A.2)	CO_2	b	0.021	0.8	0.55	$\left(\frac{\overline{c_p}}{c_{p,b}}\right)^{0.55}\left(\frac{\rho_w}{\rho_b}\right)^{0.35}$, $f(Bu)$	f(Bu)
Bishop et al. (A.4)	water	b	0.0069	0.9	0.66	$\left(\frac{\overline{c_p}}{c_{p,b}}\right)^{0.66}\left(\frac{\rho_w}{\rho_b}\right)^{0.43}$	-
Cheng et al. (A.8)	water	b	0.023	0.8	1/3	$f(\pi_A)$	f(π_A)
Cui & Wang (A.11)	R134a	b	0.0291	0.762	0.706	$\left(\frac{\overline{c_p}}{c_{p,b}}\right)^{0.706}\left(\frac{\rho_w}{\rho_b}\right)^{0.353}$ $\left(10^5 Bu\right)^{-0.046}$	upward
			0.0189	0.812	0.685	$\left(\frac{\overline{c_p}}{c_{p,b}}\right)^{0.685}\left(\frac{\rho_w}{\rho_b}\right)^{0.394}$ $\left(10^5 Bu\right)^{-0.0176}$	downward
Jackson & Hall (A.20)	water	b	0.0183	0.82	0.5	$\left(\frac{\overline{c_p}}{c_{p,b}}\right)^{n}\left(\frac{\rho_w}{\rho_b}\right)^{0.3}$	n(T_b, T_w, T_{pc})
Mokry et al. (A.32)	water	b	0.0061	0.904	0.684	$\left(\frac{\overline{c_p}}{c_{p,b}}\right)^{0.684}\left(\frac{\rho_w}{\rho_b}\right)^{0.564}$	-
Swenson et al. (A.41)	water	w	0.0046	0.923	0.613	$\left(\frac{\overline{c_p}}{c_{p,b}}\right)^{0.613}\left(\frac{\rho_w}{\rho_b}\right)^{0.231}$	-
Watts & Chou (A.42)	water	b	0.021	0.8	0.55	$\left(\frac{\overline{c_p}}{c_{p,b}}\right)^{0.55}\left(\frac{\rho_w}{\rho_b}\right)^{0.35}$, $f(Bu)$	f(Bu)
Yamagata et al. (A.43)	water	b	0.0135	0.85	0.8	$\left(\frac{\overline{c_p}}{c_{p,b}}\right)^{n}$	n(Pr_{pc}, T_b, T_w, T_{pc})
Zhang (A.45)	R134a	b	0.023	0.8	0.4	$f(\pi_A)$	f(π_A)

Correlation based on Gnielinksi

Other authors tried to modify the correlation of Gnielinksi, which shows better prediction results for different fluids [Gnielinski, 1975]. Either the friction factor f, the Prandtl numbers Pr_1 and

Pr_2 were modified or a correction factor F_G was added in equation 2.24 in the same way as for the Dittus-Boelter equation. Well known correlations are from Petchukov and Kurganov et al. [Petukov et al., 1988, Kurganov & Kaptil'ny, 1992].

$$Nu_b = \frac{(f/8)\ Re_b\ Pr_1}{1.07 + 12.7\ \sqrt{f/8}\ (Pr_2 - 1)} F_G \qquad (2.24)$$

Modified parameters of selected correlations are listed in table 2.3. The most common parameter for the correction factor is the heat capacity ratio using the mean capacity of equation 2.22. The mean heat capacity is likewise included in some Prandtl number as indicated by the overline in table 2.3. As described before, some authors use parameter ranges to change the correlation depending on heat transfer regions.

Table 2.3.: Selected correlations in form of Gnielinksi

Authors	Fluid	f	Pr_1	Pr_2	F_G	Ranges
Grass et al. (A.17)	water	$(1.82\log(Re_b)$ $-1.64)^{-2}$	Pr_b	$Pr_G c_{p,G}$	-	$Pr_G(Pr_b,\ Pr_w)$ $c_{p,G}(Pr_b, Pr_w)$
Krasnoshchek-ov et al. (A.27)	CO_2	$(1.82\log(Re_b)$ $-1.64)^{-2}$	$\overline{Pr_b}$	$\overline{Pr_b}^{2/3}$	$\left(\frac{\overline{c_p}}{c_{p,b}}\right)^n \left(\frac{\rho_w}{\rho_b}\right)^{0.3}$	$n(T_b, T_w, T_{pc})$
Kurganov et al. (A.29)	water & CO_2	$(1.8\log(Re_b)$ $-1.5)^{-2}F_{G,K}$	Pr_b	$\overline{Pr_b}$	$F_{G,K} =$ $\left(\frac{\rho_w}{\rho_b}\right)^{0.35} \left(\frac{\mu_w}{\mu_b}\right)^n$	-
Petukhov (A.36)	water	$(1.82\log(Re_b)$ $-1.64)^{-2}$	$\overline{Pr_b}$	$\overline{Pr_b}^{2/3}$	$\left(\frac{\eta_b}{\eta_w}\right)^{0.11} \left(\frac{\lambda_w}{\lambda_b}\right)^{0.33}$ $\left(\frac{\overline{c_p}}{c_{p,b}}\right)^{0.35}$	-
Razumovskiy et al.(A.39)	water	$\left(1.82\log\left(\frac{Re_b}{8}\right)\right)^{-2}$ $\left(\frac{\eta_w}{\eta_b}\frac{\rho_w}{\rho_b}\right)^{0.18}$	$\overline{Pr_b}$	$\overline{Pr_b}^{2/3}$	$\left(\frac{\overline{c_p}}{c_{p,b}}\right)^{0.65}$	-

Résumé

Based on the reviews, it can be concluded that the correlations developed by Bishop et al. [Bishop et al., 1965], Watts and Chou [Watts & Chou, 1982], Mokry et al. [Mokry et al., 2011], Chen and Fang [Chen & Fang, 2014] and the correlation of Jackson [J.D. Jackson, W. B. Hall, 1979] predict the experimental data with the highest accuracy.

Correlations from Cui et al. and Zhang et al. [Cui & Wang, 2017, Zhang et al., 2014] are directly applicable for R134a in vertical tubes. Also the correlation of Jackson and Cheng et al. should be applicable to R134a due to their validation for different fluids [J.D. Jackson, W. B. Hall, 1979, Cheng et al., 2009b].

As a consequence of the changing influences of buoyancy on the heat transfer at supercritical conditions as described in subsection 2.2.2, Jackson et al. concluded in their review [Jackson et al., 1989] that it is impossible to correlate heat transfer in the region of impairment precisely using local parameters. Therefore, correlations should be based on a factor including the distance from the start of the heated part, like l/d for example.

As concluded from many authors, no correlation can predict the heat transfer at supercritical conditions reliably and over a wide range of parameters. Hence, all authors agree that more effort must be done to describe the heat transfer at supercritical conditions.

2.2.6.2. Look-up table

As seen before, the HTC is difficult to predict at supercritical pressures, particularly when the fluid temperature approaches the pseudo-critical temperature, where the thermo-physical properties change rapidly. A look-up table lists heat transfer coefficients for given and schematically distributed parameters. Compared to correlations a look-up table can capture these high property gradients better. Therefore, look-up tables show an higher accuracy in predicting the HTC at supercritical conditions. The first look-up table made for heat transfer at supercritical conditions was established by Löwenberg in 2007 [Löwenberg, 2007]. Löwenberg based his table including the methods to build, fill in and interpolation considerations on Groeneveld's et al. look-up tables for the critical heat flux and film boiling [Groeneveld et al., 2003, Groeneveld et al., 2007].

Groeneveld at al. implemented experimental data in their tables calculating a weighted averaged value for every point with experimental data nearby. Löwenberg used another method to fill in the experimental data. He interpolated the experimental data to the fixed parameters of his look-up table using dimensionless correlations. Correlations can be locally used, especially if the parameters are only changing little and the thermal-physical properties vary linearly. Compared with linear interpolation, less data are needed for interpolation. For linear interpolation, 15 experimental data points would be needed for one table point, considering 5 input parameters and 3 points each for non-linear behavior. Limits and correlations must be chosen carefully [Löwenberg, 2007]. However, for using the look-up table, Löwenberg suggested the linear interpolation in regions between the table grid points.

Zahlan et al. extended the look-up table by Löwenberg to subcritical pressures and named it "transcritical look-up table" [Zahlan, 2015, Zahlan et al., 2015b]. But, the look-up table from Zahlan is predicting heat flux based on a given wall temperature whereas the look-up table of Löwenberg is predicting the wall temperature based on a given heat flux. However, the same methods for building and smoothing the table were used. For incorporation of experimental data, Zahlan et al. used a procedure to calculate the local HTC slope of every parameter. Löwenberg and Zahlan et al. showed the advantages of look-up tables compared to correlations for predicting the heat transfer at supercritical conditions, particularly nearby the pseudo-critical point [Löwenberg, 2007, Zahlan et al., 2015b].

Normally, the tables are fixed to one diameter. Therefore, all authors scaled experimental data from other diameters using equation 2.25 with a different exponent n. Yildiz and Groeneveld concluded that the heat transfer would decrease with increasing tube diameter for the normal heat transfer [Yildiz & Groeneveld, 2014] and is well described by n = -0.2. However, the effect of diameter shows different trends and no exact dependence has been found in deteriorated heat transfer.

$$\frac{\alpha}{\alpha_{ref}} = \left(\frac{d}{d_{ref}}\right)^n \tag{2.25}$$

Another promising idea for predicting the HTC at supercritical conditions is the look-up list from Cheng and Liu [Cheng & Liu, 2017]. Therefore, the original experimental data are compiled in one list. In contrast to the look-up table, the look-up list contains the original data without loss of accuracy and more parameters such as the inlet temperature. The challenge is to develop an effective and accurate interpolation methodology [Cheng & Liu, 2017].

2.2.6.3. Neural network

The artificial neural network (ANN) is a computing system inspired by biological neural systems. The ANN learns tasks from examples. It stores empirical knowledge and evolves its own set of relevant characteristics. In order to do this, it changes the connection weight of internal neurons

as the brain does. In the mid 1990s, ANNs have been successfully applied to different topics, as Chang et. al summarized [Chang et al., 2017]. However, ANNs were also used to predict and analyze complex thermal-physicals parameters [Dubey et al., 1998] or CHF [Moon et al., 1996].

As shown previously, many factors influence the heat transfer at supercritical conditions. These include the heat flux, mass flux, tube diameter, flow geometry, pressure, inlet conditions and maybe even more. Additionally, these influences and dependencies are complex, non-linear and only understood partially, as described in section 2.2.4. Hereby, ANN is a great opportunity because it learns the characteristics autonomous. Scalabrin and Piazza [Scalabrin & Piazza, 2003] were the first to predict heat transfer at supercritical conditions using ANN with CO_2 as fluid.

Recently, an ANN was also trained to predict heat transfer at supercritical conditions for water by Chang et al. [Chang et al., 2017] and Ma et al. [Ma et al., 2017] by using data from the literature. All authors mentioned that ANN predicts heat transfer at supercritical conditions much more accuratly than any other methods or correlation.

In the study of Dhanuskodi et al. [Dhanuskodi et al., 2015], the ANN predict all data in a range of $\pm 7\,°C$. Chang et al. [Chang et al., 2017] found that the ANN of Dhanuskodi et al. only predicts $80\,\%$ in a range of $\pm 7\,°C$ using their data. Chang et al. mentioned that this is due to the over-fitting of the ANN, which is one of the frequent and critical problems of ANN. In this case, the ANN fits the training data too closely and cannot describe the heat transfer globally. Chang et al. describe several methods to pretend the over-fitting of the ANN. ANNs can not be described and distributed easily because of their hidden layers of neural connections. Nevertheless, to train an ANN takes around one hour and to calculate a new data takes several milliseconds with a standard personal computer [Chang et al., 2017].

2.2.7. Multi-solutions

Zhao et al. [Zhao et al., 2017] found in their assessment of experimental data of different authors deviations in the heat transfer coefficient of more than $100\,\%$ when the bulk temperature reaches the pseudo-critical value for the same mass flux, heat flux and pressure. The stated reasons for the deviations are inlet effect, tube diameter and roughness of the tube, which also strongly influences the HTC at supercritical conditions. Also Cheng and Liu [Cheng & Liu, 2017] found in their collected data deviations in the HTC for the same parameters. Deviations are found between different authors and facilities but also within the same facility and test section. Cheng and Liu proposed an idea of multi-solutions for the heat transfer at supercritical conditions. This means that the wall temperature can have different values for the same experimental conditions as geometry, mass flux, heat flux, pressure and bulk temperature. This can be pictured in figure 2.11. The black line is the trend of the HTC as it could occur in an experiment with constant wall temperature. The heat capacity of the coolant has its maximum at the pseudo-critical point. This can lead to a local maximum of the HTC as discussed in section 2.2.2. This is shown in many experiments with constant low heat flux [International Atomic Energy Agency, 2014]. Additionally, most correlations also show this trend as Cheng et al. [Cheng et al., 2009a] reported. The grey dashed line in figure 2.11 is defined by the convective heat transfer according to equation 2.4.

As shown by the crossing of the HTC trends in figure 2.11, it is obvious that HTC could theoretically have more than one solution. Thus, correlations using the wall temperature could lead to converging problems or numerical instabilities as Cheng et al showed in [Cheng et al., 2009a]. Therefore, Cheng et al. suggested to eliminate the dependencies on wall temperature in the correlations. This idea of multi-solutions could explain the deviations in HTC from equal experimental conditions but the experimental proof is missing [Cheng & Liu, 2017].
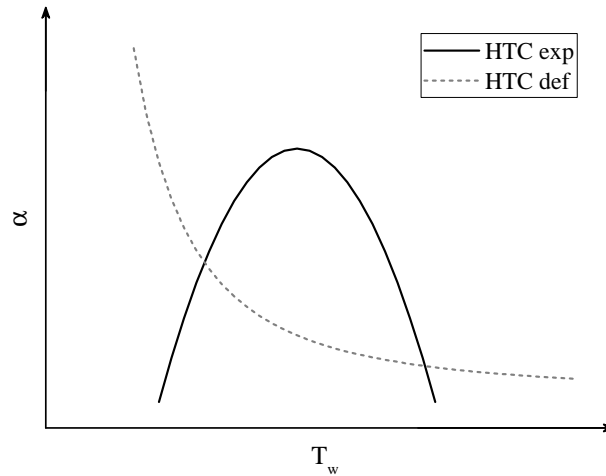
Figure 2.11.: Multi-solution given by the empirical HTC trend of experiments (HTC exp) and the definition of HTC (HTC def) [Cheng et al., 2009a]

2.3. Critical heat flux

Critical heat flux (CHF) is the most important limiting parameter in the design and operation of boilers, steam generators and reactors for maximum efficiency and maximum power throughput. CHF is the highest heat flux that can be dissipated into a nucleate boiling system before the local transition to film boiling occurs. This transition implicates a fast increase of the surface temperature for a heating power driven system because of a significantly reduced heat transfer in the film boiling regime. The boiling crisis can lead to an irreversible thermal damage of the heated surface. Therefore, the knowledge of the critical heat flux is important for a safe operation of a boiling system. Subcritical pressure is mandatory for boiling. This can happen in a SCWR at an accidental scenario, at start-ups such as the sliding pressure start-up or shut downs of the plant. Therefore, it is important to know the limits set by the CHF for operating a SCWR as well.

Due to the fact that CHF is a wide research field, the present description of the state of the art is limited to tubes with forced convection with upward flow at high subcritical pressures. Nevertheless, the phenomena leading to CHF will be discussed subsequently.

The boiling process generates a high heat transfer from the heated surface into the fluid due to the phase change from liquid to vapor. The required latent heat of vaporization is removed from the hot surface. Bubbles are generated in cavities or impurities on the surface. Their departure into the liquid enhance the heat transfer further by increasing the convection in the boundary layer. Influencing parameters on the two-phase heat transfer are pressure, mass flux, heat flux, geometry, fluid and surface properties as well as the interaction between fluid and surface. The boiling curve was introduced by Nukiyama [Nukiyama, 1966] and shows the variation of the HTC through the transmitted heat flux by a given wall temperature or wall superheat. The boiling curve is shown in figure 2.12 for a system with constant wall temperature and constant heat flux respectively.

The boiling heat transfer capability is intensified with increasing power, as seen at the steep gradient of the boiling curve in figure 2.12. However, the region of nucleate boiling is limited by the CHF. At this point, the heated wall is completely covered with vapor and the regime is called "film boiling". The heat transfer is reduced dramatically due to the bad heat transfer capabilities of the vapor compared to a boiling liquid. In a heating power driven system, the produced heat remains constant. Consequently, the temperature of the wall increases immediately until the temperature difference between the wall and the bulk is high enough to transfer the given heat flux. This can be derived from equation 2.4. Depending on the system and flow parameters, the temperature of the
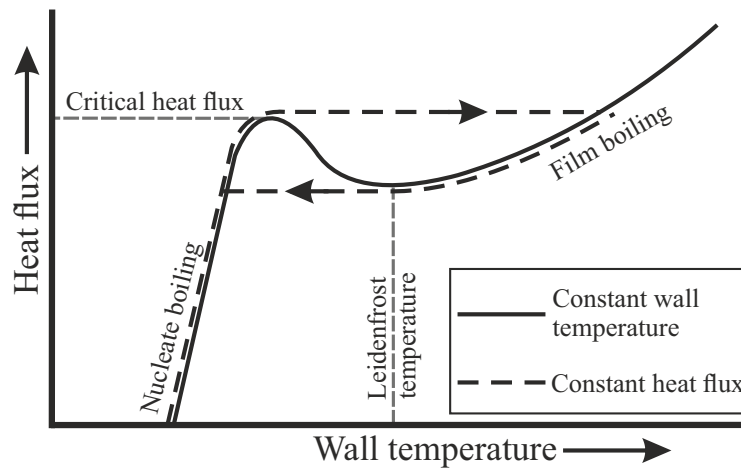
Figure 2.12.: Heat transfer mechanism at two-phase flow [Verein Deutscher Ingenieure, 2013, Nukiyama, 1966]

heated wall can reach the melting point and cause critical thermal damage of the heated structure. This could lead to a complete failure of the whole power system and has to be avoided [Groeneveld & Snoek, 1986]. There are two main patterns leading to the boiling crisis of the heated wall, which are explained in the following sections.

Dryout

The liquid tends to form a film on the wall at high vapor qualities. Some droplets are dispersed in the continuous vapor phase in the middle of the tube. The liquid film vaporizes while heating and the entrainment of the vapor collaterally narrow the liquid film. At some point the liquid film drys out and the wall is only cooled by the continuous vapor phase. This point is shown in the right side of figure 2.13. This happens rather at lower mass fluxes and lower subcooled inlet temperature [Bejan & Kraus, 2003, Verein Deutscher Ingenieure, 2013]. At small heat fluxes, droplets can touch the wall, which increases the heat transfer and is called "deposition controlled burnout" [Groeneveld & Snoek, 1986].
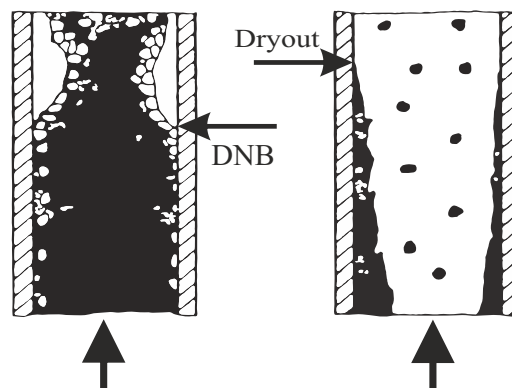
Figure 2.13.: Scheme of DNB (left) and dryout (right) for constant heat flux in a cross section of a tube; liquid in dark and vapor in white [Verein Deutscher Ingenieure, 2013]

Departure from nucleate boiling (DNB)

The bulk flow is liquid at low vapor qualities. At high heat fluxes, the bubbles depart slower than they are produced. At some point, the bubbles form a vapor sheet which separates the wall from the liquid and contingently subcooled bulk flow. This can be seen on the left side of figure 2.13. Due to the low heat conduction of the vapor, the heat transfer is deteriorated. This is called "departure from nucleate boiling" (DNB) and the heat transfer region downstream is called "inverted annular film boiling" [Bejan & Kraus, 2003, Verein Deutscher Ingenieure, 2013]. The heat transfer in this regime is smaller compared to the post-dryout because of the absence of the vapor convection and the droplets at the wall.

2.3.1. CHF reviews and influencing parameters

The first studies of CHF in tubes were carried out in the 1960s [WESTWATER, 1963]. Many detailed reviews on forced flow boiling were published throughout the last decades [Hendricks et al., 1970, Groeneveld & Snoek, 1986, Cheng, 1991, Celata & Mariani, 1999, Hall & Mudawar, 2000b, Hall & Mudawar, 2000a, AGENCY, 2001, Cheng & Müller, 2003, Chang & Baek, 2003, Behnke, 2009, Ahmed et al., 2010, Haas, 2012, Yang et al., 2017]. These studies introduce an excellent review on the parametric influences and prediction methods. Most of the studies aim to understand the phenomena leading to CHF for transient conditions in nuclear reactors. The pressure conditions of the Boiling Water Reactor and the Pressurized Water Reactor are examined the most. Nevertheless, the understanding of the phenomena of CHF at high pressures up to the critical pressures is mandatory for the design of the SCWR. The magnitude and the occurrence of the CHF are affected by many parameters such as thermal-physical, geometric and external parameters. A summarization of the most important parameters is given in the next sections.

2.3.1.1. Influence of mass flux on CHF

The CHF increases with increasing mass flux in the low quality region. In this region, DNB occurs and an increase of mass flux increases the turbulence of the flow. This leads to a higher departure rate of the bubbles from the wall and hence allows to a higher CHF [Groeneveld & Snoek, 1986].

Furthermore, the IAEA reported a decreasing influence on CHF for increasing mass fluxes in the higher and positive quality region [AGENCY, 2001]. This phenomena was also observed from Liu et al. [Liu et al., 2016], Moon et al. [Moon et al., 1996] and Pioro et al. [Pioro et al., 2001]. Tong and Tang [Tong & Tang, 1997] refer this phenomena to an inverse mass flux effect. This effect occurs at high vapor quality combined with high vapor velocities. This promotes droplet entrainment from the liquid layer on the heated wall. An increase in mass flux causes an increase of vapor velocity which results in a higher droplet entrainment and thereby decreases the CHF. Additionally, a higher vapor quality and higher vapor velocity reduce the liquid film thickness of an annular flow which results in a lower CHF as well. Tong and Tang [Tong & Tang, 1997] summarize that there is a critical velocity of the vapor phase at which the CHF drops suddenly. This velocity is dependent on pressure, inlet enthalpy, heat flux, fluid and geometry.

At high pressures and high mass fluxes, the CHF increases with increasing mass flux. This is due to the smaller and faster droplets that can connect and sustain the liquid layer at the wall [Groeneveld & Snoek, 1986].

2.3.1.2. Influence of vapor quality on CHF

An increasing vapor quality leads to a smaller CHF. The influence gets stronger as the regime changes from DNB to dryout until it vanishes at the deposit controlled dryout region [Verein Deutscher Ingenieure, 2013]. Additionally, Groeneveld [Groeneveld, 2011] reported a limiting quality phenomenon. At the boundary from the entrainment controlled region and the deposition controlled region, the CHF drops by 30 % to 90 % for a nearly constant vapor quality. This causes

problems for correlations using the vapor quality as variable for the CHF predicting. The vapor quality gets higher with decreasing subcooling of the inlet temperature. Consequently, a higher subcooled temperature leads to a higher CHF as well [Cheng, 1991].

2.3.1.3. Influence of pressure on CHF

Pressure has a weak influence on the CHF in the subcooled boiling at low pressures up to 5 MPa in water. In contrary, the influence is very complex at higher pressures. At low pressures, the CHF increases with increasing pressure, passes through a maximum and decreases afterwards. This maximum depends on parameters as geometry, mass flux and subcooling [Celata & Mariani, 1999]. As Cheng and Müller [Cheng & Müller, 2003] concluded, the pressure influence on the CHF is a consequence of the fluid properties. Increasing the pressure leads to a smaller CHF because of the lower latent heat, a higher rate of evaporation and a lower surface tension. However, a higher pressure can also lead to a higher CHF because of a higher vapor density [Cheng & Müller, 2003]. Theoretically, the CHF must approach zero as the latent heat gets zero at the critical point.

2.3.1.4. Influence of tube diameter on CHF

When the diameter of the tube increases from 2 to 8 mm, the CHF is decreased for the same exit conditions. The effect is less significant for higher diameters and decreased mass fluxes. Cheng and Müller [Cheng & Müller, 2003] summarized that the effect of tube diameter is not well understood and more work is needed. Groeneveld [Groeneveld et al., 2007] suggested to use equation 2.26 to scale the diameter effect on the CHF. This is similar to equation 2.25 to scale the CHF from the LUT, which is developed for a 8 mm tube, to the needed diameter.

$$\frac{CHF}{CHF_{LUT}} = \left(\frac{d}{8}\right)^{-1/2} \tag{2.26}$$

2.3.2. CHF experiments

Many studies about CHF experiments have been published in the past. Here, only studies relevant for the topic of high pressures are discussed. The reduced pressure is defined as P/P_c. Table 2.4 summarizes CHF experiments conducted with R134a or at high reduced pressures above 0.9.

Zhu et al. [Zhu et al., 2009] observed in their experiments that the dryout point is shifted to lower vapor qualities by increasing the pressure for the same conditions. As the pressure approaches the critical point, the regime is changed from dryout to DNB.

The same behavior in terms of the vapor quality was observed by Hong et al [Hong et al., 2004]. Further, the authors reported a sharp decrease of the CHF at increasing pressures above 3.8 MPa. The trend converges to zero as the pressure approaches the critical point. This could be caused by the stronger changes of fluid-properties near the critical point. The decrease of the CHF matches the decrease of the latent heat very well which could be an explanation of the CHF reaching zero. Consequently, the CHF does not lead to an abrupt temperature rise close to the critical pressure because of the small heat fluxes and similar densities of liquid and vapor. The same observations are reported from Vijayarangan, Kang and Kariya et al. [Vijayarangan et al., 2006, Kang et al., 2009, Kariya et al., 2013] as well as Chun et al. [Chun et al., 2007b] for a rod bundle.

Transient experiments with decreasing pressures in R134a were conducted by Hong et al. [Hong et al., 2003, Hong et al., 2004]. The authors observed a rapid rise of wall temperatures to high values as the pressure passes the critical point. The high values are explained by the DNB caused by the small vapor qualities near the critical point, as discussed before.

Table 2.4.: Experiments about CHF at high pressures or with R134a as coolant

Authors	Fluid	P/P_c	Remaining parameters and conditions [*]
Pioro et al. [Pioro et al., 2001]	R134a	0.24 – 0.59	tube, d=4.67, 6.92, G=500–3000, x=-0.1–0.9, T_{in}=3–22, graphs
Lee et al. [Lee et al., 2008]	R134a	0.29 – 0.49	annular, d=9.5, A=19x19, G=100–600, q=76–238, x=0.07–0.84, T_{in}=25–40, tables
Noel [Noel, 1966]	Ammonia	0.1 – 0.93	tube, d=4.4, 6.1, G=480–23306, q=3.4–16, x=-2.62– -0.03, x_{in}=-2.98– -0.07, tables
Nishikawa et al. [Nishikawa et al., 1982]	R22	0.84 – 0.962	tube, d=13, G=200–1300, q=0.015–0.092, x=-0.22–0.59, x_{in}=-1.38–0.06, N/A
Kariya et al. [Kariya et al., 2013]	R12, R134a	0.961 – 0.992	tube, d=4.4, G=400–1000, q=8–61, h_{in}=255–363, graphs, cor
Vijayarangan et al. [Vijayarangan et al., 2006]	R134a	0.24 – 0.98	tube, d=12.7, G= 200–2000, q=2–80, x=0.17–0.94, ΔT_{in}=3, table, cor
Chun et al. [Chun et al., 2007b]	R134a	0.74 – 0.99	5x5 rod bundle, d=9.5, pitch=12.85, G=50–2000, Δh_{in}=40–84, graphs
Hong et al. [Hong et al., 2004]	R134a	0.16 – 0.98	annular, d=9.54, D=19.4, G=500–1500, q=30–220 ΔT_{in}=15–44, graphs
DeBortoli et al. [DeBortoli et al., 1958]	Water	0.156 – 0.935	tube, d=1.9, 10.3, G=38–10596, q=230–12000, x=-1.15–0.98, ΔT_{in}=-8–272, N/A
Becker et al. [Becker et al., 1972]	Water	0.544 – 0.906	tube, d=10, G=1100–7000, q=130–3530, x=-1.15–0.98, x_{in}=-2.34– -0.06, graphs
Zhu et al. [Zhu et al., 2009]	Water	0.408 – 0.997	tube, d=22, G= 600–1200, q=200–600, N/A
Chen et al. [Chen et al., 2011, Chen et al., 2015b, Chen et al., 2017]	Water	0.01 – 0.94	d=2.32, 5.16, 7.89, 8.05, 8.2, 10, 16, G=454–4055, q=260–9300, x=-0.97–0.53 ΔT_{in}=19–354, graphs, cor

[*] d= diameter in mm, G= mass flux in kg/m^{2}s, q= heat flux in kW/m^2, x= vapor quality at CHF location, x_{in}= vapor quality at inlet, T_{in}= inlet temperature in $°$C, ΔT_{in}= subcooled inlet temperature in K, h_{in}= enthalpy at inlet in kJ/kg, Δh_{in}= subcooled enthalpy at inlet in kJ/kg, N/A= data not available, graphs= data available in graphs, table= data available in tables, cor= correlation

2.3.3. CHF prediction methods

Many correlations are listed in the reviews mentioned in section 2.3.2. Additionally, the authors of the VDI heat atlas [Verein Deutscher Ingenieure, 2013] provide a suggestion for CHF predicting. The correlation of Katto and Ohno [Katto & Ohno, 1984] is recommended for high pressures and mass fluxes up to 500 kg/m^{2}s. For high pressures and mass fluxes, a combination of the correlation from Doroshuck et al. and Kon'kov is suggested [Doroshchuk et al., 1975, Kon'Kov, 1965] in the VDI. In general, the authors advise to use the CHF look-up table from Groeneveld et al. [Groeneveld et al., 2007] which provides the best prediction capability. The look-up table includes data up to 21 MPa, whereby these data are interpolated from non-mentioned experimental data.

In table 2.5, correlations are listed for high reduced pressures up to 0.9. The correlations are

described in appendix C. Most correlations are made for water up to 20 MPa. The correlations of Shah as well as Katto and Ohno are applicable to most fluids. The correlation of Katto and Ohno is the most used one due to its wide applicability and good prediction results. Its parameters range was increased by several authors with more experimental data. Vijayarangan et al. [Vijayarangan et al., 2006] modified the correlation of Katto and Ohno by adding two dimensionless groups. This modification fits both, R-134a and steam water data.

Table 2.5.: Correlations for CHF at high pressures with given parameter ranges for tubes

Authors	Fluid	d [mm]	P/P_c [$-$]	G $\left[\frac{kg}{m^2 s}\right]$	Inlet[*]
Chen et al. [Chen et al., 2016]	Water	4.62 – 10.89	0.085 – 0.934	454 – 4055	ΔT_{in}=53 – 361
Chen et al. [Chen et al., 2017]	Water	8.2	0.3 – 0.943	1157 – 3776	ΔT_{in}=19 – 337
Kariya et al. [Kariya et al., 2013]	Water, R22, R134a	4.4	0.635 – 0.992	400 – 1000	ΔT_{in}=1 – 40
Katto and Ohno [Katto & Ohno, 1984]	Water, R12, R22, R134a, H_2, N_2, He	1 – 30	0.1 – 0.9	100 – 8800	x_{in}<0
Shah [Mohammed Shah, 1987]	23 fluids (water, refrigerants, cryogens, chemicals, and liquid metals)	0.315 – 37.5	0.0014 – 0.96	4 – 29051	x_{in}=-4 – 0.85
Vijayarangan et al. [Vijayarangan et al., 2006]	Water, R134a	12.7 – 15	0.13 – 0.95	200 – 3000	ΔT_{in}=2 – 10
Shim and Lee [Shim & Lee, 2006]	Water	1 – 44.7	0.005 – 0.937	10 – 18619	Δh_{in}=-610 – 1655
Hall and Mudawar [Hall & Mudawar, 2000a]	Water	0.25 – 15	0.005 – 0.906	300 – 30000	x_{in}=-2 – 0
Lombardi [Lombardi, 1995]	Water	0.3 – 37.5	0.005 – 0.974	100 – 90000	ΔT_{in}=13 – 338
Groeneveld et al. [Groeneveld et al., 2007]	Water	3 – 25	0.005 – 0.952	0 – 8000	–
Doroshchuk et al. [Doroshchuk et al., 1975]	Water	4 – 25	0.131 – 0.906	500 – 5000	ΔT_{in}=0 – 75
Kon'kov [Kon'Kov, 1965]	Water	4 – 32	0.022 – 0.906	200 – 5000	–
Becker et al. [Becker et al., 1972]	Water	10	0.544 – 0.906	1100 – 7000	ΔT_{in}=8 – 272

[*] x_{in}= vapor quality at inlet, ΔT_{in}= subcooled inlet temperature in K, Δh_{in}= subcooled enthalpy at inlet in kJ/kg
all properties are taken from REFPROP of NIST [Lemmon et al., 2007]

2.4. Fluid-to-fluid scaling models

Scaling or similarity methods are often used in fluid dynamics to reduce experimental time and costs. Dimensionless numbers and proper scaling methods ensure the correct transfer of the experimental data. Physical similarity is given if the relevant dimensionless numbers are the same for the model and the prototype. For example, the flow behavior of new wings are tested as smaller models in wind tunnels. The same geometric proportions and the same Reynolds number as from the prototype are used to conduct the experiments.

Heat transfer experiments at supercritical conditions in water require high-pressure and temperature test facilities which are very expensive to construct, maintain and operate. It is therefore more economical to perform experiments in a modeling fluid at water-equivalent conditions and transform the modeling fluid data into water. Supercritical test facilities using modeling fluids operate at much lower pressures, temperatures, are less costly and easier to construct. Smaller heating and cooling power are needed due to the lower latent heat, heat conductivity, specific heat capacity and temperatures. This also reduces the operation costs and risk, the time to conduct a similar experiment and the test section design plus allowing a wider spectrum of feasible experiments.

2.4.1. Derivation of scaling models

The same number of dimensionless number as parameters of the experiment are needed for a complete scaling process. For example, 5 dimensionless numbers are needed for CHF experiments to scale the diameter, pressure, mass flux, vapor quality and CHF, respectively. Dimensionless numbers can be derived from the dimensionless forms of the governing equations, by application of the Buckingham π theorem or by similarity transformation. These methods will be described in the following sections. Often more dimensionless numbers are found than independent parameters. In such cases, the number must be reduced by exclusion of unimportant numbers or by combination of multiple numbers as described by Ahmad. These methods are introduced subsequently.

2.4.1.1. Dimensionless forms of the governing equations

The conservation equations for continuity, momentum and energy, which are relevant and customized to the physical problem, are used for this method. Boundary conditions and characteristic values are introduced to transform the equations to a dimensionless form. Then, the dimensionless numbers describing this problem can be derived. The dimensionless governing equations have the same solution for different fluids that have identical values of the derived dimensionless numbers. A detailed description with an example can be found in [Zierep, 1972, Cheng et al., 2011].

2.4.1.2. Buckingham π theorem

The Buckingham π theorem is a dimension analysis introduced by Buckingham [Buckingham, 1914] and is based on Rayleighs work [Rayleigh, 1892]. First, the relevant variables, which describe a physical problem, are identified. The relationships between the physical quantities is then described in a dimensional matrix by identifying their independent base quantities. The dimensionless numbers can be derived from this matrix, which together describe the physical problem. Buckingham stated that if there are n variables in a problem and these variables contain m primary dimensions, the equation relating all the variables will have (n-m) dimensionless groups. A detailed description with an example can be found in [Cheng, 1991, Löwenberg, 2007].

2.4.1.3. Similarity transformation

Similarity transformation is used to simplify or reduce differential equations in fluid dynamics. Thereby, complex equations can be solved analytically or numerically with less computing power. The solutions are substituted by similar non-differential solutions to simplify the differential equations. A well known example is the Blasius equation for the boundary layer which was derived in this way [Blasius, 1907].

2.4.1.4. Compensating distortion approach by Ahmad

Buckingham [Buckingham, 1914] proposed that a combination of dimensionless numbers π is sometimes more useful in practice. Ahmad [Ahmad, 1973] improved this approach and combined dependent numbers to one. However, the single numbers have different potential at scaling a certain parameter. Ahmad proposed that the dimensionless numbers get different power coefficients to compensate this distortions as described in equation 2.27.

$$\pi = \pi_1 \pi_2^{n_1} \pi_3^{n_2} \tag{2.27}$$

In that way every parameter of the experiment is described by one dimensionless product. This allows each parameter to be scaled and individually controlled in the experiment to satisfy the original parameters.

2.4.2. Validation of scaling models

The fluid-to-fluid scaling models must be validated to proof their capability. Depending on the available data, there are different ways for the validation, which are described in the following sections.

2.4.2.1. Direct Validation

The ideal method for the validation of fluid-to-fluid scaling models is the direct approach. This means that experimental sets of two different fluids can be compared directly. Thus, no additional uncertainties of correlations or other methods are added to the results. Therefore, the differences in the comparison results are only caused by the scaling models. However, this is limited by obtaining experimental data with comparable parameters. The database of at least one fluid must be resolved very finely in all parameters which results in a huge set of experimental data. Further interpolation of at all parameters is needed to obtain identical parameters for the comparison that also results in a huge data base and experimental effort.

2.4.2.2. Indirect Validation

Most authors mentioned that there are basically insufficient data available for the direct approach. In these cases, experimental data of one fluid are scaled with equivalent conditions to another fluid. These data are compared with data predicted by either correlations, look-up tables or simulations. Thus, in the indirect approach the prediction methods introduce its uncertainty to the uncertainty of the scaling models. Therefore, the accuracy of the correlations is crucial to determine the validity of the fluid-to-fluid scaling models. Consequently, prediction methods with smaller uncertainties, such as the look-up tables, should be preferred. When using simulations, no experimental data are necessary and both fluids can be simulated numerically. Thus, no interpolation and correlations are needed and data with varying parameters can be produced quickly. A disadvantage is the high uncertainty of numerical methods for heat transfer at supercritical conditions and CHF.

2.4.3. Fluid-to-fluid scaling of heat transfer at supercritical conditions

Scaling models for convective heat transfer at supercritical pressures were first developed by Jackson and Hall. The authors identified 8 dimensionless numbers needed for complete similarity between two systems [J.D. Jackson, W. B. Hall, 1979]. Jackson and Hall derived the numbers with similarity considerations and by examination of the governing equations and the boundary conditions in non-dimensional form [J.D. Jackson, W. B. Hall, 1979]. These 8 dimensionless numbers are the base for further developed models of Pioro and Duffey [Pioro & Duffey, 2007] as well as Zwolinski [Zwolinski et al., 2011]. Other authors used the dimensionless governing equations as well to derive the same or similar dimensionless groups. The derivation methods and

the method for the validation are listed in table 2.6 for selected fluid-to-fluid scaling models. The models are described in appendix B. No author used the Buckingham π theorem for the derivation of the dimensionless groups. The similarity transformation was only used by Tian et al. to derive a new number to scale the mass flux. For that, similar heat transfer cases with water and R134a were analyzed numerically. Based on the numerical results, the thermal resistance analogy was used to derive a dimensionless number in a similar way as Pandey et al. as well as Kim and Kim [Pandey & Laurien, 2015, Kim & Kim, 2011b]. Tian derived a solution for a tube with constant heat flux from the energy conservation for the axial velocity gradient. The resulting dimensionless number for scaling the mass flux is shown in equation 2.31 in section 2.4.3.5 [Tian et al., 2018].

Table 2.6.: Selected fluid-to-fluid scaling models and used methods for derivation and validation

Authors	Year	Condition	Derivation	Validation
Jackson and Hall (B.5)	1979	inlet	governing equations	direct
Pioro and Duffey (B.6)	2007	local	from Jackson and Hall	-
Cheng et al. (B.3)	2011	local	governing equations	correlations
Zwolinski (B.9)	2011	local	from Jackson and Hall	simulations
Ambrosini B.1)	2011	inlet	governing equations	simulations
Zahlan (B.8)	2014	local	from Cheng et al.	look-up table
Azih and Yaras (B.2)	2017	inlet	governing equations	direct
Tian et al. (B.7)	2018	local	similarity transformation and governing equations	direct and correlations

As seen in table 2.6, some authors used the direct approach for their validation. All authors stated that only a few cases could be found for their comparison which is insufficient for a reliable validation. Most authors mentioned a lack of experimental data for the direct approach and used correlations, look-up tables or simulations instead. Nearly all authors stated that large databases are required for developing and validating fluid-to-fluid scaling models.

Scaling models are either based on local or on inlet conditions. Most authors developed scaling models based on local bulk properties. This is because the thermal-physical properties vary differently between different fluids. As a result, the factors to scale these different trends vary, too. This can be seen in figure 2.14. Jackson and later Ambrosini and Azih and Yaras [Jackson, 2008, Ambrosini, 2011a, Azih & Yaras, 2017] proposed that heat transfer data at supercritical conditions, especially HTD data, are only scalable with an inlet based approach. Reynold, Richard and Prandtl number must be distributed similar along the tube for heat transfer similarity in a mixed-convection. Ambrosini pointed out that these numbers play a key role for the similarity of different fluids at heat transfer at supercritical conditions.

2.4.3.1. Scaling of geometry

Jackson noted that strong presence of buoyancy, compressibility or viscous losses would hinder a complete similarity between two systems. Therefore, the diameter of the tube must be big enough to prevent significant effects of viscous pressure losses and it must be small enough to minimize the buoyancy effects [Jackson, 2008]. For a scaled local HTC, the energy balance between the inlet and the location must be calculated with considering the l/d ratio at the scaled condition. Zwolinski as well as Pioro and Duffey included this parameter in their models.

Cheng et al. and Zahlan [Cheng et al., 2011, Zahlan, 2015] define a similar tube diameter and thus eliminating possible tube size effects in the other dimensionless numbers. Moreover, the approach is at local conditions which eliminates the need of similar inlet conditions and the bounding l/d ratio. The other authors listed in table 2.6 did not state any limitation on the geometry scaling.

2.4.3.2. Scaling of pressure

Except Ambrosini, all authors scale the pressure using the reduced pressure defined in equation 2.28. The A in the following equations is a placeholder and can stand for a system or a fluid. Ambrosini [Ambrosini, 2011a] stated the importance of similar Prandtl number for scaling heat transfer coefficients. Therefore, Ambrosini chose the pressure where the maxima of the Prandtl numbers at the pseudo-critical temperature are equal.

$$P^* = \left(\frac{P}{P_c}\right)_A \tag{2.28}$$

2.4.3.3. Scaling of bulk temperature

Figure 2.14 shows the trends for different dimensionless temperatures for the specific heat capacity, thermal conductivity and the density. Concerning the scaling, equal trends of the thermal-physical properties would be ideal or if the trends would differ with an constant factor. Most authors use the ratio of bulk temperature to pseudo-critical temperature to scale the bulk temperature. This normalization shows a closer trend of the thermal-physical properties than the normalization by the critical temperature as seen in figure 2.14. Cheng et al. [Cheng et al., 2011] introduced a new dimensionless number θ to scale the local bulk temperature as seen in equation 2.29 (c). Cheng proposed a better similarity between normalized fluid properties for water, CO_2 and R134a using θ. Figure 2.14 shown exemplarily this better agreement for the normalized thermal-physical properties.

However, Zwolinksi [Zwolinski et al., 2011] was concerned that θ limits the model to close pressures around the pseudo-critical point. Despite closer similarity, Zahlan also decided to use the pseudo-critical temperature to scale the bulk temperature.

$$(a): \ T_c^* = \left(\frac{T_b}{T_c}\right)_A; \ (b): T_{pc}^* = \left(\frac{T_b}{T_{pc}}\right)_A; \ (c): \theta = \left(\frac{T_b - T_{pc}}{T_{pc} - T_c}\right)_A; \ (d): h^* = \left(\left(h_{pc} - h_b\right)\frac{\beta_{pc}}{c_{p,pc}}\right)_A \tag{2.29}$$

Ambrosini and Sharabi [Ambrosini & Sharabi, 2008] derived a new dimensionless enthalpy h* to scale the bulk enthalpy instead scaling the bulk temperature. The dimensionless density can be effectively described as a function of the dimensionless enthalpy, where different supercritical pressures coincide. They also coincide for different fluids as seen in figure 2.15 (c) [Ambrosini & Sharabi, 2008]. Therefore, Tian et al. uses this dimensionless number as well. However, the dimensionless enthalpy shows no improvement for the dimensionless heat capacity and heat conductivity compared to the other dimensionless numbers as seen in figure 2.15 (a) and (b).

2.4.3.4. Scaling of heat flux

The thermal loading number q* of equation 2.30 (a) with different reference temperatures is used to scale the heat flux. Jackson [Jackson, 2008] used the bulk temperature. Cheng et al. [Cheng et al., 2011] identified the difference between critical and pseudo-critical temperature as reference temperature, which is dependent on their dimensionless temperature θ. Zahlan [Zahlan, 2015] determined the pseudo-critical temperature as reference.

$$(a): \ q^* = \left(\frac{qd}{\lambda_b T_{ref}}\right)_A ; \ (b): \ \pi_{A,pc} = \left(\frac{q\beta_{pc}}{Gc_{p,pc}}\right)_A \tag{2.30}$$

Ambrosini [Ambrosini & Sharabi, 2008] as well as Azah and Yaras [Azih & Yaras, 2017] used the dimensionless acceleration number π_A, which is defined at the pseudo-critical temperature, to scale the heat flux.

(a) Normalized specific heat capacity versus temperature normalized by the critical temperature

(b) Normalized thermal conductivity versus temperature normalized by the critical temperature

(c) Normalized density versus temperature normalized by the critical temperature

(d) Normalized specific heat capacity versus temperature normalized by the pseudo-critical temperature

(e) Normalized thermal conductivity versus temperature normalized by the pseudo-critical temperature

(f) Normalized density versus temperature normalized by the pseudo-critical temperature

(g) Normalized specific heat capacity versus dimensionless temperature θ

(h) Normalized thermal conductivity versus dimensionless temperature θ

(i) Normalized density versus dimensionless temperature θ

Figure 2.14.: Normalized fluid properties versus different dimensionless temperatures at pressure from 1.13 times of the critical pressure, which correspond to 25 MPa in water

(a) Normalized specific heat capacity versus dimensionless enthalpy h^*

(b) Normalized thermal conductivity versus dimensionless enthalpy h^*

(c) Normalized density versus dimensionless enthalpy h^*
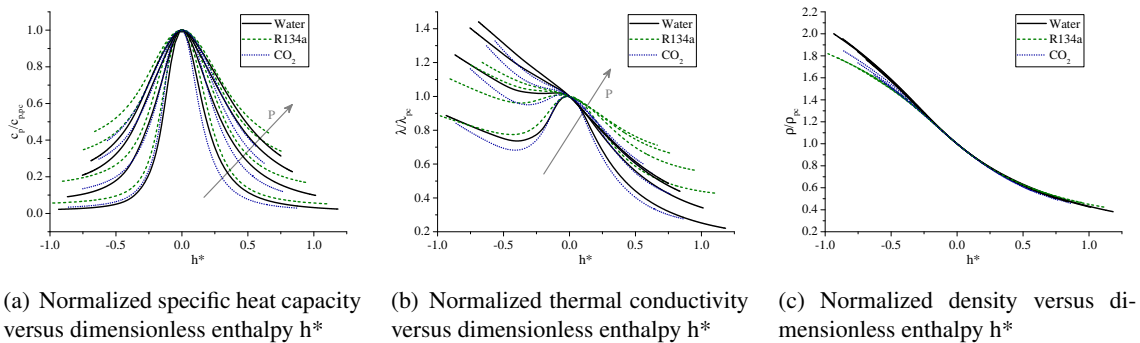
Figure 2.15.: Normalized fluid properties versus dimensionless enthalpy h^* at pressure from 1.04, 1.13, 1.27 and 1.36 times of the critical pressure, which correspond to 23, 25, 28 and 30 MPa in water

38

2.4.3.5. Scaling of mass flux

Jackson and Hall [J.D. Jackson, W. B. Hall, 1979] applied the Reynolds number to scale the mass flux. This is shown in equation 2.31 (a) with $m_1=0$. Using the compensated distortion approach of Ahmad [Ahmad, 1973] and based on the correlation of Dittus-Boelter [Dittus & Boelter, 1985], Cheng et al. [Cheng et al., 2011] derived $m_1=5/12$ for equation 2.31 (a). Zahlan [Zahlan, 2015] developed two sets of fluid-to-fluid scaling models using own CO_2 data and the established transcritical look-up-table. The author modified Cheng's model by changing the exponent m_1 to 0.63 for the supercritical region. The exponent for the dimensionless number of Zahlan's model was fitted to 0.66.

Tian et al. derived a scaling number for the mass flux, which includes the Reynolds number and the acceleration number π_A to include buoyancy effects and is shown in equation 2.31 (b). The authors found a exponent of $m_2=-0.9$ based on the similarity transformation of the dimensionless equations.

$$(a):\ G_1^* = \left(\frac{GPr_b^{m_1}d}{\mu_b}\right)_A\ ;\ \ (b):\ G_2^* = \left(Re^{m_2}\pi_{A,pc}\right)_A \tag{2.31}$$

In the scaling models of Ambrosini [Ambrosini & Sharabi, 2008] and Azih and Yaras the mass flux is determined by the acceleration number π_A ($m_2=0$ in equation 2.31 (b)) and by the preserved inlet conditions, as discussed in the next section.

2.4.3.6. Scaling of inlet conditions

As mentioned before, Ambrosini as well as Azih and Yaras [Azih & Yaras, 2017] proposed that HTD data are only scalable properly with similar inlet conditions. Therefore, it was stated that the dimensionless bulk enthalpy, the Richardson number and the Reynolds number at the inlet must be preserved. The dimensionless numbers are defined in equation 2.32.

$$(a):\ h_{in}^* = \left((h_{pc}-h_{in})\frac{\beta_{pc}}{c_{p,pc}}\right)_A\ ;\ \ (b):\ Re_{in} = \left(\frac{Gd}{\mu_{in}}\right)_A\ ;\ \ (c):\ Ri_{in} = \left(\frac{\rho_{in}^2 g d^2}{G^2}\frac{\beta_{in}q^2}{\lambda_{in}}\right)_A \tag{2.32}$$

2.4.4. CHF fluid-to-fluid scaling models

It is well accepted that the scaling models of Ahmad [Ahmad, 1973, Ahmad & Groeneveld, 1972] work well and give the best results for the fluid-to-fluid scaling for CHF data [Verein Deutscher Ingenieure, 2013]. Ahmad followed the methodology of Barnett [Barnett, 1963, Barnett, 1964] and used the Buckingham π theorem to identify 13 dimensionless numbers. Ahmad showed that six numbers are not significant for the scaling. The four numbers showed in equations 2.33 – 2.36 can be controlled independently by test section geometry, pressure, inlet temperature and heat flux, respectively. A and B stands for different fluids in the equations. The pressure is determined by the ratio of the density of the liquid to the vapor phase. The inlet enthalpy is scaled using the subcooled enthalpy Δh_{sub} and the latent heat of vaporization Δh_{vap}. The CHF itself is scaled with mass flux and latent heat of vaporization.

$$\left(\frac{L}{d}\right)_A = \left(\frac{L}{d}\right)_B \tag{2.33}$$

$$\left(\frac{\rho_l}{\rho_g}\right)_A = \left(\frac{\rho_l}{\rho_g}\right)_B \tag{2.34}$$

$$\left(\frac{\Delta h_{sub}}{\Delta h_{vap}}\right)_A = \left(\frac{\Delta h_{sub}}{\Delta h_{vap}}\right)_B \tag{2.35}$$

$$\left(\frac{q_{CHF}}{G \Delta h_{vap}}\right)_A = \left(\frac{q_{CHF}}{G \Delta h_{vap}}\right)_B \tag{2.36}$$

Ahmad [Ahmad, 1973] used his distortion approach, which is described in section 2.4.1.4, to combine the remaining three dimensionless numbers to the scale the mass flux. The coefficients were determined empirically with data of R12 and water. The resulting dimensionless number is shown in equation 2.37 with the surface tension σ.

$$\Phi = \left(\frac{Gd}{\mu_l}\right)\left(\frac{\mu_l^2}{\sigma d \rho_l}\right)^{2/3}\left(\frac{\mu_g}{\mu_l}\right)^{-1/5} \tag{2.37}$$

Cheng and Groeneveld et al. [Cheng, 1991, Groeneveld et al., 1997] suggested the Weber number We of equation 2.38 to scale the mass flux.

$$We = \left(\frac{\rho_l u^2 d}{\sigma}\right)_A = \left(\frac{\rho_l u^2 d}{\sigma}\right)_B \tag{2.38}$$

Additionally, the authors determined the vapor quality x as an important parameter for the hydrodynamic similarity, which should be the same for both fluids A and B.

$$(x_{CHF})_A = (x_{CHF})_B \tag{2.39}$$

Pioro et al. [Pioro et al., 2001, Pioro et al., 2002] used the dimensionless number shown in equation 2.40 of Katto [Katto, 1978] to scale the mass flux. This number is based on the Weber number as well. Chen et al. [Chen et al., 2010] suggested to use the mean value of the numbers proposed by Ahmad and Katto (equation 2.37 and 2.40) to scale the mass flux. Chen et al. published scaling factors for pressure, inlet subcooling, mass flux and the critical heat flux for scaling CHF from R134a to water.

$$\left(G\sqrt{\frac{d}{\sigma \rho_l}}\right)_A = \left(G\sqrt{\frac{d}{\sigma \rho_l}}\right)_B \tag{2.40}$$

Several authors showed that the scaling models implemented by Ahmad are valid for R134a and water. Equation 2.39 as well as the number proposed by Katto et al. (equation 2.40) are often used additionally to the scale mass flux [Pioro et al., 2001, Pioro et al., 2002, Kim & Chang, 2005, Chun et al., 2007a, Lee et al., 2008, Eter et al., 2017a].

2.4.5. Modeling fluids R134a and CO_2

1,1,1,2-tetrafluorethane (CF_3CH_2F), former known as R134a, substituted R12 as modeling fluid, coolant in refrigerators, other cooling machines and experimental loops because of its smaller global warming potential and non-existing ozone depletion. It is widely used as coolant for refrigerants and air-conditioners, in particular for vehicles. Thus, the properties of R134a are well known and documented in detail.

Carbon dioxide is used in many facilities as well because of the high availability of high purity CO_2. It has a very low global warming potential and is none-toxic. Additionally, the thermal-physical properties are know in detail. Therefore, many heat transfer experiments are conducted with CO_2 as well.

Table 2.7.: Critical point and properties of water, CO_2 and R134a

Fluid	Critical temperature	Critical pressure	Critical density	Specific heat[*]	Heat conductivity[*]
	$[°C]$	$[MPa]$	$\left[\frac{kg}{m^3}\right]$	$\left[\frac{kJ}{kgK}\right]$	$\left[\frac{W}{mK}\right]$
Water	373.95	22.064	322	6.75	49.1×10^{-2}
R134a	101.06	4.059	511.9	1.86	5.9×10^{-2}
CO_2	30.978	7.3773	467.6	2.81	9.7×10^{-2}

[*] at 0.95 of critical temperature and 0.99 of critical pressure
all properties are taken from REFPROP of NIST [Lemmon et al., 2007]

The critical points of water, R134a and CO_2 are shown in table 2.7. It can be seen that the critical temperature and pressure of R134a and CO_2 are much smaller than of water. The specific heat and heat conductivity are also smaller. Hence, the testing facilities using model fluids instead of water have much lower requirements for pressure and temperature and need less heating and cooling capacities. This significantly reduces the costs and time of constructing the facility and conducting experiments. Compared to CO_2, R134a provides a higher critical temperature. Thus, inlet subcooling can be reached more easily without using an extra cooling machine.

A disadvantage of R134a is the thermal stability. It decomposes above $368 °C$ [Calderazzi & Di Paliano, 1997]. Dai et al. [Dai et al., 2018] affirmed this result with a decomposition temperature of $360 °C$. Additionally, the authors highlighted the importance of the pureness of the fluid. Air has a big influence on the decomposition temperature and can decrease it strongly [Dai et al., 2016]. In contrary, there is no temperature limitation for experiments with CO_2 as its decomposition temperature is at $2000 °C$ [Lietzke & Mullins, 1981].

2.5. Flow instability

A stable flow behavior is one of the important design objectives in thermal energy systems to avoid thermal and mechanical fatigue, power production variations and perturbations of the heat transfer capabilities. Nevertheless, instabilities are often encountered in fluid systems. They are produced by delays between causes and effects due to the transport of perturbations or due to non-monotonic trends in pressure drop versus flow characteristics. The strong variations of the density in a heated channel at supercritical conditions can additionally cause fluid-dynamic instabilities. When dealing with nuclear reactors, the instability can be amplified or triggered due to the coupling with the neutronic processes [Ambrosini & Sharabi, 2008]. A linear stability analysis of supercritical water reactors due to the coupling of thermal hydraulics and neutronic processes was done by Yi et al. [Yi et al., 2004] and is discussed in detail in the book of Oka et al. [Oka et al., 2010].

Flow instability at subcritical flow conditions has received considerable, in-depth studies by many investigators. Flow instability at supercritical conditions, however, has not been investigated to a similar degree. At supercritical conditions, most investigations were done concerning flow instabilities at natural convection as done by Chatoorgoon [Chatoorgoon, 2001] and Sharma et al. [Sharma et al., 2014].

Oka et al. [Oka et al., 2010] described the occurrence of flow instabilities in a fuel channel at supercritical conditions with the physical mechanism shown in figure 2.16. If the coolant temperature passes the pseudo-critical point, the density undergoes a huge reduction as shown in figure 2.2. As a result of the density variation along the channel, the local pressure drop changes at each axial position. These changes are carried along by the passing coolant. The sum of all these local pressure drops causes a change in the total pressure drop. The thermal-physical instability occurs if the channel pressure drop perturbations become out-of-phase with the inlet flow perturbations due to the time taken by the flow transportation. The chronological order of the included physical mechanisms are shown in figure 2.16.
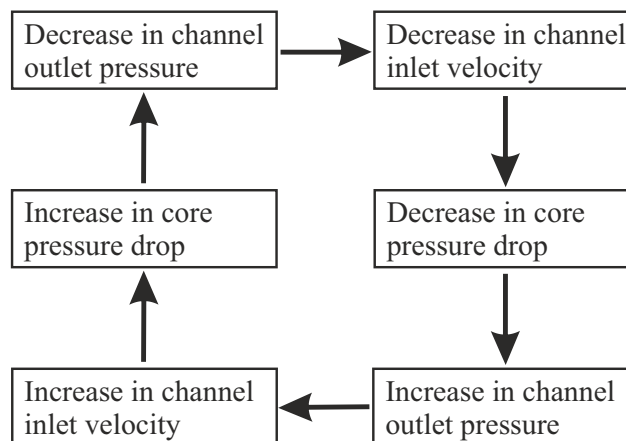
Figure 2.16.: Physical mechanism causing thermal hydraulic instability [Oka et al., 2010]

Flow instabilities are divided into static and dynamic flow instabilities. The best known static flow instability is the Ledinegg instability [Ledinegg, 1938] with its origin in the two-phase flow. Ambrosini et al. showed that the Ledinegg instability can also occur at supercritical conditions [Ambrosini & Sharabi, 2008]. Due to the added heat, the fluid changes its state from liquid (-like) to vapor (-like). The change is vice versa if the mass flow rate increases for a constant heat flux. Due to the different densities, the pressure drop Δp_{drop} changes. However, as the flow rate increases, the actual characteristic must make a transition from the all-vapor line to the all-liquid line as seen in figure 2.17. This can lead to a negative slope for the pressure drop in the channel and can lead to an quasi-static point 0 at the characteristic line of the pump Δp_{pump}.
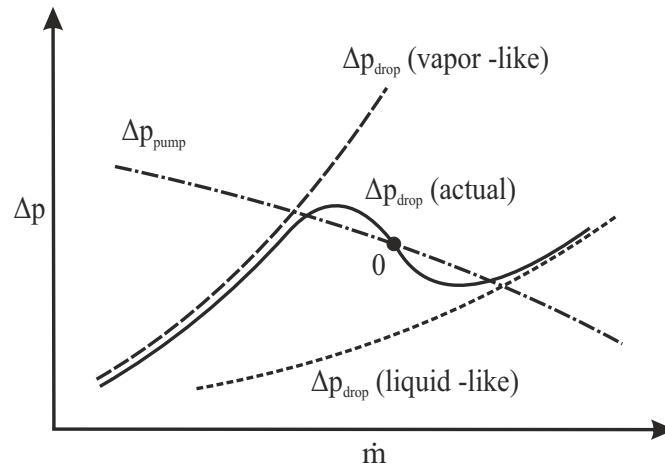
Figure 2.17.: Sketch illustrating the Ledinegg instability caused by density changes [Ambrosini, 2011b]

The pressure drop oscillations occur when a system, that would be prone to the static Ledinegg instability, is coupled with compressible devices. This allows dynamic oscillations of the system [Ambrosini, 2011b]. An example is the density-wave oscillations described by Oka et al. [Oka et al., 2010] before. Here, regions of different densities traveling through the channel affect pressure and velocities at the inlet and outlet. The occurrence of these different regions depends on the dynamic characteristics of the system as it must have a negative hydraulic impedance for sustaining the oscillation.

2.6. Deficiencies in the literature and need for research

Much effort has been taken and many papers have been published about heat transfer at supercritical conditions, but the occurring phenomena are still not fully understood. Due to the time intensive and expensive experiments, there is no investigation performing a quantitative analysis of multiple parameters affecting the heat transfer at supercritical conditions on a wide range of the parameters [Ma et al., 2017]. Most studies investigate only few pressures and mass fluxes. No study focusing exclusively on the inlet effect on the heat transfer was found in this literature research. Therefore, *a wide set of experiments with a extensive range of input parameters* will be conducted in this study to investigate the influence of mass flux, heat flux, pressure and inlet temperature systematically. A symmetrical and evenly distributed matrix of experiments will help to understand the phenomena of heat transfer at supercritical conditions. Especially, the effects of buoyancy forces and the thermal-induced bulk flow acceleration should be investigated. Additionally, the literature review reveals that the heat transfer at supercritical conditions is difficult to reproduce. This could be due to the high sensibility of the heat transfer at the known but also at unobserved parameters like the wall thickness or the surface roughness of the heated wall. All parameters should be documented in detail and considered for the heat transfer investigations. Only if all parameters for possible deviations are excluded, the idea of multi-solutions for the heat transfer at supercritical conditions can be proofed. Moreover, it is important to identify flow instabilities because of a crucial change of the heat transfer conditions. This data must be excluded for the investigation of the fundamental heat transfer. These detailed and conscientious investigations potentially enables a reliable description of the heat transfer at supercritical conditions.

With this wide set of experiments, a huge database will be build with R134a for heat transfer at supercritical conditions. A huge database of water data is built at the IATF as well. Additionally, a database of CO_2 will be build with own and literature data. These three databases enable: (a) understanding of various phenomena, (b) assessment of correlations and availability for correlation development, (c) reliable assessment of fluid-to-fluid scaling models using the direct method

and (d) improvement of the existing fluid-to-fluid scaling models if necessary. These databases overcome the lack of sufficient experimental data that almost every author stated to verify the single fluid-to-fluid scaling models.

Due to the limited investigations on CHF at high subcritical pressures, more CHF experiments are necessary for further understanding. With the produced data, correlations and the fluid-to-fluid scaling should be validated at high pressures. Based on the validation, a further need for research will be identified on correlations and scaling at the end of this study.

3. Experimental Setup and Methodology

This chapter introduces the experimental setups, the test procedures and parameters, the data reduction and the propagation of uncertainty. This includes the description of the test facilities, the test sections and the measurement devices. Also the validation of the measurement systems is shown by the heat balance, comparison with correlations and the reproducibility of the results. Two facilities and three different test sections have been used. The CHF and heat transfer experiments at supercritical conditions with R134a have been conducted at the KIMOF of the IATF with two different test sections. Additionally, heat transfer experiments at supercritical conditions with CO_2 have been done at the Supercritical University of Ottawa Loop (SCUOL).

3.1. Experimental facilities

3.1.1. KIT Model Fluid Facility - KIMOF

The KIT Model Fluid Facility was constructed by ANNEN Verfahrenstechnik. It consists of a closed loop with a forced circulation of R134a and several auxiliary loops as shown in figure 3.1. The parts filled with freon are colored. The R134a is delivered from Linde and has a mass purity of 99.7 % with mainly incondensable gases as impurity. There are two test sections with different sizes. Single tubes and annuli can be easily installed at the small one and rod bundle geometries at the other. The Freon is preheated before the test section to the required temperature by a heat exchanger fed by hot water. Four heat exchangers cool the fluid before it returns to the circulation pump.

The water for the preheater is heated by a gas burner. The mass flow rate through the heat exchanger is regulated with a mixing valve. The power of the burner isn't adjustable during the experiments. To buffer the off times and high temperature impacts of the burner, a tank with 500 liters is installed.

Two heat exchangers for each test section are needed to adapt the cooling capacities. The heat is removed by a cooling tower. The cooling machine ensures a subcooled fluid at the inlet of the pump at high heating rates. It also enables low inlet temperatures below room temperature.

A pressurizer, which consists of three piston accumulators, is connected to the loop and controls the system pressure at the outlet of the test sections. The mass flow through the test sections is kept constant and adjusted by two bypasses. The design temperature and pressure of the KIMOF is 250 °C and 7 MPa, respectively. The data acquisition system consists of Wago programmable logic controllers and three 2640A data loggers from FLUKE connected to a PC with LABVIEW.
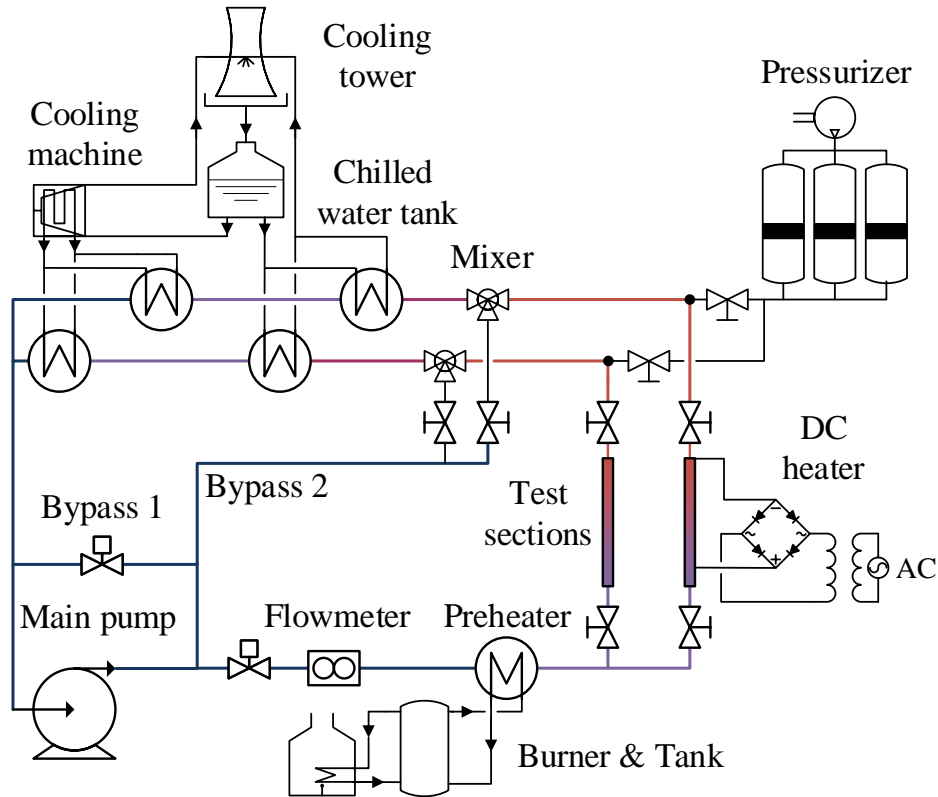
Figure 3.1.: Schematic concept of the KIMOF

3.1.2. Supercritical University of Ottawa Loop - SCUOL

A detailed description of the loop is provided by Kline et al. in [Kline, 2017, Kline et al., 2018] and Jiang [Jiang, 2015]. The SCUOL is designed for different fluids up to 10 MPa. For this study the loop is filled with CO_2 with a purity of 99.998 %. It is a closed loop whose pressure is controlled by the mass and temperature of CO_2 in it. As example, for decreasing the pressure, CO_2 is removed or the temperature in the loop (e.g. at the pump) is decreased.

A scheme of the SCUOL is shown in figure 3.2. Two gear pumps circulate the fluid through the loop. An electric preheater provides temperature adjustment and control of the fluid entering the test section. The loop has three circular tubes with 22 mm, 8 mm and 4.6 mm inner diameter and one rod-bundle test section. For this study, the 8 mm tube is used and is described in the following section 3.2. Two pairs of heat exchangers, with chilled water and cooled ethylene glycol as secondary fluids, are installed downstream from the test sections. They ensure a liquid-like state of the fluid for protection of the pumps. Furthermore, they enable inlet temperatures at the test section close to 0 °C.
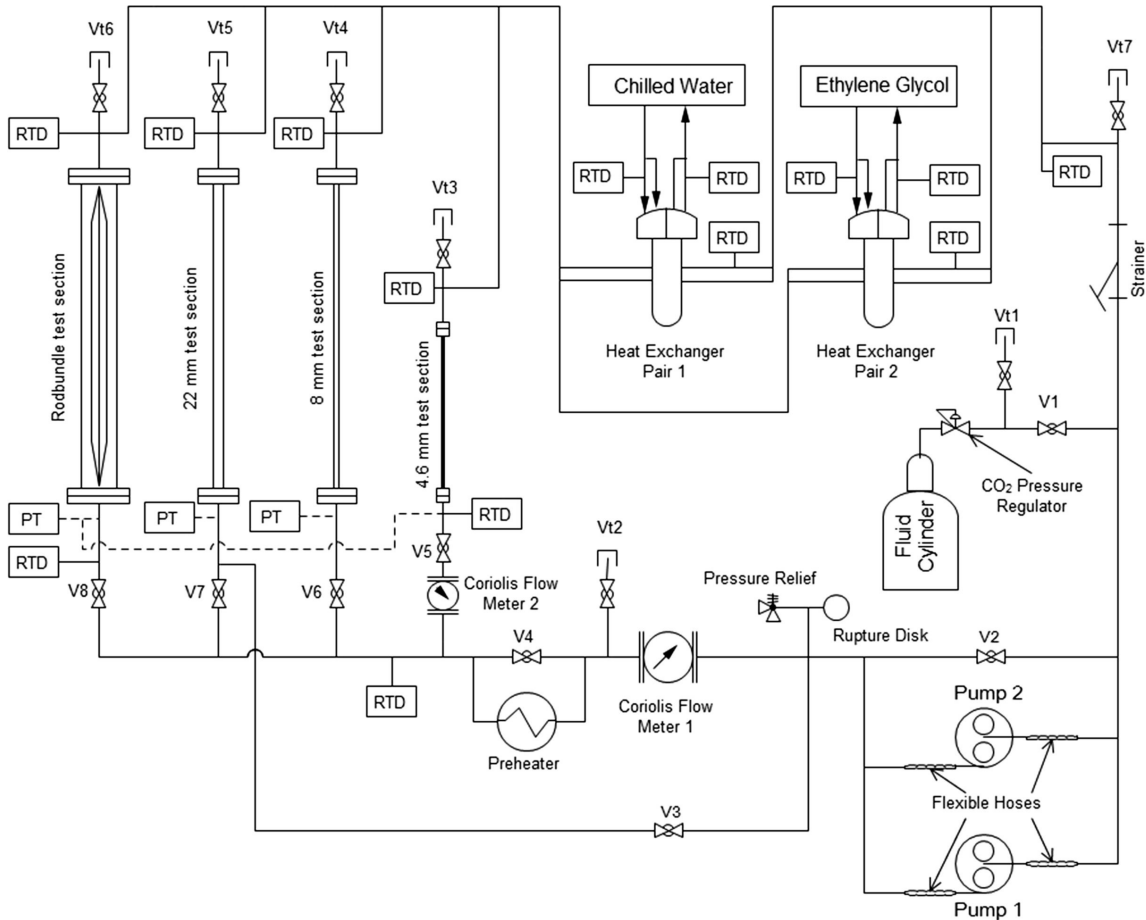
Figure 3.2.: Schematic concept of the SCUOL from [Kline et al., 2018]

3.2. Test sections

In this study, three different test section are used for the investigations. The most important parameters of the three test sections are listed in table 3.1 for an overview. Two test sections on the SCUOL and the KIMOF are used to measure the heat transfer at supercritical conditions. A third test section is used to measure the CHF at high subcritical pressures. The test sections are described in detail in the following paragraphs.

Table 3.1.: Used test sections for experiments for heat transfer at supercritical conditions (HT SC) and critical heat flux (CHF)

Name	Experiments	Loop	Fluid	d [mm]	L_h [m]	L_{un} [m]	Material
ts-1	HT SC	KIMOF	R134a	10	3.1	0.5	1.4301
ts-2	HT SC	SCUOL	CO_2	8	1.94	0.89	2.4816
ts-3	CHF	KIMOF	R134a	10	2.5	0.5	1.4301

A schematic of ts-1 and ts-3 is shown in figure 3.3. Similar tubes from ETHEN Rohre GmbH are used as test section for the heat transfer at supercritical conditions and the CHF experiments. They consist of stainless steel (1.4301) with an inner and outer diameter of 10 and 12 mm, respectively. They are installed vertically with an upward flow of R134a. The test sections are heated with direct current provided by a transformer and rectifier. To ensure the full development of the turbulent flow, the heating length starts after 500 mm, 50 times the tube diameter. The heated length is 3.1 m

and 2.5 m for ts-1 and ts-3, respectively. The test sections are electrically insulated to the rest of the loop by two insulating flanges. Pressure and temperature sensors are placed at the tubes' inlet and outlet to measure the fluid properties. The voltage drop is measured at the connectors. To minimize heat loss the test sections are insulated by 50 mm thick mineral wool.
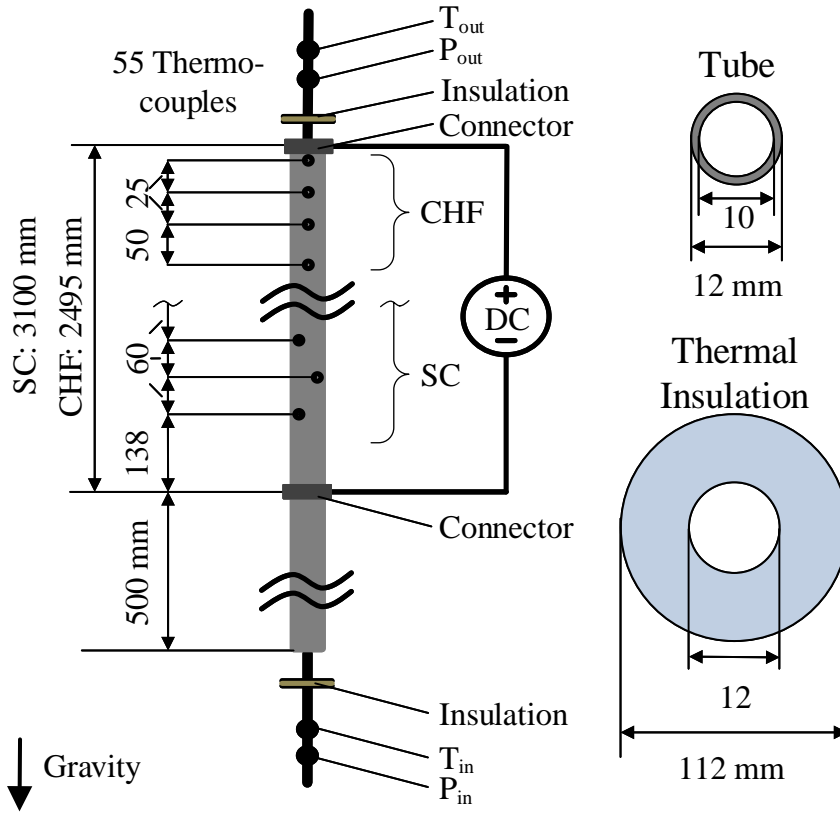
Figure 3.3.: Schematic concept of the test section of ts-1 (SC) and ts-3 (CHF)

55 thermocouples are mounted in total at ts-1. These are attached in 60 mm intervals at the tube's outside wall with the first starting at 138 mm after the connector. Consequently, the last one is 2 mm below the upper connector. They are mounted alternating at the opposite sides of the tube like implied in figure 3.3. Numbered from the inlet, the thermocouples 12 and 13, 22 and 23, 32 and 33, 42 and 43, 52 and 53 are on the same height to evaluate the temperature measurement directly at opposite sides.

To measure the CHF in ts-3, one thermocouple is attached at the very top of the test section, next to the upper connector of the DC power, as can be seen in figure 3.3. More thermocouples are fixed at distances of 25 mm, 50 mm and 100 mm from the top. The other 31 thermocouples are spread along the tube for observation.

For the experiments with CO_2, ts-2 with 8 mm inner diameter is used at the SCUOL. Detailed descriptions can be found in publications of Kline and Jiang et al. [Kline, 2017, Jiang, 2015, Kline et al., 2018]. The tube from Special Metals Corporation of Huntington consists of Inconel 600 and has a wall thickness of 1 mm. The heated length is 1940 mm after a 890 mm long unheated developing section. The heat is produced by direct current provided by a power supply. Dielectric flange gasket kits, which are constructed with PTFE (Teflon) sealing rings, insulate the test section from the loop. Two layers of insulation minimize the heat loss to the environment. One layer of

fiberglass cloth ribbon is wraped around the test section for added protection of the thermocouples from the outer layer of insulation. The outer layer consists of 40 mm thick fiberglass pipe insulation. To measure the wall temperature, 38 thermocouples are attached to the tube in 50 mm intervals on one side of the tube.

Additionally, the roughness of the tube's inside wall of ts-1 and ts-3 along the flow direction is detected with a confocal microscope μsurf from Nanofocus. Therefore, a piece of the tube was cut in half. The measured arithmetical mean deviation of the assessed profile (Ra) is 0.45 μm with a Gaussian filter of 0.25 mm . The roughness is unstructured and irregularly distributed with no visible grooves of the manufacturing process as seen in figure 3.4.
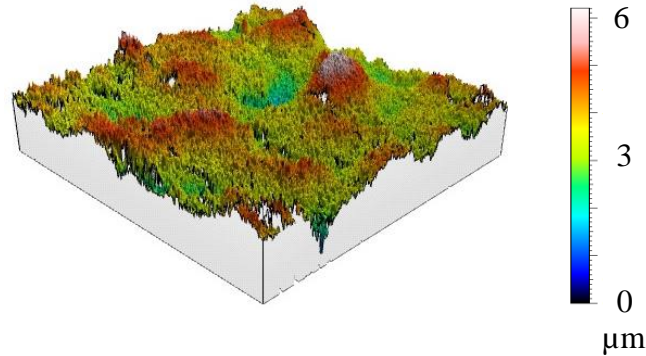
Figure 3.4.: Image of surface with colored roughness of the tube's inside wall of ts-3

3.3. Measurement devices

For the heat transfer experiments, several measurement devices are needed to measure the distributed power, heated wall temperature, mass flow rate, fluid temperature and pressure. The types for these measurements are listed as overview for the three test sections in table 3.2. The devices are described in detail in the following subsections. The uncertainties of all measurement devices are listed in section 3.6.

Table 3.2.: Measurement devices listed for used test sections

	ts-1	**ts-2**	**ts-3**
Wall thermocouples	type T, self-adhesive	type T, self-adhesive	type T, ungrounded
Numbers of T_w	55	38	35
Spacing of T_w	60 mm	50 mm	50, 25 mm at top
Temperature at inlet	type T	PT1000	type T
Temperature at outlet	type T	PT1000	type T
Pressure at inlet	8227-5100 from Burster	PX01C1-3KA5T from Omega	8227-5100 from Burster
Pressure at outlet	8227-5100 from Burster	none, therefore differential pressure	8227-5100 from Burster
Flow meter	Coriolis flow meter	Coriolis flow meter	Gear flow meter

3.3.1. Thermocouples for the wall temperature

All thermocouples at the test sections are type T because of the smaller uncertainties compared to other types. Due to the direct current applied to the tube, the wall thermocouples must be

insulated electrically. At ts-3, they are shielded but ungrounded ones from Omega (TJC400-CPSS-IM100U-30). The gap between the shielding and the thermo wires is filled with magnesium-oxide for electrical insulation. This protects the thermocouples and data logger and ensures a correct measurement of the temperature. The shielding consists of stainless steel. Therefore, the thermocouples must be mounted in a way, that only the tip (measurement point) is touching the tube. Otherwise it will conduct current and heat up. This would result in a different measured value than the actual wall temperature. A scheme and a mounted wall thermocouple are shown in figure 3.5.

(a) Picture of mounted thermocouple   (b) Schematic diagram of the shielded thermocouple
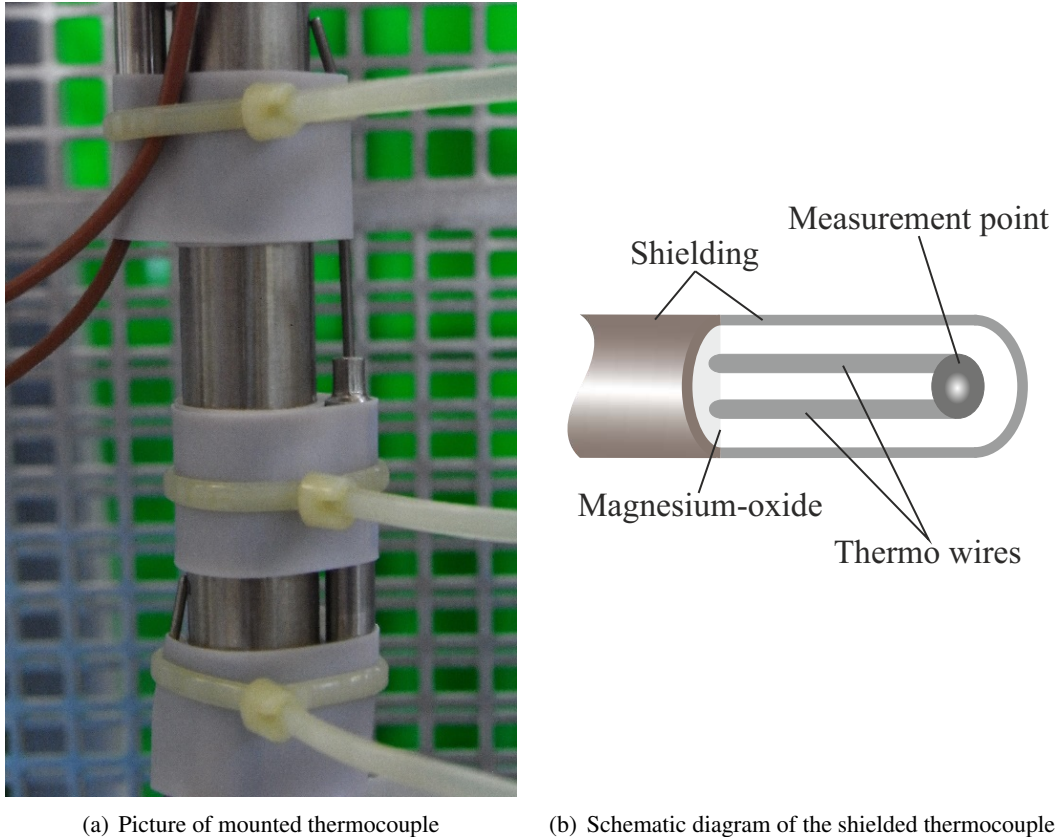
Figure 3.5.: Ungrounded thermocouples used to measure the wall temperature of ts-3

But the size of the touching area of the thermocouples at the wall slightly influences the measured temperature. Therefore, thermocouples using a silicone-based adhesive, reinforced with additional fiberglass for electrical isolation, are used for the heat transfer experiments at supercritical conditions. Due to the adhesive, the risk of mounting the thermocouple incorrectly is minimized. The several µm thick fiberglass ensures a measurement of the real wall temperature. 55 thermocouples of the type SA1XL-TI-3M from Omega are mounted at ts-1. For the 8 mm test section at the SCUOL (ts-2) the Canadian equivalent SA1XL-T-SRTC from Omega are used. Mounted wall thermocouples with a scheme are shown in figure 3.6.

3.3.2. Thermocouples for the fluid temperatures

There are no mixing chambers to mix the fluid before the measurement. For the inlet temperature it is not needed because the fluid is transferred through several meters and bends from the preheater to the test section. Also the outlet temperature shows a homogeneous mixed temperature. Further the outlet temperature is not needed directly for determining the HTC or CHF.

At ts-1 and ts-3 the thermocouples type T from Tecsis GmbH (TEK00X211027) at the inlet and outlet of the test section measuring the bulk temperature have been bent to point into the flow. They

(a) Picture of mounted thermocouple

(b) Schematic diagram of the self-adhesive thermocouple
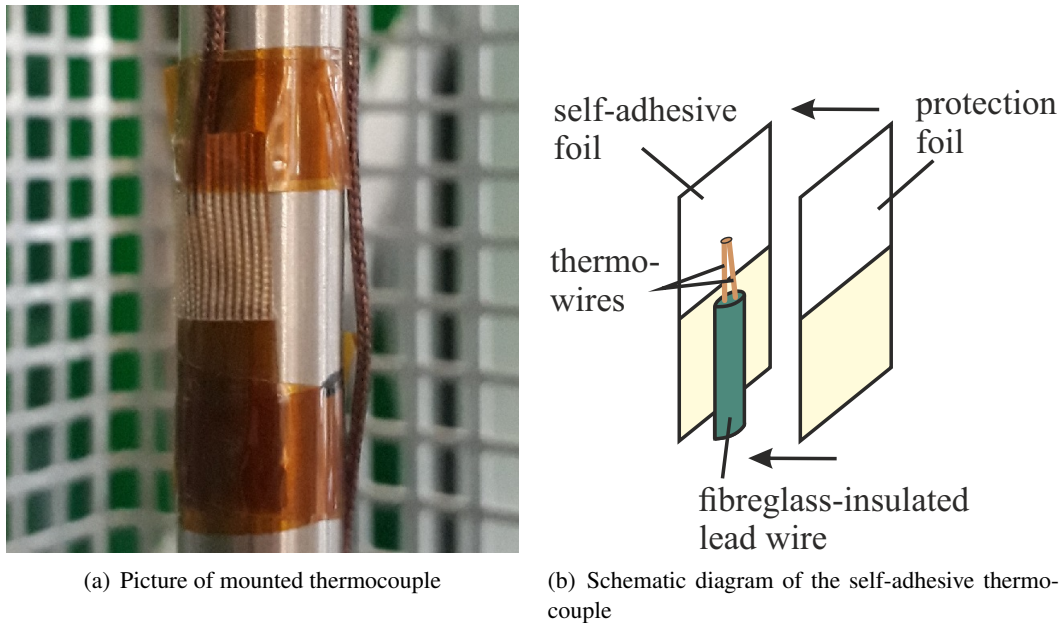
Figure 3.6.: Adhesive wall thermocouples used in ts-1 and ts-2

are mounted in SAE flanges to easily integrate them into the loop and for easy access. The inlet and outlet bulk temperatures at the ts-2 are measured with ultra-precise immersion RTD sensors (Omega P-M-1/10-1/8-5-1/2-G-15).

3.3.3. Pressure transducers

The pressure transducers of ts-1 and ts-3 are also installed in SAE flanges beside the thermocouples. They measure the static pressure at the inlet and outlet of the test section of the fluid. Type 8227-5100 from the company Burster are used. They have been calibrated before shipping and before installation.

At ts-2 the inlet absolute pressure is measured by a pressure transducer PX01C1-3KA5T from Omega. Additionally, the pressure loss in the test section is measured with a differential pressure transducer 3051TG4M2B21AM5C6Q4 from Rosemount.

3.3.4. Flow meters

For ts-1, a Coriolis mass meter RCUS34S-20TG90-0C6A-NN00-4-JA1/L005 from YOKOGAWA Deutschland GmbH is used. The mass flows investigated in this study are at the lower end of the measurement range of this mass flow meter, but with guaranteed uncertainty smaller than 0.42 %.

A Coriolis mass meter ELITE CFM050M320N0A2E2ZZ from Micro Motion measures the coolant mass flow rate for ts-2. It has a small uncertainty of 0.05 %.

For ts-3, a gear wheel flow meter VS 0.2 EPO12V 32N11/4 - 10 from VSE Volumentechnik GmbH and a SVC-40-A1F1F1S1 from Kracht GmbH for high volume flows are used. The VSE parameter ranges fits the mass fluxes requirements for the 10 mm diameter tube well up to a mass flux of 2500 kg/m^{2}s. It was calibrated by the manufacturer. A pressure transducer Jumo dTRANS p20 DELTA and a PT1000 type TF65 from S+S Regeltechnik GmbH are installed to measure the fluid temperature and static pressure respectively. These measurements are needed to determine the exact density of the fluid at the flow meter of ts-3 to calculate the mass flow.

3.3.5. Heat power measurement

The heat, which is generated in the tubes, is calculated from the measured current and voltage of ts-1 and ts-3. The current is measured by the power supply directly. The voltage is measured in parallel with wires connected to the tube directly at the connectors with a data logger 2640A.

For ts-2, the voltage drop at the tube is measured in parallel with a data logger NI 9225. The produced heat is calculated with the measured voltage and an estimated resistance of the test section using data provided by Special Metals and Sandvik.

3.4. Test procedure and parameters

The experiments need to be conducted at steady state. Therefore, the pressure, inlet temperature, heat flux and mass flux are set and hold constant. To save time and resources, the parameters are varied in an order which allows to quickly reach a steady state for the next measurement point. Following, the parameters are listed in a time order starting with the one with the shortest time: heat flux, mass flux, inlet temperature and pressure. The pressure is the last one because a transient in pressure is shortening the life time of the main pump and leakage could occur. On a regular day of measurement, a set of experiments at constant inlet temperature and constant pressure with different mass and heat fluxes is conducted.

For the supercritical experiments, the data are measured when all parameters and the wall temperatures are steady. It is measured for 60 s with 2 Hz. The CHF experiments are recorded in total to measure all parameters until the boiling crisis occurs. For that the pressure, inlet temperature and mass flux are set and hold constant. When all these parameters are steady, the heat flux is increased slowly by steps with a maximum of $200\,W/m^2$ until the boiling crisis occurs. The detection of the CHF is done by LABVIEW by a given pressure dependent wall temperature of 120 - 140 °C. At this temperature, the heating power is automatically shut down. The exact parameter values are calculated by a Matlab function. The function identifies the boiling crisis by the rapid increase of the wall temperature and calculates the mean for every parameter after the last increase of the heat flux.

Table 3.3.: Parameters for heat transfer experiments at supercritical conditions with R134a at the KIMOF (ts-1)

Pressure $[MPa]$	Inlet Temperature $[°C]$	Mass flux $\left[\frac{kg}{m^2 s}\right]$	Heat flux $\left[\frac{kW}{m^2}\right]$
4.22	50	300	5, 10, 20, 30, 40
4.59	60	500	20, 30, 40, 50
4.78	70	750	40, 50, 55, 60
5.15	80	1000	50, 60, 70, 80, 90, 100, 110, 120
5.51		1500	80, 90, 100, 110, 120, 130, 140, 150, 160
		2000	80, 90, 100, 110, 120, 130, 140, 150, 160 170, 180, 190, 200

For the heat transfer experiments at supercritical conditions with R134a (ts-1), each mass flux and heat flux combination shown in table 3.3 are conducted at every pressure and inlet temperature. This leads to 47300 data points in total. The parameters are chosen using the model of Cheng for the fluid-to-fluid scaling from the existing water data from the Shanghai Jiao Tong University (SJTU). Thus, 23 MPa, 25 MPa and 26 MPa in water correspond to 4.22 MPa, 4.59 MPa and 4.78 MPa in R134a. Additionally, two pressure values of 5.15 MPa and 5.51 MPa (28 MPa and 30 MPa in water) are added to observe the influence of the pressure on the heat transfer in a wider spectrum. The mass fluxes are scaled in the same way with steps surrounding the steps of the

water database. The inlet temperatures are varied to observe the inlet temperature effect on the heat transfer and to extend the range of the conducted bulk enthalpy.

The experiments with CO_2 at supercritical conditions (ts-2) are summarized in table 3.4. The aim is to extend the investigations of Kline et al. [Kline, 2017] with additional experiments for a pressure value of 7.69 MPa (23 MPa in water) and one additional mass flux. The investigations focus on the influence of the inlet temperature on the onset of HTD. The steps of inlet temperature and heat flux are irregular but not higher than 5 °C and 10 kW/m^2, respectively. In total there are 21113 data points for heat transfer with supercritical CO_2.

Table 3.4.: Parameters for heat transfer experiments at supercritical conditions with CO_2 at the SCUOL (ts-2)

Pressure $[MPa]$	Mass flux $\left[\frac{kg}{m^2 s}\right]$	Inlet Temperature $[°C]$	Heat flux $\left[\frac{kW}{m^2}\right]$
7.69	200	11 − 30	2 − 50
	300	7 − 30	12 − 115
	400	9 − 33	25 − 94
	500	5 − 30	43 − 164
	600	4 − 31	70 − 135
	1000	2 − 31	140 − 330
	1200	3 − 30	190 − 320
	1500	3 − 31	280 − 450
8.33	1500	6 − 33	280 − 420

Table 3.5 summarizes the condition ranges of the 96 CHF experiments (ts-3). The aim is to investigate the influence of the pressure, vapor quality and mass flux at the CHF near the critical point. Therefore, the pressures are varied from 2.8 MPa to 4 MPa and the inlet temperature and mass fluxes are varied in ranges limited by the KIMOF.

Table 3.5.: Parameters for critical heat flux experiments (ts-3)

Pressure $[MPa]$	Subcooling at inlet $[°K]$	Mass flux $\left[\frac{kg}{m^2 s}\right]$	Critical heat flux $\left[\frac{kW}{m^2}\right]$
2.8	10	525	25 - 245
3.3	20	1050	
3.8	30	2100	
4.0	40	3150	
	50	4200	
	60		

Nevertheless, for some CHF experiments with high inlet temperatures or high mass fluxes the heating power of the preheater or the DC power supply is not sufficient. The conducted experiments are highlighted in green in table 3.6. The saturation temperatures are 82.9 °C, 90.8 °C, 97.8 °C and 100.3 °C at 2.8 MPa, 3.3 MPa, 3.8 MPa and 4.0 MPa, respectively. Due to the preheating system, which can only provide inlet temperatures up to 85 °C, the low subcooling of 10 K at 3.8 and 4.0 MPa couldn't be conducted. Table 3.6 shows, that at high mass fluxes and high subcooling the electric heating power for the tube is not sufficient.

All experiments listed in the tables 3.3, 3.4 and the subcritical experiments for the validation of ts-1 and ts-3 described in section 3.7 were conducted by myself. The experiments listed in table 3.5 and 3.6 were conducted together with Patrick Schindler [Schindler, 2016], who wrote his bachelor

Table 3.6.: List of conducted critical heat flux experiments (ts-3) with pressure in MPa

Mass flux $\left[\frac{kg}{m^2 s}\right]$	Subcooling											
	10 K		20 K		30 K		40 K		50 K		60 K	
500	2.8	3.3	2.8	3.3	2.8	3.3	2.8	3.3	2.8	3.3	2.8	3.3
	-	-	3.8	4.0	3.8	4.0	3.8	4.0	3.8	4.0	3.8	4.0
1000	2.8	3.3	2.8	3.3	2.8	3.3	2.8	3.3	2.8	3.3	2.8	3.3
	-	-	3.8	4.0	3.8	4.0	3.8	4.0	3.8	4.0	3.8	4.0
2000	2.8	3.3	2.8	3.3	2.8	3.3	2.8	3.3	2.8	3.3	2.8	3.3
	-	-	3.8	4.0	3.8	4.0	3.8	4.0	3.8	4.0	3.8	4.0
3000	2.8	3.3	2.8	3.3	2.8	3.3	2.8	3.3	-	-	-	-
	-	-	3.8	4.0	3.8	4.0	3.8	4.0	3.8	4.0	-	4.0
4000	2.8	3.3	2.8	3.3	2.8	3.3	-	-	-	-	-	-
	-	-	3.8	4.0	3.8	4.0	3.8	4.0	-	4.0	-	-

thesis about this experiments. Due to the latest calibration of the mass flux of ts-2, as will be described in section 3.5.3, the results shown in his thesis differ from the results produced in this study. I used the Matlab function from Patrick Schindler [Schindler, 2016] for the reduction of the data of ts-3 with the corrected data. The data reduction of ts-1 and ts-2 and the data analysis of all data were done by myself.

3.5. Data reduction

3.5.1. Experiments at supercritical conditions of ts-1

The heat transfer coefficient and the Nusselt number are describing the heat transfer for forced convection. Therefore, they're the final value to calculate for the experiments at supercritical conditions. The data reduction is based on local parameters because the heat transfer in supercritical fluid flow is a local phenomenon due to the local variation of the physical fluid properties. The local HTC α is defined in equation 3.1 whereas n stands for the number of the measurement point which are defined by the wall thermocouple locations.

$$\alpha_n = \frac{q_{w,n}}{T_{w,n} - T_{b,n}} \tag{3.1}$$

3.5.1.1. Heat flux

The heat in the tube is produced by direct current and the electric resistance of the tube. The local heat flux defined in equation 2.5 is dependent on current, the material, the temperature and the geometry of the tube. These influences are evaluated in the following paragraphs.

Electrical Resistivity due to temperature

The resistance is dependent on the cross section of the tube and the resistivity of the material. The tube of ts-1 is made of the stainless steel 1.4301 whose resistivity increases with temperature. Because the wall thickness is assumed to be constant, the cross section of the tube doesn't change along the tube. The maximum temperature difference of 98 K at the tube in one experiment is found at the pressure of 4.22 MPa, inlet temperature of 70 °C, mass flux of 750 kg/m^{2}s and heat flux of 60 kW/m^2. The produced volume heat flux at the highest temperature, due to the higher resistivity, is 10 % higher than at the lowest temperature. The average deviation in the heat flux of all experiments is 2.4 % between the maximum and minimum local volume heat fluxes in one experiment. Therefore, a non-uniform heat flux is caused by the temperature differences of the tube itself.

This non-uniform heat flux is addressed in the calculations of the heat transfer coefficient. The mean electrical resistivity of the total test section R_{tot} is calculated using Ohm's law with the measured voltage and current. In the paper of Ho and Chu [Ho & Chu, 1977], data of electrical resistivity and heat conduction are given with dependency on temperature for 1.4301. These data are chosen because they have the smallest deviation to the measured resistivity of all data found in the literature. They show a mean deviation of 1.5 % to the measured values. A correlation is plotted over the temperature range of 20 °C to 227 °C. The correlation is used to calculate the reference resistivity ρ_0 with the mean temperature of the test section and the partial resistivity ρ_n. For ρ_n, the tube is divided into volumes with the beginning and the end of the heated length and the levels of the thermocouples as boundaries as exemplarily shown in figure 3.7. For every volume, the partial resistivity is calculated with the mean temperature of the two or three thermocouples at the boundary using the plotted correlation.

Assuming that the deviation between real resistivity and the resistivity of the correlation remains constant, the local resistance R_n of every volume can be determined using the temperature dependent specific resistivities ρ_{tot} and ρ_n and the length of the heated part L_h and of the volume L_n. This is seen in equation 3.2, which is used to calculate the heat power $\dot{Q}_n$ of every volume with the current I and the voltage drop U. The sum of all volume heat powers has a mean deviation of 0.18 % to the power calculated by the total voltage drop and current. This method is unneeded for the CHF experiments due to small temperature differences at the tube caused by boiling at the whole test section. It is also unneeded for the CO_2 experiments due to the fact that the electric resistivity of Inconel is not as sensitive to temperature as steel.
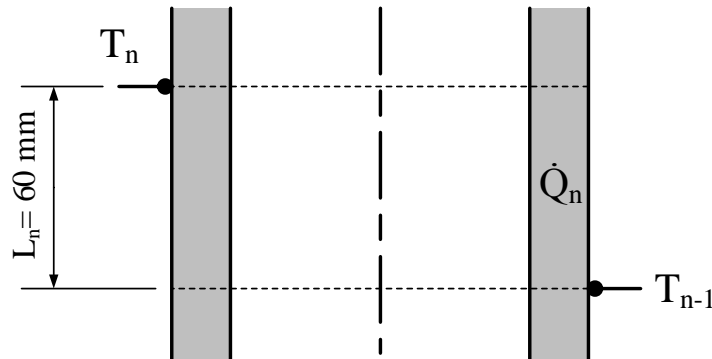
Figure 3.7.: Schematic illustration of nodalization for calculation of partial heating power due to electrical resistivity

$$\dot{Q}_n = I^2 \cdot R_n = UI \cdot \frac{\rho_n}{\rho_{tot}} \frac{L_n}{L_h} \qquad (3.2)$$

Heat conduction due to temperature

Another issue of local temperature peaks is an induced heat conduction along the tube caused by high temperature differences in small distances. The driving force for heat conduction is the temperature difference as seen in the known equation 3.3.

$$\dot{Q} = -\lambda \cdot A \frac{dT}{dx} \qquad (3.3)$$

The highest conducted heat along the tube must therefore occur in the experiment with the highest temperature difference between two neighboring thermocouples. This is 80 K at 4.59 MPa, inlet

temperature of $70\,°C$, mass flux of $750\,kg/m^2s$ and heat flux of $60\,kW/m^2$. The small cross section of the tube limits the heat conduction to $0.7\,W$, which is only $0.6\,\%$ of the heat transfered to the fluid in this part of the tube. Therefore, heat conduction along the tube is negligible.

Heat flux due to wall thickness

The tubes used for ts-1 and ts-3 have tolerances due to the manufacturing. The given tolerance for the outside diameter is $\pm\,0.03\,mm$ and $\pm\,5\,\%$ for the wall thickness. There is no statement for the inside diameter or the eccentricity. Because of the tolerances of the outside diameter and the wall thickness, the inner diameter can vary from 9.87 to $10.13\,mm$. The wall thickness can be constant or it can vary from the maximum to the minimum value because of the eccentricity as shown in figure 3.8. Due to the tolerance of the wall thickness, the eccentricity e can be maximally $0.05\,mm$. These different wall thicknesses at the opposite sides could influence the outside wall temperature and heat flux at the same level and will be examined in the following paragraphs.
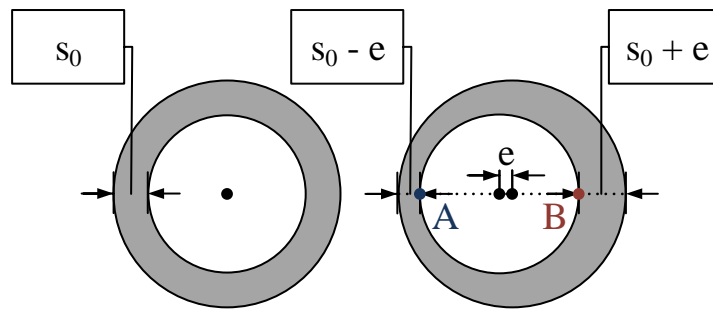
Figure 3.8.: Left: concentric hole with constant wall thickness; Right: Eccentric hole with varying wall thickness

In all experiments at subcritical and supercritical conditions, the outside wall temperature profiles of ts-1 show always a similar 'zig-zag' profile as recognizable in figure 3.9 (a). All hot thermocouples are positioned on one side of the tube and all cold ones on the other side as seen in figure 3.9 (b). This behavior could not be changed by new thermocouples, different data logger, different input terminals in the data logger or turning the test section 180 degrees to exclude inlet effects.
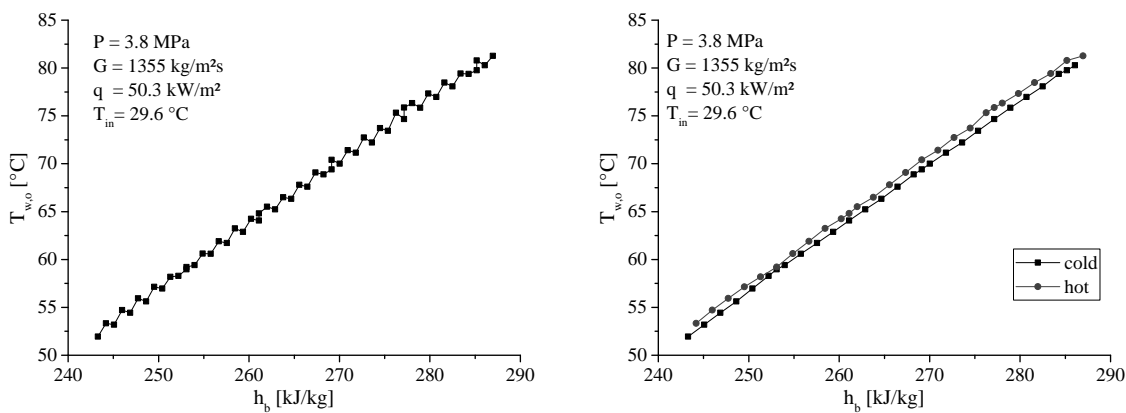
(a) Diagram of outside wall temperature versus bulk enthalpy for a subcritical experiment with zig-zag profile

(b) Separation of thermocouples of the same side named the cold and hot side

Figure 3.9.: Zig-zag wall temperature profile of ts-1 in R134a at subcritical conditions and the dependency on the tube's side

The fact, that all hot wall temperatures are on one side and the cold ones on the other side shows that the wall thickness must be always smaller on one side. The comparison with data of electrical

resistivity from the literature shows a very good agreement. This proofs that the mean area of the tube's cross-section must be close to the ideal one. The only way to reach a different wall thickness on opposite sides of the tube is an eccentricity of the centers of the inner and outer diameter as seen in figure 3.8. This can be due to the manufacturing of seamless tubes.

[Watts & Chou, 1982]. Also other authors like Yamagata et al. [Yamagata et al., 1972] and Kim et al. [Kim et al., 2008]

In the past, other authors, as Fewster [Fewster, 1976] and Watts and Chou [Watts & Chou, 1982], experienced tubes with different circumferential wall thicknesses as described in section 2.2.4. Only Fewster proposed a correction of the calculated inside wall temperature due to the different wall thickness in the heat conduction equation 3.7, which will be discussed in section 3.5.1.2.
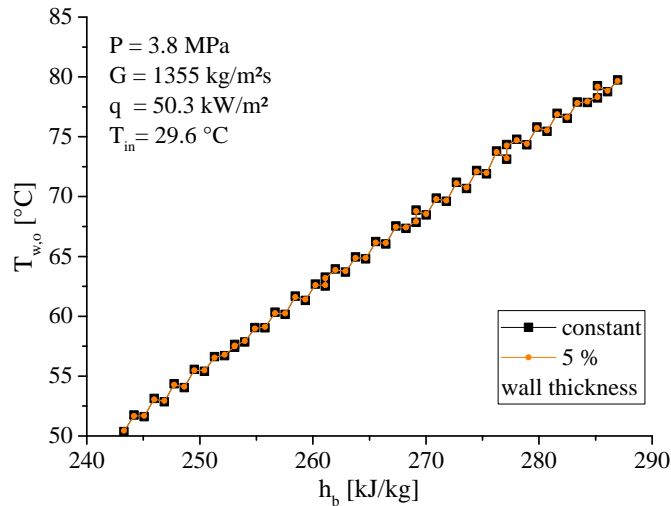
Figure 3.10.: Inside wall temperature with constant and 5 % changed wall thickness in heat conduction equation at subcritical condition of ts-1 in R134a

But as seen in figure 3.10, a change of the wall thickness in the heat conduction equation 3.7 does not change the inside wall temperature significantly. The profile is smoothed slightly, but the changes of the temperature difference from outside to the inside are too small. The only reason left is a different heat production due to the different wall thicknesses.

Parts of the tube were cut after the experiments to see the cross sections at different heights. In the process, it was payed extra attention to planarity and perpendicularity of the cross section. The specimen are embedded cold in resin and polished for the microscopy. The wall thickness is measured using a VHX-600 microscope from KEYENCE with an objective with 100x magnification. This was done in cooperation with the Institute for Applied Materials. A picture is shown in figure 3.11 (a) from a wall thickness of 1.027 mm. In total, at three different cross sections, the wall thickness is measured at the sides of the thermocouples and between the thermocouples with an offset of 90 degree. The wall thickness varies from 0.96 to 1.04 mm and is within of the tolerance given by the manufacturer. The side, where the warmer temperatures are measured, is always thicker than the colder side.

Additionally, to investigate the assumption of the different heat flux due to the different wall thicknesses, a CAD-model of a tube with an eccentricity of 0.04 mm is generated. With the program COMSOL Multiphysics 5.3 from COMSOL, the produced heat, the resulting temperature field and the resulting heat flux are simulated and shown in figure 3.11. Therefore, the outside wall is set adiabatic and the inside surface as heat sink. In figure 3.11 (b), it can be seen that the volume heat flux is constant in the cross section. Due to the larger area, the tube has a higher temperature at the side with the thicker wall. This shows the influence of the wall thickness on the measured outside wall temperature. As the heat is transported to the inside wall, the heat flux is higher at the side with the thicker wall as seen in figure 3.11 (d). The heat flux is normalized by the mean heat

flux. With the eccentricity of 0.04 mm, the software computed a maximum difference of 7 % in the heat flux. This simulation was done in cooperation with the Institute of Biomedical Engineering.

Assuming that the current is distributed equally across the cross-section, every infinitesimal small area produces the same heat. All heat must be transferred through the inner diameter into the fluid. Hence, higher heat fluxes are induced at location with the bigger area due to the higher wall thickness as shown in figure 3.11 (d). These different sized areas are schematically shown as point A and B in figure 3.8. Looking at the heat flux at exact these two points, the heat flux depends directly on the wall thickness at these points. That means that the relative difference of the heat flux is equal to the relative difference of the wall thickness. In the same plane (dotted line in figure 3.4) of the two centers of the diameters, the heat flux can be described with equation 3.4 with s_0 as mean wall thickness.

$$\frac{\dot{q}_n}{\dot{q}_0} = 1 \pm \frac{e}{s_0} \qquad (3.4)$$

(a) Photo of tube with local wall thickness of 1.027 mm at the warm side

(b) Diagram of cross section distribution of volume heat flux in the wall of the tube

(c) Diagram of cross section distribution of temperature in the wall of the tube

(d) Diagram of heat flux distribution of the tube with 0 degree at the top, clockwise

Figure 3.11.: Photo and distribution of volume heat flux temperature and heat flux of the tube due to an eccentricity of 0.04 mm with the thick wall at the left side (x=0)

The wall thickness or eccentricity is not constant along a 3 m long tube. This means, a value of every eccentricity must be found for every level with thermocouples. Therefore, data of experiments with subcritical pressure without boiling and with supercritical pressure at low inlet temperature and low heat fluxes are collected. This is to ensure that the wall and bulk temperature are far below the pseudo-critical value. In these cases, the heat transfer coefficient can be described with a polynomial function of the second grade as described by Dittus-Boelter and Gnielinski as seen in figure 3.15.

Firstly, the heat transfer coefficients are calculated assuming a constant heat flux. Then, for every experiment, a polynomial function is fitted for the heat transfer coefficients over the bulk enthalpy, as exemplarily shown in figure 3.12. For every point, the difference of the heat transfer coefficient from the experiment calculated with a uniform heat flux to the fitted curve is determined. This difference seems to be dependent on the heat flux, which can be explained with the eccentricity as well. An example for the difference can be seen in figure 3.12 for the first point. The mean and standard deviation for the relative eccentricity of every thermocouple are calculated from the relative differences of the heat transfer coefficients of all 97 experiments. Minimum and maximum values are -0.048 and 0.042, respectively. This is within the given tolerance of 5 % for the wall thickness of the manufacturer. This calculated mean eccentricity is used to correct the heat flux for every single thermocouple. The mean standard deviation of all thermocouples is 0.007. Therefore, this method is reliable to determine the heat flux due to a varying wall thickness.
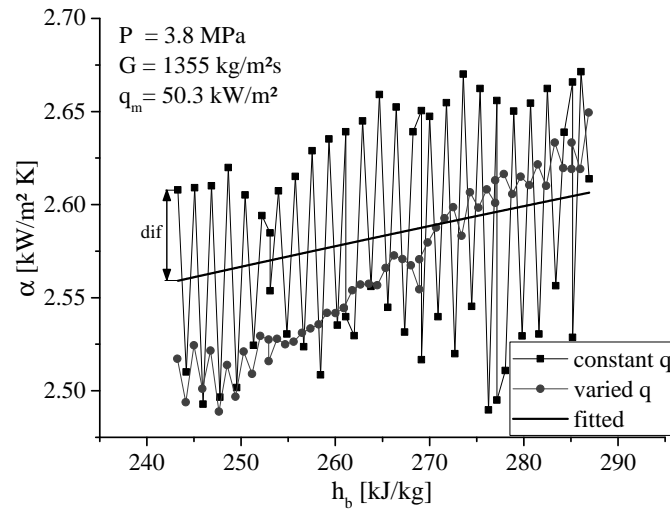
Figure 3.12.: Heat transfer coefficient calculated with constant wall thickness and heat flux and varied wall thickness and temperature dependent electrical resistivity of ts-1 in R134a

Figure 3.12 shows the effect on the calculated heat transfer coefficient assuming a constant wall thickness and heat flux compared to a wall thickness variation and heat flux variation due to eccentricity and temperature distribution along the tube. The amplitude of the zig-zag profile is decreased drastically. Due to the nodalization of the produced heat, the points of the adapted calculated HTC are at slightly different bulk enthalpies. In summary, all implemented assumptions show a more accurate calculation of the heat transfer coefficient.

The different heat flux at the same height could have an influence on the heat transfer regime or mode. Therefore, at 5 levels two thermocouples are mounted at the same height of the tube. Observations for HTD or CHF show, that the wall temperatures at the same height behave in the same manner. If the heat flux is increased, the opposing thermocouples react at the same time. This shows that the heat transfer mode is not influenced by the different heat flux generated by the different wall thickness.

Heat loss

For calculating the heat flux to the coolant, the heat loss of the test sections must be considered. The driving force for the heat loss is the temperature difference between the test section and the environment as described in equation 3.3. The test section was vacuumed to eliminate the influence of convective cooling of the coolant. Then, the test section was heated by small heating power. If the wall temperatures are steady, there is an equilibrium between the heat loss and the supplied heat. Four points are measured and the fitted correlation is shown in equation 3.5 for ts-1 and ts-3. Whereas T_{env} is the temperature of the environment, $T_{w,m}$ is the mean of all wall temperatures in °C and $\dot{Q}_{loss}$ is the rate of heat loss in W. At a difference of 100 K between the environment and the test section, the heat loss is around 40 W for the whole test section.

$$\dot{Q}_{loss} = \left\{ \begin{array}{ll} 0.00097(T_{w,m} - T_{env})^2 + 0.29(T_{w,m} - T_{env}) + 0.13 & ; \text{ts-1} \\ 0.00085(T_{w,m} - T_{env})^2 + 0.268(T_{w,m} - T_{env}) + 0.176 & ; \text{ts-3} \end{array} \right\} \tag{3.5}$$

Summary for heat flux

As seen, due to the imperfect geometry of the tube and the temperature dependency of the electrical resistivity, the heat flux at the inner surface of the tube is not uniform. Therefore, the heat flux $\dot{q}_{w,n}$ (following only q) can be expressed as in equation 3.6. $\dot{Q}_n$ is defined in equation 3.2. $\dot{Q}_{loss}$ is determined by a separate heat loss test and described in chapter 3.5.1.1.

$$\dot{q}_{w,n} = \frac{\dot{Q}_n - \dot{Q}_{loss}\frac{L_n}{L_h}}{\pi \cdot d_i \cdot L_n} \left(1 \pm \frac{e}{s_0}\right) \tag{3.6}$$

3.5.1.2. Inside wall temperature

The temperature on the inner surface $T_{w,i}$ of the tube is determined from the outer surface temperature $T_{w,o}$. By neglecting the axial heat conduction, the heat transfer is a one-dimensional case and is given in equation 3.7 with the radius r.

$$\frac{1}{r}\frac{d}{dr}(r\frac{dT}{dr}) + \frac{\dot{q}_v}{\lambda_w} = 0 \tag{3.7}$$

$$T(r_{w,o}) = T_{w,o} \tag{3.8}$$

$$-\lambda_w \frac{dT}{dr}\bigg|_{r=r_{w,o}} = \dot{q}_{loss} \tag{3.9}$$

The boundary condition 3.8 and 3.9 are the measured temperature at the outer surface and the heat loss flux $\dot{q}_{loss}$ at the outer surface, respectively. The final derivation is shown in equation 3.10 with the volumetric heat flux $\dot{q}_v$ (3.11), the heat loss flux $\dot{q}_{loss}$ (3.12), the diameter d and the thermal conductivity of the tube λ_w.

$$T_{w,i} = T_{w,o} + \frac{\dot{q}_v}{16\lambda_w}\left(d_o^2 - d_i^2\right) + \frac{d_o}{2\lambda_w}\left(\frac{\dot{q}_v \cdot d_o}{4} - \dot{q}_{loss}\right)\ln\frac{d_i}{d_o} \tag{3.10}$$

$$\dot{q}_v = \frac{4\dot{Q}_n}{\pi(d_o^2 - d_i^2) \cdot L_n} \tag{3.11}$$

$$\dot{q}_{loss} = \frac{\dot{Q}_{loss}}{\pi \cdot d_o \cdot L_h} \tag{3.12}$$

Equation 3.10 is valid for an ideal tube with constant wall thickness. However, as discussed in section 3.5.1.1, the wall thickness of ts-1 is not constant. To include this finding, equation 3.13 is defined to approximately determine the correct wall temperature at the inside. As seen in figure 3.10, the changes of the calculated values are small but more accurate.

$$T_{w,i} = T_{w,o} + \frac{\dot{q}_v}{16\lambda_w}\left(d_o^2 - (d_i \pm e)^2\right) + \frac{d_o}{2\lambda_w}\left(\frac{\dot{q}_v \cdot d_o}{4} - \dot{q}_{loss}\right)\ln\frac{d_i \pm e}{d_o} \tag{3.13}$$

3.5.1.3. Bulk temperature

The local bulk temperature T_b is determined using the NIST Standard Reference Database 23, Version 8.0 [Lemmon et al., 2007] and the energy balance equation 3.14. For the first control volume, the previous bulk enthalpy $h_{b,n-1}$ is the inlet enthalpy h_{in}.

$$h_{b,n} = h_{b,n-1} + \frac{\dot{Q}_n - \dot{Q}_{loss}\frac{L_n}{L_h}}{\dot{m}} \tag{3.14}$$

The NIST database is used to estimate the inlet enthalpy h_{in} with the measured inlet temperature and pressure. Also the local bulk temperature $T_{b,n}$ is estimated using the local bulk enthalpy $h_{b,n}$ and the pressure. In ts-1 and ts-2, the mass flow rate $\dot{m}$ is measured directly. For ts-3, the mass flow rate is determined by the measured volume flow rate and the density. The density is calculated using NIST with the known pressure and temperature of the fluid at the volume flow meter.

3.5.2. Experiments at supercritical conditions of ts-2

In ts-2, the heat flux is calculated by the measured voltage and determined electrical resistivity of the heated part of the tube. The wall thickness is assumed to be constant and the temperature dependency of the resistivity as well as the heat loss is neglected. This simplifies the heat flux calculation to equation 3.15.

$$\dot{q}_{w,i} = \frac{U^2}{R \cdot \pi \cdot d_i \cdot L_h} \tag{3.15}$$

The negation of the heat loss results also in a simplified heat conduction equation 3.10 for the inner wall temperature. Detailed description of derivations and calculations for the ts-2 can be seen in [Jiang, 2015, Kline, 2017, Kline et al., 2018].

3.5.3. CHF experiments of ts-3

For the CHF, the heat flux is the final parameter to determine. Due to small temperature differences at the tube caused by boiling at the whole test section, a constant heat flux can be assumed. The eccentricity is part of the uncertainty of the heat flux described in section 3.6.3. For the CHF results, the heat flux is calculated with equation 3.16, the mass flux with equation 2.7 and the pressure and temperature as averaged value of the measurements. The vapor quality at the dryout point is calculated with the calculated bulk enthalpy. Because the dryout appears at the end of the test section, the full heating length is assumed for the bulk enthalpy in equation 3.17. With the given enthalpy of saturation (h') and evaporation(Δh_v) at the measured pressure, the vapor quality can be determined using equation 3.17.

$$\dot{q}_{w,i} = \frac{UI - \dot{Q}_{loss}}{\pi \cdot d_i \cdot L_h} \tag{3.16}$$

$$x_{chf} = \frac{h_{b,chf} - h'(p)}{\Delta h_{vap}(p)} \quad \text{with} \quad h_{b,chf} = \frac{UI - \dot{Q}_{loss}}{\dot{m}} \tag{3.17}$$

ts-3 showed firstly a higher difference than expected in heat balance and to subcritical correlations. The heat balance and comparison with the subcritical correlations will be explained in the sections 3.7.1 and 3.7.2, respectively. With the mass flow meter of ts-1, it is found that the volume flow meters of ts-3 shows a 5 % lower mass flux. With this correction, the heat balance is shifted from 6.8 % to 2.1 % for ts-3. This is in the same range as ts-1. Also the differences to the subcritical correlations are similar. A reason for the difference could be a leakage through the gears and the casing of the gear flow meter used in ts-3 due to the small viscosity of R134a.

3.6. Uncertainty analysis

The instrumentation used to measure the loop and test section parameters are thoroughly checked and calibrated. The uncertainties of the instrumentations are listed in table 3.7 and are determined by the manufactures' specifications as well as the calibration results.

Table 3.7.: Uncertainties for measured parameters given by the manufactures

Parameter	ts-1	ts-2	ts-3
Fluid temperatures	max(0.5 K, 0.4 %[*])	0.35 K	max(0.5 K, 0.4 %[*])
Wall temperatures	max(0.5 K, 0.4 %[*])	max(0.5 K, 0.4 %[*])	max(0.5 K, 0.4 %[*])
Pressure	0.25 %	21 kPa	0.25 %
Flow rate	0.15 − 0.3 %	0.05 %	0.3 %
Datalogger voltage	0.03 %	0.034 V	0.03 %
Datalogger temperature	0.5 K	0.25 K	0.5 K
Datalogger frequency	0.02 %	0.02 %	0.02 %
Current/Resistivity	1.5 %	2 %	1.5 %
Length	0.5 mm	0.5 mm	0.5 mm
Wall thickness	5 %	–	5 %
Outer diameter	0.03 mm	–	0.03 mm

[*] of temperature in °C

In addition to the measured parameters, fluid properties are required to calculate the heat transfer coefficient and the Nusselt number as described in section 3.5. These calculated fluid properties have also uncertainties due to their measurements and models and must be considered. Table 3.8 lists all used properties of R134a with their given uncertainties. There is no uncertainty given for the enthalpy for R134a. Instead, the uncertainty of the specific heat is used. A detailed breakdown in pressure and temperature is found in appendix D. The data are taken from [Tillner-Roth & Baehr, 1994, Wirbser, 1995, Richard A. Perkins et al., 2000]. For CO_2, the uncertainties of 0.7 % for the enthalpy was reported by Span and Wagner [Span & Wagner, 1996] for all regions. For the heat conductivity, a conservative uncertainty of 5 % was suggested from Vesovic et al . [Vesovic et al., 1990]. An uncertainty of 0.18 K for the CO_2 and R134a is given to calculate the bulk temperature with bulk enthalpy and pressure.

These uncertainties cause an inaccuracy on the computed heat transfer coefficient. Because the HTC is calculated in steps, an error propagation method must be used. Firstly, all interim results are calculated. These results are used as input parameters in the following calculations. Therefore, the uncertainties of heat flux, mass flux, HTC and Nu can be given. This method for the uncertainty analysis is based on the master thesis of Coelho Silva [Coelho Silva, 2015] and the bachelor thesis of Gao [Gao, 2017]. I adapted the method to the new test section and data reduction by myself.

Table 3.8.: Uncertainties for calculations using REFPROP of NIST for R134a

Parameter	Sub-critical	Trans-critical	Super-critical
	T<370 K or P<3.73 MPa	370<T<385 K and 3.73<P<4.77	T>385 K
Fluid temperatures	0.18 K	0.18 K	0.18 K
Heat conductivity	5 %	5 %	5 %
Specific heat	0.15 – 1.5 %	1.5 – 7 %	0.15 – 1.5 %
Density	0.05 %	0.05 – 1.6 %	0.05 %

With the given sensitivity ($\delta f/\delta P_i$) from the sensitivity analysis and the standard deviation of each parameter, the resulting inaccuracies for every data point is computed. With the assumptions that the input parameters obey to a Gaussian distribution and are independent from each other, the resulting inaccuracy is given by equation 3.18.

$$\sigma_f^2 = \sum_{i=1}^{n} \left(\frac{\delta f}{\delta P_i} \sigma_i \right)^2 \tag{3.18}$$

Whereas the sensitivity is calculated by partial derivation of the known function f with the investigated input parameter P_i. If the function is unknown, like the fluid properties calculations of REFPROP, the sensitivity is calculated with a perturbation of 1 % of the input parameter P_i and the resulting alternation of the result of function f. All uncertainties σ^2 must be given either in relative or absolute values. In this study, all uncertainties are calculated in absolute values.

In the calculations of REFPROP of NIST for the fluid properties, the uncertainty of the results is not only affected by the input parameters but also by the uncertainty of the used database and models as listed in table 3.8. This results in an additional uncertainty term σ_{NIST} for fluid property calculation steps as shown in equation 3.19.

$$\sigma_f^2 = \sum_{i=1}^{n} \left(\frac{\delta f}{\delta P_i} \sigma_i \right)^2 + \sigma_{NIST}^2 \tag{3.19}$$

3.6.1. Uncertainty analysis of ts-1

The uncertainty of the mass flux depends only on the mass meter itself and the datalogger. The mass flux has an uncertainty of 1.61 % for all data points. The mean uncertainty of the heat flux is 1.86 %. Whereas the uncertainty at the first thermocouple is always around 3.48 % and the uncertainty of the others close to the mean value. The small variations is caused by the independence of the heat flux on fluid properties.

The mean uncertainty of the heat transfer coefficient is 6.15 %. It ranges from 2.37 % to 44.59 %. The high uncertainties appear as the bulk temperature reaches the pseudo-critical value at very low heat fluxes and consequently low temperature difference between bulk and wall. However, as seen in figure 3.13 (a), 92 % of all HTC have an uncertainty below 10 %.

The uncertainties of all Nusselt numbers of ts-1 have a mean value of 8.26 %. They vary from 5.6 % to 44.88 % for the same reasons as the HTC. The percentile distribution is shown in figure 3.13 (b). Compared to the percentile distribution of the HTC, the same trend is shifted to higher uncertainties. Therefore, 87 % of all Nusselt numbers have an uncertainty below 10 %.
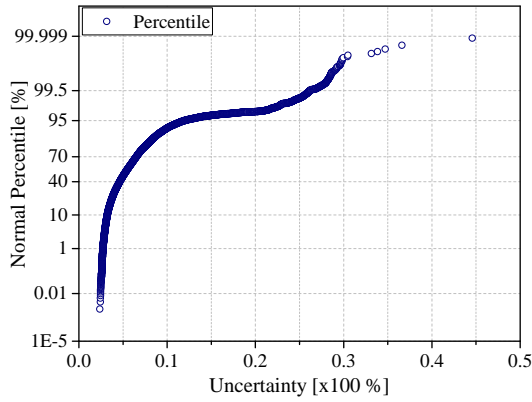
(a) Distribution of uncertainties of the heat transfer coefficient of ts-1
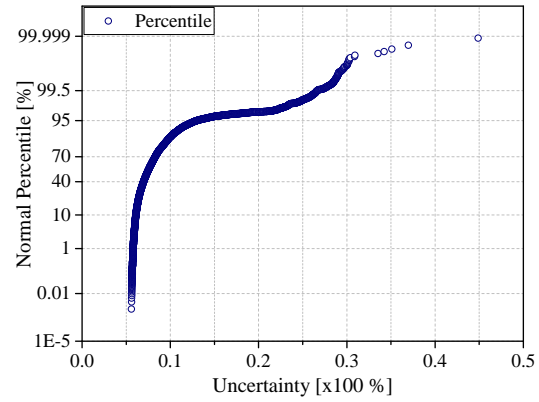
(b) Distribution of uncertainties of the Nusselt numbers of ts-1

Figure 3.13.: Distribution plots of uncertainties of HTC and Nu of ts-1 for all data points

3.6.2. Uncertainty analysis of ts-2

The uncertainty of the mass flux is only dependent on the mass meter and datalogger uncertainty and is 0.07 %. The heat flux has a mean uncertainty of 2.07 %. The minimum and maximum uncertainty for the heat flux are 1.99 % and 3.31 %, respectively.

The heat transfer coefficients have a mean uncertainty of 4.56 %. The uncertainties range from 0 % to 114.5 % . Like in ts-1, the high uncertainties appear as the bulk temperature reaches the pseudo-critical value at very low heat fluxes. Nevertheless, 90 % of the data have an uncertainty smaller than 10 % as can be seen in figure 3.14 (a).

The Nusselt numbers' mean uncertainty is 9.7 %. For the same reasons as the HTC, it ranges from 0 % to 116 %. 70 % are below 10 % uncertainty and 95 % of all data have an uncertainty of less than 20 % , as shown in figure 3.14 (b).
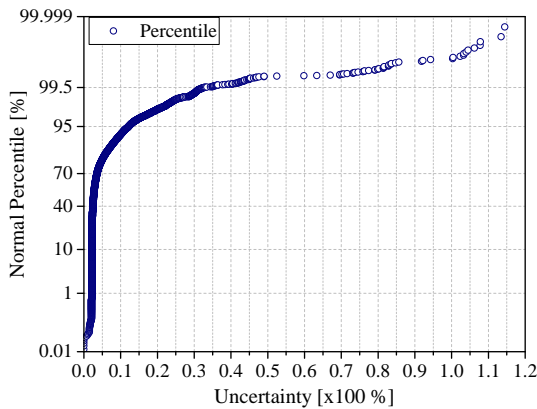
(a) Distribution of uncertainties of the heat transfer coefficient in the CO_2 experiments of ts-2
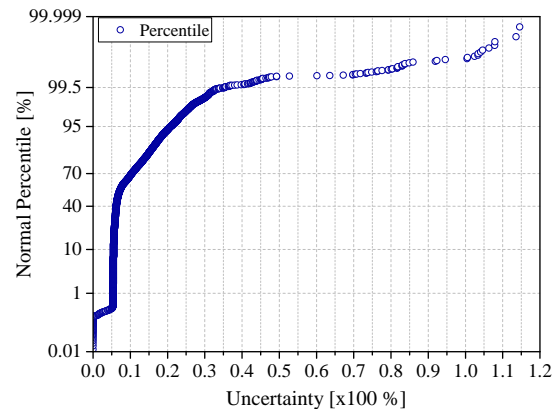
(b) Distribution of uncertainties of the Nusselt numbers in the CO_2 experiments of ts-2

Figure 3.14.: Distribution plots of uncertainties of HTC and Nu of ts-2 for all data points

3.6.3. Uncertainty analysis of ts-3

The uncertainty analysis of the CHF experiments of ts-3 shows a uncertainty of the mass flux of 2 % for all data points. By virtue of the mass flow rate correction mentioned in section 3.5.3, the

uncertainty of the volume flow rate is increased from 0.3 %, which was given by the manufacturer, to 1 %.

The mean uncertainty of the heat flux is 1.7 % for all data points. The minimum and maximum uncertainty are 1.698 % and 1.714 % and are thus very close to the mean value. The increment of 200 W/m^2 of the heat flux increasing steps must be added as negative uncertainty. Thus, the uncertainty of the heat flux is $\pm\, 0.017 \cdot q_{CHF} - 200$ W/m^2.

The uncertainty of the vapor quality at the dryout location strongly depends on pressure. Due to the decreasing heat of vaporization with increasing pressure, the uncertainty of the vapor quality is increasing, too. Therefore, the uncertainty of the vapor quality is given with respect of the pressure in table 3.9. It can be seen that, at 4 MPa, the uncertainty of the vapor quality gets high enough for the fluid to be superheated. This is due to the uncertainty of the pressure combined with the fact that at the critical pressure the heat of vaporization becomes zero. If the bulk temperatures are superheated, an increase of the wall temperatures must be recognized, which is not the case. To optimize the calculation of the local sensitivity of pressure on the heat of vaporization, the perturbation is set to 0.2 %. The minimum uncertainty at 4 MPa is 0.084 of the vapor quality. This is more realistic and a mean uncertainty of 0.1 for the vapor qualities at 4 MPa is proposed.

Table 3.9.: Uncertainties for vapor qualities of ts-3 with respect of the pressure

Pressure [*MPa*]	Mean [−]	Minimum [−]	Maximum [−]
2.8	0.021	0.019	0.028
3.3	0.027	0.025	0.033
3.8	0.046	0.042	0.051
4.0	1.74	0.084	9.51

3.7. Validation of measurement system

3.7.1. Heat balance

The heat balance is an important tool for excluding major failures in the measurement setup and in the devices. Therefore, two methods of calculating the enthalpy rise in the test section are compared. The first enthalpy difference (3.20) is calculated with local enthalpies at the inlet and outlet of the test section. The measured temperatures and pressures at the inlet and outlet and REFPROP are used for the determination. For the second method (3.21), the increase of the enthalpy is calculated with the first law of thermodynamics for an adiabatic system with forced flow. For this calculation, the mass flow rate and heat rate are needed. The difference (3.22) of these two enthalpy differences is divided by the second one for a relative difference. The higher the deviation of the relative difference is, the higher is the probability of a failure in the measurement set-up or devices. The heat loss is neglected for comparison with heat balance tests from the literature.

$$\Delta h_1 = h_{out}\left(T_{out}, P_{out}\right) - h_{in}\left(T_{in}, P_{in}\right) \tag{3.20}$$

$$\Delta h_2 = \frac{\dot{Q}}{\dot{m}} \tag{3.21}$$

$$\Delta h = \frac{\Delta h_2 - \Delta h_1}{\Delta h_2} \tag{3.22}$$

Heat balance tests have been performed at three different days with the same parameters for comparison. The mass fluxes are ranging from 300 kg/m^{2}s to 2400 kg/m^{2}s and are therefore in the

same range as the planned experiments at supercritical conditions with heat fluxes low enough to ensure a subcooled outlet temperature. The first set was conducted before the supercritical tests and the other two sets during the tests. The mean relative difference of all heat balance tests of ts-1 is 1.7 %. The standard deviation of 1.8 % shows that all differences are close to the mean value. ts-3 has a mean relative deviation of 2.1 %, as discussed in section 3.5.3. The heat balance of ts-2 is well discussed by [Kline, 2017, Kline et al., 2018] and shows similar results. This proofs that the measurement devices for the test sections are reliable and accurate.

3.7.2. Comparison with subcritical correlations

For further validation of the measurement setup and calculation methods, the data of ts-1 at subcritical conditions are compared with the accepted correlations of Dittus-Boelter and Gnielinski [Dittus & Boelter, 1985, Gnielinski, 1975]. There is no comparison for ts-3 because the heat transfer coefficient is not the objective of this test section. Kline [Kline, 2017, Kline et al., 2018] proofs the validation of ts-2 of the SCUOL by comparison with other facilities at supercritical conditions.

The heat transfer coefficients of ts-1 can be described well by the correlations of Dittus-Boelter and Gnielinski as shown in figure 3.15. It can be easily seen that the HTCs of the experiments are located between the Dittus-Boelter and Gnielinski correlation. Additionally, the qualitative trend is very similar. This proofs, that the measurement setup and the data reduction is working reliably at subcritical conditions.

(a) Experiment with low mass and heat flux   (b) Experiment with high mass and heat flux
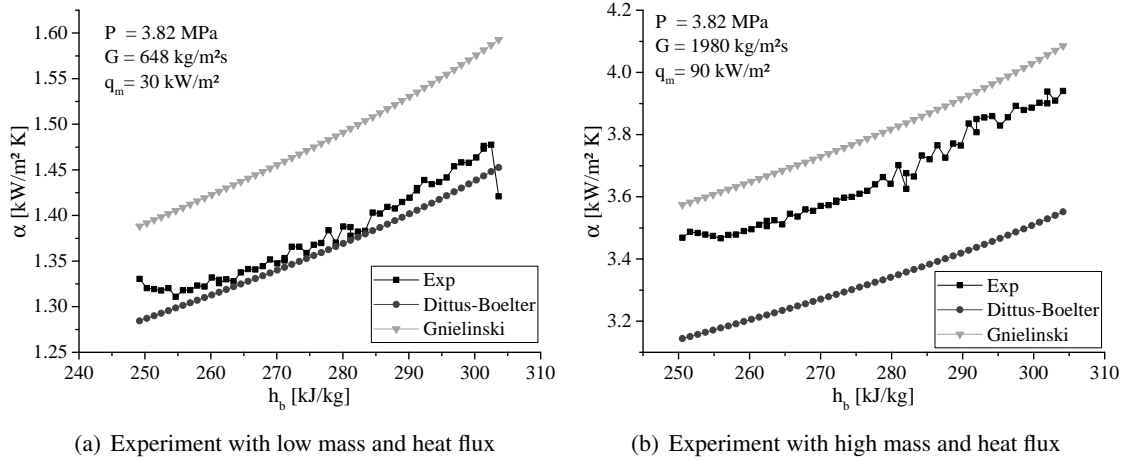
Figure 3.15.: Comparison of subcritical experiments with correlation of Dittus-Boelter and Gnielinski of ts-1 in R134a

Additionally, a statistical analysis is done for the comparison of the subcritical experiments with the predicted values of the correlations. In equations 3.23 to 3.26, the deviation dev, the mean deviation MD, the mean absolute deviation MAD and the standard deviation STD are defined.

$$dev_i = \frac{\alpha_c - \alpha_{exp}}{\alpha_{exp}} \cdot 100 \qquad (3.23)$$

$$MD = \frac{1}{N} \sum_{i=1}^{N} dev_i \qquad (3.24)$$

$$MAD = \frac{1}{N} \sum_{i=1}^{N} |dev_i| \qquad (3.25)$$

$$STD = \sqrt{\frac{1}{N-1}\sum_{i=1}^{N}(dev_i - MD)^2} \qquad (3.26)$$

The results of the statistical analysis are listed in table 3.10. All numbers are close to zero which is due to close values of experimental and predicted HTCs with small variances of the deviation. The negative MD shows the tendency of Dittus-Boelter to underpredict the experimental data. The closest prediction shows the Gnielinski correlation. The similar trend and small deviations of the correlations and experimental data show that the assumption defined in section 3.5 and the data reduction are correct.

Table 3.10.: Deviations of correlations of Dittus-Boelter and Gnielinski to subcritical experiments of ts-1

Correlation	MD [%]	MAD [%]	STD [%]
Dittus-Boelter	- 8.31	8.45	4.18
Gnielinski	2.51	3.62	3.5

3.7.3. Reproducibility of subcritical experiments

The three sets of experiments for the heat balance are also used to demonstrate the reproducibility capability of the experimental data. Therefore, an equal set of inlet temperature, mass flux, heat flux and pressure are used. The measured wall temperatures of all three sets are thoroughly similar for similar conditions. Figure 3.16 presents exemplarily the good reproducibility of the wall temperature of the three sets at different days for low and high mass fluxes at subcritical conditions.

(a) Experiment with low mass and heat flux

(b) Experiment with high mass and heat flux
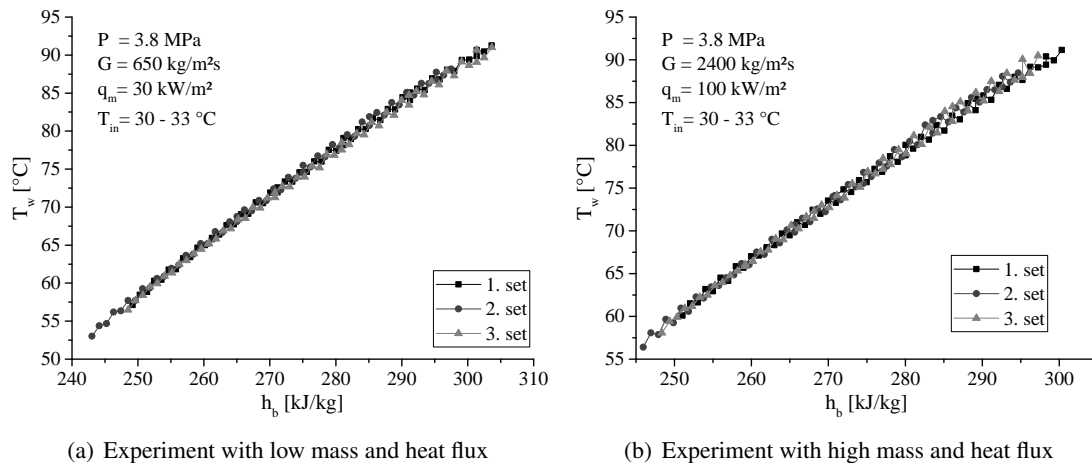
Figure 3.16.: Reproducibility of wall temperature at subcritical conditions from three sets of ts-1 in R134a

4. Definition, Evaluation and Data Selection for Heat Transfer at Supercritical Conditions

This chapter first discusses and defines the regimes for heat transfer at supercritical conditions. Then, the data are examined thoroughly for errors and outliers by checking the consistency and the reproducibility. Here, local depositions are found for the experiments with R134a in ts-1. Additionally, flow instabilities are found and explanations are given. At the end, the verified databases for R134a and CO_2 are given for the further analysis by excluding inconsistent data.

4.1. Definition of heat transfer deviation

4.1.1. Discussion about definition of literature

In the literature, the heat transfer at supercritical conditions is mainly separated into normal (NHT), deteriorated (HTD) and enhanced (HTE), as discussed in section 2.2.2. Detection of wall temperature spikes are the most common method to define HTD. At low mass fluxes up to $750 \, \text{kg/m}^2\text{s}$, there is a sharp boundary between heat fluxes with and without wall temperature peaks, as exemplarily shown in figure 4.1 (a). At high mass fluxes, the peak does not occur suddenly, instead, the spike grows slowly with rising heat fluxes. In this case, it is hard to distinguish between normal and deteriorated heat transfer. There is no clear border between the heat transfer modes anymore. This can be exemplarily seen in figure 4.1 (b). Further, there is no clear and common definition how high the peak must be to be determined as HTD. Therefore, this method is strongly subjective.

(a) Wall temperature trends for low mass flux at different heat fluxes

(b) Wall temperature trends for high mass flux at different heat fluxes
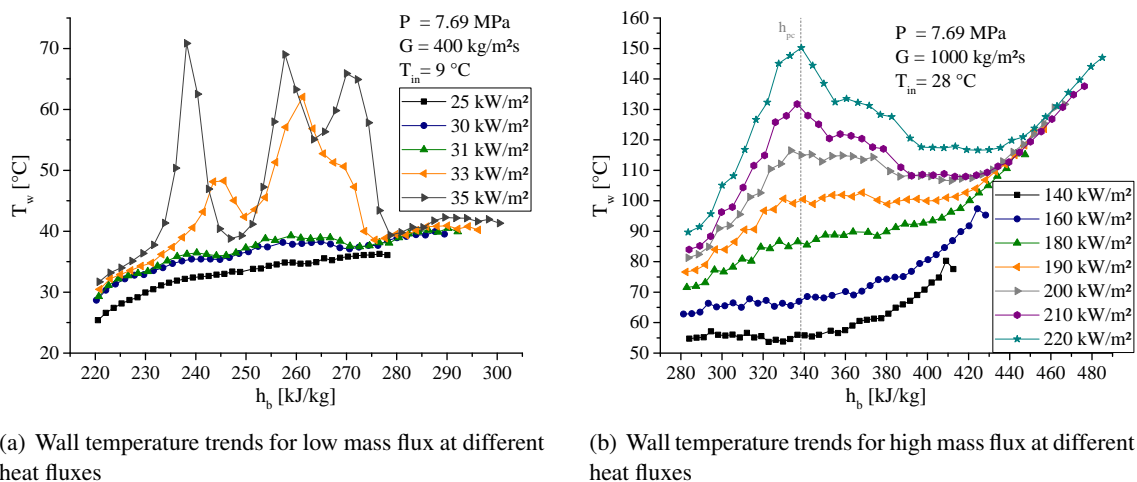
Figure 4.1.: Wall temperature trends for low and high mass fluxes with varying heat fluxes of ts-2 in CO_2

Another widely used method to determine the heat transfer regimes is to compare the HTC of the experiment to the ones predicted by the correlation of Dittus-Boelter. Figure 4.2 (a) shows

the HTC at mass flux of $500\,\text{kg/m}^2\text{s}$ with all proposed heat transfer modes. The heat transfer is normal until the bulk enthalpy of $335\,\text{kJ/kg}$ as the experimental values are close to the Dittus-Boelter correlation. As the HTC trends drops far below the values predicted by Dittus-Boelter, the heat transfer is defined as deteriorated. After the local minimum, the HTC increases sharply and exceeds the predicted values. In this case, the heat transfer is defined as enhanced.
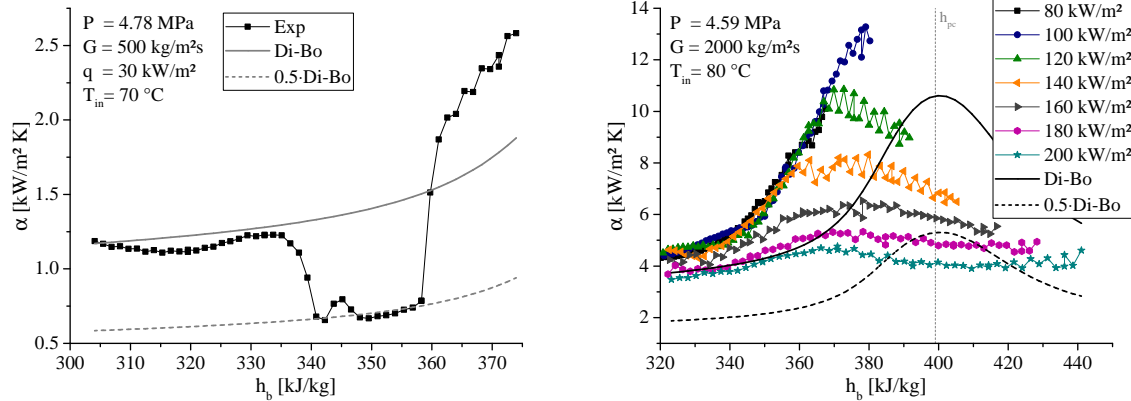
(a) Deviation of experimental results to correlation of Dittus-Boelter at low mass fluxes

(b) Deviation of experimental results to correlation of Dittus-Boelter at high mass fluxes

Figure 4.2.: Heat transfer coefficient trend deviation of experimental results to correlation of Dittus-Boelter at different heat fluxes of ts-1 in R134a

In figure 4.2 (b), it can be seen that the HTC trends of $80\,\text{kW/m}^2$ and $100\,\text{kW/m}^2$ match well over the total range. At low bulk enthalpies, the trends of $120\,\text{kW/m}^2$ and $140\,\text{kW/m}^2$ also match this trend. Starting from $120\,\text{kW/m}^2$, the HTC trends start to deviate until it drops below the Dittus-Boelter correlation. The HTC decreases with increasing heat flux. The most used definition in the literature is $\alpha/\alpha_{DB}<0.3$ for the heat transfer to be deteriorated. As for the wall temperature peak, there is no physical background for this limit and it is defined randomly. The limit of 0.5 is used in figure 4.2. None of the data in figure 4.2 would be deteriorated for a limit of 0.3. Additionally, using the definition of the literature, only the heat fluxes $180\,\text{kW/m}^2$ and $200\,\text{kW/m}^2$ in figure 4.2 (b) up to the bulk enthalpy of $360\,\text{kJ/kg}$ would be defined as normal heat transfer. All other cases would be defined as enhanced heat transfer as their HTC are higher as the one predicted by the correlation of Dittus-Boelter. A correlation can not show if there exists a real difference between the normal and the enhanced heat transfer cases as their HTC are so close at bulk enthalpy until $350\,\text{kJ/kg}$ in figure 4.2 (b). A correlation has a high uncertainty and is only valid for defined boundaries and limited parameters. Therefore, it is highly questionable to use heat transfer correlations to distinguish the borders between NHT, HTD and HTE.

In the literature, the HTD is often associated with a change in the heat transfer mechanism. This was proposed because the appearance of the HTD looks similar to the phenomenon of the dryout in a two-phase flow. Here, a change in the heat transfer mechanism cause the reduction in the heat transfer. At supercritical conditions, there is no phase change and fluid properties vary continuous with temperature. These continuously variations influence the heat transfer, but they occur gradually, as exemplarily seen in figure 4.2 (b) Therefore, it is not possible to define an exact onset and criteria of the HTD. This explains why there is no common and clear definition for the onset of the HTD in the literature.

4.1.2. Own definition for heat transfer deviation

As there is no clear definition and no clear boundary between the different heat transfer regimes, as discussed in section 4.1.1, the heat transfer at supercritical condition must be considered as one

coherent regime. If the heat transfer deviates from the one of forced convection, effects like the buoyancy force and the thermally-induced bulk flow acceleration become stronger. Both effects are described in more detail in section 2.2.2.2 and 2.2.2.3, respectively.

Therefore, there is no categorization of the heat transfer data into different regimes as normal, enhanced or deteriorated in this study. Instead, the influence of the buoyancy and acceleration on the heat transfer are evaluated. If their influence can not be neglected and cause the heat transfer to change from forced to mixed convection, it will be just called heat transfer deviation (HTDe). To identify if the influence cannot be neglected, the criteria of Jackson are used. For the buoyancy, the Buoyancy number defined in equation 2.13 and 2.10 for $T_w > T_{pc}$ with the proposed criteria of 10^{-5} is used. The thermally-induced bulk flow acceleration has an influence if the Acceleration number of equation 2.14 is higher than the proposed criteria of 4×10^{-6} [Jackson, 2011].

Kline [Kline et al., 2018] showed that the limits for Buoyancy and Acceleration number must be adapted for different fluids and parameters. The influence of these two numbers on the heat transfer will be shown and discussed in detail in section 5.1.

The coherence between Buoyancy number, Acceleration number and the heat transfer at supercritical conditions will be investigated and discussed in detail in chapter 5.

4.2. Reproducibility and data selection

4.2.1. Reproducibility of ts-1

Some cases were reproduced to show the reliability of the produced experimental results. The tests show that most data can be reproduced well. Figure 4.3 shows exemplarily for ts-1 at $500\,\text{kg/m}^2\text{s}$ that the results are reproduced well at different days, even for cases with influences of buoyancy.
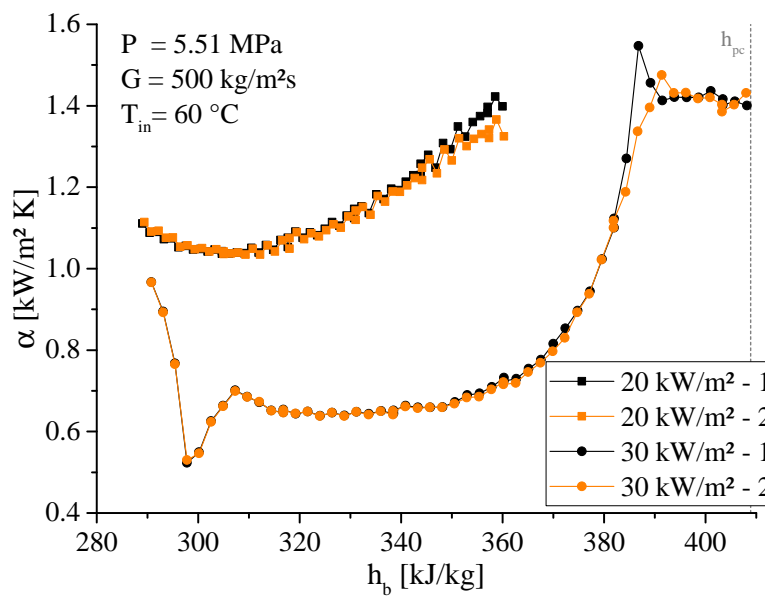
Figure 4.3.: Results of repeated experiments at $500\,\text{kg/m}^2\text{s}$ of ts-1 in R134a with and without influence of buoyancy

4.2.1.1. Low pressure

There are difficulties to reproduce the data at HTDe cases at $4.22\,\text{MPa}$ for the heat fluxes of $20 - 40\,\text{kW/m}^2$ at the mass fluxes of $300\,\text{kg/m}^2\text{s}$ and $500\,\text{kg/m}^2\text{s}$. There is a threshold for the pressure of $4.20\,\text{MPa}$ below the HTC trends changes suddenly. Figure 4.4 (a) shows the decrease of the HTC near the pseudo-critical bulk enthalpy for a pressure below $4.20\,\text{MPa}$ compared with $4.22\,\text{MPa}$.

This is only 1.04 times of the critical pressure. Here, minimal variation leads to strong changes in the thermal-physical properties of the coolant. This leads to a high sensibility of the HTC at small pressures. To avoid this sudden change of the HTC trend, all experiments are conducted at a minimum pressure of 4.2 MPa.
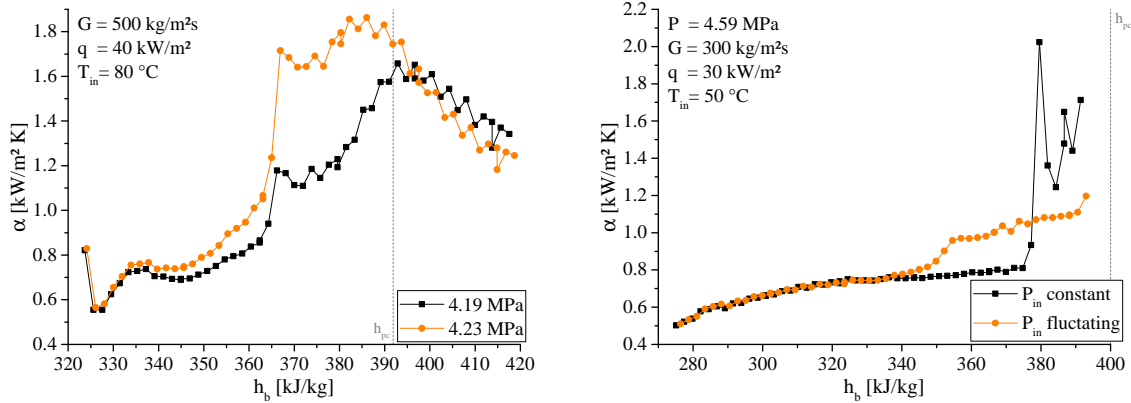
(a) Difficulty of reproduction of experimental results at 4.22 MPa at low mass fluxes

(b) Difficulty of reproduction of experimental results at cases with oscillating inlet pressure

Figure 4.4.: Difficulties of reproduction of experimental results at sensible stages of ts-1 in R134a

4.2.1.2. Flow instabilities

Some cases are difficult to reproduce at low mass fluxes, low inlet temperatures and high heat fluxes. An example is shown in figure 4.4 (b). It is found that, in one case, the inlet pressure is fluctuating whereas, in the other case, the inlet pressure remains constant. Reasons for this dynamic instabilities are discussed in section 2.5. These flow instabilities depend on the system [Ambrosini & Sharabi, 2008]. The total pressure loss in the facility is responsible for the instabilities. If there are different settings for the cooling and preheating of the coolant, the total pressure loss is changed. Especially if the valve positions are changed to adjust the mass flux in the test section, the total pressure drop in the loop varies strongly. This can lead to an appearance of the flow instabilities or a different amplitude of the oscillations. Figure 4.4 (b) shows exemplarily the result of the HTC trend with and without flow instabilities.
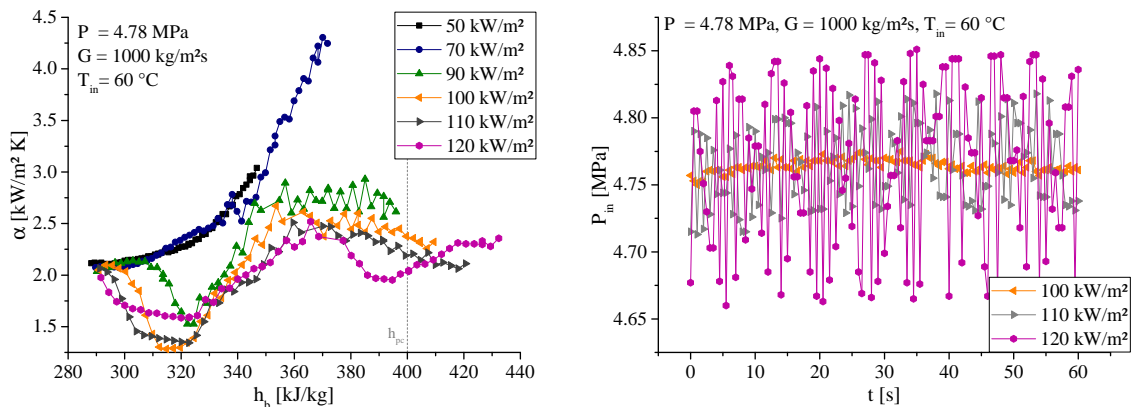
(a) Heat transfer trends deviations caused by flow instabilities at different heat fluxes

(b) Oscillating fluctuation of inlet pressure at cases with deviation of the HTC trend

Figure 4.5.: Heat transfer trends deviations caused by oscillating fluctuation of inlet pressure at 1000 kg/m^{2}s and different heat fluxes of ts-1 in R134a

But there are also parameter regions where these inlet pressure fluctuations always occur for ts-1. Due to the strong density variation, a change of the local velocities in the test section is possible as Oka proposed [Oka et al., 2010]. The buoyancy influenced HTDe occurs due to the reduction of the turbulence production [Petukov et al., 1988, Jackson, 2011], as discussed in section 2.2.2.2. The oscillating velocity fluctuations would increase the turbulence production in the viscous layer and lead to a recovery of the heat transfer. This mitigation of the HTDe and coherent increase of the HTC is observed as shown in figure 4.5 (a). Normally, the buoyancy induced HTDe increases with increasing heat flux but at $750 \, \mathrm{kg/m^2 s}$ and $1000 \, \mathrm{kg/m^2 s}$, this phenomenon can be inversed at high heat fluxes. Figure 4.5 (a) shows this inverse heat flux influence starting at $110 \, \mathrm{kW/m^2}$ for $1000 \, \mathrm{kg/m^2 s}$. The buoyancy influenced HTDe gets less, whereas the reduction of the HTC near the pseudo-critical bulk enthalpy is reduced as expected. As figure 4.5 (b) shows, the larger the amplitudes and frequency of the pressure fluctuation are, the more the HTDe is mitigated.
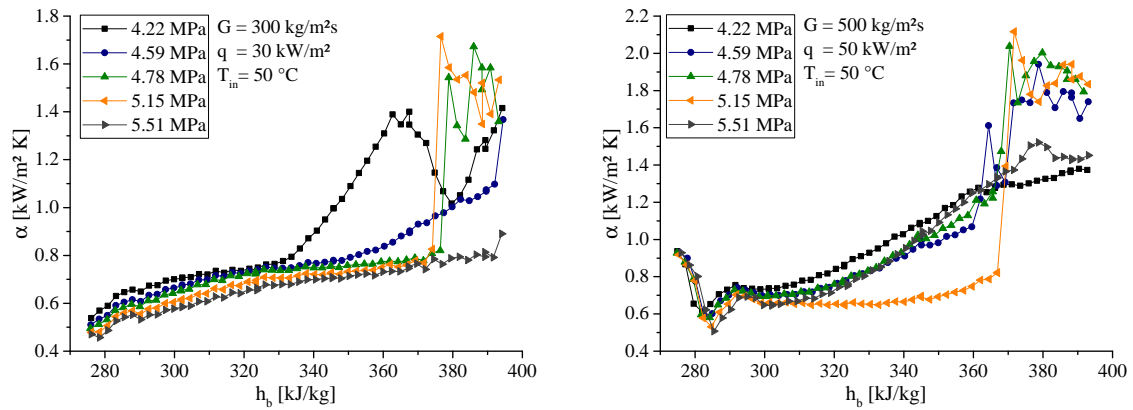
(a) Heat transfer coefficient trends deviation for $300 \, \mathrm{kg/m^2 s}$ at different pressures

(b) Heat transfer coefficient trends deviation for $500 \, \mathrm{kg/m^2 s}$ at different pressuress

Figure 4.6.: Heat transfer trends deviations for ts-1 in R134a at mass fluxes of $300 \, \mathrm{kg/m^2 s}$ and $500 \, \mathrm{kg/m^2 s}$

At the mass fluxes of $300 \, \mathrm{kg/m^2 s}$ and $500 \, \mathrm{kg/m^2 s}$, the sudden increase of the HTC after the bulk enthalpy of $370 \, \mathrm{kJ/kg}$ differs for low pressures as seen in figure 4.6. It changes from a sudden increase in a very narrow bulk enthalpy range to a gradually increasing HTC along a wide range of the bulk enthalpy. The gradually increasing HTC trend occurs more likely at small pressures and only at inlet temperatures of $50 \, °C$ and $60 \, °C$ when the inlet pressure oscillate.

Table 4.1 lists all experiments with oscillating inlet pressure. The fluctuations occur more likely at low pressures and inlet temperatures. In these cases, the change in density is stronger. It was found that a minimum amplitude of $0.05 \, \mathrm{MPa}$ is required in the oscillations, otherwise no influence on the HTC can be observed. The data of the experiments listed in table 4.1 are not at steady state and their HTC deviates because of the system dependent flow instabilities. Therefore, this data are not included in the data analysis, the assessment of correlations or for the fluid-to-fluid scaling models.

Table 4.1.: List of experiments at ts-1 with oscillating inlet pressure given for heat fluxes in kW/m^2

P	T_{in}	G in $\left[\frac{kg}{m^2 s}\right]$				
[MPa]	[°C]	300	500	750	1000	1500
4.22	50	30	40 - 50	50 - 60	110 - 120	150 - 160
	60	-	40 - 50	-	110 - 120	150
4.59	50	30	40 - 50	-	110 - 120	-
	60	-	-	-	110 - 120	-
	70	-	-	-	100 - 120	-
4.78	50	30 - 40	40 - 50	-	-	-
	60	-	-	-	110 - 120	-
5.15	50	30 - 40	40	-	-	-
	60	-	40	-	110 - 120	-
	70	-	-	-	110 - 120	-
5.51	50	30 - 40	50	-	-	-
	60	-	-	-	120	-
	70	-	-	-	120	-

4.2.1.3. Change of heat transfer surface

Local depositions

Local wall temperature peaks occurred in the test section after approximately 50 % of all experiments for ts-1 have been conducted. These peaks stayed at the same axial position independent of heat flux, mass flux, pressure or inlet temperature. Only the height of the peaks was influenced by these parameters as exemplarily seen for the heat flux in figure 4.7 for the marked peaks. The overall trend of the heat transfer coefficient remains unchanged compared to reproduced experiments and experiments with similar parameters. The data from these local disturbance are excluded from the database used for the data analysis and correlation assessment.
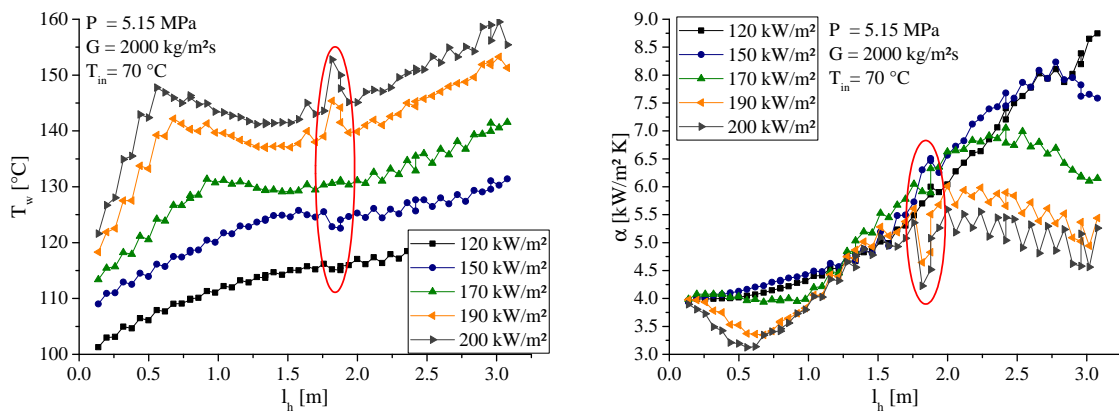
(a) Occurrence of local wall temperature peak due to deposition on the wall

(b) Occurrence of local heat transfer coefficient minimum due to deposition on the wall

Figure 4.7.: Local heat transfer deviation due to deposition on the tube's wall of ts-1 in R134a

Due to this strong local appearance, a local disturbance is assumed. Therefore, the test section was opened and cleaned multiple times with and tissue pulled through the tube. Figure 4.8 shows brown powder at the tissue which have been deposit at the tube's inside wall. After the cleaning of the test section, the local heat transfer deviation vanished. From these observations, it can

be concluded that this deposition disturbed the local heat transfer. The source of the deposition is unknown, but it is assumed that oil from the pressurizer has leaked into the loop. It deposits at the wall of the test section, where the temperature exceed its decomposition temperature of 120 °C [FINKE MINERALÖLWERK GMBH, 2017].

Figure 4.8.: Tissue after cleaning the tube of test section ts-1

Widespread deposition

A set of post-dryout (PDO) experiments with high wall temperatures were conducted after all experiments listed in table 3.3 had been finished. The trend of the HTC changed for all experiments at supercritical conditions after these PDO experiments. Cleaning attempts could not restore the behavior. This change of the HTC trend can be seen in figure 4.9 for low and high mass fluxes. At low mass fluxes and heat fluxes, the trends are similar at the beginning, but the differences are increasing as the bulk enthalpy reaches the pseudo-critical value. These differences are getting more evident as the mass flux and heat flux increases until almost the whole test section show different results. However, the buoyancy-influenced HTDe near the inlet is not affected by the change, as seen in figure 4.9.
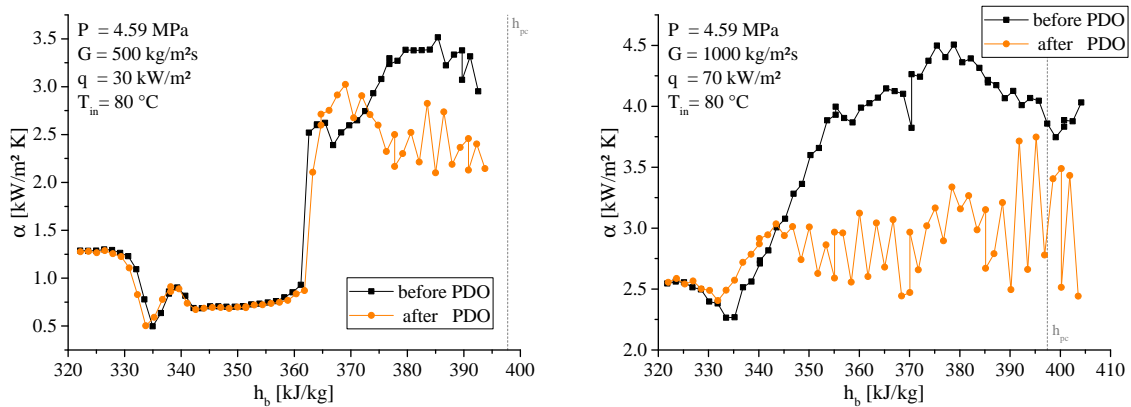
(a) Deviation of heat transfer after long used test section at low mass flux

(b) Deviation of heat transfer after long used test section at high mass flux

Figure 4.9.: Deviation of heat transfer after long used test section at mass fluxes of $500\,\mathrm{kg/m^2s}$ and $1000\,\mathrm{kg/m^2s}$ of ts-1 in R134a

A reason could be a change of the thermal-physical properties of the coolant due to decomposition or other accumulating impurities. To verify this statement, another set of subcritical experiments, as described in section 3.7.1, is performed. The resulting heat balance of 0.9 % is in the same range as before. Therefore, a change of the fluid properties can be excluded. For the same conducted parameters, the measured data of mass flow rate, current and voltage drop along the test section are the same. This shows that the measurement system and electric resistance of the test section did not change. The subcritical experiments before and after the PDO are compared to verify the wall temperature measurement. The reproducibility of the HTC is acceptable. Nevertheless, a tendency of a minor smaller HTC is recognizable at the test section with decompositions compared to the experiments before the post-dryout experiments. This can be seen in figure 4.10 (a). This reduction of the HTC could be amplified at supercritical conditions, as seen in figure 4.9, whereas the HTC trend of the experiments after the PDO is always smaller. Nevertheless, a change of the fluid properties due to minor impurities is rather excludable. Another indication is the HTDe caused by buoyancy forces which is not changed, as seen in figure 4.9 (a), which location and magnitude is only dependent on the fluid properties. Further, figure 4.10 (b) shows a reproduced experiment for heat transfer in the post-CHF region at subcritical conditions. Normally at these experiments, it is assumed that a minor deviation should have a huge influence on the heat transfer, too. In fact, almost no difference is recognizable. There is a tendency that the CHF occurs at minor lower vapor qualities, as seen in 4.10 (b). This is also a small indication for a heat transfer reduction.
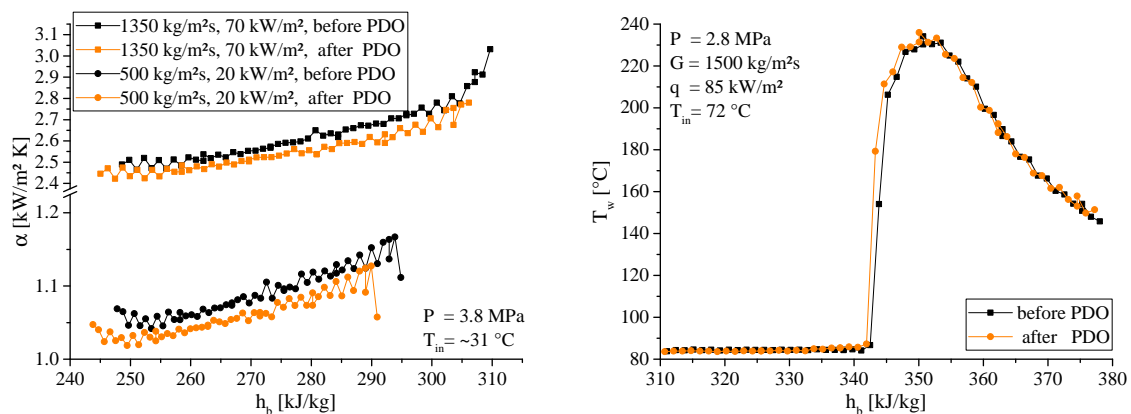
(a) Comparison of heat transfer at subcritical single-phase conditions

(b) Comparison of wall temperature at subcritical two-phase conditions in post-CHF region

Figure 4.10.: Comparison of heat transfer at subcritical conditions in single-phase and two-phase for the deviated test-section before and after the PDO experiments of ts-1 in R134a

Another reason for the observed heat transfer deviation could be a deposition at the heated wall inside the tube. Figure 4.11 shows the wall at the inside of the tube of different heights after all experiments. The deposition at the wall gets darker and thicker along the tube.

An investigation with the energy-dispersive X-ray spectroscopy shows that, in the deposition layer, elements occur, which are additive in oils. The results of the spectroscopy are listed in table 4.2. At the unheated part, only elements from the material of the tube are found. At the heated parts, elements as sodium, potassium and zinc are found, which are additive of the oil. In particular, the atomic percent of carbon and fluorine are increased. Both could be from the oil or from the coolant R134a. Calderazzi and Dai et al. found a decomposition temperature of 360 °C for the R134a [Calderazzi & Di Paliano, 1997, Dai et al., 2018]. Nevertheless, it could be possible that R134a decompose earlier due to the direct contact to current or the remaining oxygen in the facility [Dai et al., 2016]. The spectroscopy only detects elements, so it could be that the R134a is still intact and bound as molecules at the wall. However, it is more likely that the deposition is from the hydraulic oil, which decomposes at 120 °C. The oil can leak into the R134a loop by bypassing the dynamic sealing of the pistons in the accumulator.
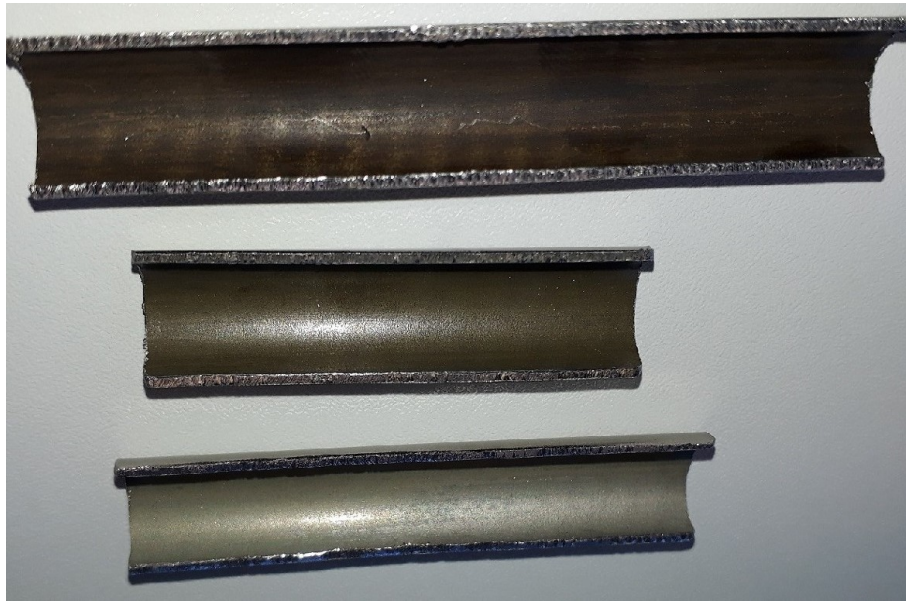
Figure 4.11.: Deposition on inside wall along the tube with parts of unheated, middle and end of heating length from bottom to top of ts-1

Table 4.2.: Atom percent of elements found with the Energy-dispersive X-ray spectroscopy of the surface of the unheated and the heated tube

Location	C	O	F	Na	Al	Si	P	S	K	Ca	Cr	Mn	Fe	Ni	Cu	Zn
unheated	11.5	42.5	0	0.3	1.1	1.3	0.1	0.1	0	0	12	2.5	25.3	3.1	0.1	0
top heated	30.7	31	17.8	6	0.3	0.3	2.9	1.3	0.8	0.3	2.4	0.6	6.3	0.4	0.4	0.5

Detailed pictures with a high magnification of the unheated part and the part of the end of the heated length are shown in figure 4.12. The pictures are taken with a scanning electron microscope with a magnification of 2000x. The surface gets more smooth as the deposition layer grows thicker.
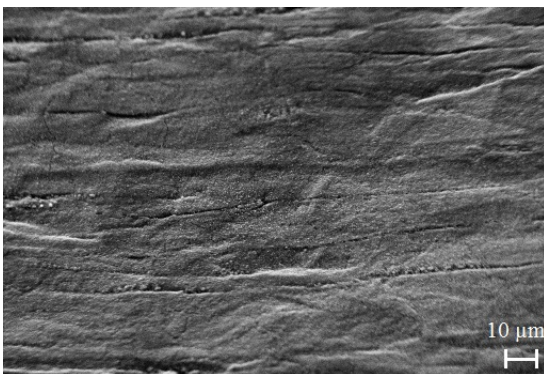
(a) Scanning electron microscope picture of unheated part

(b) Scanning electron microscope picture of heated part

Figure 4.12.: Deposition on inside wall of ts-1 at unheated and heated part with scanning electron microscope picture

This layer could influence the boundary layer of the flow which causes different results for the heat transfer. The heat transfer at supercritical conditions is very sensible to the flow regime in the boundary layer. The roughnesses of the pieces shown in figure 4.11 are listed in table 4.3 with the values from the unused tube shown in section 3.2. It can be concluded that the roughness decreases

with increasing deposition layer for both, the mean roughness Ra and the averaged maximum peak to valley roughness Rz. This could lead to a different development of the boundary layer and thus to the different observed heat transfer trends.

Table 4.3.: Mean roughness Ra and the averaged maximum peak to valley roughness Rz of unused, unheated and heated tube of ts-1 at different heights in μm

Roughness	Unused	Unheated	Middle	End
Ra	0.45	0.41	0.37	0.33
Rz	2.5	2.2	2	1.9

As discussed in section 2.2.2.3, the HTC can decrease near the pseudo-critical point due to the thermally-induced bulk flow acceleration. The heat transfer reduction is caused by a laminarization of the flow induced by a pressure gradient near the wall. As know, the roughness of the tube has a strong influence on the pressure gradient. This means, a reduction of the roughness could amplify the heat transfer reduction due to the smaller pressure gradient and causing a wider ranged or an earlier onset of laminarization. This could explain why the tube with the lower roughness shows a smaller HTC around the pseudo-critical as seen in figure 4.9. This statement cannot be proofed with the lack of the flow velocity distribution measurements, but the given measurements show how sensible the heat transfer is to the surface of the tube at these conditions.

Luckily, this deviation of the HTC trends occurred after the whole set for ts-1 were completed and thus, this permanent layer has no further influence on the data which are used in this work. Nevertheless this observation is still important for the general evaluation of different experimental setups because it shows how sensible the heat transfer at supercritical conditions is on the surface condition. Especially around the pseudo-critical point, where the thermally-induced bulk flow acceleration has a strong influence on the heat transfer. As seen, the surface has an influence on this heat transfer regime and could be an explanation for different results in the literature as discussed in section 2.2.7.

4.2.2. Reproducibility of ts-2

Kline [Kline, 2017] showed the reproducibility of the experimental results at the SCUOL and additionally a good agreement with experiments from Fewster and Jackson. Additional reproducibility test are done at ts-2 and showed a good reproducibility in general. This is exemplarily shown in figure 4.13 for two cases with mass fluxes of $500\,kg/m^2s$ and $1200\,kg/m^2s$ at high heat fluxes conducted at different days.

(a) Results of repeated experiments at $500\,kg/m^2s$ (b) Results of repeated experiments at $1200\,kg/m^2s$
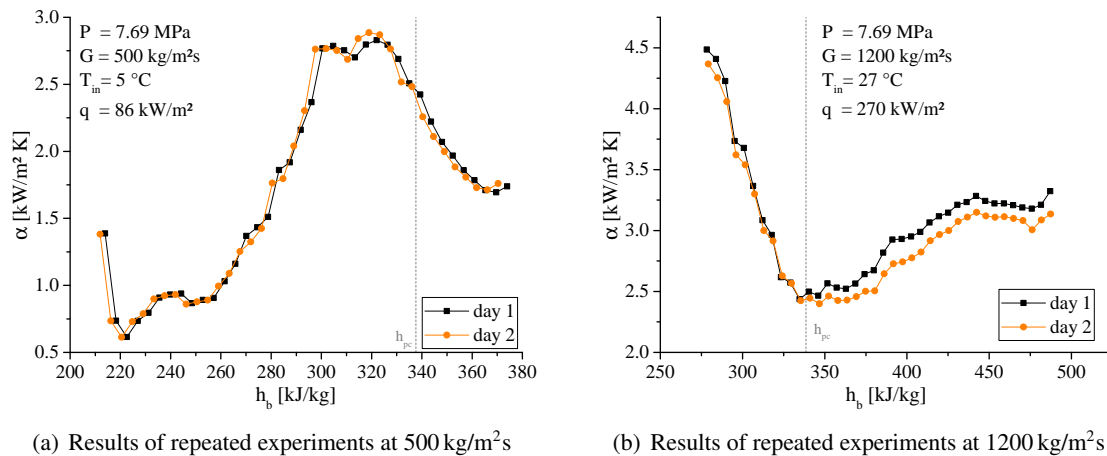
Figure 4.13.: Reproducibility of heat transfer at supercritical conditions of ts-2 in CO_2

4.2.2.1. Flow instabilities

The reproducibility capability of the experimental results of ts-2 at low mass fluxes is shown by Kline [Kline, 2017]. Also at high mass fluxes the reproducibility is fine. Only for mass fluxes of $1000\,kg/m^2s$ and high heat fluxes, the reproducibility is difficult, as seen in figure 4.14. Flow instabilities are maybe the reason for the reproducibility issues as discussed in section 4.2.1.2.
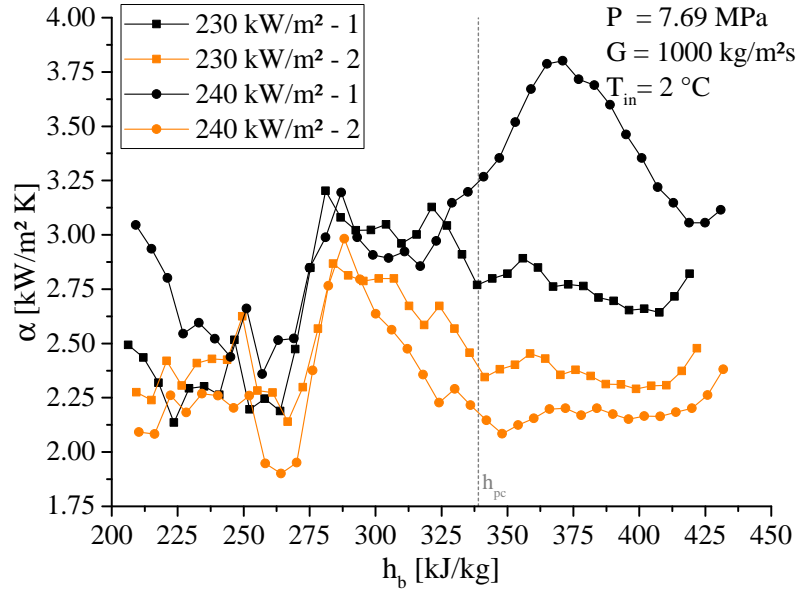
Figure 4.14.: Difficulty of reproduction of experimental results at $1000\,kg/m^2s$ with ts-2 in CO_2

Figure 4.15 shows the HTC trends for different heat fluxes at $1000\,kg/m^2s$ for the inlet temperatures of $20\,°C$ and $28\,°C$. As shown before and seen in the literature, the HTC decreases normally with increasing heat flux. However, the HTC trend changes drastically in figure 4.15 (a) as the heat flux is increased from $200\,kW/m^2$ to $205\,kW/m^2$ and the HTC is increased hugely after the pseudo-critical bulk enthalpy. After that, the HTC decreases again for increasing heat flux. In figure 4.15 (b), the HTC also increase as the heat flux is increased from $180\,kW/m^2$ to $220\,kW/m^2$. Its increase is much lower and it is increasing in several steps. The HTC decreases again for increasing heat flux starting at $220\,kW/m^2$.

In figure 4.15 (c) can be seen that the frequency of the oscillating inlet pressure increases after the drastic HTC trend change happens from $200\,kW/m^2$ to $205\,kW/m^2$ for $20\,°C$. No change of the frequency can be seen for the smooth change of the HTC trends in figure 4.15 (d). Therefore, it is assumed that the smooth change of the HTC trend as seen in 4.15 (b) is an actual phenomenon of heat transfer at supercritical conditions at high heat fluxes. Similar trends can be seen at other inlet temperatures and mass fluxes. The drastic change seen in 4.15 (a) in combination with an increase of the frequency of the oscillating inlet pressure is assumed to be caused by flow instabilities.

Because the HTC trend changes suddenly for the heat fluxes listed in table 4.4 for the mass fluxes of $1000\,kg/m^2s$, it differs from the flow instabilities discussed in section 4.2.1.2. This sudden change in the heat transfer is like a threshold which is overpassed. An explanation could be the Ledinegg instability [Ledinegg, 1938], as discussed in section 2.5. With the change from a liquid-like pressure drop to the vapor-like pressure drop locally in the test section, the heat transfer may change as well. In fact, no changes in mass flux or pressure at the outlet was measured. One day, a remarkable change in the pressure loss swas observed. At $1000\,kg/m^2s$ and inlet temperatures of $2\,°C$, the pressure drop at the whole test section increased from $4\,kPa$ to $21\,kPa$ as the heat flux increased from $230\,kW/m^2$ to $240\,kW/m^2$ and the change in the HTC trend occurred. An increase of the pressure drop normally means an increase of shear stress and a higher turbulence production

which has a positive effect on heat transfer. This could be an indication for the Ledinegg instability.

(a) Heat transfer coefficient trends for mass fluxes of 1000 kg/m^{2}s and inlet temperatures of 20 °C

(b) Heat transfer coefficient trends for mass fluxes of 1000 kg/m^{2}s and inlet temperatures of 28 °C

(c) Inlet pressure for mass fluxes of 1000 kg/m^{2}s and inlet temperatures of 20 °C

(d) Inlet pressure for mass fluxes of 1000 kg/m^{2}s and inlet temperatures of 28 °C
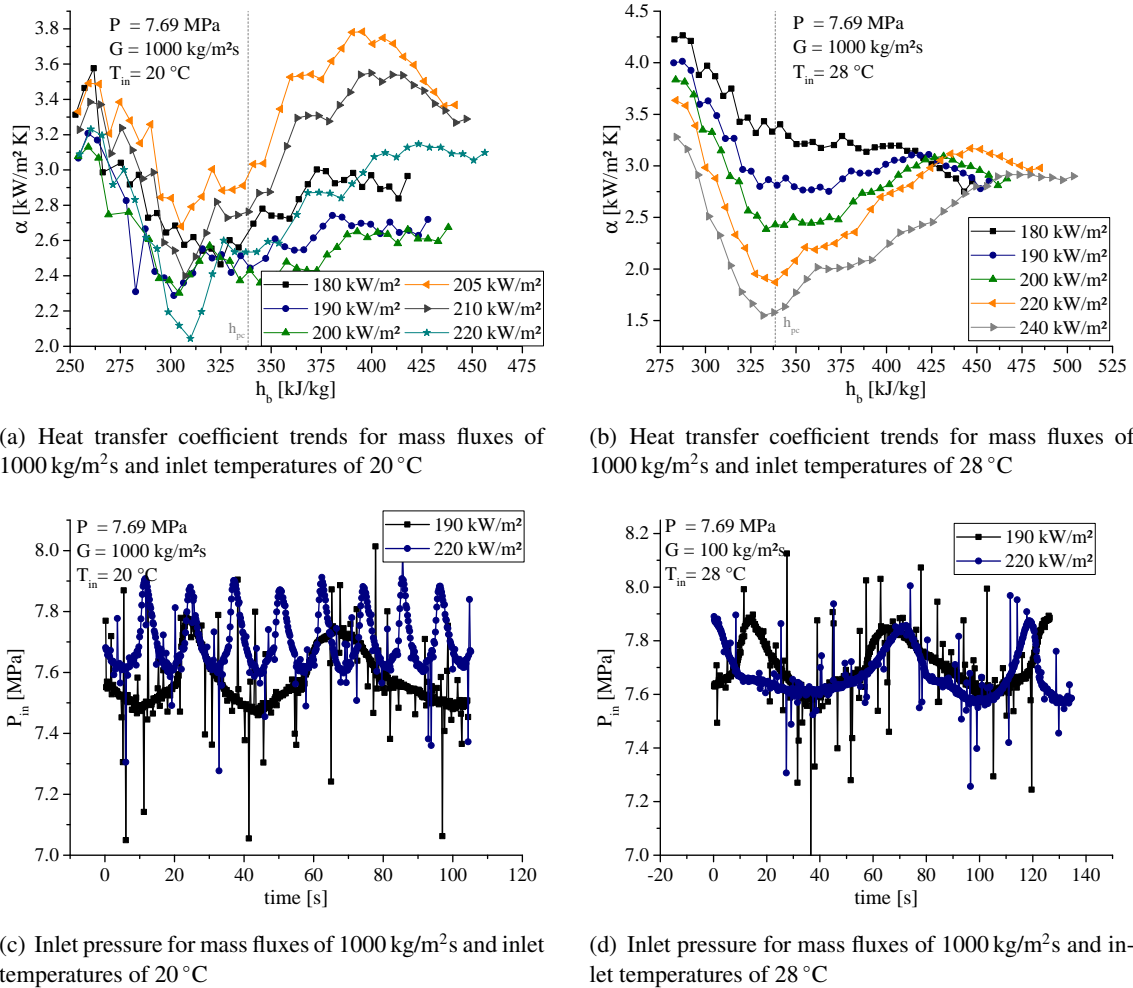
Figure 4.15.: Changing heat transfer trends for mass fluxes of 1000 kg/m^{2}s for oscillating pressure with different heat fluxes of ts-2 in CO_2

This instability depends on the system and its parameters. This means that the heat flux threshold differs for different mass fluxes, inlet temperatures and different system conditions as cooling temperatures or positions of the valves. If cases near this Ledinegg threshold are reproduced, the change of the HTC can occur at different heat fluxes which leads to high deviations, as seen in figure 4.14.

Because these phenomena of instabilities are not proofed, another explanation could be the idea of multi-solutions for the heat transfer at supercritical conditions of Cheng and Liu [Cheng & Liu, 2017]. This is discussed in section 2.2.7. An evidence could be the difficult reproducibility, as seen in figure 4.14, where the same parameters of pressure, mass flux, inlet temperature and heat flux can have different results for the heat transfer. Also no other parameter differences are noticed, except the increase of the inlet pressure oscillation. If there is no multi-solution, there must be an unknown and unnoticed parameter or the whole system must be concerned for the heat transfer at supercritical conditions.

The heat fluxes at which this drastic change starts to occur are listed in table 4.4. All experiments with the listed mass fluxes, inlet temperatures and starting from the listed heat fluxes are excluded in the following data analysis, assessments of correlations and fluid-to-fluid scaling models.

Table 4.4.: List of experiments at ts-2 with oscillating inlet pressure given for heat fluxes in kW/m^2

G $\left[\frac{kg}{m^2 s}\right]$	T_{in} [°C]			
	2	7	10	20
300	-	100	100	-
1000	220	230	-	205

Enhancement

For the mass fluxes of 300 kg/m^{2}s listed in table 4.4, the HTC trend also changes differently for heat fluxes of 100 kW/m^2 and higher. It can be seen in figure 4.16 (a) that the HTC starts to increase with increasing heat flux just before the pseudo-critical bulk enthalpy.
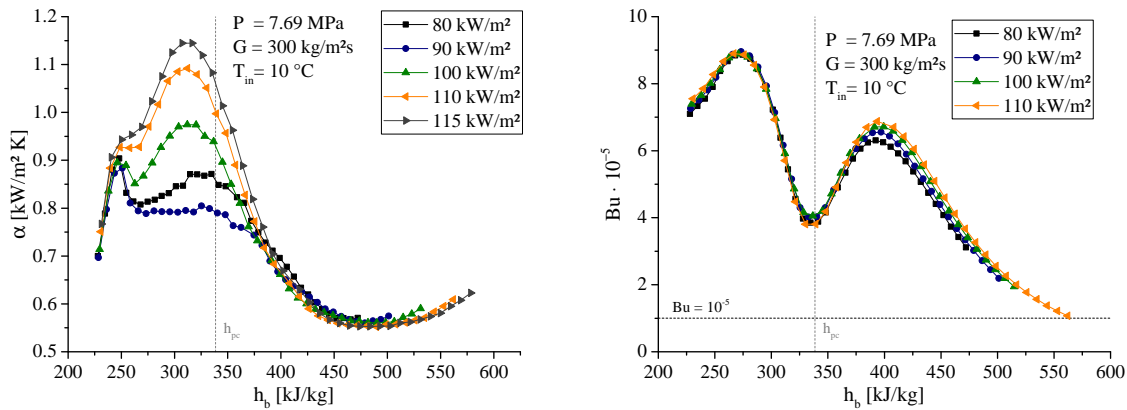
(a) Heat transfer coefficient trends for mass fluxes of 300 kg/m^{2}s and very high heat fluxes

(b) Buoyancy number trends for mass fluxes of 300 kg/m^{2}s and very high heat fluxes

Figure 4.16.: Enhancement of heat transfer at mass fluxes of 300 kg/m^{2}s and very high heat fluxes at ts-2 in CO_2

As discussed in section 2.2.2.1, Jackson [Jackson, 2011] and Zhang [Zhang et al., 2018] stated that the enhancement of the heat transfer is due to strong influences of buoyancy. Jackson proposed the onset of enhancement by the increase of the buoyancy number beyond the range of the occurrence of the HTD [Jackson, 2011]. In 4.16 (b) the buoyancy number Bu is shown for the same cases as in figure 4.16 (a). It can be seen that the Bu is much higher than the onset for the HTD. There is no change of the Bu for different heat fluxes. Therefore, the buoyancy alone can not be the reason for the heat transfer enhancement seen in figure 4.16 (a). In figure 4.17 (a) it can be seen that, at this point, the wall temperature is constant and the increase of the HTC is due to the higher transfered heat flux. This could be due to the increased turbulence caused by the increased oscillating inlet pressure as seen in figure 4.17 (b) and discussed in section 4.2.1.2.

The enhancement in the heat transfer seen in figure 4.16 (a) and 4.17 (a) is not meant as the regime HTE as defined in the literature. The enhancement is due to the increased heat transfer to the expected heat transfer from similar cases and is caused by flow instabilities. Nevertheless, due to the abnormal behavior, these data are excluded in the following data analysis and assessments of correlations or fluid-to-fluid scaling models and listed in table 4.4.
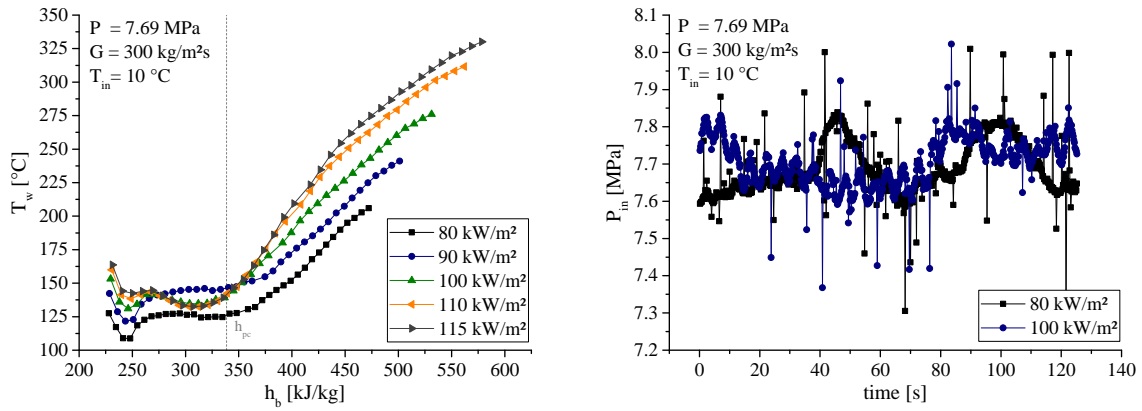
(a) Wall temperature trends for mass fluxes of $300\,\mathrm{kg/m^2s}$ and very high heat fluxes

(b) Oscillating inlet pressure at mass fluxes of $300\,\mathrm{kg/m^2s}$ and very high heat fluxes

Figure 4.17.: Wall temperature and inlet pressure at enhancement of heat transfer at mass fluxes of $300\,\mathrm{kg/m^2s}$ and very high heat fluxes at ts-2 in CO_2

4.3. Databases for R134a and CO_2

For the heat transfer at supercritical conditions with R134a and CO_2, all experiments listed in the tables 3.3 and 3.4 were conducted. Several data points and complete cases must be removed for the data analysis due to local disturbances or damaged single thermocouples and flow instabilities described in the previous sections. Nevertheless, there are still 44 679 data points for R134a and 19 966 data points for the database of CO_2 left, as seen in table 4.5. This are sufficient data points for a detailed analysis and assessment of correlations or fluid-to-fluid scaling models.

Table 4.5.: Data points for the heat transfer at supercritical conditions of R134a and CO_2

Fluid	All data	Valid data
R134a	47 300	44 679
CO2	21 164	19 966

5. Results and Discussion of Heat Transfer at Supercritical Conditions

This chapter presents the results of the experiments with supercritical R134a and CO_2 for the data selected in section 4.3. The influences of pressure, mass flux, inlet temperature and heat flux are discussed in detail. The experimental data are compared with data from the literature and are discussed. At the end, an assessment of correlations with the produced data is done.

5.1. Results and discussion of heat transfer experiments of ts-1

The influence of the four adjustable parameters mass flux, inlet temperature, pressure and heat flux on the HTC in R134a are discussed in this section. Due to the fact that the heat transfer at supercritical conditions is a complex phenomena, the single influences cannot be explained in a general manner. As Kurganov et al. [Kurganov et al., 2014] showed, the qualitative behavior of the heat transfer is determined by the mass flux. Therefore, the influence of heat flux, pressure and inlet temperature will be discussed for each mass flux.

5.1.1. Mass flux of 300 kg/m^{2}s

Influence of heat flux

The qualitative behavior of the wall temperature of all experiments with mass fluxes of 300 kg/m^{2}s is varying similarly with heat flux. At the heat flux of 5 kW/m^2, the wall temperature trend looks similar to trends at subcritical conditions. A small peak is formed at 310 kJ/kg with increasing heat flux, which moves upstream, as seen in figure 5.1 (a). At the heat flux of 20 kW/m^2 and 30 kW/m^2, the wall temperature suddenly drops to a lower level. The small temperature peaks are caused by local minimums in the heat transfer coefficient, as seen in figure 5.1 (b). The sudden drop of the wall temperature is caused by an increasing HTC.

Figure 5.1 (c) shows the Buoyancy and Acceleration number for the same cases. A Buoyancy number over 10^{-5} means that the buoyancy force has an influence on the heat transfer. The higher the value is, the stronger is the influence. The buoyancy force caused by density variations in the cross section can lead to a laminarization of the flow which decreases the heat transfer capability. This is explained in detail in section 2.2.2.2. This could explain the local wall temperature peaks at small bulk enthalpies of figure 5.1 (a). Further, it can be seen that the sudden increases of the HTC at 20 kW/m^2 and 30 kW/m^2 coincide with a sudden drop of the Buoyancy number below the limit of 10^{-5}. At 40 kW/m^2 the Buoyancy number decreases in the same way as at 30 kW/m^2, but the sudden increase of the HTC does not appear. At this enthalpy, the Acceleration number increases above the limit of 4×10^{-6}, as seen in figure 5.1 (c). The thermally-induced bulk flow acceleration has a strong influence on the heat transfer above that limit and leads to a reduction of the HTC as discussed in section 2.2.2.3.
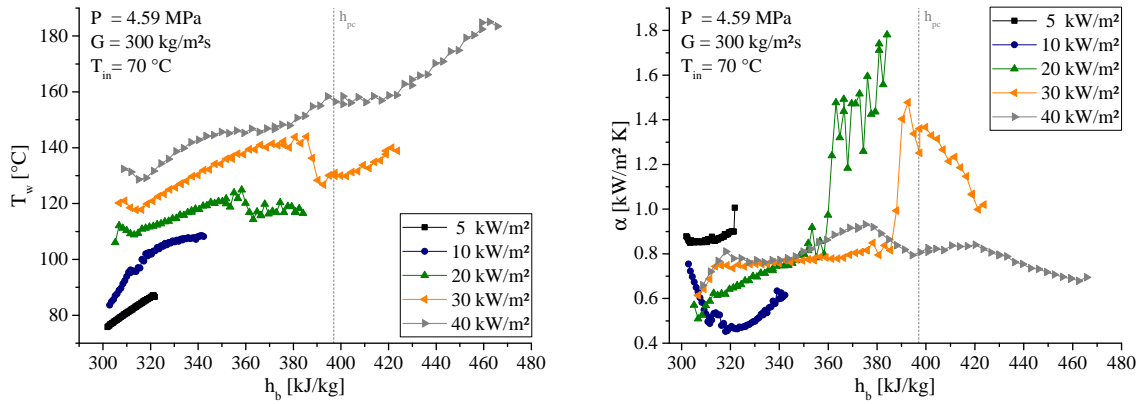
(a) Wall temperature trends for $300\,\text{kg/m}^2\text{s}$ at different heat fluxes

(b) Heat transfer coefficient trends for $300\,\text{kg/m}^2\text{s}$ at different heat fluxes
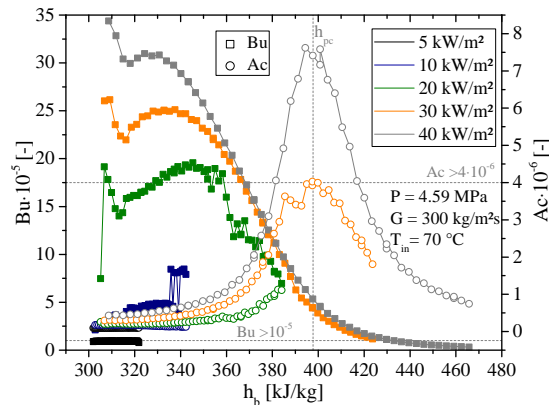
(c) Buoyancy and Acceleration number for $300\,\text{kg/m}^2\text{s}$ at different heat fluxes

Figure 5.1.: Wall temperature, heat transfer coefficient, Buoyancy and Acceleration number for $300\,\text{kg/m}^2\text{s}$ at different heat fluxes of ts-1 in R134a

Influence of pressure

The influence of pressure on the heat transfer is seen in figure 5.2. With increasing pressure, the HTC drops to smaller values. The sudden increase of the HTC at $20\,\text{kW/m}^2$ and $30\,\text{kW/m}^2$ is moved to lower bulk enthalpies, as seen exemplary in figure 5.2 (a). The pressure of 4.22 MPa is an exception and doesn't fit into the systematic trend. The reason for the postponed increase of the HTC at 4.22 MPa could be the higher and postponed decrease of the Buoyancy number at high bulk enthalpies and a higher Acceleration number as seen in 5.2 (b). Buoyancy number and Acceleration number increase with decreasing pressure due to the stronger variation of the fluid properties closer to the pseudo-critical pressure.

Influence of inlet temperature

The influence of the inlet temperatures at experiments with heat fluxes of $20\,\text{kW/m}^2$ and $30\,\text{kW/m}^2$ can be seen in figure 5.3. The sudden increase of the HTC at $20\,\text{kW/m}^2$ is postponed downstream and to higher bulk enthalpies for decreasing inlet temperatures. The increase does not occur at low inlet temperature. However, at $30\,\text{kW/m}^2$, the sudden increase of the HTC occurs more downstream and at higher bulk enthalpies with increasing inlet temperature, as seen in figure 5.3 (b). Here, the increase vanishes if the inlet temperature is too high. While conducting these experiments, it was observed that the location of the sudden increase is very sensible to small changes of the parameters. In some cases, the sudden increase changes to a local peak, as seen for the
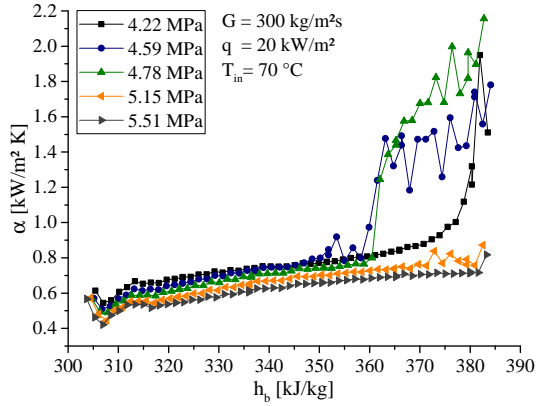
(a) Heat transfer coefficient trend at different pressures for $300\,\mathrm{kg/m^2s}$ at different pressures
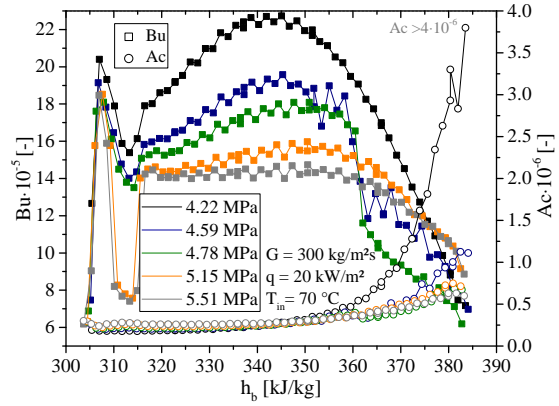
(b) Buoyancy and Acceleration number for $300\,\mathrm{kg/m^2s}$ at different pressures

Figure 5.2.: Heat transfer coefficient trends, Buoyancy and Acceleration number for $300\,\mathrm{kg/m^2s}$, $70\,°\mathrm{C}$ and heat flux of $20\,\mathrm{kW/m^2}$ at different pressures of ts-1 in R134a
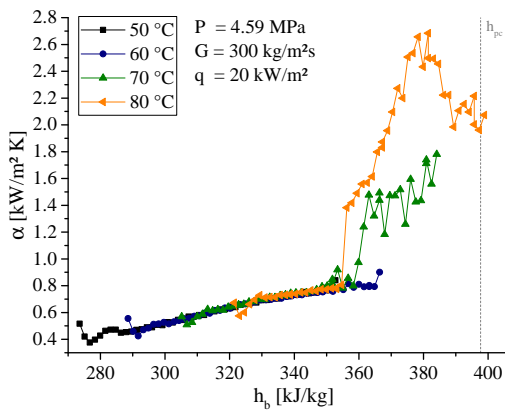
(a) Heat transfer coefficient trends for $300\,\mathrm{kg/m^2s}$ with $20\,\mathrm{kW/m^2}$ at different inlet temperatures
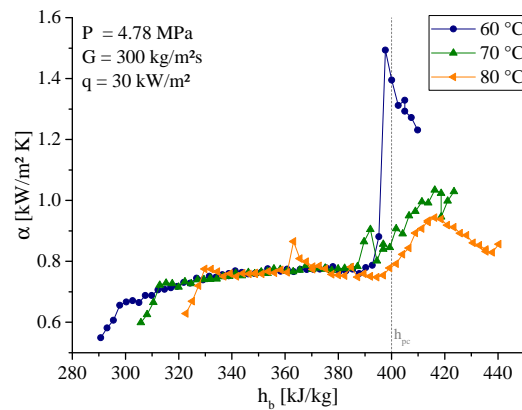
(b) Heat transfer coefficient trends for $300\,\mathrm{kg/m^2s}$ with $30\,\mathrm{kW/m^2}$ at different inlet temperatures
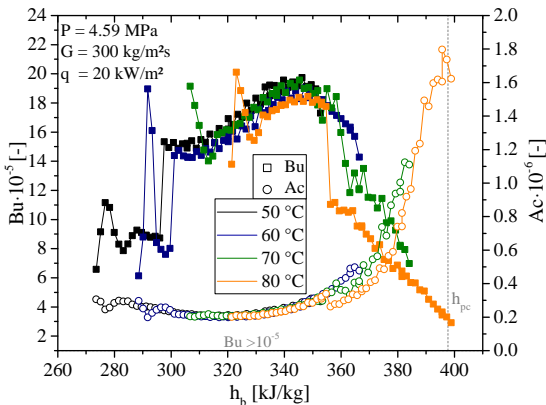
(c) Buoyancy and Acceleration number for $300\,\mathrm{kg/m^2s}$ with $20\,\mathrm{kW/m^2}$ at different inlet temperatures
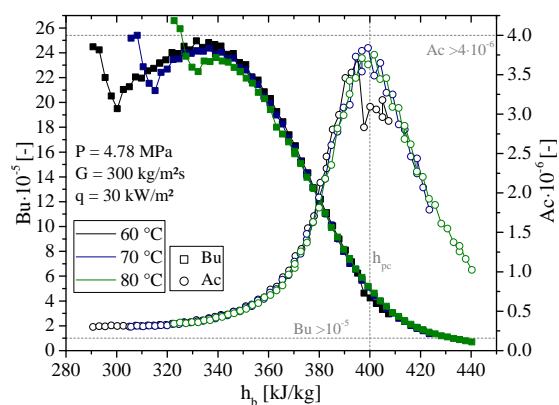
(d) Buoyancy and Acceleration number for $300\,\mathrm{kg/m^2s}$ with $30\,\mathrm{kW/m^2}$ at different inlet temperatures

Figure 5.3.: Heat transfer coefficient trends, Buoyancy and Acceleration number for $300\,\mathrm{kg/m^2s}$ at different inlet temperatures at heat flux of $20\,\mathrm{kW/m^2}$ and $30\,\mathrm{kW/m^2}$ of ts-1 in R134a

inlet temperatures of 70 °C and 80 °C in figure 5.3 (b). Comparing the Buoyancy and Acceleration number for the same cases in figure 5.3 (c) and (d), only a small deviation in the Acceleration number is recognizable. The Acceleration number at 20 kW/m^2 is smaller at 80 °C than at 70 °C in figure 5.3 (c). This results in a higher HTC at 80 °C in figure 5.3 (a). It seems that in this region the HTC is sensible to the Acceleration number. However, no systematic pattern for this change from a sudden increase to a local peak of the HTC near the pseudo-critical point can be found due to the fact that this appears at different pressures and inlet temperatures. This shows how sensible the heat transfer is near the pseudo-critical bulk enthalpy. Another explanation could be the idea of a multi-solution of the heat transfer at supercritical conditions as discussed in section 2.2.7.

5.1.2. Mass flux of 500 kg/m^{2}s

Influence of heat flux

At 500 kg/m^{2}s, a local sharp peak followed by a broad plateau appears in the wall temperature at high heat fluxes, as seen in figure 5.4 (a). The peaks move upstream and to lower bulk enthalpies as the heat flux increases. Additionally, the plateaus occupy a broader range of the bulk enthalpy, followed by a decrease of the wall temperature at higher bulk enthalpies. The figure 5.4 (b) shows the HTC trend for the same parameters as figure 5.4 (a). It can be seen that local peaks result from a decrease of the heat transfer coefficient.
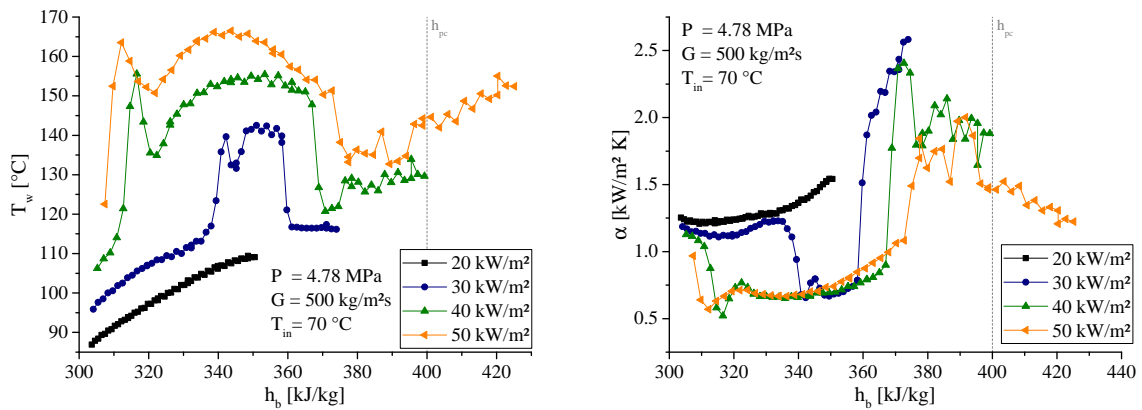
(a) Wall temperature trends for 500 kg/m^{2}s at different heat fluxes

(b) Heat transfer coefficient trends for 500 kg/m^{2}s at different heat fluxes
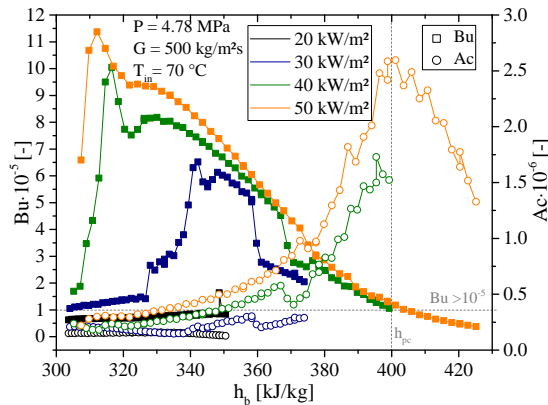
(c) Buoyancy and Acceleration number for 500 kg/m^{2}s at different heat fluxes

Figure 5.4.: Wall temperature, heat transfer coefficient trends, Buoyancy and Acceleration number for 500 kg/m^{2}s at different heat fluxes of ts-1 in R134a

The local wall temperature peaks can be explained with the Buoyancy number seen in figure 5.4 (c) in the same manner as discussed in section 5.1.1 for $300 \, \text{kg/m}^2\text{s}$. As the peaks occur, the Buoyancy number increases above the limit of 10^{-5}. The sharp increase of the HTC coincident with the sharp decrease of the Buoyancy number. The trend of the wall temperature is similar to the trend of the Buoyancy number. This shows the direct influence of buoyancy on heat transfer at these conditions.

Influence of pressure

The influence of pressure on the heat transfer is shown in figure 5.5 (a). It can be noticed that the local minimum of the HTC between the bulk enthalpies of $310 \, \text{kJ/kg}$ to $320 \, \text{kJ/kg}$ moves to higher bulk enthalpies and downstream for increasing pressures. The bulk enthalpy at which the sudden rise of the HTC occurs is reduced for smaller pressures. The Buoyancy and Acceleration number can be seen in figure 5.5 (b) for the same parameters. The Buoyancy number increases and decreases at higher bulk enthalpies for increasing pressure, which explains the trend for the HTC described before. The strong variations of the thermal-physical properties occur at the pseudo-critical point. This point is shifted to higher bulk enthalpies for higher pressures. Hence, the buoyancy effects occur at higher bulk enthalpies for higher pressures.

Figure 5.5 (b) further shows that the Acceleration number increases above the limit of 4×10^{-6} at $4.22 \, \text{MPa}$. This could explain the less pronounced increase of the HTC trend at $4.22 \, \text{MPa}$ in figure 5.5 (a) around $370 \, \text{kJ/kg}$ compared to the other pressures. This is due to the fact that the closer the pressure gets to the pseudo-critical value, the stronger the variations of the thermal-physical properties are.
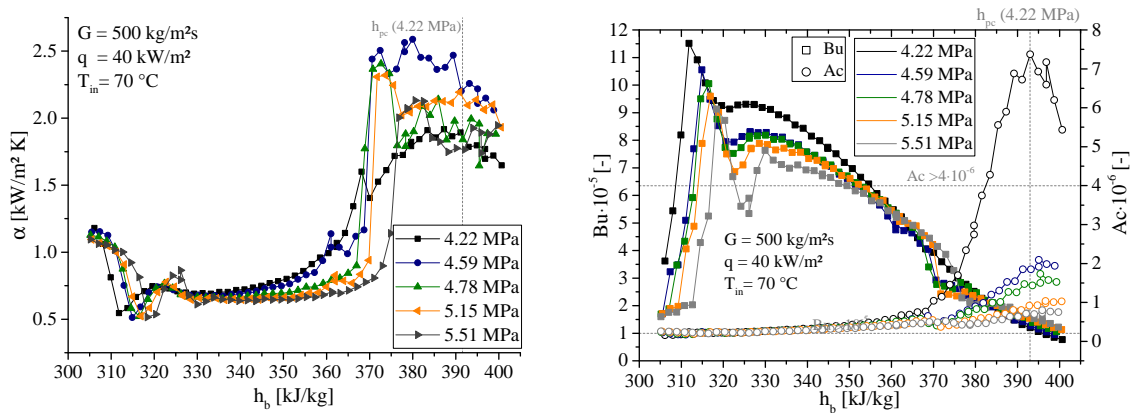
(a) Heat transfer coefficient trends at $500 \, \text{kg/m}^2\text{s}$ at different pressures

(b) Buoyancy and Acceleration number for $500 \, \text{kg/m}^2\text{s}$ at different pressures

Figure 5.5.: Heat transfer coefficient trends, Buoyancy and Acceleration number at $500 \, \text{kg/m}^2\text{s}$ at different pressures of ts-1 in R134a

Influence of inlet temperature

In figure 5.6 (a) the influence of the inlet temperature on the heat transfer coefficient is shown exemplarily at $4.78 \, \text{MPa}$ and $40 \, \text{kW/m}^2$. The first local minimum is moved to higher bulk enthalpies but further to the inlet with increasing inlet temperature, as additionally seen at in figure 5.10 (a). The HTC of different inlet temperatures merge together after the first peak. Even the sudden rise of the HTC is at the same bulk enthalpy. This is seen for all pressures and heat fluxes. The dependency of the location and bulk enthalpy of the minimum on the inlet temperature means that the buoyancy effect depends not only on the property change of the fluid itself but also on the development of the boundary layer. The layer is influenced by the inlet conditions as discussed in section 2.2.4.2. This means that the inlet conditions must be considered to predict the heat transfer at these conditions.

(a) Heat transfer coefficient trends at $500\,\text{kg/m}^2\text{s}$ at different inlet temperatures

(b) Buoyancy and Acceleration number for $500\,\text{kg/m}^2\text{s}$ at different inlet temperatures
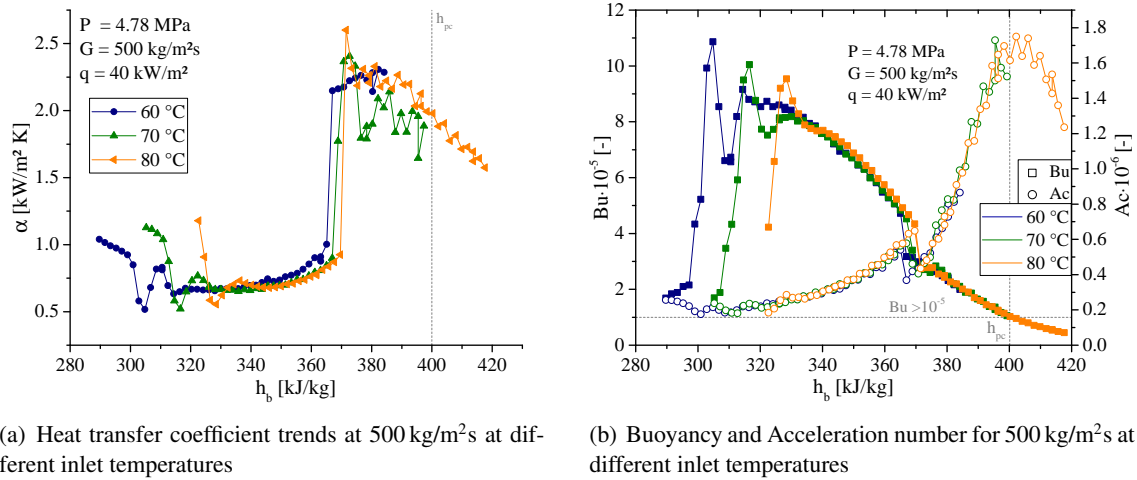
Figure 5.6.: Heat transfer coefficient trends, Buoyancy and Acceleration number at $500\,\text{kg/m}^2\text{s}$ at different inlet temperatures of ts-1 in R134a

Pressure or inlet temperature do not effect the minimum value of the HTC, which is $500\,\text{W/m}^2\text{K}$. This seems to be the absolute minimum which can be reached for the HTC at $500\,\text{kg/m}^2\text{s}$. Assuming a laminarization of the flow near the wall as discussed in section 2.2.2, only heat conduction can effectively transport the heat. Therefore, this limit of $500\,\text{W/m}^2\text{K}$ is defined by the heat conductivity of the coolant itself and the thickness of the laminarized layer.

5.1.3. Mass flux of $750\,\text{kg/m}^2\text{s}$

Influence of heat flux

Figure 5.7 shows the influence of the heat flux on wall temperature and HTC for $750\,\text{kg/m}^2\text{s}$. A sharp and growing wall temperature peak is formed if the heat flux increases. The peak is pushed to lower bulk enthalpies with increasing heat flux. This peak is caused by a local minimum in the HTC trend, where the HTC can drop nearly to $500\,\text{W/m}^2\text{K}$.

The local wall temperature peak can be explained with the Buoyancy number in figure 5.7 (c) as for the mass fluxes before. Compared to the mass fluxes of $300\,\text{kg/m}^2\text{s}$ and $500\,\text{kg/m}^2\text{s}$, the maximum Buoyancy number is smaller at $750\,\text{kg/m}^2\text{s}$ and decreases from $30\text{x}10^{-5}$ to $4\text{x}10^{-5}$. This is due to the definition of the Buoyancy number in equation 2.13, where the denominator is based on the Reynolds number. The Reynold number increases with increasing mass flux and the Buoyancy number is decreased therefore. Another consequence is that the Buoyancy trends vary with mass flux, which could also explain the different HTC trends at different mass fluxes. Nevertheless, the highest wall temperature peak occurs at $750\,\text{kg/m}^2\text{s}$. As discussed in section 5.1.2, the minimum HTC due to the laminarization caused by the buoyancy is around $500\,\text{W/m}^2\text{K}$. That minimum is reached at higher heat fluxes due to the higher mass flux. From equation 2.4 can be derived that a higher heat flux at constant HTC and bulk temperature results in a higher wall temperature. Because of that, the wall temperature peaks increase from $300\,\text{kg/m}^2\text{s}$ to $750\,\text{kg/m}^2\text{s}$.

Influence of pressure

Figure 5.8 (a) shows the influence of the pressure on the HTC at $60\,\text{kW/m}^2$. The local minimum moves downstream and to higher bulk enthalpies with increasing pressure. The minimum value is also weakened with increasing pressure. In all cases the HTC trends after the local minimum show the same manner, as seen in figure 5.8 (a), with ascending order from 4.22 MPa, 5.51 MPa, 5.15 MPa, 4.78 MPa, 4.59 MPa. The wall temperature peak occurs at lower heat fluxes for a decreasing pressure. The Buoyancy number for the same parameters can be seen in figure 5.8 (b). The reasons for the varying HTC trends due to the pressure are discussed in section 5.1.2.
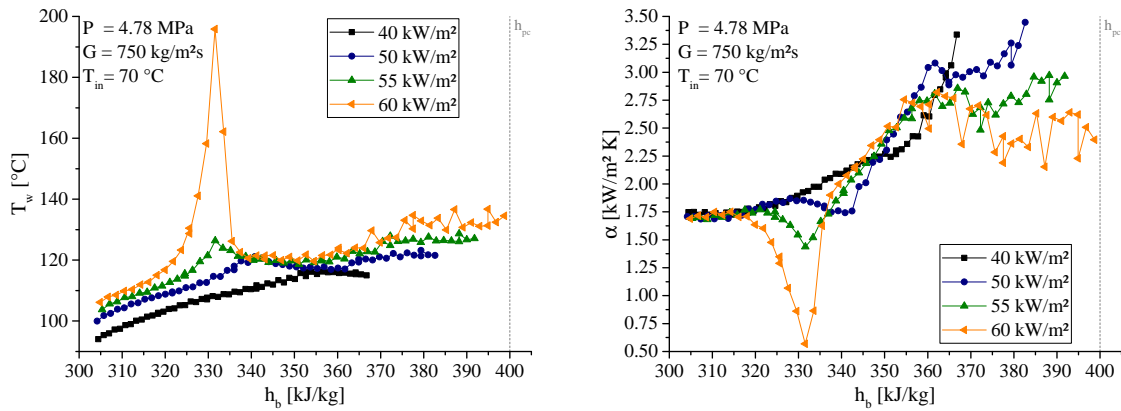
(a) Wall temperature trends for $750\,kg/m^2s$ at different heat fluxes

(b) Heat transfer coefficient trends for $750\,kg/m^2s$ at different heat fluxes
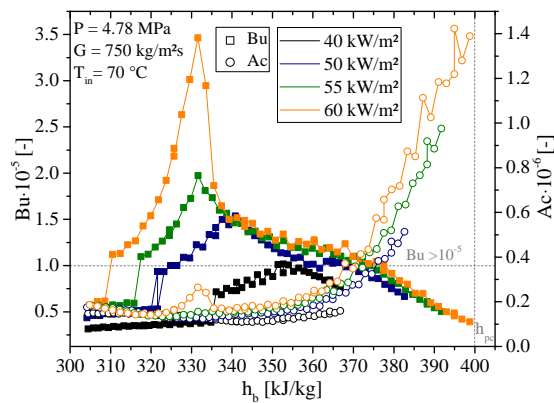
(c) Buoyancy and Acceleration number for $750\,kg/m^2s$ at different heat fluxes

Figure 5.7.: Wall temperature, heat transfer coefficient trends, Buoyancy and Acceleration number for $750\,kg/m^2s$ at different heat fluxes of ts-1 in R134a
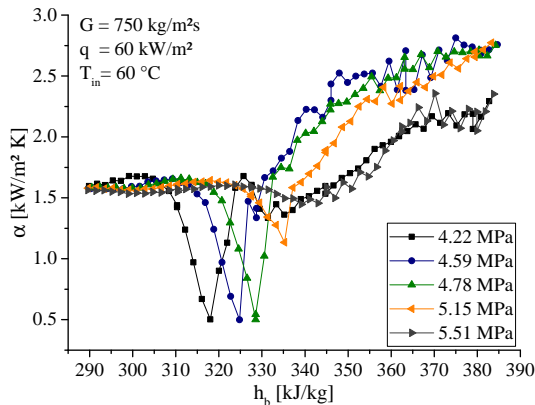
(a) Heat transfer coefficient trends for $750\,kg/m^2s$ at different pressures
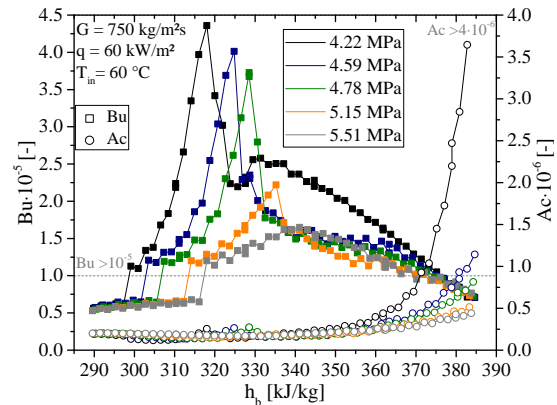
(b) Buoyancy and Acceleration number for $750\,kg/m^2s$ at different pressures

Figure 5.8.: Heat transfer coefficient trends, Buoyancy and Acceleration number for $750\,kg/m^2s$ at different pressures of ts-1 in R134a

Influence of inlet temperature

The influence of the inlet temperature is shown in figure 5.9 for a constant heat flux of $60 \, \text{kW/m}^2$. The local HTC minimum occurs nearly at the same bulk enthalpy and the value of the HTC at the minimum is nearly the same for all inlet temperatures. Only for the $50 \, ^\circ\text{C}$ the HTC is significantly higher. The small differences of the minimum location of $50 \, ^\circ\text{C}$, $60 \, ^\circ\text{C}$ and $70 \, ^\circ\text{C}$ can be explained with small variations of the mass flux, heat flux and pressure. The peak is postponed downstream if the inlet temperature is too high for the flow to develop, as seen for the HTC trend of $80 \, ^\circ\text{C}$. The trends of HTC of the different inlet temperature match well. At lower heat fluxes, the local minimum is less strong at lower inlet temperatures and vanishes sometimes, as shown in figure 5.7 . Also the Buoyancy numbers match well for different inlet temperatures, as shown in figure 5.9 (b).

(a) Heat transfer coefficient trends for $750 \, \text{kg/m}^2\text{s}$ at different inlet temperatures

(b) Buoyancy and Acceleration number for $750 \, \text{kg/m}^2\text{s}$ at different inlet temperatures
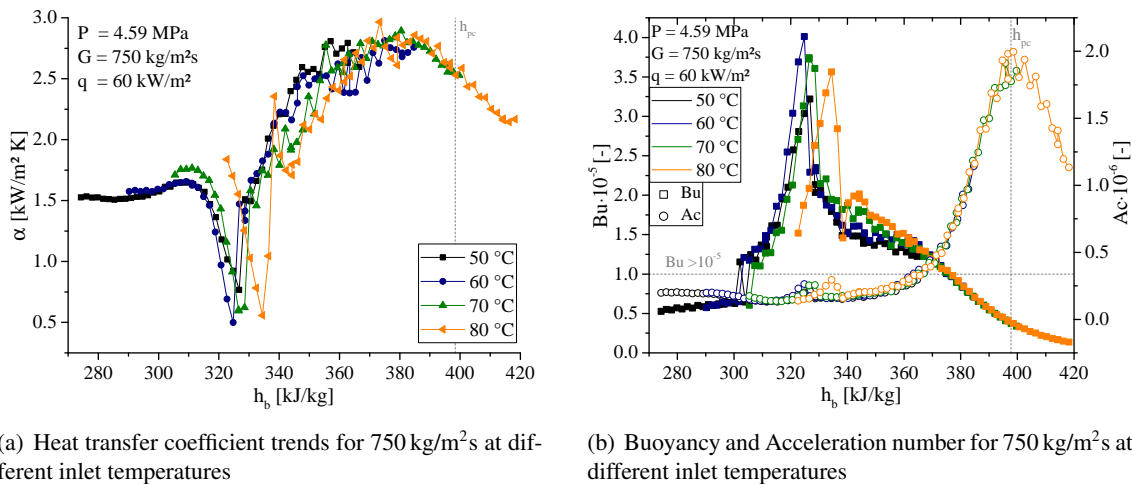
Figure 5.9.: Heat transfer coefficient trends, Buoyancy and Acceleration number for $750 \, \text{kg/m}^2\text{s}$ at different inlet temperatures of ts-1 in R134a

The location of the buoyancy induced minimum of the HTC mainly depends on the local conditions at the mass flux of $750 \, \text{kg/m}^2\text{s}$. The inlet conditions only effect the heat transfer in a short entrance length as the minimum occurs at the same bulk enthalpy. At $500 \, \text{kg/m}^2\text{s}$, the inlet conditions effect the heat transfer in a much longer entrance length, as seen in figure 5.10. Therefore, the HTC minimums occur at different bulk enthalpies at $500 \, \text{kg/m}^2\text{s}$. In the literature, it is concluded that extreme variations in physical properties may extend the thermal entrance region, as discussed in section 2.2.4.2. But in the literature it is not discussed that the thermal entrance region can be reduced and the location of the buoyancy induced minimum of the HTC is the same for different inlet temperatures. Therefore, no explanation in the literature can be found.

The observation, that the inlet effect depends on the mass flux, shows that the reason could be the increasing Reynolds number. It is increased from 33 000 at $500 \, \text{kg/m}^2\text{s}$ to 50 000 at $750 \, \text{kg/m}^2\text{s}$. Due to the increased turbulence at higher Reynolds numbers, the buoyancy force must be higher to laminarize the flow as discussed in section 2.2.2.2. The buoyancy depends on the density difference of the fluid caused by temperature differences. The temperature difference between the bulk and wall is reduced due to the increased heat transfer coefficient caused by the higher Reynold number. Therefore, the density difference due to the temperature difference of the wall to the bulk temperature at the inlet can be high enough to laminarize the flow at low mass fluxes. At $300 \, \text{kg/m}^2\text{s}$, this can occur directly at the inlet, as seen in figure 5.1. In this case, the difference between the wall temperature and the inlet temperature is high enough for the laminarization. At $500 \, \text{kg/m}^2\text{s}$ and $40 \, \text{kW/m}^2$, the difference between the wall temperature and the inlet temperature is also high enough. Caused by the development of the thermal boundary layer, the laminarization occurs downstream of the inlet. A higher density difference is needed at higher mass fluxes. The
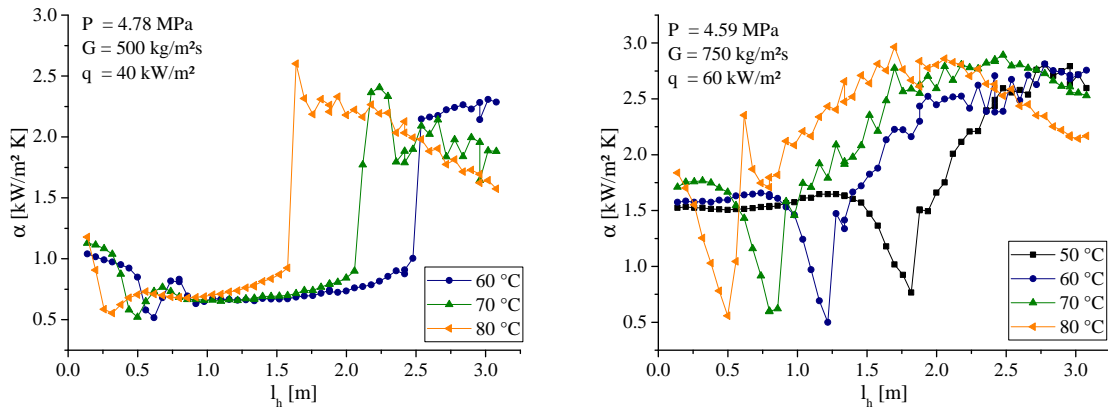
(a) Heat transfer coefficient trends for $500\,kg/m^2s$ at different inlet temperatures over heated length

(b) Heat transfer coefficient trends for $750\,kg/m^2s$ at different inlet temperatures over heated length

Figure 5.10.: Heat transfer coefficient trends for $500\,kg/m^2s$ and $750\,kg/m^2s$ at different inlet temperatures over heated length of ts-1 in R134a

density decreases stronger as the temperature approaches the pseudo-critical point. Depending on the mass flux and heat flux, the critical density difference to laminarize the flow is reached at higher bulk enthalpies. Therefore, the inlet conditions can only effect the buoyancy induced HTC minimum when the inlet temperature is above the critical bulk temperature at which the laminarization occurs, as exemplarily shown for $750\,kg/m^2s$ in figure 5.9 (a).

The idea of the critical density difference and the development of the thermal boundary layer, as discussed in the paragraph before, explains why the buoyancy induced HTC minimums occur at different bulk enthalpies for different inlet temperatures. Additionally, the idea can also explain why the HTC minimum moves to the inlet for increasing inlet temperatures. This is because the critical density difference between the wall and the bulk is reached faster if the inlet temperature is higher due to the stronger variations of the density close to the pseudo-critical point.

5.1.4. Mass flux of $1000\,kg/m^2s$

Influence of heat flux

The wall temperature and HTC trends for different heat fluxes at mass fluxes of $1000\,kg/m^2s$ are shown in figure 5.11. A local peak in the wall temperature at low bulk enthalpies is noticeable. This peak grows in height and width and moves to smaller bulk enthalpies with increasing heat flux. This is also noticeable as local minimum in the HTC trend in figure 5.11 (b). Additionally, it is shown that the HTC is reduced for increasing heat fluxes over the whole test section. It is reduced from a monotonically increasing trend to a trend with a maximum before the bulk temperature reaches the pseudo-critical value.

Figure 5.11 (c) shows the corresponding Buoyancy and Acceleration number. It can be seen that both numbers increase with increasing heat flux. For both numbers the limit is overpassed which means, as discussed in previous sections, that the heat transfer is reduced due to the increasing influence of buoyancy and flow acceleration. Contrary to small mass fluxes, the heat transfer along the whole test section can be influenced strongly as either the buoyancy or the acceleration limit is exceeded.

The HTC trends of different heat fluxes match well at low heat fluxes, as seen for $50\,kW/m^2$ and $60\,kW/m^2$ in figure 5.11 (b). At $70\,kW/m^2$, the HTC start to decrease locally around $340\,kJ/kg$ and again as the bulk enthalpy approaches the pseudo-critical point. In figure 5.11 (c) can be seen that the Buoyancy number exceeds only $0.4x10^{-5}$ at $340\,kJ/kg$. Although it does not exceed the

(a) Wall temperature trends for 1000 kg/m²s at different heat fluxes

(b) Heat transfer coefficient trends for 1000 kg/m²s at different heat fluxes

(c) Buoyancy and Acceleration number for 1000 kg/m²s at different heat fluxes
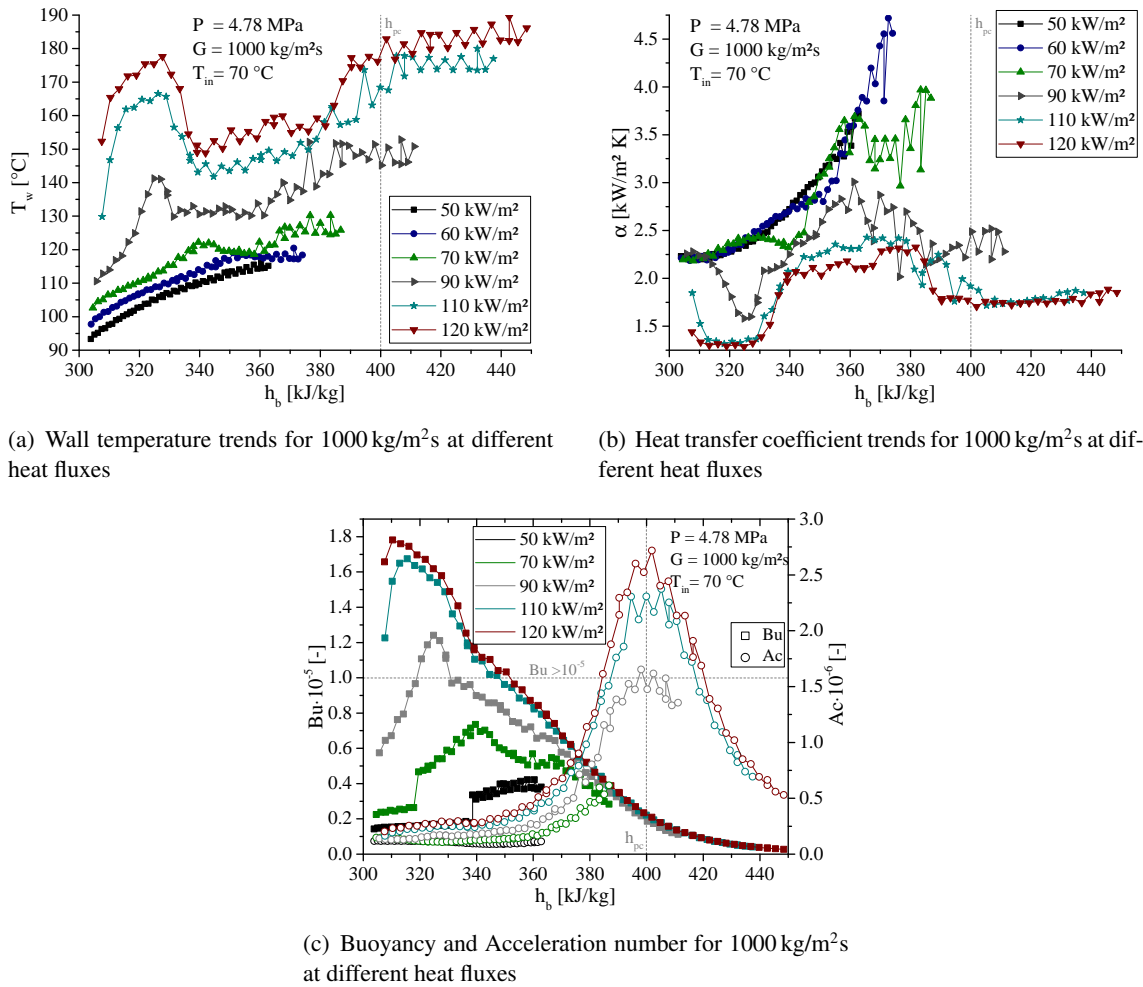
Figure 5.11.: Wall temperature, heat transfer coefficient trends, Buoyancy and Acceleration number for 1000 kg/m²s at different heat fluxes of ts-1 in R134a

limit of Jackson, the buoyancy seems start to effect the heat transfer. The Acceleration number exceeds 0.25×10^{-6} at 360 kJ/kg. As the Acceleration number increases for higher heat fluxes, the HTC trends decreases more and more. Therefore, it must be assumed that the acceleration starts to effect the heat transfer at an Acceleration number of 0.25×10^{-6}.

Another phenomena, which is conspicuous in figure 5.11, is the amplified zig-zag of the wall temperature and HTC. The reason for the zig-zag is discussed and a method is implemented to accommodate this phenomenon for the calculations of the HTC in section 3.5. This method smoothed the zig-zag at subcritical conditions very well but at certain supercritical conditions, the zig-zag appears to strengthen again. This shows that the HTC here is sensible to the heat flux itself. The zig-zag gets stronger as the bulk enthalpy reaches the pseudo-critical value. In this region the HTC decreases strongly for increasing heat flux. At a certain heat flux, a minimum HTC is reached and the zig-zag disappears again. This can be seen for the heat flux of 110 kW/m² and 120 kW/m² in figure 5.11 (b). The Acceleration number has its maximum at the pseudo-critical bulk enthalpy and depends directly on the heat flux. It shows the same zig-zag trend in figure 5.13 (a) and could explain the HTC zig-zag due to its strong influence on the heat transfer at this point. There is a range of the Acceleration number where the zig-zag occurs. This is between 0.25×10^{-6} and 2×10^{-6}. This confirms the assumption that the heat transfer is influenced by acceleration effects at the Acceleration number of 0.25×10^{-6}.

The fact that no zig-zag is observed at the buoyancy induce HTC minimums near the inlet shows that the HTC here is not highly sensible to the heat flux. The heat transfer depends mainly on the flow conditions. This can be also seen at low mass fluxes in figures 5.1, 5.4 and 5.7 at the smooth trends of the HTC despite the high Buoyancy number.

Influence of pressure

The influence of pressure depends on the given heat flux, as seen in figure 5.12. The HTC trend is monotonically increasing up to $70\,kW/m^2$ as at subcritical conditions. An increase of pressure declines the HTC slope, as seen for pressures of $4.59 - 5.51\,MPa$ in figure 5.12 (a). At $70\,kW/m^2$, the buoyancy force starts to effect the heat transfer trend of $4.22\,MPa$, which shows the lowest HTC by forming the local minimum first. All trends show the minimum of the HTC near the inlet at $100\,kW/m^2$. The minimum is moved to lower bulk enthalpies with decreasing pressure. The width is independent of pressure, but the minimum value is smaller for smaller pressures. No tendency for the HTC on pressure is obvious after the heat transfer recovered from the minimum. As for the mass fluxes before, the HTC trend can be explained by the Buoyancy and Acceleration number, which are shown in figure 5.12 (c) and (d). The HTC trend forms the local minimum for $4.22\,MPa$ exactly as the Buoyancy number exceeds the limit of 10^{-5}. Also the low HTC for $4.22\,MPa$ and $100\,kW/m^2$ at high bulk enthalpies can be explained with the high Acceleration number. The increasing Buoyancy and Acceleration number are caused by the stronger variations of the fluid properties at low pressures as discussed before.
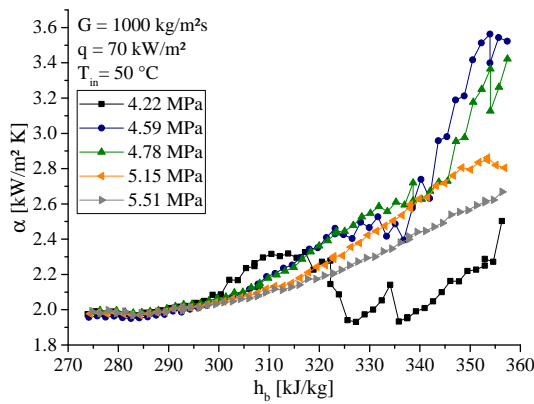
(a) Heat transfer coefficient trends for $70\,kW/m^2$
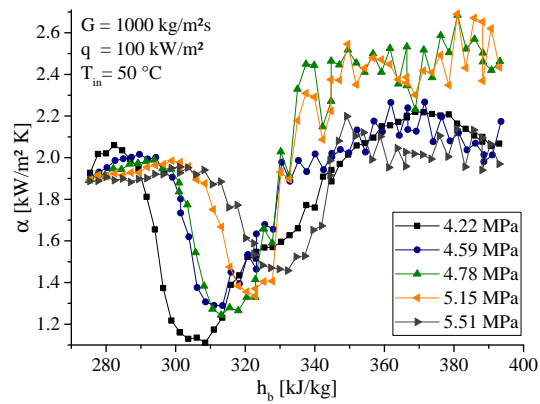
(b) Heat transfer coefficient trends for $100\,kW/m^2$
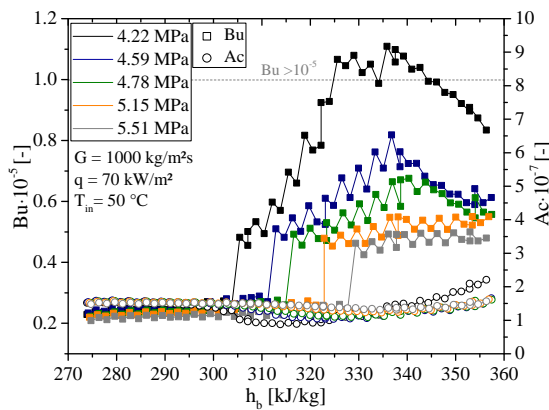
(c) Buoyancy and Acceleration number for $70\,kW/m^2$
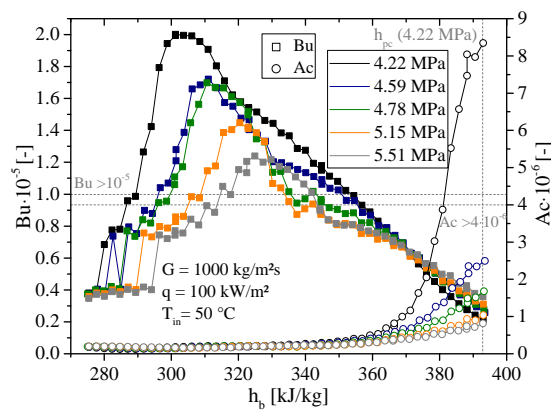
(d) Buoyancy and Acceleration number for $100\,kW/m^2$

Figure 5.12.: Heat transfer trends, Buoyancy and Acceleration number for $1000\,kg/m^2s$ at different pressures for heat fluxes of $70\,kW/m^2$ and $100\,kW/m^2$ of ts-1 in R134a

Influence of inlet temperature

The influence of the inlet temperature on the HTC trend is shown in figure 5.13 (a). The minimum of the HTC forms near the inlet and at enthalpies around 315 kJ/kg for all inlet temperatures. The minimum at 70 °C is in all cases less strong and slightly downstream. All trends overlap each other starting from the minimum. A HTC maximum is formed for all measurements near the pseudo-critical bulk temperature, even for 80 °C, which starts after the minimum. Figure 5.13 (b) shows that the Buoyancy and Acceleration number are the same for all inlet temperatures.
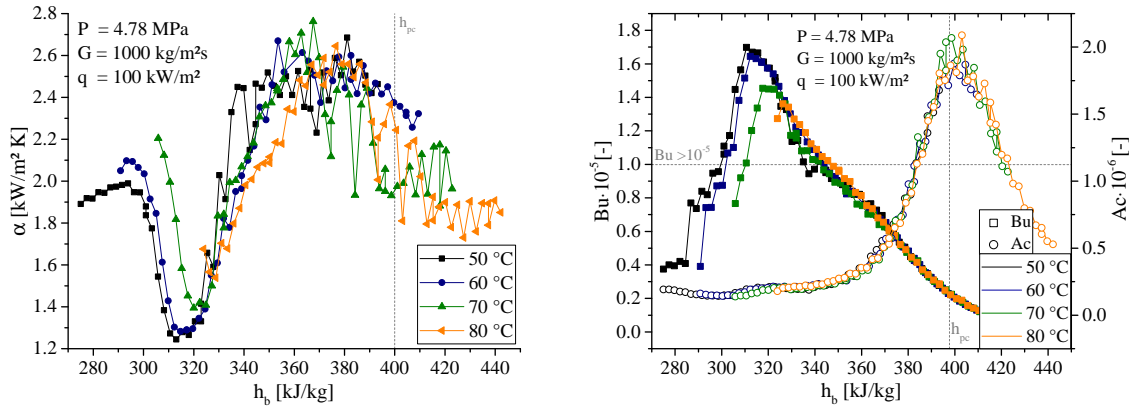
(a) Heat transfer coefficient trends for 1000 kg/m²s at different inlet temperatures

(b) Buoyancy and Acceleration number for 1000 kg/m²s at different inlet temperatures

Figure 5.13.: Heat transfer coefficient trends, Buoyancy and Acceleration number for 1000 kg/m²s at different inlet temperatures of ts-1 in R134a

5.1.5. Mass flux of 1500 kg/m²s

Influence of heat flux

Figure 5.14 shows the influence of the heat flux on wall temperature and HTC at mass fluxes of 1500 kg/m²s. With increasing heat flux, a small peak is formed in the wall temperature. It changes to a steep incline moving towards the inlet followed by a flat part, as seen in figure 5.14 (a). As the heat flux reaches 150 kW/m², a second peak is formed at the flat part before the pseudo-critical bulk enthalpy. This peak occurs at lower heat fluxes for lower pressure or higher inlet temperatures.

The HTC trend is influenced by the heat flux in the same manner as the trends at 1000 kg/m²s, as noticeable in figure 5.14 (b). The HTC change from a monotonically increasing trend to a curve with a maximum before the pseudo-critical bulk enthalpy. The maximum is flattened by increasing the heat flux further. The minimum at the inlet is less distinct as at 1000 kg/m²s. Additionally, a second minimum is formed before the pseudo-critical bulk enthalpy at high heat fluxes. It can be easily seen in figure 5.14 (b) that the zig-zag of the HTC increases near the pseudo-critical bulk enthalpy. This means that the heat transfer is very sensible to the heat flux at these conditions, as discussed in section 5.1.4.

Figure 5.14 (c) shows the Buoyancy and Acceleration number for the same parameters. Neither the Buoyancy nor the Acceleration number exceed their limits. Nevertheless, two minimums in the HTC trend occur. The first one near the inlet is most probably caused by buoyancy forces and occurs as the Buoyancy number exceeds 0.2×10^{-5}. From this it must be assumed that the buoyancy starts to effect the heat transfer at $Bu > 0.2 \times 10^{-5}$. Jackson determined his limits by screening his data for wall temperature peaks. However, as seen in figure 5.11, before a wall temperature peak is formed, a local HTC minimum occurs, which is caused by buoyancy effects.

The second minimum is caused by a combination of buoyancy and acceleration because both numbers are high but not above the limits of Jackson, as seen at 375 kJ/kg in figure 5.14 (c).

(a) Wall temperature trends for $1500\,kg/m^2s$ at different heat fluxes

(b) Heat transfer coefficient trends for $1500\,kg/m^2s$ at different heat fluxes

(c) Buoyancy and Acceleration number for $1500\,kg/m^2s$ at different heat fluxes
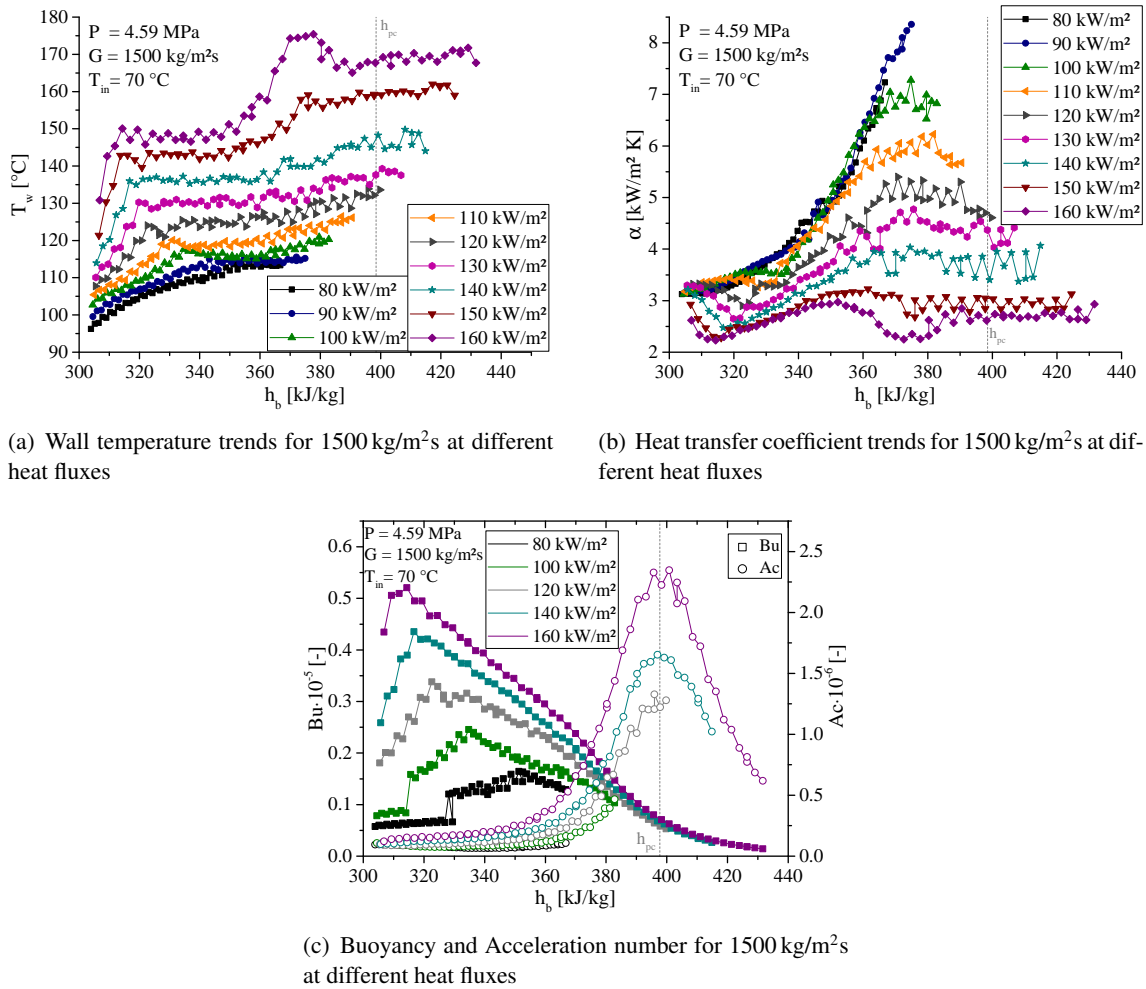
Figure 5.14.: Wall temperature, heat transfer coefficient, Buoyancy and Acceleration number for $1500\,kg/m^2s$ at different heat fluxes of ts-1 in R134a

No second minimum occurs at low mass fluxes, the acceleration effect only decreases the HTC trend as a whole around the pseudo-critical point. The Buoyancy and the Acceleration number at $500\,kg/m^2s$ and $50\,kW/m^2$ in figure 5.4 (c) at $375\,kJ/kg$ has a higher Buoyancy number and the same Acceleration number as in figure 5.14 (c) for $1500\,kg/m^2s$ and $160\,kW/m^2$. Nevertheless, no minimum occurs at $500\,kg/m^2s$, instead the HTC is increases, as seen in figure 5.4 (b). This means either the heat transfer is more sensible to heat flux because the heat flux is with $160\,kW/m^2$ much higher at $1500\,kg/m^2s$ or the heat transfer is more sensible to buoyancy forces at high mass fluxes.

As seen before, the HTC starts to decrease as the Acceleration number exceeds $0.25x10^{-6}$ for $100\,kW/m^2$ in figure 5.14 (b) and (c). Also the zig-zag in the HTC trend occurs for Acceleration number between $0.25x10^{-6}$ and $2x10^{-6}$. As discussed before, this is due to the high sensibility of the heat transfer on the acceleration effects.

Influence of pressure

The influence of the pressure on the HTC is similar to the one of $1000\,kg/m^2s$. The highest HTC is at $4.22\,MPa$ with decreasing order of the pressure at low heat fluxes. With increasing heat flux, the HTC of $4.22\,MPa$ drops first and forms first the minimum at the inlet. The minimum value is increasing for increasing pressure. However, the minimum gets broader with higher pressures. Additionally, the second minimum in the HTC trend occurs only at pressures of $4.59\,MPa$ or smaller. The minimum value gets lower for decreasing pressure and occur at lower bulk enthalpies, as seen in figure 5.15 (a).

Figure 5.15 (b) shows that the limit of 10^{-5} is not exceeded by the Buoyancy number although a minimum occurs in the HTC trend. The second minimum at 4.22 MPa occurs at 350 kJ/kg, but no obvious increase of the Buoyancy or the Acceleration number can be seen. Nevertheless, the zig-zag in the wall temperature in figure 5.15 (a) occurs for Acceleration numbers between 0.25×10^{-6} and 2×10^{-6}, as discussed before.
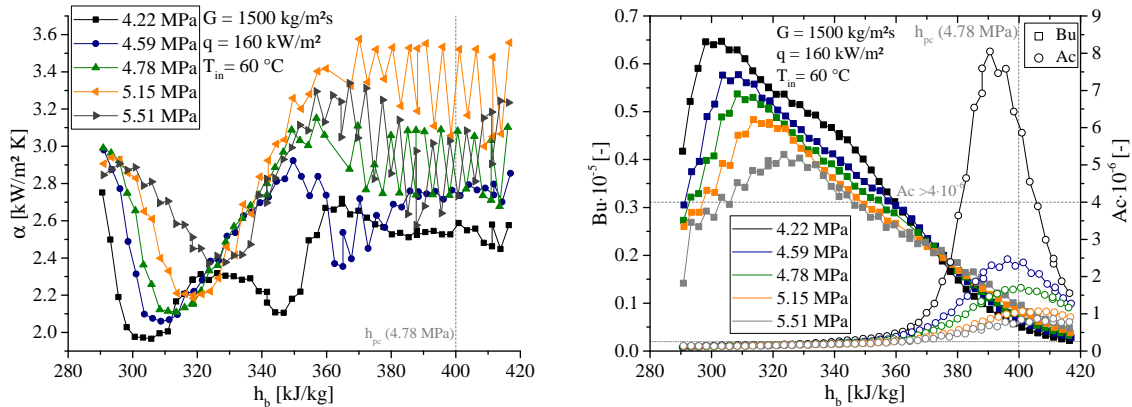
(a) Heat transfer coefficient trend for 1500 kg/m²s at different pressures

(b) Buoyancy and Acceleration number for 1500 kg/m²s at different pressures

Figure 5.15.: Heat transfer coefficient trend, Buoyancy and Acceleration number for 1500 kg/m²s at different pressures of ts-1 in R134a

Influence of inlet temperature

The influence of the inlet temperature on the HTC is shown in figure 5.16 for 130 kW/m² and 160 kW/m². The trends for all inlet temperatures match very well until 130 kW/m². Actually, magnitude and location of the HTC minimum at the bulk enthalpy of 320 kJ/kg are equal for every inlet temperature. The HTC differ in the region after 350 kJ/kg with no obvious tendency at higher heat fluxes, as shown in figure 5.16 (b). At high inlet temperatures and heat fluxes, a small inlet effect can be noticed as the local minimum is shifted upstream. The HTC trend deviates for 24 times of tube diameter in figure 5.16 (b) starting from 70 °C. The inlet effect is reduced for increasing inlet temperature and the HTC trends match earlier.

Figure 5.16 (c) and (d) show the Buoyancy and Acceleration number for the heat fluxes of 130 kW/m² and 160 kW/m². The small inlet effect can be noticed in the Buoyancy number. The small differences of the Acceleration number could explain the differences of the HTC after 350 kJ/kg. Here, the Acceleration number is between 0.25×10^{-6} and 2×10^{-6} where the HTC varies strongly with heat flux.

5.1.6. Mass flux of 2000 kg/m²s

Influence of heat flux

The HTC trends with 2000 kg/m²s are similar to the HTC trends of 1500 kg/m²s. This can be seen in figure 5.17 where the influence of the heat flux is similar to the one of figure 5.14. Due to the higher mass flux, the heat transfer coefficients are higher at 2000 kg/m²s with resulting lower wall temperatures. The influence of pressure and inlet temperature are the same and hence not shown. Compared with 1500 kg/m²s the second peak before the pseudo-critical bulk enthalpy occurs only at 4.22 MPa.

In figure 5.17 (c) can be seen that neither the Buoyancy nor the Acceleration number exceed the limits of Jackson. Nevertheless, a reduction of the HTC trend is noticeable in figure 5.17 (b).
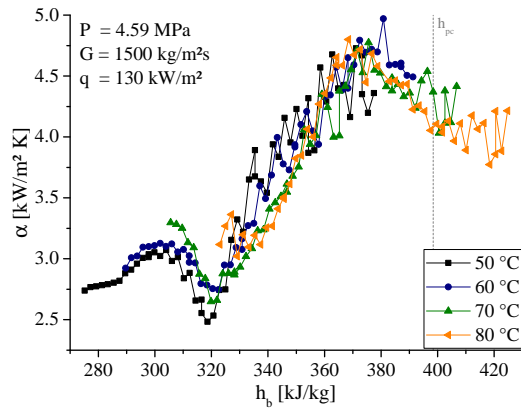
(a) Heat transfer coefficient trends for $1500\,\mathrm{kg/m^2s}$ and $130\,\mathrm{kW/m^2}$ at different inlet temperatures
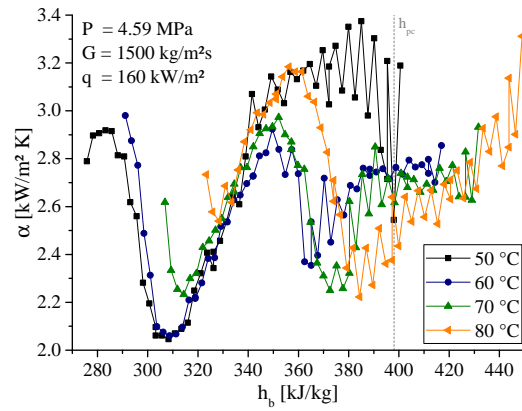
(b) Heat transfer coefficient trends for $1500\,\mathrm{kg/m^2s}$ and $160\,\mathrm{kW/m^2}$ at different inlet temperatures
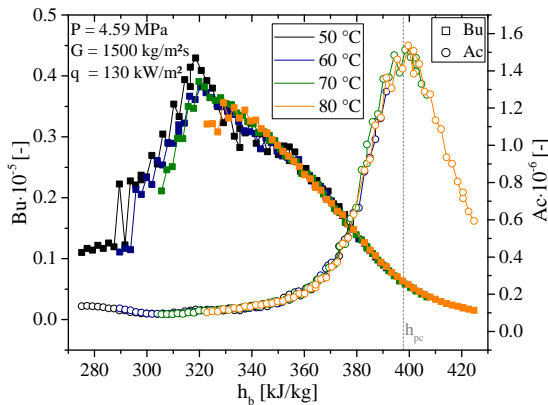
(c) Buoyancy and Acceleration number for $1500\,\mathrm{kg/m^2s}$ and $130\,\mathrm{kW/m^2}$ at different inlet temperatures
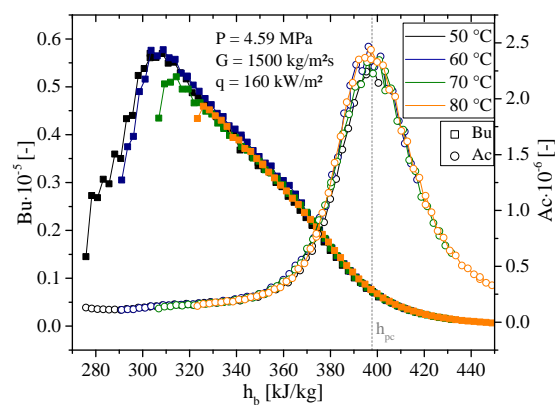
(d) Buoyancy and Acceleration number for $1500\,\mathrm{kg/m^2s}$ and $160\,\mathrm{kW/m^2}$ at different inlet temperatures

Figure 5.16.: Heat transfer coefficient trends, Buoyancy and Acceleration number for $1500\,\mathrm{kg/m^2s}$ at $130\,\mathrm{kW/m^2}$ and $160\,\mathrm{kW/m^2}$ at different inlet temperatures of ts-1 in R134a

The HTC trend of $120\,\mathrm{kW/m^2}$ starts to decrease from the merging trends at low heat fluxes as the Acceleration number exceeds $0.25\mathrm{x}10^{-6}$, as observed at lower mass fluxes. Also the zig-zag in the HTC trend starts to occur at this point.

5.1.7. Influence of mass flux

The HTC trends for the single mass fluxes are discussed in the previous sections. Overall, the HTC increases from about $1\,\mathrm{kW/m^2K}$ at $300\,\mathrm{kg/m^2s}$ to about $6\,\mathrm{kW/m^2K}$ at $2000\,\mathrm{kg/m^2s}$. This is due to the increasing Reynolds number, which is an indicator for higher turbulence causing an increase of the heat transfer. Further, the mass flux dominates the qualitative behavior of the HTC trend as it influences the buoyancy and acceleration. This results in different phenomena in the thermal and near wall layer and causes different heat transfer trends, as observed in this study. The heat transfer is determined by buoyancy forces at low mass fluxes. As the mass flux increases, the major influence shifts to the thermally-induced bulk flow acceleration. This confirms the findings by Kurganov et al., who classified the heat transfer trends in six different groups according to their wall temperature trend appearance using a derivation of the Archimedes number. The correlation between the qualitative behavior of the wall temperature and the inlet velocity shown by Kurganov et al. coincide with the ones shown in this study.
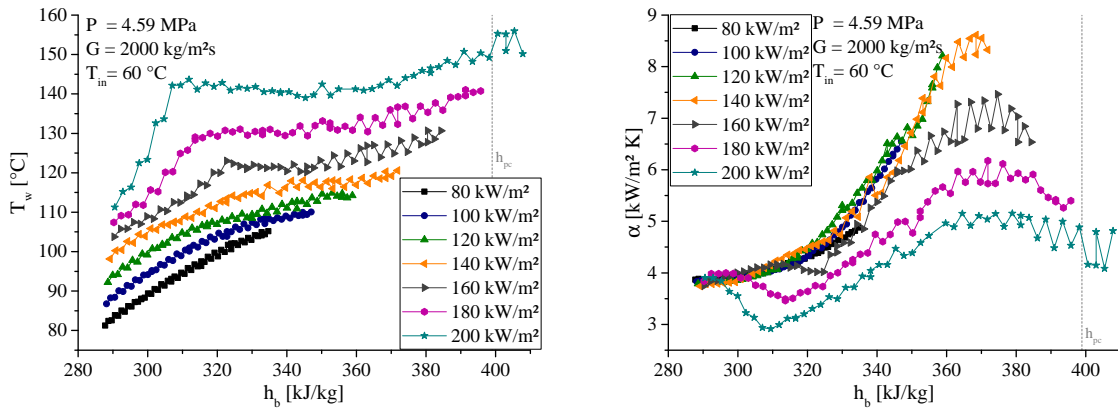
(a) Wall temperature trends for $2000\,kg/m^2s$ at different heat fluxes

(b) Heat transfer coefficient trends for $2000\,kg/m^2s$ at different heat fluxes
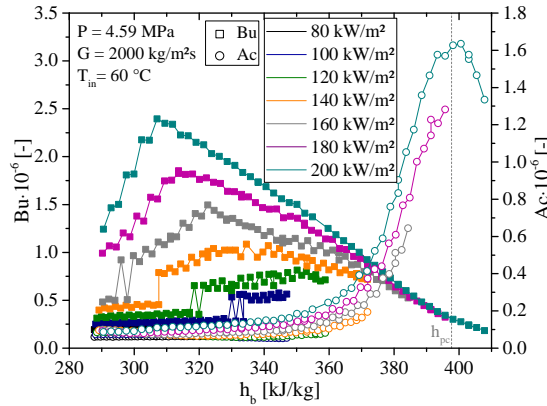
(c) Buoyancy and Acceleration number for $2000\,kg/m^2s$ at different heat fluxes

Figure 5.17.: Wall temperature, heat transfer coefficient trends, Buoyancy and Acceleration number for $2000\,kg/m^2s$ at different heat fluxes of ts-1 in R134a

5.1.8. Mass flux of $300\,kg/m^2s$ at subcritical conditions

It is proposed in the literature that the phenomena discussed in the previous sections are normally restricted to supercritical conditions. However, wall temperature peaks can also occur at subcritical conditions, as seen in figure 5.18 (a). The peaks are below the boiling point of $97.8\,°C$ at $3.8\,MPa$. The wall temperature peaks are also caused by an decreased heat transfer due to the buoyancy forces as seen in the Buoyancy number in figure 5.18 (b). This was also found by Jackson et al. [Jackson et al., 1989] who interpreted the experimental results of Fewster [Fewster, 1976] and Kenning et al. [Kenning et al., 1973].

This shows that the general case of heat transfer is the mixed convection as defined in section 2.2. The heat transfer at pure forced convection, as known of subcritical conditions, is a special case of that. It is characterized by negligible influence of buoyancy and acceleration effects due to almost constant fluid properties. This finding supports the assumption of section 4.1 that the heat transfer at supercritical conditions must be treated as one regime with varying influences of buoyancy and acceleration.

5.1.9. Summary of experiments of ts-1

In this section, the results of the experiments of ts-1 separated in the influences of heat flux, pressure and inlet temperature are shown and discussed for every mass flux, respectively. It was
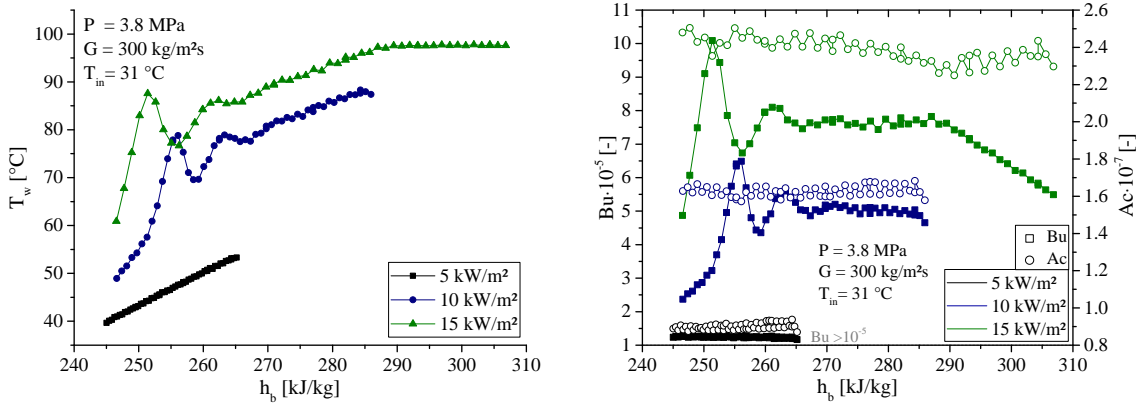
(a) Wall temperature trends for 300 kg/m²s at different heat fluxes at 3.8 MPa

(b) Buoyancy and Acceleration number for 300 kg/m²s at different heat fluxes at 3.8 MPa

Figure 5.18.: Wall temperature, Buoyancy and Acceleration number for 300 kg/m²s at different heat fluxes at subcritical pressure of 3.8 MPa of ts-1 in R134a

found that the heat is transfered by mixed convection at supercritical conditions. The buoyancy and the thermally induced bulk flow acceleration have a decisive influence on heat transfer at high heat fluxes. The influences are dominated by the mass flux as seen at the different qualitative behaviors of the wall temperatures. Heat flux, pressure and inlet temperatures can have a strong influence on buoyancy and acceleration and thereby on the heat transfer. The influences of every parameter are summarized in detail in section 5.5 at the end of this chapter.

5.2. Results and discussion of heat transfer experiments of ts-2

With the ts-2 of the SCOUL, the influence of mass flux, heat flux and inlet temperature was investigated on the HTC at 7.69 MPa in CO_2 which is equivalent to 4.22 MPa in R134a. The phenomena are similar to the one observed in R134a but shifted to lower mass fluxes. This can be seen in the typical wall temperature trends for each mass flux of CO_2 in figure 5.19.
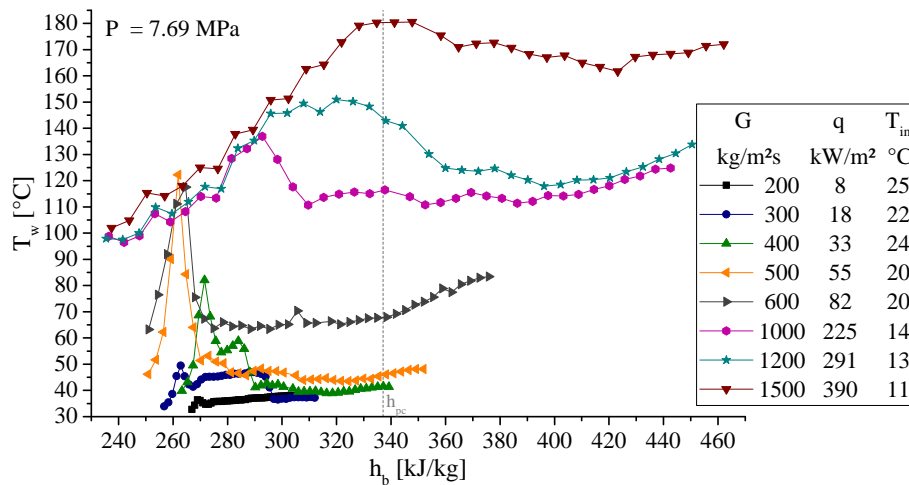
Figure 5.19.: Typical wall temperature trends for different mass flux a heat flux combinations at 7.69 MPa of the CO_2 experiments at ts-2

The mass flux of 200 kg/m²s in CO_2 has a similar shape in wall temperature as 300 kg/m²s in R134a. Same trends are noticeable for 300 kg/m²s and 500 kg/m²s, 500 kg/m²s and 750 kg/m²s, 1000 kg/m²s and 1200 kg/m²s, 1500 kg/m²s and 2000 kg/m²s in CO_2 and R134a, respectively.

The trends seen in figure 5.19 are similar to the qualitative wall temperature trends described by Kurganov et al. in figure 2.7. It can be seen that the groups defined by Kurganov et al. can be found in figure 5.19 determined by the mass flux.

The influence of mass flux, heat flux, inlet temperature, the Buoyancy and Acceleration number on the heat transfer, as discussed in section 5.1 for R134a of ts-1, are the same for CO_2 at ts-2 and is therefore not discussed. Because of the lower temperatures of the critical point of CO_2 and its higher temperature of chemical stability, higher heat fluxes can be conducted with CO_2 compared to R134a.

Figure 5.20 shows the influence of the heat flux on the HTC for the mass fluxes of $300\,kg/m^2s$ and $500\,kg/m^2s$. The trends are similar to the trends of $500\,kg/m^2s$ and $750\,kg/m^2s$ in R134a. All cases show a minimum at low bulk enthalpies and near the pseudo-critical bulk enthalpy. In general, the HTC decreases for increasing heat flux. The Buoyancy and Acceleration number are also shown in figure 5.20 and increase for increasing heat flux. The value of the buoyancy induced minimum of the HTC at the bulk enthalpy of $220\,kJ/kg$ stays constant at $700\,W/m^2K$. As discussed in 5.1.2, this is determined by the thermal conductivity of the coolant due to the laminarization of the flow. The HTC trends at the pseudo-critical point show no minimum but decrease totally to a flat curve.
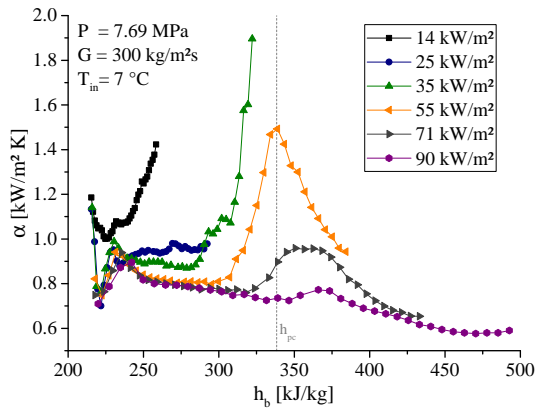
(a) Heat transfer coefficient trends for $300\,kg/m^2s$
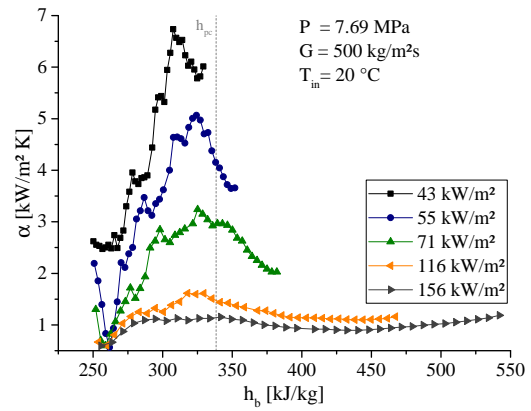
(b) Heat transfer coefficient trends for $500\,kg/m^2s$
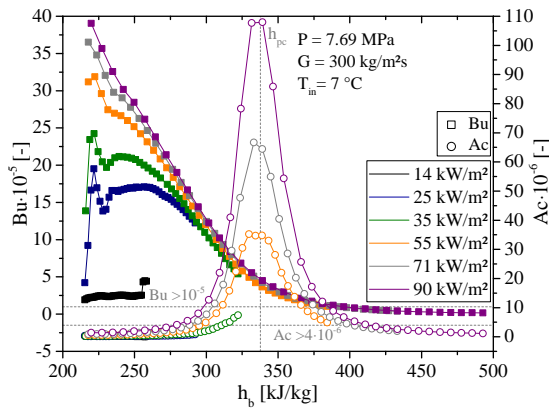
(c) Buoyancy and Acceleration number for $300\,kg/m^2s$
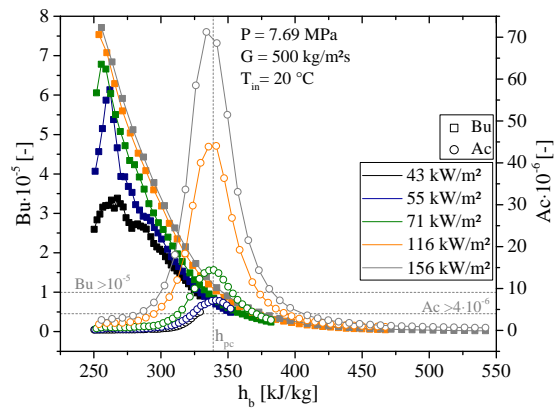
(d) Buoyancy and Acceleration number for $500\,kg/m^2s$

Figure 5.20.: Heat transfer trends, Buoyancy and Acceleration number for $300\,kg/m^2s$ and $500\,kg/m^2s$ with different heat fluxes of the CO_2 experiments at ts-2

A second minimum in the HTC trend can occur near the pseudo-critical bulk enthalpy at high mass fluxes. This can be seen in figure 5.21 for the mass fluxes of $1200\,kg/m^2s$ and $1500\,kg/m^2s$. This phenomena also occurs in R134a at $1500\,kg/m^2s$ and $2000\,kg/m^2s$. The minimum value is reduced more with increasing heat flux. No lower limit for this HTC minimum is observed for

the conducted heat fluxes of this study. The minimum is pushed to lower bulk enthalpies as the heat flux increases. At higher mass fluxes, the minimum gets broader and occurs at higher bulk enthalpies. Figure 5.21 shows the influence of the inlet temperature on the HTC minimum at $1200\,kg/m^2s$ and $1500\,kg/m^2s$. The minimum moves to higher bulk enthalpies with increasing inlet temperature at $1000\,kg/m^2s$ and $1200\,kg/m^2s$. At $1500\,kg/m^2s$, the minimum is moving to smaller bulk enthalpies. However, the minimum moves towards the pseudo-critical bulk enthalpy at all mass fluxes. No difference between the different inlet temperatures can be observed for the Buoyancy number, as seen in figure 5.21 (c) and (d). The Acceleration number varies slightly at the pseudo-critical bulk enthalpy. There is no correlation observable between the variation of the Acceleration number to the HTC trend. Therefore, it must be assumed that the HTC trend is influenced by the inlet conditions. To evaluate the acceleration effect, the density variation along the whole test section must be considered as discussed in section 2.2.2.3. Thus, the inlet temperature effects the thermally-induced bulk flow acceleration and eventually the HTC trend at high heat fluxes.
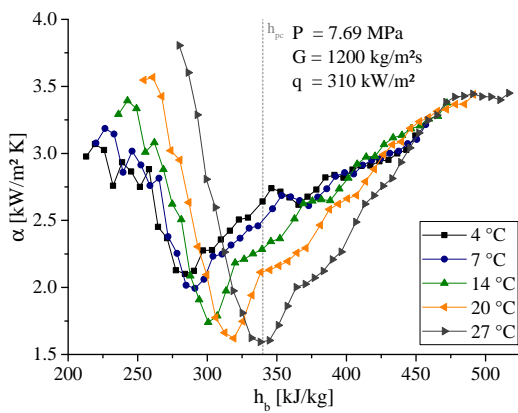
(a) Heat transfer coefficient trends for $1200\,kg/m^2s$ at different inlet temperatures
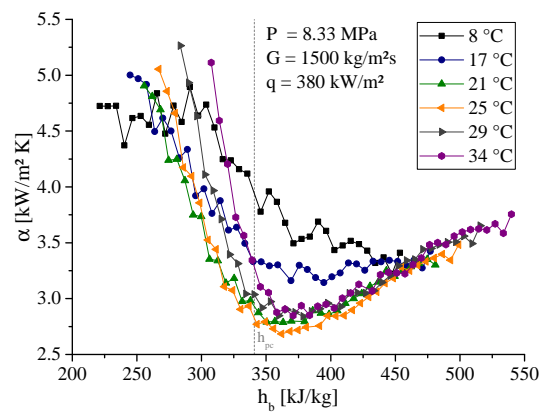
(b) Heat transfer coefficient trends for $1500\,kg/m^2s$ at different inlet temperatures
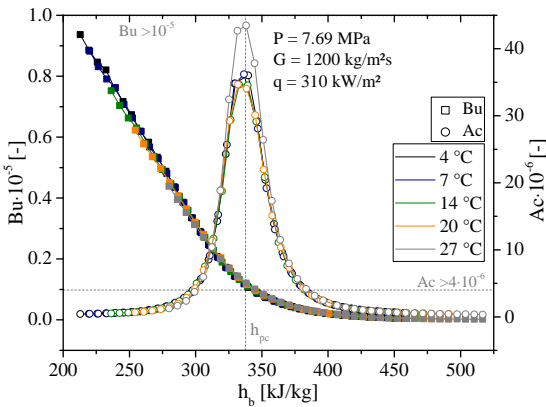
(c) Buoyancy and Acceleration number for $1200\,kg/m^2s$ at different inlet temperatures
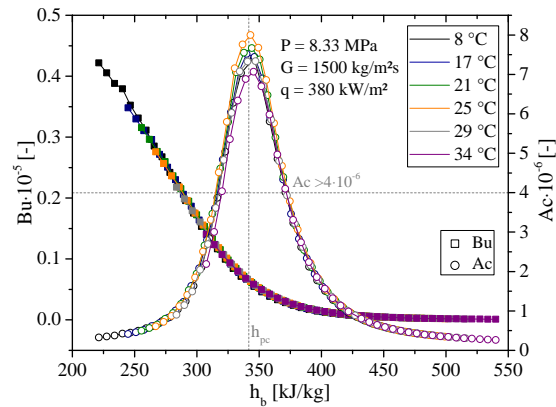
(d) Buoyancy and Acceleration number for $1500\,kg/m^2s$ at different inlet temperatures

Figure 5.21.: Heat transfer trends, Buoyancy and Acceleration number for $1200\,kg/m^2s$ and $1500\,kg/m^2s$ with different inlet temperature of the CO_2 experiments at ts-2

5.3. Onset of heat transfer deviation

The heat transfer at supercritical conditions is grouped in one regime in this study, as discussed in section 4.1. The buoyancy force and the thermally-induced bulk flow acceleration can have a strong influence on the heat transfer. This can lead to a heat transfer which deviates from the one of conventional fluids. In the literature, authors proposed that correlations or fluid-fluid scaling models are partially developed for normal heat transfer or show a better prediction accuracy at normal heat transfer. The data in this study are also separated for a better comparison by using the limits and definitions of Jackson, which are discussed in section 4.1. The normal heat transfer in this study is referred to heat transfer with negligible influence of buoyancy and acceleration. Table 5.1 lists the data points separately for influenced by buoyancy or acceleration. For R134a, 242 data points and 129 points for CO_2 exceed both limits. Due to the high inlet temperatures and high heat fluxes, more data points exceed the limits in the CO_2 database than in the R134a database.

Table 5.1.: Data point distribution of R134a and CO_2 with Bu and Ac

Fluid	None-influenced	Bu>10^{-5}	Ac>4 x 10^{-6}	Bu-Ac-influenced
R134a	35 036	9 203	682	242
CO2	5 563	9 264	5 268	129

To see the onset of the heat transfer deviation, the minimal heat flux at which points exceed the limits of Jackson are listed in the tables 5.2 - 5.4. Pressure and inlet temperature are also listed to see their influence on the onset. It is evident that the onset of the heat transfer deviation strongly depends on mass flux for both fluids.

Table 5.2.: Minimum heat flux of Bu>10^{-5} and Ac>4 x 10^{-6} of ts-1 in kW/m^2

P [MPa]	T_{in} [°C]	G in $\left[\frac{kg}{m^2 s}\right]$ for Bu>10^{-5}				G in $\left[\frac{kg}{m^2 s}\right]$ for Ac>4 x 10^{-6}					
		300	500	750	1000	300	500	750	1000	1500	2000
4.22	50	5	30	40	70	40	-	-	100	140	190
	60	10	30	40	70	30	-	-	90	130	170
	70	10	20	40	70	30	40	55	70	110	160
	80	5	20	40	70	20	30	50	70	110	160
4.59	50	5	30	50	90	40	-	-	-	-	-
	60	5	30	40	90	30	-	-	-	-	-
	70	10	20	40	80	30	-	-	-	-	-
	80	10	20	40	80	30	-	-	-	-	-
4.78	50	5	30	50	90	-	-	-	-	-	-
	60	10	30	50	90	40	-	-	-	-	-
	70	10	20	40	90	40	-	-	-	-	-
	80	10	20	40	90	40	-	-	-	-	-
5.15	50	10	20	50	100	-	-	-	-	-	-
	60	5	30	50	90	-	-	-	-	-	-
	70	10	30	50	90	-	-	-	-	-	-
	80	10	20	50	90	-	-	-	-	-	-
5.51	50	5	30	50	100	-	-	-	-	-	-
	60	10	30	50	100	-	-	-	-	-	-
	70	10	30	50	100	-	-	-	-	-	-
	80	10	30	50	100	-	-	-	-	-	-

Table 5.2 shows that the onset occurs at lower heat fluxes for decreasing pressures and increasing inlet temperatures. The pressure seems to have a stronger influence on the minimum heat flux than the inlet temperature. Almost no data exceed the acceleration limit at pressures above 4.22 MPa. The buoyancy has only an influence on the heat transfer for mass fluxes up to $1000\,kg/m^2s$. The onset of the buoyancy occurs at smaller heat fluxes than the onset of the acceleration for low mass fluxes up to $750\,kg/m^2s$.

Table 5.3.: Minimum heat flux of Bu>10^{-5} of ts-2 in kW/m^2 at 7.69 MPa

G $\left[\frac{kg}{m^2s}\right]$	T_{in} in [°C]

G $\left[\frac{kg}{m^2s}\right]$	4	5	6	7	9	10	12	15	16	17	18	19	20	21	22	24	25	27	28	30	31	33
200							2		2				2				2		2			
300		14					14			14					14					12	12	
400				25			25	25				25			25		25		25		25	25
500		49					49		46				43				46		46			
600	70		80				70						73				73	76				
1000	180			220		210																

Table 5.4.: Minimum heat flux of Ac>4 x 10^{-6} of ts-2 in kW/m^2 at 7.69 and 8.33 MPa

G $\left[\frac{kg}{m^2s}\right]$	4	5	7	10	12	15	17	18	20	22	24	25	27	28	30	31	33
200															10		
300			35		30		30			25							
400					40				34		31		30		33		30
500		61		55		52			43			46			46		
600	73		73	70				73				73		76		101	
1000	180		220		210			160						140		160	
1200	270		280		270				260				220		190		
1500	390			375		370				365			280			335	
1500*			330		380		370			360		340			330		390

* only one at 8.33 MPa

A more detailed investigation of the inlet temperature is done at ts-2, where inlet temperatures closer to the pseudo-critical value are feasible. The results are shown in table 5.3 and 5.4. It can be seen that the inlet temperature at which the onset of the HTD occurs is varying with mass flux. For low mass fluxes, the onset is shifted to lower inlet temperatures for increasing mass flux. At higher mass fluxes starting from $1000\,kg/m^2s$, the inlet temperatures is always close to the pseudo-critical value. The buoyancy only has an influence on the heat transfer up to $600\,kg/m^2s$. The onset for the acceleration can be smaller than the onset of the buoyancy starting at mass fluxes of $600\,kg/m^2s$.

For comparison with the literature, the minimum onset of either the buoyancy or the acceleration was plotted in figure 5.22 for every mass flux for the experimental data of R134a and CO_2. The correlation of equation 2.17 is fitted to the data. Additionally, the applicable correlations of Bae [Bae et al., 2010], Kirillov and Grabezhnaia [Kirillov & Grabezhnaia, 2006] are plotted in figure 5.22.

The correlation found in this study differs from the ones described in previous studies. One reason is the use of dimensional parameters in the correlation and the usage of different fluids. The onset even differs for the correlation from Kirillov and Grabezhnaia [Kirillov & Grabezhnaia, 2006], although it was developed for different fluids using a ratio of the molar mass.
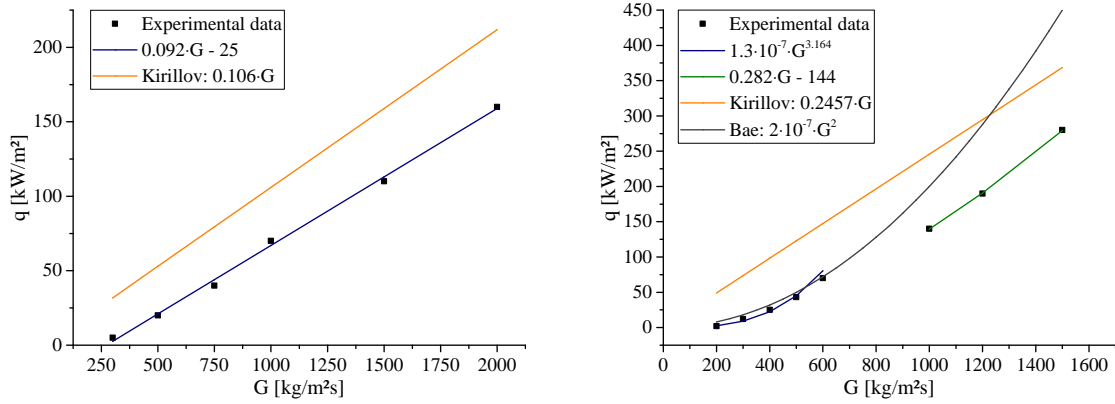
(a) Minimum onset of heat transfer deviation of R134a for every case of pressure, inlet temperature and mass flux

(b) Minimum onset of heat transfer deviation of CO_2 for every case of pressure, inlet temperature and mass flux

Figure 5.22.: Onset of heat transfer deviation of experiments ot ts-1 and ts-2 with R134a and CO_2 according to the limits of Jackson compared with onsets of the literature

Another reason for the differences between the correlations for the onset can be the varying results from different experiments and loops, as shown in section 5.4.1. Additionally, the onset also depends on inlet temperature, tube diameter and pressure as found by Schatte et al. [Schatte et al., 2016] and Kline et al. [Kline et al., 2018]. Moreover, different used definitions for the onset itself lead to different correlations. Some authors using wall temperature spikes, other deviations from heat transfer correlations, other the buoyancy parameter (equation 2.13) from Jackson with varying limit, as Kline showed in his thesis [Kline, 2017].

5.4. Comparison of heat transfer data with literature and correlations

In this chapter, the produced data of this study are compared with similar data of the literature. Thus, the results of this study are classified. In addition, correlations are assessed with the produced data of this study and their prediction capability is evaluated.

5.4.1. Comparison with literature data

The influence of mass flux, heat flux, pressure, inlet temperature on the heat transfer is discussed and compared with the trends found in the literature in section 5.1 and 5.2. The influences found in this study are the same as those described in the open literature, with the exception of the inlet temperature. Experimental data from heat transfer found with R134a and CO_2 flowing upward in a tube are compared in this section. Unfortunately, data with these specifications are limited.

As part of the cooperation between the School of Nuclear Science and Engineering (SNSE) from the SJTU and the IATF, data for heat transfer at supercritical conditions with R134a are exchanged. The data are partially published by Zhang et al. [Zhang et al., 2014]. The wall temperature and HTC trends of $600\,kg/m^2s$ from SJTU is very similar with the trends of $500\,kg/m^2s$ in this study. Mass fluxes used in both institutions are $1000\,kg/m^2s$, $1500\,kg/m^2s$ and $2000\,kg/m^2s$.

In figure 5.23 the highest and lowest common heat flux is shown for $1000\,kg/m^2s$ and $2000\,kg/m^2s$, respectively. Inlet temperatures and pressures vary. However, the HTC of SJTU and ts-1 are similar at low bulk enthalpies but start to differ as the bulk enthalpy approaches the pseudo-critical point. At high heat fluxes the difference is reduced, but the difference can be more than $100\,\%$ for the HTC at similar parameters. The differences are reduced if the data from the tube is used with the depositions after the post-dryout experiments. This could be caused by the decreased roughness of the heated wall after the PDO experiments as discussed in section 4.2.1.3.

(a) Comparison of HTC of ts-1 with data from SJTU at 1000 kg/m²s and 60 kW/m²

(b) Comparison of HTC of ts-1 with SJTU at 1000 kg/m²s and 100 kW/m²

(c) Comparison of HTC of ts-1 with data from SJTU at 2000 kg/m²s and 100 kW/m²

(d) Comparison of HTC of ts-1 with SJTU at 2000 kg/m²s and 160 kW/m²
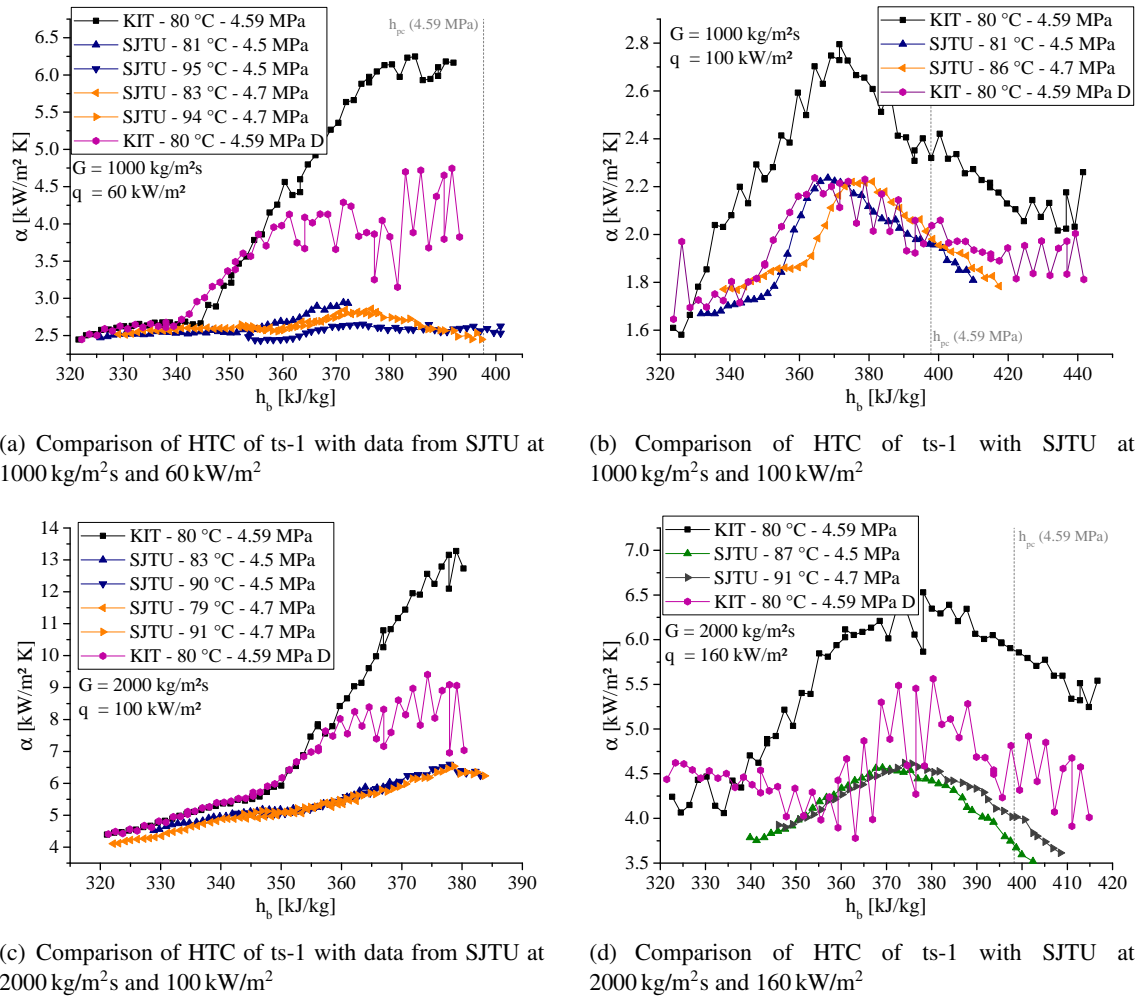
Figure 5.23.: Comparison of HTC of ts-1 with data from SJTU with R134a [Zhang et al., 2014], with D for the tube with deposition (section 4.2.1.3)

Cui and Wang [Cui & Wang, 2017] conducted some experiments with R134a in a 8 mm tube. Unfortunately, only one diagram is published with comparable parameters in their paper. The authors were not allowed to provide more data due to restrictions of the government, which supported the study. The comparison with the experimental data of this study can be seen in figure 5.24. In this case, the HTC differ at low bulk enthalpies and merge as it approaches the pseudo-critical point, which is between 392 kJ/kg and 400 kJ/kg for this pressures. The results of the two institutes fits very well especially at low pressure. There is no buoyancy-influenced HTD near the inlet for the data of Cui and Wang. Therefore, pressure has a much higher influence on the HTC around the pseudo-critical bulk enthalpy for the results of Cui and Wang. Whether these two phenomena and the differences are induced by the smaller tube diameter of 8 mm cannot be determined.

Kline [Kline, 2017] showed a good reproducibility for the CO_2 experiments at the SCUOL in his thesis. Nevertheless, some experiments are compared with the data of Zahlan [Zahlan et al., 2015a], who also conducted his experiments at the SCUOL. Here, the HTC also starts to differ as the bulk enthalpy approaches the pseudo-critical point, as seen in figure 5.25. The deviation in figure 5.25 could be due to the different inlet temperatures but probably not that much.

From the observations in this section, it can be concluded that the reproducibility of the HTC at different facilities depends on heat flux and bulk enthalpy. The reproducibility is given at low bulk enthalpies. The HTC can differ for low heat fluxes at bulk enthalpies around the pseudo-critical point. At high heat fluxes, the reproducibility is better around the pseudo-critical bulk enthalpy but

still differs. A reason could be the high sensibility of the HTC on the heat flux near the pseudo-critical bulk enthalpy as discussed in section 5.1.4. This sensibility can be dependent on the surface of test section or even at the total system as discussed in section 4.2. Of course another explanation for the big differences in the HTC is the idea of multi-solutions from Cheng and Liu [Cheng & Liu, 2017].

Therefore, HTC data close to the pseudo-critical point show a high uncertainty and must be used carefully. Nevertheless, the data produced in this study are used to assess correlations and fluid-to-fluid models due to the high transparency, the high consistency throughout all varied parameters and the existent physical explanations.
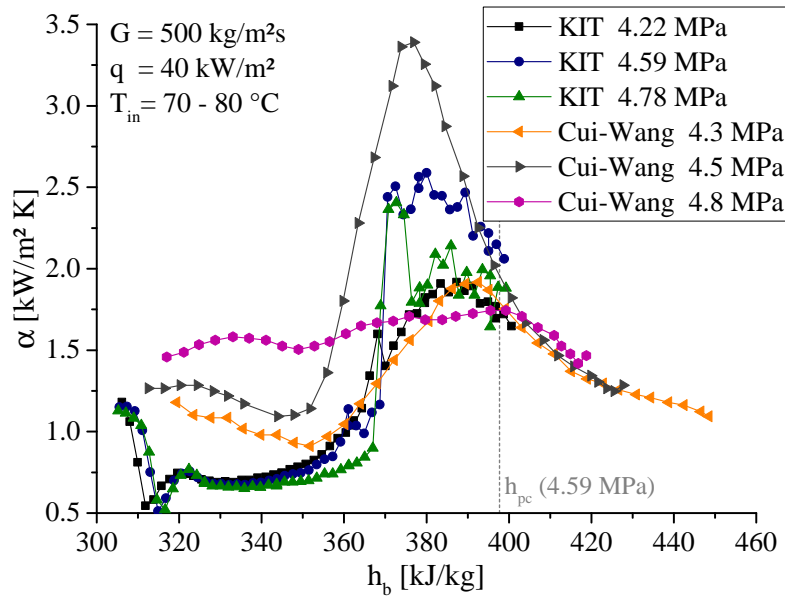
Figure 5.24.: Comparison of HTC of ts-1 with data from Cui and Wang at $500\,\text{kg/m}^2\text{s}$ and $40\,\text{kW/m}^2$ with different pressures in R134a [Cui & Wang, 2017]
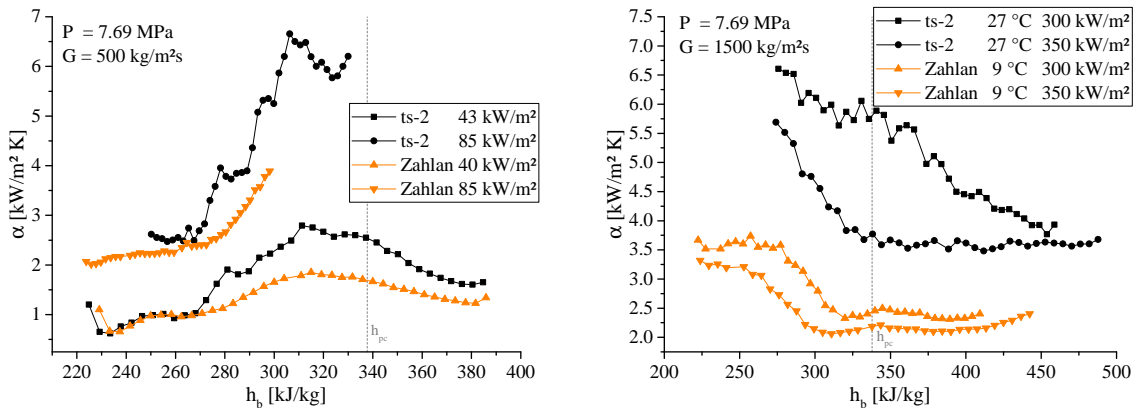
(a) Comparison of HTC of ts-2 with data from Zahlan at $500\,\text{kg/m}^2\text{s}$

(b) Comparison of HTC of ts-2 with data from Zahlan at $1500\,\text{kg/m}^2\text{s}$

Figure 5.25.: Comparison of HTC of ts-2 with data from Zahlan [Zahlan et al., 2015a] at low and high mass flux with CO_2

5.4.2. Comparison of heat transfer data with correlations

After excluding invalid data, the experimental datasets of R134a and CO_2 described in section 4.3 are used to assess the correlations at a wide range of parameters. It was found in the literature that

some correlations are developed for normal heat transfer. As described in section 4.1, the normal heat transfer is referred to HTC with negligible influence of buoyancy and acceleration. The data are split into influenced and none-influenced data, as described in section 5.3, to investigate if the correlation can predict the influenced HTC. The data are defined as influenced if they exceed the limits of Jackson: $Bu > 10^{-5}$ or $Ac > 4 \times 10^{-6}$ [Jackson, 2011]. The classification of the data is shown in table 5.5.

Table 5.5.: Distribution of R134a and CO_2 for none-influenced and influenced data points

Database	All	None-influenced	Influenced
D-R134a	44 679	35 036	9 643
D-CO_2	20 095	5 563	14 532

The mean deviation (MD) and standard deviation (STD) of the predicted heat transfer coefficients to the experimental ones are defined in the equations 3.23–3.26 and listed in table 5.6. A lot of correlations can predict the data with negligible influence of buoyancy and acceleration of both fluids very well, like the correlations of Bishop, Chen and Fang, Deev et al., Jackson, Nicholas and Zhu et al.. The correlation of Jackson and Fewster reproduces the HTC with negligible influence for R134a the best. For CO_2, the correlation of Chen and Fang gives the best results. The higher deviations of the CO_2 data, especially for the correlation of Gnielinksi and Dittus-Boelter, compared to the R134a data can be explained with the higher number of data with bulk temperatures close to the pseudo-critical point. The subcritical correlations overpredict the HTC in this region, as seen in the positive MD.

The correlation of Chen and Fang [Chen & Fang, 2014] shows the closest prediction for R134a data influenced by buoyancy and acceleration with a MD of -3.2 % and a STD of 12.5 %. This can be explained by the usage of the Grashof number and the usage of the wall temperature in their correlation, as seen in the appendix A.7. Also other correlations predict the HTC acceptable well with a MD below 10 % and a STD below 30 % as Bae, Nicholas or the water based one of Mokry et al.. For the influenced data of CO_2, the correlation of Chen and Fang also fits the data the best with a MD of -4.1 % and a STD of 8.1 %. This and the correlation of Bae are the only correlations with a STD below 30 %. Although a lot of the listed correlations are based on CO_2, the prediction capability of the CO_2 data of this study is very low. The high deviations in the CO_2 assessment could be due to the high number of data with very high heat fluxes. No correlation was developed for these high heat fluxes. Correlations developed for R134a are from Cui and Wang as well as Zhang et al.. Both correlation doing quite well for the none-influenced data of R134 but have large STD at influenced data, as seen in table 5.6.

Kurganov et al. [Kurganov et al., 2014] discovered that correlations predict the different HTC trends of the buoyancy and acceleration influenced HTC with varying accuracy. As seen in section 2.2.2, the different HTC trends correlate with the mass flux. Therefore, the MD and STD are split into the different mass fluxes for a more detailed analysis of the correlation assessment. The results for all correlations are shown in the appendix E. The results for the overall best correlations and the best correlation for each mass flux are listed in table 5.7 and 5.8 for R134 and CO_2, respectively. Thus, the correlation of Chen and Fang predict the experimental data of R134a at $300 \, kg/m^2 s$ and $500 \, kg/m^2 s$ the best. After that, the correlations of Watts and Chou, Bae, Komita and the heat flux based correlation of Cheng (Cheng-q) show the best reproduction for different mass fluxes. It is also apparent that the accuracy of the correlations itself vary strongly with the mass flux. For example, Komita varies from a MD of -112.1 % and a STD of 54.9 % at $300 \, kg/m^2 s$ to a MD of 5.9 % and STD of 6.1 % at $1500 \, kg/m^2 s$.

The MD and STD of chosen correlations to the influenced CO_2 data split into mass fluxes are listed in table 5.8. The mass flux of $1200 \, kg/m^2 s$ is close to $1000 \, kg/m^2 s$ and $1500 \, kg/m^2 s$ and hence

Table 5.6.: Mean deviation (MD) and standard deviation (STD) of correlations to experimental heat transfer coefficient in % separated into influenced (I) and none-influenced (NI)

Correlation	R134a - NI		R134a - I		CO$_2$ - NI		CO$_2$ - I	
	MD	STD	MD	STD	MD	STD	MD	STD
Badea et al. A.1	25.6	35.6	61.8	50.4	-2.1	24.5	46.5	56.5
Bae A.2	-10.2	10.8	-9.7	20.3	-17.2	14	-1.8	20.4
Bae & Kim A.3	58.6	232	-11.4	33.1	-45.7	82.6	-21.4	61.1
Bishop et al.A.4	8.5	11.1	25.7	30.8	-8.7	13.4	28.3	39.1
Bogachev et al. A.5	13.1	21.2	57.4	41.9	37.5	31.3	97.6	66.9
Bringer & Smith A.6	84.5	83	145	133	40.7	37.8	141	139
Chen & Fang A.7	-4.8	13	-3.2	12.5	2.9	10.2	-4.1	8.1
Cheng et al. A.8	-24.7	13.3	4.1	33.7	-24.1	26.6	23.7	53.5
Cheng-q A.9	-9.7	21.5	25.9	52.6	-43.4	20.9	13	63.1
Cheng-T A.10	-12	15.7	10	35	-5.7	19.3	0.9	38.3
Cui & Wang A.11	6.4	13.6	43.8	40.8	-18.3	16.2	42.6	55.8
Deev et al. A.12	-14.5	10.8	11.8	31.2	-16.5	12.6	6.6	40.9
Dittus-Boelter A.13	6.2	46.5	54.9	92.4	76.9	67.9	221	261
Gnielinski A.14	25.3	63.3	77	126	105	90.7	290	346
Gorban et al. water A.15	-52.3	16.6	-41.4	20.7	-5	26.1	-14.5	49.7
Gorban et al. R12 A.16	-54.9	14.8	-42.5	19	-11.2	24	-19.3	44.1
Grass et al. A.17	39.3	28.1	90.6	57.8	25.7	30.6	52.1	57.5
Griem A.18	-13.1	16.8	10.6	33.7	-9.7	20.5	1.6	45.4
Gupta et al. A.19	32.6	25.1	65.2	42	29.3	48.7	154	68.2
Jackson A.20	-3.3	14.1	24.6	32.3	1	18.6	41.5	37.4
Jackson & Fewster A.21	-2	11.9	25.9	31.8	-2.8	16.5	36.1	38.5
Kim et al. A.22	17.4	49.5	3.2	55.9	83.2	48.8	17.5	50
Kim & Kim A.23	69.8	97.9	149	118	174	146	296	169
Kirillov et al. A.24	-20.3	18	-16.5	35.1	-41.5	14.7	-30.3	59
Komita et al. A.25	-21.7	9.2	-62.8	57	-27.8	11.7	-47.9	55.6
Kondratev A.26	-44.2	17.9	-23.2	27	1.8	27.6	16	65.6
Krasnoshchekov et al. A.27	4	20.3	31.6	45.2	-36.9	14.3	5.6	77.8
Kuang et al. A.28	769	253	752	344	959	347	912	394
Kurganov et al. A.29	1.4	108	67	290	108	132	552	913
Mayinger & Scheidt A.30	-4.5	41.6	27.5	87.8	37.6	67.1	140	254
Miropolskii & Shitsman A.31	9.3	31.1	34	57.1	8.9	27.6	58.1	58.3
Mokry et al. water A.32	-6	12.7	5.7	29.6	-24.7	12.9	4.9	36
Mokry et al. CO$_2$ A.33	-40.5	16	-31.1	25.1	-21	22	-19.3	31
Nicholas A.34	-13.6	10	3.9	23.9	-7.2	16	21.6	32.6
Ornatsky et al. A.35	-10.4	34.8	4.2	58.1	-17.2	24.4	12.9	46.4
Petukhov et al. A.36	27.4	29.2	68.5	58.5	-18.8	19.5	27.2	91.4
Pitla et al. A.37	13.4	33.5	38.5	54.2	11.1	34.4	28.4	76.3
Preda et al. A.38	59	66.1	52.1	75.1	16.3	30.4	91.3	92.4
Razumovskiy et al. A.39	10.6	29.5	43.2	55.8	-39.5	19	15.8	108
Saltanov et al. A.40	-42.2	13.8	-27.6	22.9	-19.2	19.9	-10.5	34.6
Swenson et al. A.41	81.4	52.8	137	79.1	53.4	72.3	206	101
Watts & Chou A.42	-9	11.4	15.1	29.6	-16.5	14.5	21.2	35.3
Yamagata et al. A.43	32.7	19.1	66.6	46.3	15.6	18.3	68.1	52.7
Yeroshenko & Yaskin A.44	-10.8	11.7	19.3	34.1	-9.6	14.5	12.3	46.6
Zhang et al. A.45	-1.6	25.7	32.3	61.7	-70.6	41.6	-5.8	122
Zhu et al. A.46	12.3	10.8	32.9	30.3	0.9	15.3	26.7	41.7

Table 5.7.: Mean and standard deviation of selected correlations split into mass fluxes in kg/m^{2}s for R134a - I in %

Correlation	300		500		750		1000		1500		2000	
	MD	STD	MD	STD	MD	STD	MD	STD	MD	STD	MD	STD
Bae A.2	-17.1	24.3	-8.1	15.4	-6.2	13	0.6	10.9	20.6	6.9	24.9	9
Chen A.7	0.5	13.6	-2.8	7.9	-11.2	6.2	-10	13.2	21.5	5.7	24.9	5.8
Cheng A.8	1.8	29.9	11.5	43.9	-10.8	25.4	16	17.6	20.7	12.8	30.4	12.5
Cheng-q A.9	21.9	48.6	36.4	65.1	14.4	43.1	42.4	41.3	-12.7	9.2	-5.7	10.1
Cui A.11	60.3	52	44	29.7	23.3	17.8	22.4	10.9	19.3	5	21.1	7.1
Jackson A.20	34	36.7	24.3	25.9	2.9	19.6	18.1	22	71.4	10.9	78.3	13.1
Komita A.25	-112.1	54.9	-43.4	28.6	-21.4	9.2	-15.2	9.5	5.9	6.1	10.1	8
Mokry w A.32	15.4	40.7	5.3	17.2	-6.1	11	-9.8	9.2	9.3	6	14.2	7
Watts A.42	23.9	38.1	15.9	22.8	-0.1	15.5	5.6	10.9	20.9	6.8	25.1	9
Zhang A.45	27	65.5	48	66.4	23.9	45.2	39.5	50.7	-27.8	38.6	-21	26.6

not shown. The detailed tables with all mass fluxes and correlations are shown in the appendix E. Here, the correlation of Chen and Fang reproduces the data of all mass fluxes the best. The second best correlation varies between Badea et al., Bae et al., Bishop, Cui and Wang as well as Komita. Every correlation seems to have a mass flux region where it works best, like Zhu at 600 kg/m^{2}s. This variation of prediction agreement for different mass fluxes supports the proposal of Kurganov et al. [Kurganov et al., 2014] that the HTD trends are catched differently well by the correlations.

Table 5.8.: Mean and standard deviation of selected correlations split into mass fluxes in kg/m^{2}s for CO$_2$ - I in %

Correlation	200		300		400		500		600		1000		1500	
	MD	STD	MD	STD	MD	STD	MD	STD	MD	STD	MD	STD	MD	STD
Bae A.2	22.7	23.1	-9.5	17.7	-8.2	16	-8.9	15.6	-1.7	20.2	9.5	18.3	8.2	17.7
Bishop A.4	111	59.3	45.7	34.6	26.1	25.5	9.7	19.4	9.8	16.3	12.3	15.6	11.3	14.7
Chen A.7	8.9	9.3	-1.1	7.5	-5.3	7.1	-8.4	5.6	-7.9	4.4	-7.4	6.1	-1.1	5.7
Cui A.11	160	79.8	74.7	47.2	44.7	34.7	21.2	26.6	16.9	16.4	6.3	11.3	-1.8	12.2
Jackson A.20	98.5	44.3	54.2	26.9	30.7	34	25.9	31.1	28	37.3	48.2	30	37.6	18.4
Komita A.25	-95	74.9	-99	67.9	-46	39.9	-40	29.8	-20.8	17	-5.8	16.5	-5.1	15.4
Mokry w A.32	88.6	54.6	19.8	30.5	4	19.1	-12.1	13.4	-11.8	12.5	-12.6	12.6	-15	10.1
Watts A.42	92.8	48.2	36.9	28.4	16.3	26.9	5.1	22.7	4.8	19.8	10.9	17.6	8.5	17.7
Zhu A.46	108	66.9	43.2	35.4	22.6	31.1	7.7	26.6	4.5	16.3	10.8	15.8	21.3	21.1

Figure 5.26 shows exemplarily the predicted HTC of some correlations for mass flux of 500 kg/m^{2}s and 1500 kg/m^{2}s. The correlations of Bae, Chen and Fang as well as Mokry predict the experimental HTC very closely at the mass flux of 500 kg/m^{2}s and low bulk enthalpies. The recovery of the heat transfer is underpredicted by each correlation. From this point, the correlations of Chen and Fang as well as Cui and Wang are the closest. At high mass fluxes, the closest correlation changes along the bulk enthalpy from Jackson over Cui and Wang to Bae. The correlation of Chen and Fang, which predict very well at low mass fluxes, show high deviations to the experimental results. The zig-zag of the heat transfer coefficient of the correlation of Chen and Fang show the strong dependency of the correlation to the wall temperature. Cheng [Cheng et al., 2009b] suggested that a correlation should not contain the wall temperature to avoid iteration problems in the prediction. As seen, the correlations can predict the heat transfer at different parameter ranges differently well. There is no correlation which predicts the overall HTC trend the best.
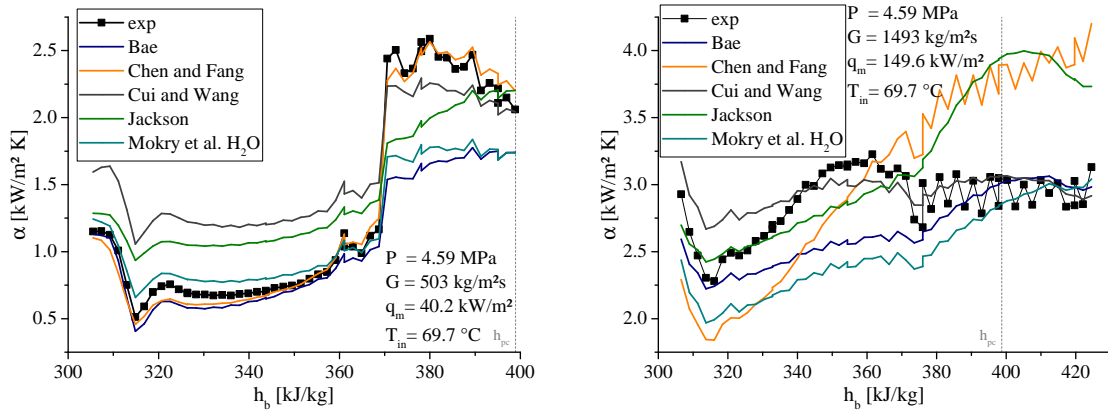
(a) Experimental and predicted heat transfer coefficient trend for $500\,kg/m^2s$ of ts-1

(b) Experimental and predicted heat transfer coefficient trend for $1000\,kg/m^2$ of ts-1

Figure 5.26.: Experimental and predicted heat transfer coefficients for $500\,kg/m^2s$ and $1000\,kg/m^2s$ of ts-1 in R134a

5.5. Summary of the heat transfer experiments at supercritical conditions

Heat flux - buoyancy and acceleration

It was found that, at supercritical conditions, the heat is transferred by mixed convection. The heat transfer must be treated as one regime with varying influences of buoyancy and thermally-induced bulk flow acceleration. At low heat fluxes, the HTC trends match qualitatively and quantitatively very well for different heat fluxes like trends of conventional fluids as at subcritical conditions. As the heat flux increases high enough such that the buoyancy and the acceleration starts to have an influence on heat transfer, the HTC starts to deviate, mostly to decrease. The recent theories of the mechanisms of buoyancy and thermally-induced bulk flow acceleration are described in section 2.2.2.2 and 2.2.2.3 and are able to explain the observed local heat transfer reductions very well. The HTC minimums cause mainly local peaks in the wall temperature. These peaks occur as the Buoyancy or the Acceleration number exceed the limits of $Bu>10^{-5}$ or $Ac>4x10^{-6}$ of Jackson [Jackson, 2011]. However, it is found that the HTC starts to decrease from the trends of low heat fluxes at $Bu>0.2x10^{-5}$ or $Ac>0.25x10^{-6}$. Therefore, it must be assumed that the buoyancy and thermally-induced bulk flow acceleration start to influence the heat transfer at these limits. Here, the flow changes from forced to mixed convection.

The buoyancy effects the heat transfer at bulk enthalpies smaller than the pseudo-critical point. The Buoyancy number and the bulk enthalpy range where the buoyancy effects the heat transfer decreases for increasing mass flux. A minimum HTC of $500\,W/m^2K$ and $700\,W/m^2K$ for a buoyancy influenced heat transfer was found for R134a and CO_2, respectively. The thermally-induced bulk flow acceleration occurs mainly at the pseudo-critical point caused by strong density variations. For $0.25x10^{-6}>Ac>2.5x10^{-6}$ the HTC is very sensible to the Acceleration number and thus on the heat flux. This can be seen at the strong HTC decrease and the increasing zig-zag of the HTC trends at these conditions. Additionally, it seems that the surface has an influence on heat transfer if the thermally-induced bulk flow acceleration occurs. The heat transfer is decreased if the surface roughness is decreased due to the earlier laminarization of the flow caused by a smaller pressure gradient. This high sensibility of the heat transfer on the heat flux and on the surface could explain the high deviations between the data of different studies especially near the pseudo-critical point. It also explains why the correlations fail to predict the heat transfer at these conditions.

Mass flux

The level of the HTC increases with increasing mass flux. This is caused by the higher turbulence. Furthermore, the mass flux dominates the qualitative behavior of the HTC trend as it influences the buoyancy force and acceleration. The heat transfer is determined by buoyancy forces at low mass fluxes. As the mass flux increases, the thermally-induced bulk flow acceleration gains importance. The correlation between the qualitative behavior of the wall temperature and the mass flux shown by Kurganov et al. coincide with the ones shown in this study. Additionally, it was shown that correlations predict the heat transfer with varying accuracy according to these groups.

Pressure

Pressure has a significant influence on heat transfer at supercritical conditions. As the pressure approaches the pseudo-critical point, the variations of the thermal-physical properties of the fluid increase drastically, as shown in figure 2.2 and discussed in section 2.1. Additionally, a smaller pressure results in a smaller pseudo-critical enthalpy. Therefore, phenomena of the HTC occur stronger and at lower bulk enthalpies at low pressures. HTDe sometimes occurs only at smaller pressures for similar cases. The smallest HTC are observed at the smallest pressures due to the higher Buoyancy and Acceleration number.

Inlet temperature

The influence of the inlet temperature must be discussed separately for the buoyancy and the acceleration influenced data. The influence of the inlet temperature depends on the mass flux for the buoyancy induced HTC minimum. At low mass fluxes up to $500 \, \text{kg/m}^2\text{s}$, the inlet conditions effect the HTC up to 90 times of the diameter. The inlet effect is reduced to 24 times of the diameter for mass fluxes of $750 \, \text{kg/m}^2\text{s}$ and higher. A stronger buoyancy force is needed at higher mass fluxes to cause a laminarization of the flow. Therefore, a higher difference between the density of the fluid at the wall and in the bulk is needed. The density varies stronger at bulk temperatures close to the pseudo-critical point. At a certain wall-bulk temperature combination, the critical density difference is reached to decrease the heat transfer. Almost no effect of the inlet conditions is observed if this bulk temperature is higher than the inlet temperature, as for high mass fluxes. An influence up to 90 diameters is observed if the bulk temperature is smaller than the inlet temperature. Here, the inlet effect is caused by the development of the thermal layer until the critical density difference is reached.

The HTC minimum caused by the thermally-induced bulk flow acceleration shows also a dependency on the inlet temperature. This dependency is smaller than for the buoyancy influenced HTDe at low mass fluxes and independent from mass flux. As this HTDe is induced by the acceleration due to the strong increase of the density along the whole test section, the variation of the bulk temperature along the whole test section as well as the inlet temperature must be considered. It was found that the HTC minimum moves towards the pseudo-critical point for increasing inlet temperature. Because this effect is limited to bulk enthalpies close to the pseudo-critical point, a limitation of the inlet effect in a specific length or numbers of diameters is not meaningful.

Flow instabilities

It was found that the heat transfer depends also on the whole system and on the condition of the heated surface. Flow instabilities can occur depending on mass flux, heat flux, inlet temperature and different system conditions as cooling temperature or positions of the valves. Here, the heat transfer changes its behavior and different phenomena occur. Cases close to the instability threshold are difficult to reproduce. Paired with the high sensibility to heat flux and inlet temperature, this aggravates the reproducibility and comparison from different systems. Data with flow instabilities are excluded for the assessment of the correlations.

Correlations

Summarizing all these complex dependencies of the pressure, mass flux, heat flux and inlet temperature on the heat transfer at supercritical conditions, it is not surprising that no correlation is able to cover all these phenomena. The comparison with data from the literature shows that the HTC can vary strongly around the pseudo-critical enthalpy. Therefore, there is no correlation which can predict the heat transfer at supercritical conditions well for wide parameter ranges and different data sets. Nevertheless, overall the correlation of Chen and Fang shows the closest prediction for the R134a and CO_2 data so far.

6. Fluid-to-Fluid Scaling of Heat Transfer Data at Supercritical Conditions

In previous studies, several fluid-to-fluid scaling models were developed. The authors claimed to have insufficient data for the direct validation of their models. Often correlation are used to validate the scaled data indirectly, as described in section 2.4.2. However, no correlation can reproduce experimental data reliably and accurately, as discussed in section 5.4.2. This deficiency shall be eliminated with the databases gathered in this study. Therefore, the databases and the procedure for scaling and the direct validation are introduced firstly. A new method for the interpolation of the water data is proposed. Selected fluid-to-fluid scaling models are assessed with the new method. A modified scaling model will be derived, validated and discussed at the end of this chapter.

6.1. Procedure for assessment

The huge advantage in this study is the availability of the extensive databases of R134a, CO_2 and water. The direct validation method, as described in section 2.4.2, can be used to assess the fluid-to-fluid scaling models from the literature. The advantage of the method is that the results are only affected by the scaling models. The procedure is shown schematically in figure 6.1. For the comparison, the data of R134a and CO_2 will be scaled to water using the fluid-to-fluid scaling models of the literature. An interpolation is needed to gain identical parameters because the scaled parameters will be between the given data points of the water database. The scaled data are compared with the interpolated data of the water database. The individual steps will be described in detail in the following sections.
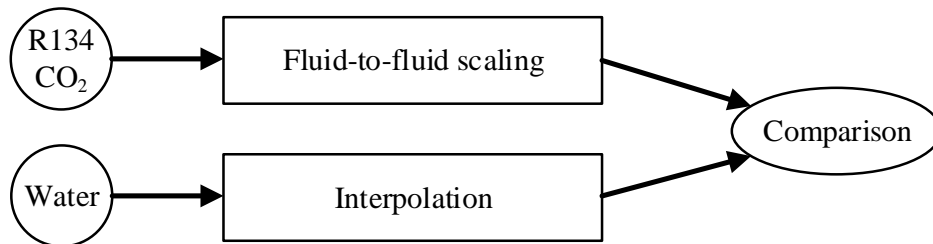
Figure 6.1.: Scheme of comparison of scaled data to water data

6.1.1. Databases for scaling model assessment

6.1.1.1. Databases from experiments

Here, the same databases are used as for the assessment of the heat transfer correlations. The data are based on the experimental results of this study. Invalid data are excluded as described in section 4.3. The parameter ranges of the databases D-R134a and D-CO_2 are listed in table 6.1.

6.1.1.2. Databases from literature

Another database D-CO$_2$-lit is established with CO$_2$ data from the literature to enlarge the dataset. This increases the significance of the assessment of the fluid-to-fluid scaling models for the pair CO$_2$ – water. The data are from Zahlan et al. of the University of Ottawa [Zahlan et al., 2015a], who published their data in tables. The second source is published by Kim et al. of the Korean Advanced Institute of Science and Technology (KAIST) [Kim et al., 2008]. This institute also participates in the cooperate research project 'Understanding and Prediction of Thermal-Hydraulics Phenomena Relevant to SuperCritical Water-cooled Reactors (SCWRs)' from the IAEA like the IATF. The data are only gained in tubes and the parameter ranges are listed in table 6.1.

Table 6.1.: Parameters for the databases used for the assessment of the fluid-to-fluid scaling models

Database	Source	d	P	G	T$_{in}$	q	Data
		[mm]	[MPa]	$\left[\frac{kg}{m^2 s}\right]$	[$°C$]	$\left[\frac{kW}{m^2}\right]$	[-]
D-R134a	Exp.	10	4.22 – 5.51	300 – 2000	50 – 80	5 – 200	44679
D-CO$_2$	Exp.	8	7.69 & 8.33	200 – 1500	2 – 33	2 – 450	19966
D-CO$_2$-lit	Zahlan	8 & 22	7.55 – 8.4	200 – 1500	1 – 34	2 – 450	10127
	Kim	9	7.75 & 8.12	200 – 1200	6 – 34	30 – 50	1148
D-water	IATF	7 – 26	22.5 – 31	200 – 3500	200 – 380	87 – 2000	24291

A huge and wide-ranged database for water is gathered at the IATF from the literature in cooperation with the SNSE of the SJTU. The database and its consistency are discussed by Badea et al. [Badea et al., 2018]. The database is checked for duplication and inconsistent data are removed. Inconsistent data are defined if given wall temperature and HTC are not consistent or if the calculated bulk temperature deviates from the heat balance calculated from the inlet temperature. Additionally, only data with diameters of 6 – 12 mm and 20 – 26 mm are included due to the diameters of 8 – 10 mm and 22 mm of the R134a and CO$_2$ data. Zahlan et al. mentioned that his scaling models were developed for normal heat transfer. In this study the normal heat transfer is referred to data with negligible influence of buoyancy and acceleration. To address the scaling capability of the scaling models for buoyancy and acceleration influenced and none-influenced data, the data are split in the same way as for the assessment of heat transfer correlations in section 5.4.2. There is no need to split the water database as it is only used to validate the previous split and scaled data of R134a and CO$_2$. The datapoint numbers of the none-influenced and influenced data from the databases D-R134a, D-CO$_2$ and D-CO$_2$-lit are listed in table 6.2.

Table 6.2.: Datapoint numbers used for the assessment of fluid-to-fluid scaling models for none-influenced and influenced data points

Database	None-influenced data	Influenced data
D-R134a	35 036	9 643
D-CO$_2$	5 563	14 532
D-CO$_2$-lit	6 136	5 139

6.1.2. Fluid-to-fluid scaling models

The fluid-to-fluid scaling models from Cheng et al., Zahlan et al., Cheng from Zahlan modified, Tian et al., Zwolinksi and Azih and Yaras [Cheng et al., 2011, Zahlan et al., 2014, Tian et al., 2018, Zwolinski et al., 2011, Azih & Yaras, 2017] are used to scale the R134a and CO$_2$ data to water. The models are described in detail in section 2.4.3 and in the appendix B. Previous models are not used since it was shown that the updated ones are more accurate.

Except Azih's model, the models are used to scale the pressure, mass flux, heat flux, bulk temperature and heat transfer coefficient from R134a and CO_2 to water. The diameter is kept constant. For the assessment of Azih and Yaras, the identified dimensionless numbers are calculated for all data from all databases because of dependency of several identified dimensionless numbers on heat flux and mass flux. The dimensionless numbers are described in the equations B.56 - B.60. The procedure of the assessment of the scaling model of Azih an Yaras is described in section 6.1.6.

6.1.3. Problem of interpolation of water data

The issue for the comparison is that the scaled data are not covered by the water database with identical parameters. Zahlan and Tian [Tian et al., 2018, Zahlan et al., 2014] searched neighbors in the database for every scaled point in chosen limits for all parameters. Then an average for all found HTC was calculated and compared to the scaled one. Thereby, the limits must be set in a way to find enough neighbor data for a statistical evaluation but also small enough for minimal deviations caused by different parameters. However, even in a small parameter range all found neighbors could be located on one side of the parameter matrix. This consequently produces a different mean value to the scaled point, as seen in figure 6.2.
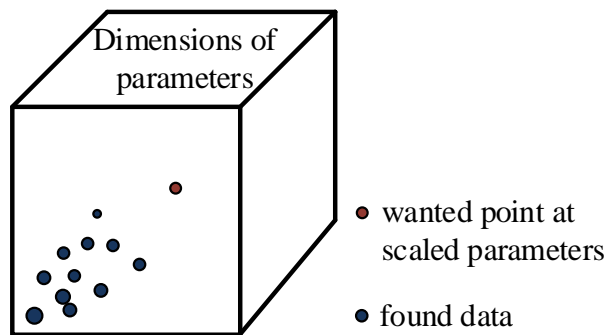
Figure 6.2.: Scheme of found neighbors of the database near the scaled data point in the parameter dimensions

However, the error of the comparison method must be minimized to validate the fluid-to-fluid scaling models. An interpolation of the data from the database to the scaled point could be helpful to increase the reliability and accuracy of the comparison method. At least 16 points are necessary for a linear interpolation for the heat transfer which depends on pressure, mass flux, heat flux and bulk enthalpy. But the heat transfer at supercritical conditions depends non-linearly on the parameters. Additionally, the data points are not distributed equally in the parameter ranges, which minimizes the chance of finding all necessary surrounding data points for the interpolation. Therefore, an interpolation is inappropriate for this objective.

6.1.3.1. New transformation method

Another method was used for the comparison in this study. The idea is inspired from Badea et al. [Badea et al., 2018] and from Löwenberg et al. [Löwenberg, 2007]. Instead of an interpolation, the authors use correlations to transform neighboring data to the wanted point. The neighboring data are used to calculate the deviation of the correlation to the experimental data. The HTC of the wanted point is calculated with the best correlation and the known deviation. Figure 6.3 shows this transformation method schematically.
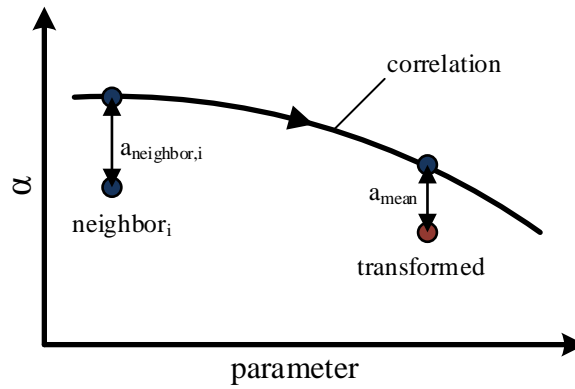
Figure 6.3.: Scheme of scaling one found neighbor to the wanted point by using a correlation

The complete method used in this study is illustrated schematically in figure 6.4 including the procedures for scaling and comparison. Firstly, all neighbors within given limits are determined for one scaled point. The best correlation is chosen based on physical and statistical aspects. Then, the HTC of the data base is transformed to the scaled parameters using the best correlation. Finally, the scaled HTC is compared with the transformed HTC from the database. This method is repeated for every point scaled from R134a and CO_2. The steps are described in detail in the following paragraphs. The advantage of this method is the usage of correlations instead an interpolation. Compared to interpolations, less neighboring data points are needed. Correlations are able to describe the local trend or dependencies of the HTC on the parameters quite well [Badea et al., 2018].
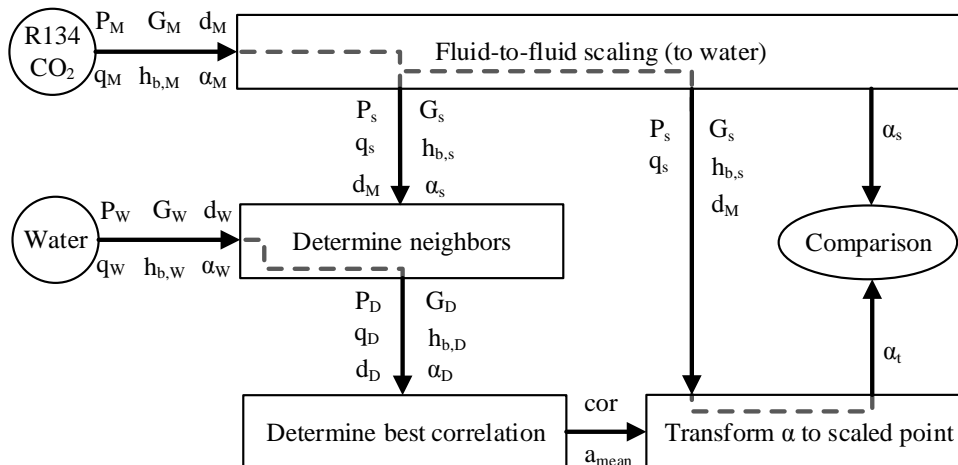
Figure 6.4.: Scheme of comparison method with transformed data using correlations with M for model fluid, W for water, s for scaled, D for determined (neighbor) and t for transformed

Determine neighbors

Neighboring data points are searched in the water database for every scaled point within the limits listed in table 6.3. The limits are chosen small enough to ensure a physical similarity of the heat transfer within the given range. The HTC is very sensible at the pseudo-critical point. This makes

it necessary to find a finer and more regular scale for the bulk state. Moreover, the bulk enthalpy varies strongly with temperature near the pseudo-critical point. Therefore, the bulk enthalpy is chosen instead of the bulk temperature.

Table 6.3.: Limits for determining neighbor data points in the water data base

Parameter	Limit
Pressure	3 %
Diameter	2 for d≤10, else 4 mm
Mass flux	10 %
Heat flux	10 %
Bulk enthalpy	1.5 %
l/d	10 %

Transform water data

The next step is to gain the HTC of the water database with identical parameters of the scaled point. The HTC was calculated for every found neighbor using ten correlations which have been stated as good in literature. These are the correlation of Badea et al. [Badea et al., 2018], Bishop, Chen and Fang, Cheng et al., Jackson and Hall, Mokry et al., Pethukov et al., Swenson et al., Watts and Chou and Yamagata et al. [Bishop et al., 1965, Chen & Fang, 2014, Cheng et al., 2009b, J.D. Jackson, W. B. Hall, 1979, Mokry et al., 2011, Petukhov, 1961, Swenson et al., 1965, Watts & Chou, 1982, Yamagata et al., 1972]. Then, the relative deviation $e_{cor,ij}$ between the HTC calculated from the correlation to the one based on the database are calculated for every neighbor i and every correlation j as defined in equation 6.1.

$$a_{neighbor,ij} = \frac{HTC_{cor,ij}}{HTC_{neighbor,i}} \tag{6.1}$$

$$a_{mean,j} = \frac{1}{N} \sum_{i=1}^{N} a_{neighbor,ij} \; ; \quad a_{std,j} = \sqrt{\frac{1}{N-1} \sum_{i=1}^{N} \left(a_{neighbor,ij} - a_{mean,j}\right)^2} \tag{6.2}$$

The mean and standard deviation $a_{mean,j}$ and $a_{std,j}$ are calculated for every single correlation over all neighbors as defined in equation 6.2. Additionally, the minimum and maximum deviation $a_{min,j}$ and $a_{max,j}$ are determined. The final step is to chose the best correlation with the corresponding mean deviation a_{mean} to calculate the transformed HTC of the database. The corresponding decision tree is shown in figure 6.5.
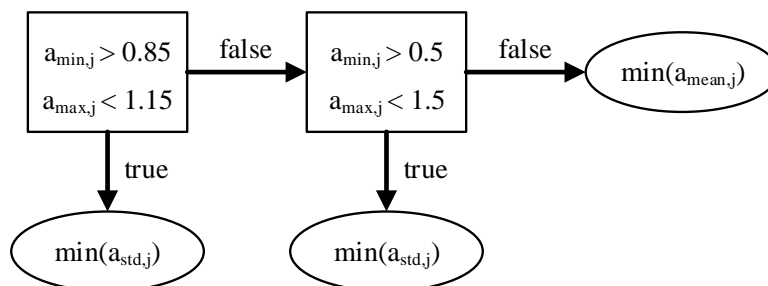
Figure 6.5.: Decision tree to find the best correlation for the wanted and scaled point

If there is one or more correlations predicting the HTC of all neighbors in a range of 15 %, then the correlation with the smallest standard deviation is chosen. If there is no correlation within the 15 %, then the range is set to 50 %. Hereby, also the correlation with the smallest standard deviation is chosen. Taking the correlation with the smallest standard deviation ensures that the mean deviation a_{mean} is most likely the same at the transformed point. The best correlation and the corresponding mean deviation a_{mean} are used to calculate the transformed HTC of the water database for the scaled parameters as defined in equation 6.3.

$$\alpha_t = \alpha_{cor} \cdot a_{mean} \tag{6.3}$$

6.1.4. Comparison of scaled model fluid data and transformed water data

At the end, the scaled HTC of the fluid-to-fluid scaling model (s) is compared to the transformed HTC (t) from the database. The MD and the STD are calculated using the equations 3.23 - 3.26 with equation 6.4 for the deviation. The results are discussed in section 6.2.

$$dev = \frac{\alpha_s - \alpha_t}{\alpha_t} \cdot 100 \tag{6.4}$$

6.1.5. Validation of method and comparison procedure

450 random and 100 directly lined up points are selected and removed from the water database to verify and validate the transformation method. This 550 selected points are treated as scaled data points. In the same way as described before, the "scaled" parameters are used to find neighbors and to determine the best correlations with corresponding deviation a_{mean} to calculate the transformed HTC using the remaining database. The transformed HTC is compared to the HTC from the selected data points. The mean deviation of all points is 0 % with a standard deviation of 3.4 %. The small deviations proof that the transformation method is working properly and can be used for the fluid-to-fluid scaling model assessment.

Usage as prediction method

As discussed before, this transformation method produces minimal errors. Therefore, this method could be used for the interpolation process in the prediction method for Look-up Lists (LUL). The advantage of the LUL is that it contains the raw and unaltered experimental data with no additional uncertainty as look-up tables or correlations. If the LUL is combined with the transformation method, the result is a reliable prediction method with small uncertainties. In this case, the needed parameters are treated as scaled parameters in figure 6.4. The only disadvantage is the huge database which is needed to cover all required parameter ranges.

6.1.6. Procedure for the model of Azih and Yaras

The fluid-to-fluid scaling model of Azih and Yaras is assessed differently. The mass flux and heat flux cannot be scaled directly because several identified dimensionless numbers depend on both parameters. The transformation method cannot be used in this case. Instead, the dimensionless numbers defined in the equations B.56 - B.60 are calculated for all databases with the dimensionless bulk enthalpy as defined by Ambrosini [Ambrosini & Sharabi, 2008] in equation B.54 and proposed by Azih and Yaras for the comparison [Azih & Yaras, 2017]. Then, data points in the water database are searched for every data point in R134a and CO_2 within the limits given in table 6.4. Two set of limits are chosen because only a few points or no points were found at the narrow limit set 1. The Nusselt number is compared with the mean Nusselt number of all found neighbors in the same manner as the HTC for the other scaling models.

Table 6.4.: Limits for parameters and numbers for the scaling model of Azih und Yaras

	Number	Limit set 1	Limit set 2
P_c	eq. B.56	3 %	5 %
h_{in}^*	eq. B.57	10 %	15 %
Re_{in}	eq. B.58	20 %	25 %
Ri_{in}	eq. B.59	20 %	25 %
π_A	eq. B.60	20 %	25 %
h_b^*	eq. B.54	3 %	5 %
d		2 for d≤10, else 4 mm	

6.2. Assessment of fluid-to-fluid scaling models

6.2.1. Statistical evaluation

The deviations from the scaled HTC to the transformed HTC from the water database are listed in table 6.5 for the assessed fluid-to-fluid scaling models. For Azih und Yaras, the deviations from the Nusselt numbers are listed for the two sets of different limits as discussed in section 6.1.6. The scaling model of Cheng modified by Zahlan, as discussed in section 2.4.3, is named Cheng-mod. The MD and STD are given in total and for differently grouped deviations to asses the scaling models at different influences of buoyancy and thermal-induced bulk flow acceleration. The groupings for the scaled data are none-influenced (None-In), influenced by buoyancy if $Bu>10^{-5}$ (Bu-In), influenced by acceleration if $Ac>4x10^{-6}$ (Ac-In) and influenced by both effects (Bu-Ac-In). There are no CO_2-lit data which exceed the limit for the acceleration parameter. In section 6.1.5, it is shown that the method for the transformation and comparison produces a negligible error on the results. All used data are experimental data and the scaled data are compared directly with the water data. Therefore, it can be assumed that the deviations shown in table 6.5 are mainly caused by the fluid-to-fluid scaling models and are used to directly assess the models.

Table 6.5 shows that no fluid-to-fluid scaling model shows the best results for all data. The models alternate in the best scaling for the different data bases and influences. The mainly positive mean deviations indicate that almost all models lead to a higher HTC. Especially, the model of Azih and Yaras as well as Zwolinski show high positive MD. The main reason could be the scaling of the mass flux by the Reynolds number only. Due to the higher viscosity of CO_2 and R134a than of water, the mass flux scaled to water is smaller than the one of the original fluids. Whereas the scaled mass fluxes of the other models are always higher than the mass flux of the origin data. A lower mass flux decreases the heat transfer and results in smaller transformed HTC of the water database. This leads to high positive deviations, as seen in equation 6.4.

The model of Zahlan shows the best results for the data scaled from D-R134a. It is remarkable that the MD of all models increases for the none-influenced data, even for the data scaled by the model of Zahlan, which was developed to scale none-influenced data. The STD increases for the buoyancy influenced data, while the data influenced by acceleration show smaller STD. A reason could be the dependency of the buoyancy at the inlet temperature for low mass fluxes, as discussed in section 5.5. The scaling models do not address the inlet temperature, except from the model of Azih. Thus, there are four different HTC for the same scaled parameters of mass flux, heat flux, pressure and bulk enthalpy due to the different buoyancy effect caused by the four different inlet temperatures. Thus, four different HTC are compared to one HTC of the water database and leading to higher STD. The HTC influenced by the acceleration are not sensible on the inlet temperature and therefore the STD decreases. In general, the MD and STD for R134a are higher than for the scaled data of CO_2. A reason could be that the development of the models are based on the pair of water and CO_2 and therefore empirical values are not fitted to R134a.

Table 6.5.: Deviations in % of data scaled to water to data of D-water for the different scaling models

Model	all		None-In		Bu-In		Ac-In		Bu-Ac-In	
	MD	STD	MD	STD	MD	STD	MD	STD	MD	STD
D-R134a:										
Azih set2	159	322	125	216	434	698	57.2	-	-	-
Cheng	18.5	20.6	22.8	20.2	10.8	19.4	12.9	14.7	29.9	22.1
Cheng-mod	5.1	23.4	10.4	19.5	-2.2	26.4	11.2	13.8	21.9	18.7
Tian	21.6	23.1	26.9	23.9	12.9	18.6	4.2	10.1	12.4	17.6
Zahlan	4	22.4	9.5	19.4	-4.3	24.3	10.7	13.1	21.3	18.2
Zwolinksi	57	60.3	69.5	64.9	31	37.1	22.6	21.4	30.9	28.5
D-CO_2:										
Azih set1	12.1	42.7	39.2	23.7	5.6	44.3	26.5	16.5	32.9	12.3
Azih set2	49.3	51.5	74.6	54.8	36.7	47.1	39	24.9	39.2	15.6
Cheng	7.9	18.1	16.2	18.5	5.9	19.1	7.3	10.6	5.8	10.5
Cheng-mod	1.8	22.6	18.5	32.3	-2	20.9	5.6	10.1	3.1	7.1
Tian	3.1	16.7	4.4	14.2	-2.1	23.4	2.5	16.9	-6.1	19.5
Zahlan	2.4	22.5	19.1	31.1	-0.7	21.4	5.7	10	3.8	8.9
Zwolinksi	39.1	38.9	43.2	22.4	46.2	45.8	20.5	16.3	25.7	19.2
D-CO_2-lit:										
Azih set1	54.1	45.6	57	44.1	0.8	39.5	-	-	-	-
Azih set2	77.7	167	91.6	175	-14.2	29.4	-	-	-	-
Cheng	10.7	18.9	15.1	19.4	0.2	12.5	-	-	-	-
Cheng-mod	-1.5	14.8	4.3	13.8	-9.5	12	-	-	-	-
Tian	1.2	13.9	4.2	13.9	-4.6	11.9	-	-	-	-
Zahlan	-2.1	13.9	4.4	12.8	-11.4	9.3	-	-	-	-
Zwolinksi	35.5	31	40	31.9	16.5	16.4	-	-	-	-

The best scaling results for the data scaled from the D-CO_2 are produced by the model of Tian. For the D-CO_2-lit, the models of Tian, Zahlan and the model of Cheng-mod show similar good results. The models of Zahlan and Cheng-mod are based on these data and therefore it is not surprising that they work well. Remarkable is the good scaling capability from the model of Zahlan for the buoyancy and acceleration influenced data . The authors aimed to scale only the none-influenced heat transfer because the buoyancy required different scaling relationships.

Tian et al. developed the fluid-to-fluid scaling model with a new dimensionless number to scale the mass flux. The number includes the acceleration number π_A of Cheng [Cheng et al., 2009b], which is also used by Jackson to identify if the heat transfer is influenced by acceleration. This leads to better results in scaling these data, as seen in table 6.5 in the column Ac-In. Here, the model of Tian shows the smallest MD an STD. The other models also show smaller MD and STD compared to the none-influenced data although it is summarized in section 5.5 that the HTC is very sensible to the heat flux as the acceleration starts to influence the heat transfer. Further, these data are close to the pseudo-critical point where huge differences were observed in the HTC for data of the literature.

The buoyancy influenced data show high MD and STD for all models. Jackson concluded in his study that a complete similarity is impossible if buoyancy effects the heat transfer. Tubes with big diameter can avoid this impediment. Nevertheless, the inlet conditions have to be the same to satisfy the similarity of all dimensionless number for the scaling [Jackson, 2008]. As summarized in section 5.5, the inlet condition can have a strong influence on the location and bulk enthalpy

where the reduction of the HTC occurs. Here, the inlet conditions must be preserved in the scaling method. This was also found by Azih and Yaras. Therefore, the authors developed the fluid-to-fluid scaling model based on inlet conditions [Azih & Yaras, 2017]. In this study, only a few pairs of data are found with similar values of dimensionless numbers identified by Azih and Yaras. However, the MD and STD are pretty high for the scaling model of Azih and Yaras, as seen in table 6.5. Another set of extended limits was tested to increase the numbers of found data, but MD and STD increased more. The high deviations could result from the relative high limit sets for the dimensionless numbers. Therefore, this results do not proof a reliable scaling capability for the model of Azih and Yaras.

It can be concluded that no model can scale all fluids and data the best. This means that the models must be adjusted for the pair of fluid they are applied for. This could be empirical constants as for example the exponent of the Prandtl number for scaling the mass flux in the models of Cheng or Zahlan. The fluid-to-fluid scaling model of Zahlan shows the best results with the mean deviation always below 5 % and the smallest standard deviations for all data of the databases. The only exception is the result for the scaled D-CO$_2$ data of this study, which has the smallest deviations with the model of Tian.

6.2.2. Parameter evaluation

The deviations of the scaled R134a data are examined in detail for the scaling models of Zahlan and Tian in the next sections. This models and data are chosen because they show the most found data points (over 7000) with the highest reliability. The high STD facilitate the graphical identification of parameter ranges with bad agreement between scaled and transformed HTC. The qualitative behavior of the parametric trends of the other databases is similar and are hence not shown. The trends of the parameter over inlet temperature, pressure, dimensionless length, heat flux or ratio of heat flux to mass flux do not show any noticeable behavior and are hence not shown.

Acceleration number

Figure 6.6 shows the deviations of the D-R134a data versus the Acceleration number for the scaling models of Tian and Zahlan. The scattering of the deviations is very high at Acceleration numbers close to zero. This could be caused by the small heat fluxes at small Acceleration numbers. At this point, the HTC is very sensitive to small changes and the uncertainty of the HTC is very high, as discussed in section 3.6. Overall, the main emphasis of the deviations is positive. This means that both models scale the HTC to high, especially for Acceleration numbers between $1x10^{-6}$ to $4x10^{-6}$. Jackson proposed that $4x10^{-6}$ is the limit where the thermally-induced bulk flow acceleration starts to influence the heat transfer. However, starting from this point, the deviations decrease as shown in figure 6.6.

Buoyancy number

The deviations are shown versus the Buoyancy number in figure 6.7 for the data scaled from D-R134 with the models of Tian and Zahlan. The behavior is similar to the one of the Acceleration number. At Buoyancy numbers close to zero, the scattering is very high. Up to the Buoyancy number of $0.5x10^{-5}$, the mean deviations is positive, which means the models scale the HTC too high. Beyond $0.5x10^{-5}$, the deviations' main emphasis is negative. Here, the models scale the HTC too low. The scattering is reduced after that and most deviations are approaching 0 % with increasing Buoyancy number. One reason could be the scaling models themselves. Another reason could be the different constellations of the databases of R134a, CO$_2$ and water concerning the parameters as heating length and inlet temperature. The onset and the location of the HTC minimums caused by buoyancy depend also on the inlet temperature, as observed and discussed in section 5.
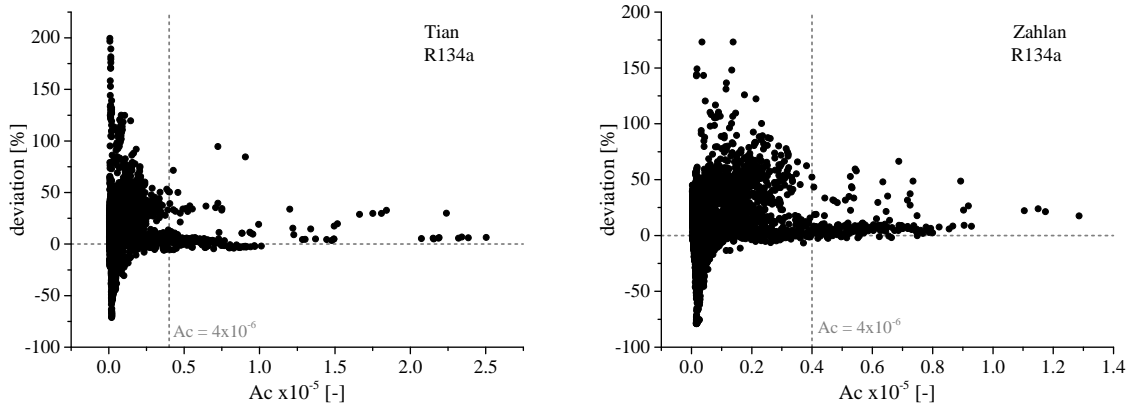
(a) Deviation of scaled data of D-R134 to D-water with model of Tian versus Acceleration number

(b) Deviation of scaled data of D-R134 to D-water with model of Zahlan versus Acceleration number

Figure 6.6.: Deviation of scaled data of D-R134 to D-water with models of Tian et al. and Zahlan et al. versus Acceleration number
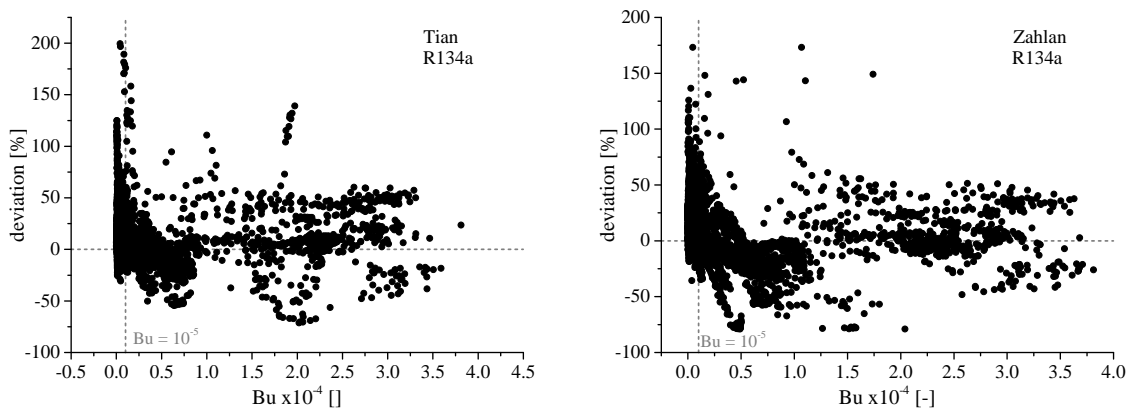
(a) Deviation of scaled data of D-R134 to D-water with model of Tian versus Buoyancy number

(b) Deviation of scaled data of D-R134 to D-water with model of Zahlan versus Buoyancy number

Figure 6.7.: Deviation of scaled data of D-R134 to D-water with models of Tian et al. and Zahlan et al. versus Buoyancy number

Mass flux

Figure 6.8 shows the deviations for different mass fluxes of the models from Tian and Zahlan for D-R134a. It can be seen that no data are found for the model of Tian for the scaled mass fluxes of 2000 kg/m^{2}s. However, as the mass fluxes increase the deviations are shifted to positive values for both models. This means at higher mass fluxes the scaling model overpredicts the HTC. On the other hand, the deviations have a smaller scattering for increasing mass flux, which results in a smaller STD.

Bulk enthalpy

The distribution of the deviations along the scaled bulk enthalpy is shown in figure 6.9. The high scattering of the deviations at the bulk enthalpies around 330 kJ/kg is conspicuous. This is the region where the local HTC minimum which is caused by buoyancy forces at the inlet often occurs. As discussed before, the HTC is very sensitive to changes of the boundary conditions and parameters at this region. Another peak of high scattering is at bulk enthalpies from around 380 kJ/kg to 420 kJ/kg. This includes the pseudo-critical bulk enthalpies for the pressures of 4.22 MPa to
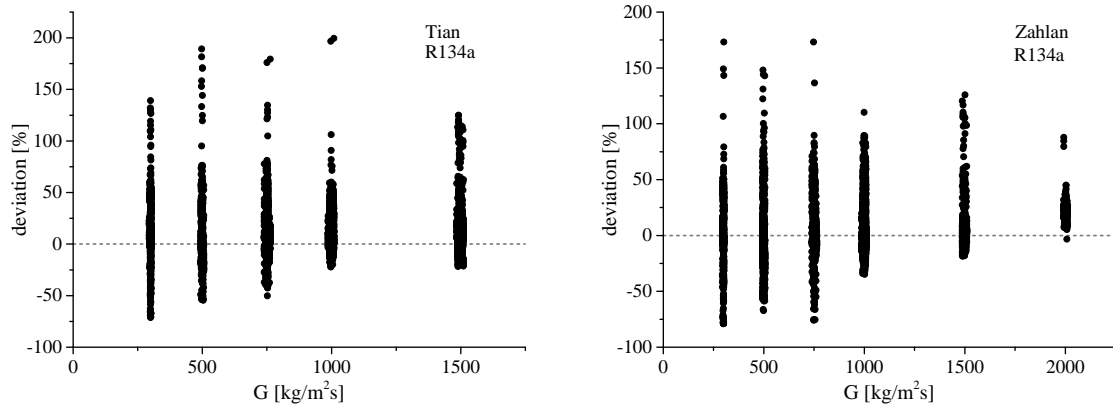
(a) Deviation of scaled data of D-R134 to D-water with model of Tian versus mass flux

(b) Deviation of scaled data of D-R134 to D-water with model of Zahlan versus mass flux

Figure 6.8.: Deviation of scaled data of D-R134 to D-water with models of Tian et al. and Zahlan et al. versus mass flux

5.51 MPa. The main emphasis of the deviations is pushed to positive values at this point. This could be due to the scaling models or due to the fact that the HTC is found to be higher nearby the pseudo-critical point in this study compared to other studies, as shown in section 5.4.1. Starting from the pseudo-critical point, the model of Tian shows better results with smaller scattering and a mean deviation closer to zero than the model of Zahlan. This could be because Tian implemented the dimensionless acceleration number π_A of Cheng to scale the mass flux. This number describes the heat transfer influenced by the thermal-induced bulk flow acceleration, which mainly occurs at bulk enthalpies close to the pseudo-critical point.
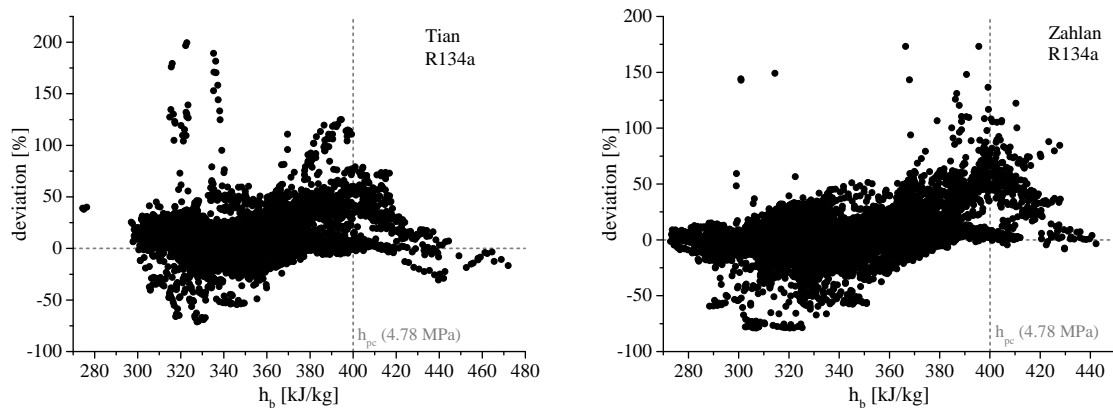
(a) Deviation of scaled data of D-R134 to D-water with model of Tian versus bulk enthalpy

(b) Deviation of scaled data of D-R134 to D-water with model of Zahlan versus bulk enthalpy

Figure 6.9.: Deviation of scaled data of D-R134 to D-water with models of Tian versus bulk enthalpy

6.3. Modified fluid-to-fluid scaling models

As discussed in section 6.2, the fluid-to-fluid scaling models work differently well for different fluid combinations. The model of Zahlan scales the CO_2-lit data quite well and no improvement is needed. The data from this study are not scaled as good as the literature data by any model. Therefore, a adaptation of the models to the produced data is needed.

6.3.1. Modified model of Cheng

The model of Cheng et al. is chosen to scale the data of R134a to water as the modified model shows similar results to the one of Zahlan. The literature review showed that the dimensionless number θ of Cheng, defined in equation 2.29 (c), shows better agreements for the fluid properties curves of different fluids, as discussed in section 2.4.3 and seen in figure 2.14. Cheng proposed that the exponent of 5/12 of the Prandtl number in equation B.67 for scaling the mass flux must be determined empirically. The databases collected in this study are used for that objective. The exponent is varied from 0.5 to 0.9 and the impact on the MD and STD of the scaled HTC to water is listed in table 6.6.

Table 6.6.: Variation of exponent for mass flux scaling of model of Cheng with MD and STD

exponent	D-R134a		D-CO$_2$		D-CO$_2$-lit	
	MD	STD	MD	STD	MD	STD
0.5	14.7	24	5.5	21.4	6.4	17.7
0.6	7.2	22.8	2.5	22.9	-0.3	14.7
0.7	4.1	23.2	0.4	22.8	-3.3	16.9
0.8	6.5	40.2	-0.4	22	-5.2	20.6
0.9	0.8	38.5	-3.6	22.1	-9.3	25.7

As seen in table 6.6, the exponent of 0.7 shows the results with the smallest deviations for scaling D-R134a to water. To scale the D-CO$_2$ data and the D-CO$_2$-lit data to water, a exponent of 0.8 or 0.6 respectively results in the smallest deviations. The varying exponent for different fluids can be explained by the different trends of the dimensionless fluid properties shown in figure 2.14. The trends of CO$_2$ and R134a differ with a different factor to the trends of water. Therefore, different exponents are needed to scale them to water. It is remarkable that for the different databases the STD behaves differently for the varying mass flux exponent. For R134as the STD suddenly increases from 23 % to 40 % as the exponent increases from 0.7 to 0.8. The STD of the scaled D-CO$_2$ data keeps almost constant. The STD of the scaled data of D-CO$_2$-lit has the same behavior as the MD and has also its minimum value at a exponent of 0.6.

6.3.2. Modified model of Tian

The model of Tian et al. shows the best results so far for D-CO$_2$. Further adaptations are made to improve the scaling applicability of it. The derived dimensionless number to scale the mass flux (equation B.89) includes the acceleration number π_A defined at the pseudo-critical temperature. Looking at the derivation of the number in their paper, it must not be defined at the pseudo-critical temperature. The acceleration number is defined at local bulk enthalpies in the modified version for a more local approach of the model. The exponent of the Reynolds number of -0.9 in the mass flux scaling was derived using an empirical friction law and does not have to be valid at supercritical conditions. Thus, the exponent can be adopted using the databases of this study as well. The MD and STD for the exponents of -1.1 to -0.4 for all data are listed in table 6.7.

Table 6.7 shows that the best exponent varies strongly for the different databases. It changes from -0.4 for D-R134a to -0.7 for D-CO$_2$ to -1.1 for D-CO$_2$-lit. The exponent must be varied stronger for the model of Tian than for the model of Cheng. Here, the STD of D-R134a keeps almost constant. The STD of D-CO$_2$-lit has the same trend as the MD. However the STD of D-CO$_2$ shows a contrary behavior to the MD. It decreases as the MD increases.

Table 6.7.: Variation of exponent for mass flux scaling of model of Tian with MD and STD

exponent	D-R134a		D-CO_2		D-CO_2-lit	
	MD	STD	MD	STD	MD	STD
-0.4	2.6	24.8	-3.4	16.8	-9.7	21.1
-0.5	3.9	22.6	-2.1	17.9	-7.9	20.0
-0.6	4.6	22.9	-1.1	17.9	-7.8	14.5
-0.7	6.3	22.1	-0.8	18.4	-6.2	13.3
-0.8	8.3	21.2	0.6	19.1	-4.7	12.5
-0.9	11.2	22.4	1.2	18.3	-3.3	12.3
-1	14.3	23.1	2.2	17.8	-1.9	12.0
-1.1	16.5	24.1	3.1	17.1	-0.3	11.8

6.3.3. Assessment of modified scaling models

The modified models of Cheng and Tian are assessed to all databases and the results are listed in table 6.8. The adapted models with the best exponent are picked for the single databases. Additionally, the original models of Cheng and Tian and the model of Zahlan are listed in table 6.8 for comparison. Better results for all databases can be seen for the modified model of Cheng. The separation of the data into none-influenced and buoyancy and acceleration influenced data show that the modified model of Cheng shows great improvements in scaling the none-influenced data compared to the original model. However, the buoyancy influenced data are scaled more precisely by the original model of Cheng. A similar behavior can be seen for the adapted model of Tian. It's scaling capability is increased for the modified version for none-influenced data, but it is decreased for buoyancy and acceleration influenced data compared to the original model.

Table 6.8.: Deviations of scaled data for the modified and unmodified scaling models

Model	all		None-In		Bu-In		Ac-In		Bu-Ac-In	
	MD	STD	MD	STD	MD	STD	MD	STD	MD	STD
D-R134a:										
Cheng	18.5	20.6	22.8	20.2	10.8	19.4	12.9	14.7	29.9	22.1
Tian	21.6	23.1	26.9	23.9	12.9	18.6	4.2	10.1	12.4	17.6
Zahlan	4	22.4	9.5	19.4	-4.3	24.3	10.7	13.1	21.3	18.2
Cheng-0.7	4.1	23.2	10.8	20.3	-5.4	24.1	11.1	13.9	18.8	16.9
Tian-0.4	2.6	24.8	13.6	18.7	-8.6	26	8.2	12.4	14.9	13.5
D-CO_2:										
Cheng	7.9	18.1	16.2	18.5	5.9	19.1	7.3	10.6	5.8	10.5
Tian	3.1	16.7	4.4	14.2	-2.1	23.4	2.5	16.9	-6.1	19.5
Zahlan	2.4	22.5	19.1	31.1	-0.7	21.4	5.7	10	3.8	8.9
Cheng-0.8	-0.3	22	-0.7	15	1.6	43.1	-0.9	20.8	-8.2	17.7
Tian-0.7	-0.8	18.3	0.8	12.9	-6.1	26.3	-1.8	21.7	-10.4	25.3
D-CO_2-lit:										
Cheng	10.7	18.9	15.1	19.4	0.2	12.5	-	-	-	-
Tian	1.2	13.9	4.2	13.9	-4.6	11.9	-	-	-	-
Zahlan	-2.1	13.9	4.4	12.8	-11.4	9.3	-	-	-	-
Cheng-0.6	-0.3	14.7	5.2	14.1	-8	12	-	-	-	-
Tian-1.1	-0.3	11.8	3.6	9.7	-7.1	12.1	-	-	-	-

6.4. Summary of the assessment of fluid-to-fluid scaling models

It can be concluded that the model of Zahlan can to scale the data of D-R134a the best. The modified model of Tian shows the best results for scaling the data of the D-CO_2 and D-CO_2-lit. However, the original model of Cheng produces the smallest deviations for data influenced by buoyancy. The data influenced by acceleration are scaled best by the original model of Tian. This shows that the models developed so far can be only fit to satisfy a certain fluid combination or certain influenced data. At this point, a combination of models is needed to reliably scale data from one fluid to another. The models must be fitted to the fluid combination and chosen for different influenced data.

Further work is needed to develop a model to reliably scale all data from one fluid to another. More improvements are needed especially for scaling data influenced by buoyancy. Table 6.8 shows that an inclusion of the acceleration number in the model of Tian improved the scaling capability of acceleration influenced data. Therefore, an inclusion of the Buoyancy number could overcome the difficulties of scaling buoyancy influenced data in a model based on local conditions. Otherwise the inlet conditions must be scaled for parameters where the HTC depends on the inlet temperature.

7. CHF Results and Discussion

The results of the CHF experiments of ts-3 are introduced in this chapter. The influence of mass flux, pressure, subcooling and vapor quality on the CHF are discussed. The results are compared with data from the literature and to correlations. Fluid-to-fluid scaling enables the comparison with the CHF look-up table and water correlations, which results are discussed at the end of this chapter.

7.1. Data selection for CHF analysis

No data must be removed from the CHF database because no fluid instabilities or other irregularities are observed. Table 7.1 lists three reproduced sets from different days. It can be seen that the reproduced CHF values and vapor qualities are very close. The deviations in the CHF values can be explained with the same relative deviations in the mass flux. This shows the good reproducibly of the CHF data at ts-3 and therefore all data are used in this study for the analysis.

Table 7.1.: Examples of reproduced CHF experiments at different days

Pressure	Mass flux	Inlet temperature	CHF	Vapor quality
$[MPa]$	$\left[\frac{kg}{m^2 s}\right]$	$[°C]$	$\left[\frac{kW}{m^2}\right]$	$[-]$
2.83	3114	42.7	220.6	0.064
2.78	3137	42.9	220.1	0.056
2.79	4317	62.8	199	0.098
2.82	4190	63.4	193.6	0.113
2.80	4428	72.9	166.2	0.176
2.80	4207	73.1	156.9	0.180

7.2. Results of ts-3

7.2.1. Based on inlet vapor quality

The experiments are conducted with different inlet temperatures to investigate the influence of inlet and local vapor quality on the CHF. The CHF is plotted over the inlet vapor quality for different mass fluxes and pressures in figure 7.1. Whereas smaller inlet temperatures result in smaller inlet vapor qualities.

7.2.1.1. Influence of inlet vapor quality on CHF

In figure 7.1 can be seen that the CHF decreases for increasing inlet vapor quality for the same mass flux and pressure. There exists a linear correlation between CHF and inlet vapor quality at
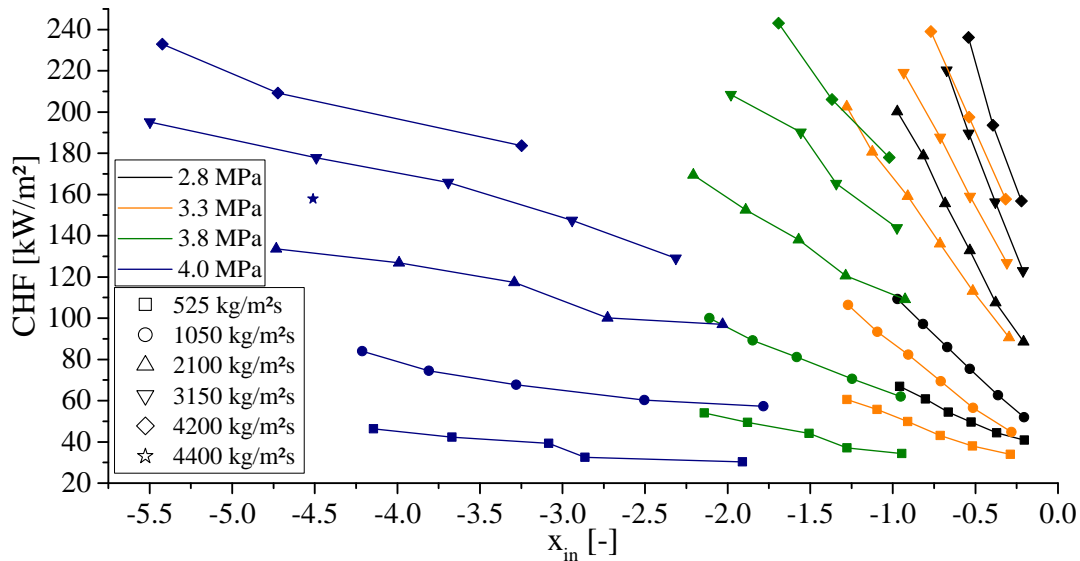
Figure 7.1.: CHF versus inlet vapor quality for all mass fluxes and pressures of ts-3 in R134a

2.8 MPa and 3.3 MPa. Most trends at the higher pressures of 3.8 MPa and 4 MPa also show this linear correlation. Some trends, as the ones of 525 kg/m²s for example, show a steeper decline between two CHF data than expected from the linear trend. An explanation for the strong decrease can be either the change of the mechanism from DNB to dryout or the limiting quality phenomenon observed by Groneveld [Groeneveld, 2011], which is described in section 2.3.1. This will be discussed in detail for the local vapor quality in section 7.2.2. The gradients of the trends with constant mass flux and pressure increase with increasing mass flux and decreasing pressure.

7.2.1.2. Influence of mass flux on CHF

The CHF is increased for increasing mass fluxes at constant inlet vapor qualities. The increase of the CHF is due to the higher energy the flow needs to reach the critical vapor quality. Also a higher mass flux strengthens the turbulence, which improves the heat transport from the wall and pushes the dryout to higher heat fluxes. A further effect is the reinforced deposition of droplets at higher turbulence and pressures. Especially at high pressures, the droplets are able to follow the turbulent flow due to the smaller droplet sizes.

7.2.1.3. Influence of pressure on CHF

The CHF decreases with increasing pressure for constant mass fluxes and inlet vapor qualities. The reduction of the CHF at 3.8 MPa and 4 MPa is more significant than at smaller pressures. The decrease is more pronounced by increasing mass fluxes and inlet vapor qualities. The CHF is theoretically defined to be zero at the critical pressure. Therefore, all CHF trends have to approach zero with increasing pressure.

7.2.2. Based on local vapor quality

In this section, the local vapor quality is the same as the vapor quality of the dryout or DNB point. The boiling crisis occurs at the end of the test section because the experiments have been conducted with increasing heat flux in small steps at constant remaining parameters. Therefore, the local vapor quality is the same as the vapor quality at the outlet of the test section. The influence of the local vapor quality on the CHF is shown in figure 7.2.
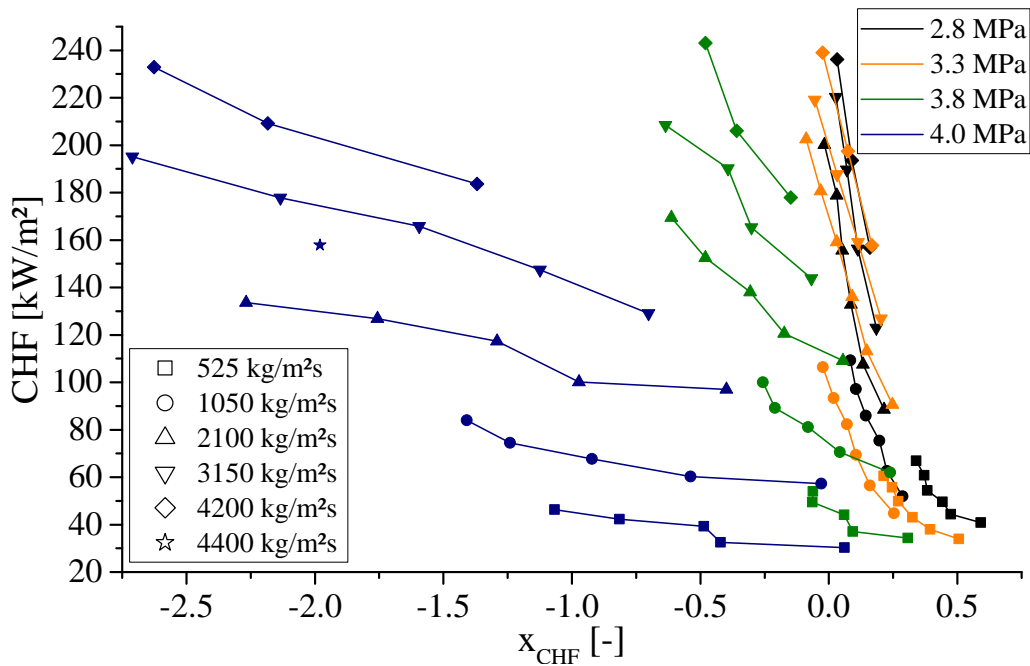
Figure 7.2.: Influence of local vapor quality on CHF for all data points of ts-3 in R134a

7.2.2.1. Influence of local vapor quality on CHF

It is obvious in figure 7.2 that the CHF decreases with increasing vapor quality for constant mass fluxes and pressures. This is a result of the increasing volume fraction of the vapor at higher vapor qualities. The wall can dry out at lower heat fluxes and the remaining liquid parts cannot rewet the heated wall sufficiently. This effect is getting stronger as the vapor quality increases due to the fact that the mechanism changes from departure of nucleate boiling to dryout, as discussed in section 2.3. Especially at positive vapor qualities, it seems that the CHF trend approaches asymptotically zero. A small difference in vapor quality causes a big difference in the CHF at this point. This effect shows no dependency on the mass flux. An explanation could be the transitions from the DNB to the dryout, as stated in the heat atlas [Verein Deutscher Ingenieure, 2013].

The trends of $525\,kg/m^2s$ for 2.8 MPa and 3.3 MPa are very sensitive to the vapor quality, not linear and show a sudden drop of the CHF. This can be explained by the transition from the entrainment-controlled region to the deposition-controlled region, as discussed in section 2.3.1. This limiting quality phenomenon only occurs at low mass fluxes and pressures below 70 % of the critical pressure [Groeneveld, 2011].

7.2.2.2. Influence of mass flux on CHF

The CHF increases with increasing mass flux at constant local vapor qualities and pressures of 3.8 MPa and 4 MPa. The reasons for this dependency are the same as for the inlet vapor quality and explained in section 7.2.1. Figure 7.3 shows the CHF for a local vapor quality of -0.1 to 0.6 for a detailed picture of the CHF trends of the pressures 2.8 MPa and 3.3 MPa.

The CHF is smaller for mass fluxes of $1050\,kg/m^2s$ than of $525\,kg/m^2s$ at 3.3 MPa. A similar trend is recognizable at 2.8 MPa. Above $1050\,kg/m^2s$, the CHF increases with increasing mass flux for all pressures. This inverse mass flux effect is caused by the mechanism change from DNB to dryout and is also observed by other authors, as described in section 2.3.1.

7.2.2.3. Influence of pressure on CHF

At constant inlet vapor quality, the CHF decreases for increasing pressures, as shown in figure 7.1. This remains true for the CHF data plotted in figure 7.2 at constant local vapor qualities for the
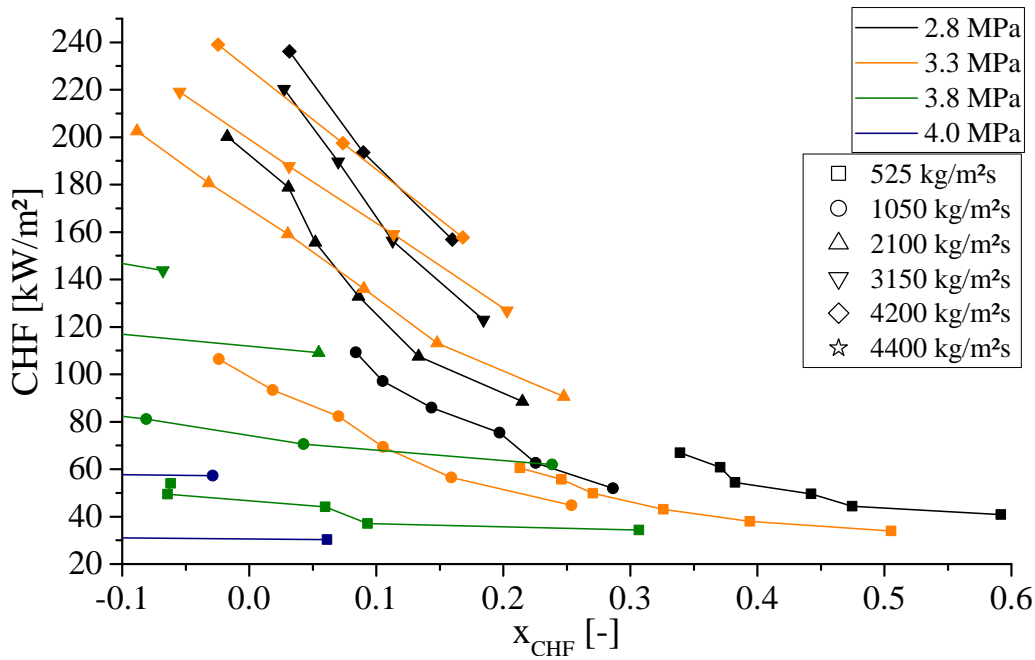
Figure 7.3.: Influence of local vapor quality on CHF at high vapor qualities of ts-3 in R134a

pressures of 3.8 MPa and 4 MPa. However, the maximum CHF changes from 2.8 MPa to 3.3 MPa at mass fluxes of 2100 kg/m^{2}s to 4200 kg/m^{2}s, as seen in figure 7.3. The trends of both pressures cross around a local vapor quality of 0.1. At a local vapor quality of 0.25 the pressure of 3.8 MPa shows the highest CHF for the mass fluxes of 1050 kg/m^{2}s.

As Cheng and Müller [Cheng & Müller, 2003] concluded, the pressure's influence on the CHF is a consequence of the changing fluid properties. A higher pressure can lead to a lower CHF because of the lower latent heat, a higher rate of evaporation and a lower surface tension. But an increasing pressure can also lead to a higher CHF because of a higher vapor density [Cheng & Müller, 2003]. Therefore, there is a maximum of the CHF depending on the pressure, as discussed in section 2.3.1. The pressure at which this maximum occurs depends on mass flux, as shown in figure 7.3 and described in the paragraph before.

7.3. Comparison of CHF data with literature and correlations

In this section, the CHF data obtained in this study are compared to available data from the literature. Additionally, an assessment of correlations applicable to R134a is done. More correlations are assessed after a fluid-to-fluid scaling of the experimental data to water equivalent parameters. Also a comparison with the 2006 CHF look-up table from Groneveld et al. [Groeneveld et al., 2007] is done.

7.3.1. Comparison with literature data

The CHF values will be compared at local conditions because of different boundary conditions like diameter, heated length and different inlet parameters. The local vapor quality at similar mass flux and pressures allows the comparison of these different data. A few CHF experiments with high pressured R134a are listed in section 2.3.2. Most data are incomparable with the ones of this study due to different geometries and pressures. Only 24 data points with similar parameters from Kariya et al. and Vijayarangan et al. [Kariya et al., 2013, Vijayarangan et al., 2006] are found.

Similar parameters were found at 4 MPa from Kariya et al. and plotted in figure 7.4 (a). Kariya et al. used a tube with 4.4 mm inside diameter. The CHF of Karyia et al. in figure 7.4 is not scaled

with equation 2.26 because Zahlan and Leung showed that the diameter effect vanishes at high pressures [Zahlan & Leung, 2018]. Using equation 2.26 would reduce the CHF values of Kariya et al. which would result in a bigger deviation. It can be seen that, for the same vapor quality, mass flux and pressure, the data of Kariya et al. show a much lower CHF than the ones obtained in this study. An explanation for the deviation could be the different diameter, heated length and different inlet conditions. Unfortunately, no more data can be obtained from their publication. Particularly, data at lower pressures would be valuable to compare and determine the effect of the diameter on the CHF.

In the publication of Vijayarangan et al., only data with similar pressures of 3.2 MPa and 3.4 MPa were listed. The data of those pressures expected to be close to the CHF values at 3.3 MPa from this study. These data are shown in figure 7.4 (b). The CHF values are scaled from 12.7 mm to 10 mm using equation 2.26. It can be easily recognized that the CHF values from Vijayarangan et al. for the same vapor quality and similar mass fluxes are much lower than the ones from this study. The authors showed in their own comparison with the correlation of Katto and Ohno [Katto & Ohno, 1984] that all their measured data are much lower than the predicted CHF values, especially at pressures above 3 MPa. An explanation could be their calculation of the CHF. Vijayarangan et al. assumed that, at constant pressure and mass flux, the local vapor quality of the dryout is independent of the heat flux. The authors used a ratio from the length where the CHF occurred to the total heated length to reduce the imposed heat flux to their CHF value. This reduces the CHF at the same local vapor quality and could explain their lower CHF values compared with other studies. Their assumption that the dryout vapor quality is independent of the heat flux is contrary to other statements in the literature, as the accepted look-up table of Groneveld [Groeneveld et al., 2007] for example.
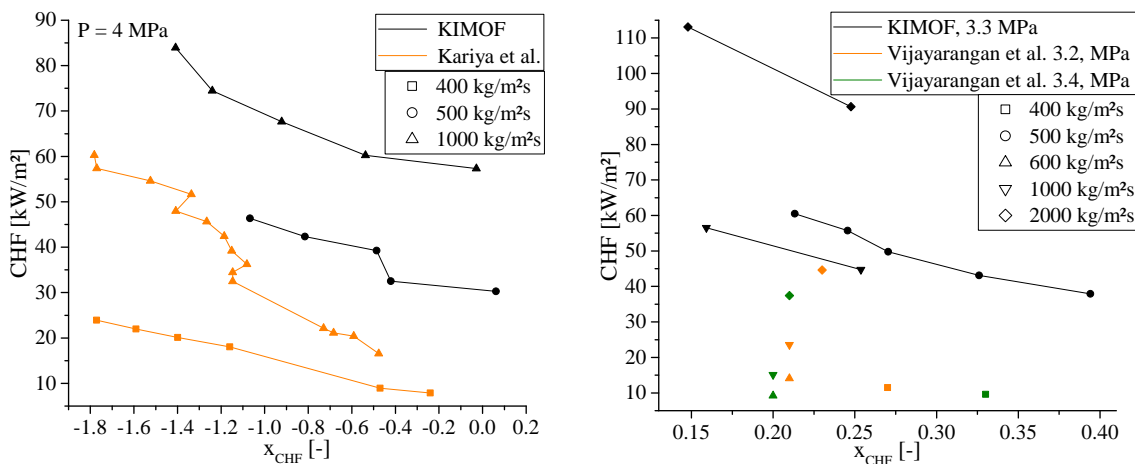
(a) Comparison with data from Kariya et al. [Kariya et al., 2013]

(b) Comparison with data from Vijayarangan et al. [Vijayarangan et al., 2006]

Figure 7.4.: Comparision of CHF data of ts-3 with literature data in R134a

7.3.2. Fluid-to-fluid scaling and look-up table

The original idea of the CHF experiments is to help understanding heat transfer phenomena concerning the SCWR. Therefore, the data must be transferred to water. This also enables comparison with correlations made for water and the 2006 CHF look-up table of Groeneveld et al. [Groeneveld et al., 2007].

The used scaling models from R134a to water are described in section 2.4.4. The pressure, inlet bulk enthalpy and the CHF itself are scaled using the scaling models of Ahmad [Ahmad, 1973]

with equations 2.34, 2.35 and 2.36. The vapor quality is kept constant to conserve the thermal-hydraulic similarity in the scaling as Cheng and Groeneveld proposed [Cheng, 1991, Groeneveld et al., 1997]. The mass flux is scaled with the mean of the results from equation 2.39 and 2.40.

Unfortunately, no water data can be found in the open literature to directly validate the fluid-to-fluid scaling models for the CHF data of this study. However, many authors describe the 2006 CHF look-up table of Groeneveld et al. [Groeneveld et al., 2007] as the most accurate tool for prediction CHF as discussed in section 2.3.3. With the scaled pressure, mass flux and local vapor quality the CHF is selected from the look-up table by linear interpolation as described by the authors. The look-up table is based on a 8 mm tube. Therefore, the found CHF value is scaled to 10 mm using equation 2.26. Due to the limits of the look-up table, there are no CHF values found for the experiments with pressure higher than 3.8 MPa and vapor quality below -0.5.
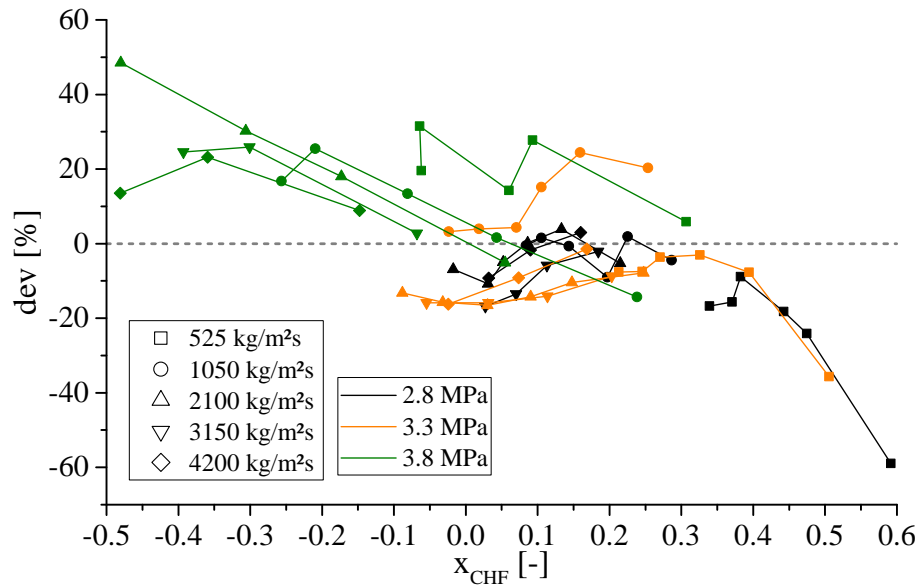
Figure 7.5.: Deviation of CHF predicted with the look-up table and the CHF data scaled to water

For the comparison, a statistical analysis is made. For that purpose, the deviation dev, mean deviation MD, mean absolute deviation MAD and the standard deviation STD are used, which are defined in section 3.7.2. The deviations between the CHF from the look-up table and the ones scaled from R134a versus the local vapor quality are shown in figure 7.5. The trends are indicated for constant mass fluxes and pressures. It can be seen that the deviation is smaller than 30 % except for three points. No general tendency of overpredicting or underpredicting is seen. As the vapor quality increases the deviation changes from high positive to negative values with the highest deviation at high vapor qualities. For the most trends, the deviations show similar values for constant mass fluxes and pressures. The positive deviations show that at subcooled vapor qualities for the pressure of 3.8 MPa the look-up table overpredicts the scaled data. Starting at the local vapor quality of 0.4 the deviations start to increase strongly.

The mean deviation between the look up table and the scaled CHF values is -0.6 % with the standard deviation of 17.1 % and the mean absolute deviation of 13 %. As mentioned before, the deviations show similar values for constant mass fluxes or pressures. Therefore, table 7.2 lists the mean and standard deviations separated in pressures and mass fluxes. Additionally, mass fluxes and pressures scaled to water are given. Because the scaling of the mass fluxes depends on the pressure as well, the values given are the mean of all mass fluxes at the listed pressure. The table 7.2 shows that the deviations are smaller at the pressure of 3.3 MPa and at high mass fluxes of 4200 kg/m²s in particular. High deviations occur at high pressure of 3.8 MPa and especially at small mass fluxes of 525 kg/m²s.

Table 7.2.: Mean and standard deviations of look-up table to scaled CHF split into mass fluxes and pressures

G_{R134a} $\left[\frac{kg}{m^2 s}\right]$	G_{water} $\left[\frac{kg}{m^2 s}\right]$	MD [%]	STD [%]	P_{R134a} [MPa]	P_{water} [MPa]	MD [%]	STD [%]
525	737	-6.4	18.2	2.8	16.2	-9	12.8
1050	1486	4.5	10	3.3	18.6	-6.2	13
2100	3006	-0.7	15	3.8	20.9	14.8	13.8
3150	4457	-3	11.1				
4200	5932	0.9	10.2				

Potential sources for the deviations are the fluid-to-fluid scaling and the prediction capability of the look-up table itself. Groeneveld et al. [Groeneveld et al., 2007] discussed the average error and the root mean square in detail. The average error is close to zero and the root mean square is 5.9 %. A systematic trend of the errors on the parameters cannot be seen, except for the mass flux. The root mean square decreases for mass fluxes increasing from 500 kg/m^{2}s to 4000 kg/m^{2}s. This trend is reflected in the deviations shown in table 7.2.

On the other side, also the uncertainties of the fluid-to-fluid scaling could lead to the deviations. An isolated consideration of the models is very difficult. Chen et al. [Chen et al., 2010] published factors for the scaling from R134a to water for pressure, mass flux, inlet subcooled enthalpy and the CHF. In this study, the same methodology is used, but the factor for the mass flux and thus the CHF are different from the factors of Chen et al. One reason could be the different data used for the fluid properties. Only the direct comparison of experimental data is qualified for a reliable validation of the fluid-to-fluid scaling models. With consideration of the look-up table prediction error, it seems that the scaling models are suitable to scale the CHF from R134a to water.

7.3.3. Comparison with correlations

As listed in section 2.3.3, there are a few correlations developed for predicting CHF at high pressure. In particular, there are two correlations based on CHF experiments with R134a as coolant. Some correlations are valid for multiple fluids and may help to validate the fluid-to-fluid scaling models. Table 7.3 shows which correlations are used for the assessment of the experimental and the scaled data. The valid parameter ranges of the correlations are listed in table 2.5 in section 2.3.3.

Table 7.3.: Used correlations for the CHF data assessment

Correlation	Equations	Condition	R134a	Water
Katto and Ohno [Katto & Ohno, 1984]	C.3	inlet	✓	✓
Shah LCC [Mohammed Shah, 1987]	C.6	local	✓	✓
Shah UCC [Mohammed Shah, 1987]	C.6	inlet	✓	✓
Kariya et al. [Kariya et al., 2013]	C.4	local	✓	✓
Vijayarangan et al. [Vijayarangan et al., 2006]	C.7	inlet	✓	✓
Lombardi [Lombardi, 1995]	C.5	inlet		✓
Chen et al. [Chen et al., 2016]	C.1	inlet		✓
Chen et al. [Chen et al., 2017]	C.2	local		✓

The predicted values of the correlation are compared with the experimental or CHF values scaled to water for the statistical analysis. The tools of MD, MAD and STD defined in section 3.7.2 are used for the assessment of the prediction capability of the correlations. Shah proposed two correlations in his paper [Mohammed Shah, 1987]. The first correlation is based on local conditions (LCC)

and the other one is an upstream condition correlation (UCC). In this study, both correlations of Shah are assessed. The results for all data points and correlations are summarized in table 7.4.

Table 7.4.: Deviations of CHF from used correlations with experimental and scaled data

Correlation	Fluid	MD	MAD	STD
Katto and Ohno	R134a	9.5 %	11.9 %	15.1 %
	water	8.7 %	11.4 %	14.6 %
Shah LCC	R134a	4.2 %	42.2 %	49 %
	water	8.7 %	40.2 %	45.9 %
Shah UCC	R134a	6 %	9.3 %	13.7 %
	water	2.9 %	9.1 %	13.6 %
Kariya et al.	R134a	16.7 %	105.6 %	137.9 %
	water	45 %	116.9 %	155.8 %
Vijayarangan et al.	R134a	9.5 %	11.9 %	15.1 %
	water	8.7 %	11.4 %	14.6 %
Lombardi	water	-7.2 %	27.7 %	34.8 %
Chen et al. 2016	water	-44.3 %	44.3 %	10.2 %
Chen et al. 2017	water	-36 %	38.9 %	23.7 %

Correlation of Kariya et al.

The correlation of Kariya et al. [Kariya et al., 2013] is not capable to predict the CHF of this study well, as seen at the high mean absolute deviation and standard deviation in table 7.4. For single points at small mass fluxes and pressures of 4 MPa in R134a and 21.9 MPa in water, the correlation's predictions are close to the experimental CHF values with deviations smaller than 10 %. The deviations could be caused by different diameters of the tubes. Karyia et al. correlation is based on data of a 4.4 mm tube, whereas the diameter of ts-3 is 10 mm.

Correlation of Vijayarangan et al.

Vijayarangan et al. [Vijayarangan et al., 2006] adapted the correlation from Katto and Ohno to their experiments with R134a. The authors adapted the second of the four equations for the heat flux, which are chosen by parameter ranges. This second equation is only chosen if the density ratio of the vapor to the liquid is smaller than 0.15. This is not the case for high pressures. Therefore, none of the data from this study corresponds to the region of the adapted equation. Consequently, no difference between the two correlations is seen. If only the adapted equation is taken instead of all four, the mean absolute deviation is 53.7 %, which is much higher than the original correlation. Because of these results, their improvement of the Katto and Ohno correlation for CHF experiments at high pressures cannot be proofed.

Correlation of Lombardi

The correlation of Lombardi [Lombardi, 1995] was developed for water only. The scaled data can be reproduced acceptably well. Especially at high subcoolings and pressures of 20.9 MPa the correlations predict the CHF very well. At subcoolings of 800 kJ/kg and higher the deviations are always smaller than 10 %.

Correlation of Chen et al.

The first correlation of Chen et al. [Chen et al., 2016] underpredicts every scaled CHF value with an average of 44.3 %. This can be seen in table 7.4 by the negative value of the mean deviation and the same value in positive of the mean absolute deviation. The standard deviation of 10 % is very small, which means that most deviations are in the range from -54 % to -34 %. The deviations are decreasing for decreasing mass flux and increasing pressure. This results in the smallest deviations of around 28 % at the scaled mass fluxes of 730 kg/m²s and the scaled pressure of 21.8 MPa.

The second correlation of Chen et al. [Chen et al., 2017] is based on local conditions. The deviations from the second correlations are more diversified as seen on the higher standard deviation. Differences between scaled and predicted CHF values are getting smaller for high mass fluxes and high pressures. Thus, the mean absolute deviation of all data points at scaled pressures of 21.8 MPa and scaled mass fluxes from 4000 kg/m²s to 6000 kg/m²s is 10.3 %.

Correlation of Katto and Ohno

The correlations of Shah and of Katto and Ohno [Katto & Ohno, 1984] are the best to reproduce the experimental data, as seen in table 7.4 by the smallest deviations. Therefore, these deviations will be discussed in detail to identify regions of good and reasonable accordance. The deviations are plotted in figure 7.6 against the local vapor quality separated in mass fluxes and pressures.
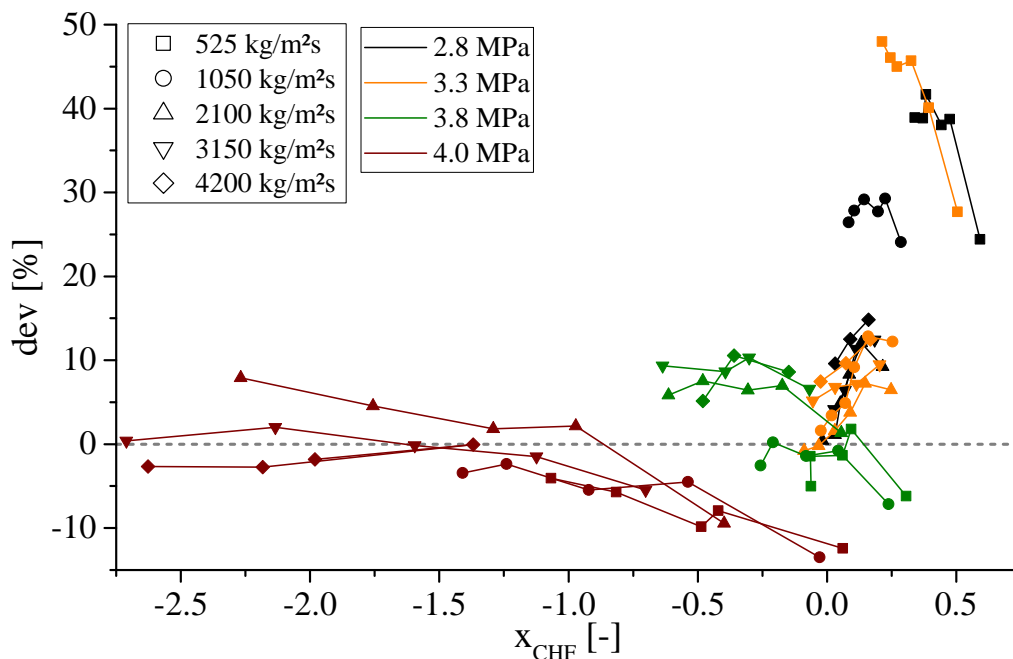
Figure 7.6.: Deviation of CHF predicted with the correlation of Katto and Ohno and CHF of ts-3 in R134a

The deviations are smaller than 10 % for subcooled local vapor qualities with no systematic pattern for the distribution, as seen in figure 7.6. Above zero, the deviations increase with higher vapor qualities. This could be also caused by smaller pressures and mass fluxes. Therefore, the deviations are averaged for the mass fluxes and pressures and listed in table 7.5. Additionally, the deviations of the Katto and Ohno correlation to the CHF data scaled to water are listed in table 7.5.

Table 7.5 shows that the deviations are the highest for small mass fluxes and pressures. The smallest deviations are at 3.8 MPa and at mass fluxes of 2100 kg/m²s. Although the correlation was not developed for pressures close to the critical value, it reproduces the experimental results well with a mean deviation of -0,5 % and a standard deviation of 12.7 % over all data at 4 MPa.

Table 7.5.: Mean and standard deviations of correlation of Katto and Ohno to CHF of R134a and scaled to water split into mass fluxes and pressures

G_{R134a} $\left[\frac{kg}{m^2 s}\right]$	MD [%]	STD [%]	G_{water} $\left[\frac{kg}{m^2 s}\right]$	MD [%]	STD [%]	P_{R134a} [MPa]	MD [%]	STD [%]	P_{water} [MPa]	MD [%]	STD [%]
525	19.1	23.5	737	18.1	22.9	2.8	19.7	13.3	16.2	18.9	13.4
1050	7.4	13.9	1486	6.3	12.8	3.3	14.9	16.4	18.6	13.7	14.9
2100	4.3	4.1	3006	3.8	4.1	3.8	2.7	5.4	20.9	2.2	5.3
3150	8.5	12.5	4457	8	12.3	4.0	-0.5	12.7	21.8	-1.1	12.5
4200	6.7	5.9	5932	6.2	6						

However, the high deviations at small mass fluxes and pressures correlate with high vapor qualities, as seen in figure 7.6. Here, the CHF is very sensitive on small changes of the vapor quality in the region above zero, as shown in figure 7.3. Therefore, small changes in the determined local vapor quality lead to higher deviations.

In table 7.4, the deviations of the CHF of R134a and the CHF scaled to water are almost similar. This also applies to the deviations listed in table 7.5. The reason is that Katto and Ohno have implemented the same dimensionless numbers in their correlation as Ahmad for the fluid-to-fluid scaling. In this case, the input parameters for the correlation keeps the same, despite a preceding scaling. The usage of the dimensionless numbers are also the reason, why the correlation of Katto and Ohno is applicable to different fluids. The commonly used dimensionless numbers are discussed in section 2.4.4.

Correlation of Shah

The upstream conditions correlation predicts the CHF data much closer than the local condition correlation of Shah, as seen in table 7.4. Inasaka and Nariari [Inasaka & Nariai, 1996] showed in their paper that this is the case for all assessed correlations. The use of the heat balance in the inlet based correlation results in smaller deviation, if the predicted vapor quality differs from the experimental one. Therefore, the correlations based on inlet conditions show a better prediction capability than the one based on local conditions, as also seen in table 7.4.

The deviations of the upstream condition correlation of Shah [Mohammed Shah, 1987] to the R134a data are plotted against the local vapor quality in figure 7.7. Compared with Katto and Ohno, the prediction is better at positive vapor qualities. Especially at high vapor qualities, Shah shows deviations less than 20 %. The correlation of Katto and Ohno reproduce the experimental CHF at negative values more accurate.

The deviations are grouped according to the mass flux and pressure for a detailed analysis like before. Table 7.6 shows that the correlation predicts the R134a data at 3.3 MPa and 3.8 MPa the best. The highest deviations are at 4 MPa and 3150 kg/m²s, where the local vapor quality is the smallest, as seen in figure 7.7. However, at small mass fluxes and pressures the correlation of Shah predicts the experimental CHF more accurately than the one of Katto and Ohno.

By comparison of the CHF of R134a and CHF scaled to water in table 7.5, it can be seen that the deviations are similar for every parameter region. Contrary to the correlation of Katto and Ohno, the correlation of Shah is not based on the same dimensionless numbers as the fluid-to-fluid scaling. Because of that, the deviations of the scaled data to the predicted CHF values can be used for the indirect validation the fluid-to-fluid scaling and two facts can be concluded. Firstly, the Shah correlations predicts in the same degree of accuracy for the same relative parameter regions for water and R134a. This is based on the fact that the correlation was developed for several fluids, which hereby seems to be valid for water and R134a. The second conclusion is that the
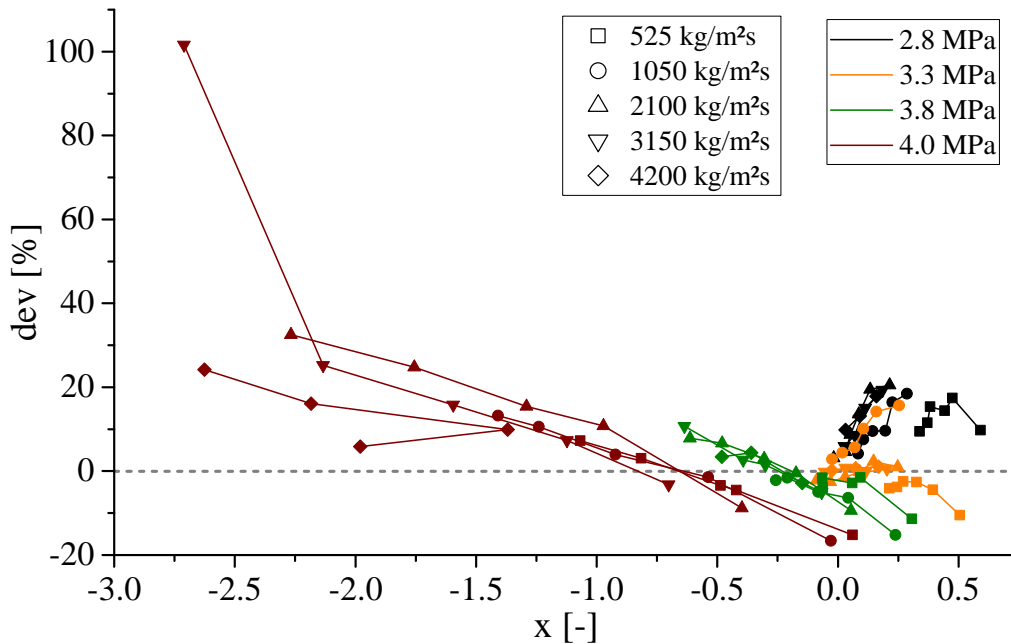
Figure 7.7.: Deviation of CHF predicted with the correlation of Shah and CHF of ts-3 in R134a

similar results can only occur if the parameters and the CHF are scaled correctly. This and the small deviations of the scaled data to the predicted CHF values show that the fluid-to-fluid scaling models are valid for scaling the CHF from R134a to water.

Table 7.6.: Mean and standard deviations of correlation of Shah to CHF of R134a and scaled to water split into mass fluxes and pressures

G_{R134a} $\left[\frac{kg}{m^2 s}\right]$	MD [%]	STD [%]	G_{water} $\left[\frac{kg}{m^2 s}\right]$	MD [%]	STD [%]	P_{R134a} [MPa]	MD [%]	STD [%]	P_{water} [MPa]	MD [%]	STD [%]
525	0.7	9	737	-2	10.4	2.8	12.1	5.2	16.2	11.8	5.1
1050	4.4	9.6	1486	1.6	10.7	3.3	1	5.7	18.6	-1.2	5.5
2100	6.8	10.7	3006	3.8	10.6	3.8	-1.3	6.2	20.9	-5-5	6.2
3150	12.1	24.5	4457	8.5	23.2	4.0	11.4	23	21.8	5.5	22.2
4200	8	8	5932	4.4	8.2						

Suggestion of correlation

The correlation of Katto and Ohno [Katto & Ohno, 1984] is recommended for predicting the CHF at high pressures of 0.936 to 0.985 of the critical value for water and R134a and subcooled conditions. The upstream condition correlation of Shah [Mohammed Shah, 1987] is recommended at local vapor qualities of -0.25 and higher.

8. Conclusion and Outlook

8.1. Conclusion

In this study, a huge set of experimental investigations for the heat transfer at supercritical conditions has been conducted with a total of 47300 data points for the fluid R134a. The investigated parameters are pressure, inlet temperature, mass flux and heat flux with systematic intervals for the set values. The chosen parameters are derived from existing water data for the following assessment of the fluid-to-fluid scaling models. Additional, a detailed study with CO_2 on the influence of mass flux and inlet temperature with more than 21100 data points is done. The used facilities and measurement setups are verified and proofed to produce reliable data. It can be concluded from the measurements that flow instabilities happen at low mass fluxes, high heat fluxes and low inlet temperatures. This flow instabilities are caused by the strong changes of the density along the test section and the corresponding local pressure drop. The occurrence of the instabilities is additionally determined by the conditions of the heated surface and the setting of the whole facility as cooling temperatures or positions of the valves. As a result of the flow instabilities, the heat transfer is increased locally. These data are excluded for further investigations and assessments and two databases are established for R134a and CO_2, respectively.

The heat transfer phenomena at supercritical conditions have been discussed with the produced data. At low heat fluxes, the heat transfer coefficient trends show a similar qualitative behavior like the trends of conventional fluids. The heat transfer starts to deviate and the HTC decreases as the heat flux increase . The recent theory of the mechanisms of buoyancy and thermally-induced bulk flow acceleration proposed by Jackson are able to explain the observed local heat transfer reductions very well. If the Buoyancy and Acceleration number exceed the limits of $Bu>10^{-5}$ or $Ac>4x10^{-6}$ proposed by Jackson [Jackson, 2011], peaks in the wall temperature trends are observed. The HTC trends fits qualitatively and quantitatively very well for different low heat fluxes. The HTC trends is decreased for increasing heat fluxes if $Bu>0.2x10^{-5}$ or $Ac>0.25x10^{-6}$. Therefore, it must be assumed that the buoyancy and thermally-induced bulk flow acceleration starts to influence the heat transfer at these limits. The qualitative behavior of the HTC trends is dominated by the mass flux as it influences the progress of buoyancy and acceleration.

There exists a certain bulk temperature at which the buoyancy induced HTC minimum occurs depending on mass flux and heat flux. This is determined by the density difference between the bulk and at the wall. The density varies stronger at bulk temperatures closer to the pseudo-critical point. Therefore, with increasing heat flux, the HTC minimums are pushed upstream and to smaller bulk enthalpies. If this certain bulk temperature is higher than the inlet temperature, like at high mass fluxes, almost no effect of the inlet conditions is observed. However, if the bulk temperature is lower than the inlet temperature, an influence up to 90 diameters in the axial direction can be observed. Here, the inlet effect is caused by the development of the thermal layer until the critical density difference is reached.

Additionally, it is observed that for $0.25x10^{-6}>Ac>2.5x10^{-6}$ the HTC is very sensible to the Acceleration number, which occurs mainly close to the pseudo-critical bulk enthalpy. It seems at this

point that the surface has an influence on the heat transfer as well. The heat transfer is decreased if the surface roughness is decreased due to the earlier forced laminarization of the flow. It was found that the HTC minimum caused by the acceleration moves towards the pseudo-critical point for increasing inlet temperature. This effect is limited to bulk enthalpies close to the pseudo-critical point, thus, a limitation of the inlet effect in a specific length is not meaningful.

Furthermore, the heat transfer at supercritical conditions also depends on the condition of the heated surface. Paired with the high sensibility to the heat flux and the inlet temperature, this aggravates the reproducibility and comparison from different systems. The assessment of correlations with the produced data shows that no correlation can predict the data well for the wide ranges of the conducted parameters. The reason could be the same as for the reproducibility. In small ranges of the parameters, single correlations have a good predicting capability. Overall, the correlation of Chen and Fang [Chen & Fang, 2014] shows the closest results for the data from R134a and CO_2.

The fluid-to-fluid scaling models are assessed with the databases of the produced R134a and CO_2 data and additional CO_2 data from the literature with the existing water database at the IATF. A new and reliable method for the comparison of the scaled data with existing experimental data is developed for this purpose. The model of Zahlan et al. [Zahlan et al., 2014] shows the best results for the most database pairs. The only exception is the pair of the CO_2 data from this study with water, which is better scaled by the model of Tian et al. [Tian et al., 2018]. However, concerning the data influenced by buoyancy, the original model of Cheng produces the smallest deviations. The acceleration influenced data are scaled best by the model of Tian et al.

The models of Cheng et al. and Tian et al. have been modified to enhance the scaling capability of the R134a and CO_2 data to water. Therefore, the empirical coefficients in the mass flux scaling are optimized with the usage of the gathered databases. A parameter study of the modified coefficients shows that the models developed so far can be only fit to satisfy a certain fluid combination or certain influenced data.

Critical heat flux experiments are conducted with R134a as coolant at high pressures. The influences of pressure, inlet subcooling and mass flux are discussed. There exists a linear correlation between CHF and vapor quality for most trends. At low mass fluxes, the change of the mechanism from DNB to dryout and the limiting quality phenomenon are observed. It is found that depending on the mass flux there is a maximum for the CHF at pressures of 2.8 MPa or 3.3 MPa. After the maximum, the CHF approaches zero as the pressure reaches the pseudo-critical point. Additionally, the inversed mass flux effect is observed. The data are scaled to water using a model based on Ahmad's model [Ahmad, 1973]. The scaled data show a good comparison with the CHF look-up table of Groeneveld et al. [Groeneveld et al., 2007]. The assessment of the look-up table and additional correlations with the data in R134a and the data scaled to water proof the reliability of the fluid-to-fluid scaling model. The best correlation to reproduce the experimental data, even at pressures close to the critical point, is developed from Shah [Mohammed Shah, 1987].

The above listed findings improve the understanding of heat transfer at supercritical conditions. The assessment of the correlations on heat transfer at supercritical conditions and the critical heat flux showed which correlation should be used for a reliable prediction of the heat transfer for designing a power unit. With the proofed scalability of R134a data to water, more work can be done to improve the knowledge and the modeling of the heat transfer near the critical point for water applications. Therefore, this work conduces to success for future power units using supercritical water as coolant like the SCWR.

8.2. Proposal for future work

In the future, some of the experiments conducted in this study should be repeated using another facility and similar or the same test section to clarify the influence of system and test section conditions on the heat transfer at supercritical conditions. The reason for possible deviations between the repeated experiments must be investigated. The proposal of the high sensibility of the HTC on small changes in system, parameters and the heated surface should be investigated.

Based on this study and findings, several tasks can be continued. The phenomena of the heat transfer at supercritical are shown and discussed in chapter 5 in detail based on the extensive experimental study. This phenomena can be considered to improve the understanding of the influences of the single parameters and especially the parameter combination on the heat transfer. The improved understanding could be used for the development of a new heat transfer model. The huge amount of data points produced in this study could be used to validate this model. Also for correlations developed for different fluids, the data of R134a and CO_2 can be used for validation purposes.

The databases for R134a, CO_2 and water collected in this study could be used for a new fluid-to-fluid scaling model. This model should focus on the influence of buoyancy since the acceleration influenced data can be scaled well with the existing models. The variations of the inlet temperature in the R134a database could help investigating if the inlet conditions must be scaled for HTC influenced by buoyancy. Maybe another local number, like the Bu number of Jackson, could be used to scale this data correctly. It can be concluded that the findings and data from this study provide a valuable basis for further work on predicting heat transfer at supercritical conditions.

Bibliography

[Ackerman, 1970] Ackerman, J. W. (1970). Pseudoboiling heat transfer to supercritical pressure water in smooth and ribbed tubes. *Journal of Heat Transfer*, 92(3), 490–497.

[AGENCY, 2001] AGENCY, I. A. E. (2001). *Thermohydraulic Relationships for Advanced Water Cooled Reactors*, volume 1203 of *IAEA TECDOC Series*. Vienna, Austria: INTERNATIONAL ATOMIC ENERGY AGENCY.

[Ahmad, 1973] Ahmad, S. Y. (1973). Fluid to fluid modeling of critical heat flux: a compensated distortion model. *International Journal of Heat and Mass Transfer*, 16(3), 641–662.

[Ahmad & Groeneveld, 1972] Ahmad, S. Y. & Groeneveld, D. C. (1972). Fluid modeling of critical heat flux in uniformly heated annuli. In *International Symposium on Two-Phase Systems*, volume AECL-4070 (pp. 45–53). Haifa in Israel: Elsevier. August 29—September 2.

[Ahmed et al., 2010] Ahmed, W. H., El-Nakla, M. A., & Ismail, B. I. (2010). Towards understanding the critical heat flux for industrial applications. *International Journal of Multiphase Flow*, 36(3), 153–165.

[Ambrosini, 2011a] Ambrosini, W. (2011a). Discussion of similarity principles for fluid-to-fluid scaling of heat transfer behaviour at supercritical pressures. *Nuclear Engineering and Design*, 241(12), 5149–5173.

[Ambrosini, 2011b] Ambrosini, W. (2011b). Flow stability of heated channels with supercritical pressure fluids: Presentation. In *Joint ICTP-IAEA Course on Science and Technology of Supercritical Water Cooled Reactors*, volume SC 15 Trieste, Italy. 27 June - 01 July.

[Ambrosini & Sharabi, 2008] Ambrosini, W. & Sharabi, M. (2008). Dimensionless parameters in stability analysis of heated channels with fluids at supercritical pressures. *Nuclear Engineering and Design*, 238(8), 1917–1929.

[Azih et al., 2012] Azih, C., Brinkerhoff, & Yaras, M. I. (2012). Direct numerical simulation of convective heat transfer in a zero-pressure-gradient boundary layer with supercritical water. *Journal of Thermal Science*, 21(1), 49–59.

[Azih & Yaras, 2017] Azih, C. & Yaras, M. I. (2017). Similarity criteria for modeling mixed-convection heat transfer in ducted flows of supercritical fluids. *Journal of Heat Transfer*, 139(12), 122501–122501–13.

[Badea et al., 2018] Badea, A. F., Zhao, M., Cheng, X., Feuerstein, F., & Liu, X. (2018). Consistency considerations on a large databank and wide range heat transfer prediction for supercritical water in circular tubes. *Nuclear Engineering and Design*, 335, 178–185.

[Bae et al., 2005] Bae, J. H., Yoo, J. Y., & Choi, H. (2005). Direct numerical simulation of turbulent supercritical flows with heat transfer. *Physics of Fluids*, 17(10), 105104–1 – 105104–24.

[Bae, 2011] Bae, Y. Y. (2011). Mixed convection heat transfer to carbon dioxide flowing upward and downward in a vertical tube and an annular channel. *Nuclear Engineering and Design*, 241(8), 3164–3177.

[Bae et al., 2011] Bae, Y. Y., Hong, S. D., & Kim, Y. W. (2011). Assessment of mixed convection heat transfer correlations at supercritical pressures. In *The 5th Int. Symp. SCWR's*, volume P106 (pp. 1–10). Vancouver, British Columbia, Canada. March 13 - 16.

[Bae & Kim, 2009] Bae, Y.-Y. & Kim, H.-Y. (2009). Convective heat transfer to CO2 at a supercritical pressure flowing vertically upward in tubes and an annular channel. *Experimental Thermal and Fluid Science*, 33(2), 329–339.

[Bae et al., 2010] Bae, Y.-Y., Kim, H.-Y., & Kang, D.-J. (2010). Forced and mixed convection heat transfer to supercritical CO2 vertically flowing in a uniformly-heated circular tube. *Experimental Thermal and Fluid Science*, 34(8), 1295–1308.

[Barnett, 1963] Barnett, P. G. (1963). *The scaling of forced convection boiling heat transfer*. Technical Report No. AEEW-R-134 (pp. 1-42), United Kingdom Atomic Energy Authority. Reactor Group, Winfrith, Dorset, England.

[Barnett, 1964] Barnett, P. G. (1964). *An Experimental Investigation to Determine the Scaling Laws of Forced Convection Boiling Heat Transfer. Part I. The Preliminary Examination Using Burnout Data for Water and Arcton 12*. Technical Report No. AEEW-R-363. (pp. 1-39), United Kingdom Atomic Energy Authority. Reactor Group, Winfrith, Dorset, England, Winfrith, Dorset, England.

[Becker et al., 1972] Becker, K. M., Djursing, D., Lindberg, K., Eklind, O., & Österdahl, C. (1972). Burnout conditions for round tubes at elevated pressures. In G. HETSRONI, S. SIDEMAN, & J. HARTNETT (Eds.), *Proceedings of the International Symposium on Two-Phase Systems* (pp. 55–73). Pergamon.

[Behnke, 2009] Behnke, L. (2009). *Vorhersage kritischer Siedezustände in Brennelementstrukturen von Leichtwasserreaktoren bei variablem Druck*. Dissertation, Universität Stuttgart, Germany.

[Bejan & Kraus, 2003] Bejan, A. & Kraus, A. D. (2003). *Heat transfer handbook*. Hoboken, New Jersey, USA: John Wiley & Sons, 1 edition.

[Bishop et al., 1965] Bishop, A. A., Sandberg, R. O., & Tong, L. S. (13-17 June 1965). Forced-convection heat transfer to water at near-critical temperatures and supercritical pressures: WCAP-5449. In Institution of Chemical Engineers (Ed.), *Chemical engineering under extreme conditions : Proceedings of Symposium no. 2*, volume 2 (pp. 77–85). London. 13-17 June 1965.

[Blasius, 1907] Blasius, H. (1907). *Grenzschichten in Flüssigkeiten mit kleiner Reibung*. Dissertation, Universtity of Göttingen, Germany. Zeitschrift für Mathematik und Physik ; 56, Leipzig: BG: Teubner.

[Bogachev et al., 1983] Bogachev, V. A., Eroshenko, V. M., & Yaskin, L. A. (1983). Relative increase in heat transfer in viscous-inertial regimes of flow of helium at supercritical pressure in a heated pipe. *Journal of engineering physics*, 44(4), 363–366.

[Bourke & Pulling, 1970] Bourke, P. & Pulling, D. (1970). A turbulent heat flux meter and some measurements of turbulence in air flow through a heated pipe. *International Journal of Heat and Mass Transfer*, 13(8), 1331–1338.

[Bourke, P. and D. Pulling, 1971] Bourke, P. and D. Pulling (1971). An experimental explanation of deterioration in heat transfer to supercritical carbon dioxide. *Atomic Energy Research Establishment*, 71-HT-24, 1–7.

[Bringer & Smith, 1957] Bringer, R. P. & Smith, J. M. (1957). Heat transfer in the critical region. *AIChE Journal*, 3(1), 49–55.

[Buckingham, 1914] Buckingham, E. (1914). On physically similar systems; illustrations of the use of dimensional equations. *Physical Review*, 4(4), 345–376.

[Cabeza et al., 2017] Cabeza, L. F., de Gracia, A., Inés Fernández, A., & Farid, M. M. (2017). Supercritical CO2 as heat transfer fluid: A review. *Applied Thermal Engineering*, 125, 799–810.

[Calderazzi & Di Paliano, 1997] Calderazzi, L. & Di Paliano, P. C. (1997). Thermal stability of R-134a, R-141b, R-13I1, R-7146, R-125 associated with stainless steel as a containing material. *International Journal of Refrigeration*, 20(6), 381–389.

[Celata & Mariani, 1999] Celata, G. P. & Mariani, A. (1999). *Critical heat flux, post dry-out and their augmentation*. Technical Report RT/ERG/98/10 (pp. 1-65), ENEA - Dipartimento Energia.

[Chang & Baek, 2003] Chang, S. H. & Baek, W.-P. (2003). Understanding, predicting, and enhancing critical heat flux. In *The 10th International Topical Meeting on Nuclear Reactor Thermal Hydraulics* (pp. 1–20). Seoul, Korea. October 5-11.

[Chang et al., 2017] Chang, W., Chu, X., Binte Shaik Fareed, A. F., Pandey, S., Luo, J., Weigand, B., & Laurien, E. (2017). Heat transfer prediction of supercritical water with artificial neural networks. *Applied Thermal Engineering*, 131, 815–824.

[Chatoorgoon, 2001] Chatoorgoon, V. (2001). Stability of supercritical fluid flow in a single-channel natural-convection loop. *International Journal of Heat and Mass Transfer*, 44(10), 1963–1972.

[Chen et al., 2010] Chen, C.-N., Han, J.-T., Shao, L., & Jen, T.-C. (2010). Fluid to fluid modeling scaling factors of r134a-water for critical heat flux. In *14th International Heat Transfer Conference* (pp. 767–772). Washington, DC, USA. August 8–13, 2010.

[Chen & Fang, 2014] Chen, W. & Fang, X. (2014). A new heat transfer correlation for supercritical water flowing in vertical tubes. *International Journal of Heat and Mass Transfer*, 78(0), 156–160.

[Chen et al., 2015a] Chen, W., Fang, X., Xu, Y., & Su, X. (2015a). An assessment of correlations of forced convection heat transfer to water at supercritical pressure. *Annals of Nuclear Energy*, 76(0), 451–460.

[Chen et al., 2016] Chen, Y., Bi, K., Zhao, M., Yang, C., & Du Kaiwen (2016). Critical heat flux with subcooled flowing water in tubes for pressures from atmosphere to near-critical point. *Journal of Energy and Power Engineering*, 10(4), 211–222.

[Chen et al., 2015b] Chen, Y., Bi, M., Zhao, M., Yang, C., & Du, K. (2015b). Critical heat flux with subcooled flowing water in tubes for pressures from atmosphere to near-critical point. In American Nuclear Society (Ed.), *NURETH-16* (pp. 8165–8176). Chicago. August 30-September 4.

[Chen et al., 2011] Chen, Y., Yang, C., Zhao, M., Bi, K., Du, K., & Zhang, S. (2011). Subcooled boiling critical heat flux of water flowing upward in a tube for lower flow and pressure up to 20 MPa. In *The 14th International Topical Meeting on Nuclear Reactor Thermal Hydraulics*, volume 620 (pp. 1–14). Toronto, Ontario. September 25-29.

[Chen et al., 2017] Chen, Y., Zhao, M., Bi, K., Yang, B., Zhang, D., & Du, K. (2017). Critical heat flux of flowing water in tube for pressure up to near critical point—experiment and prediction. *Journal of Nuclear Engineering and Radiation Science*, 4(1), 011006–1–011006–5.

[Cheng et al., 2017] Cheng, H., Zhao, J., & Rowinski, M. K. (2017). Study on two wall temperature peaks of supercritical fluid mixed convective heat transfer in circular tubes. *International Journal of Heat and Mass Transfer*, 113, 257–267.

[Cheng, 1991] Cheng, X. (1991). *Experimentelle Untersuchung zur kritischen Heizflächenbelastung in 8 mm-Kreisrohren und in 7-Stabbündeln*. Dissertation, Technische Universität Braunschweig, Germany.

[Cheng & Liu, 2017] Cheng, X. & Liu, X. J. (2017). Research challenges of heat transfer to supercritical fluids. *Journal of Nuclear Engineering and Radiation Science*, 4(1), 011003–1 – 011003–7.

[Cheng et al., 2011] Cheng, X., Liu, X. J., & Gu, H. Y. (2011). Fluid-to-fluid scaling of heat transfer in circular tubes cooled with supercritical fluids. *Nuclear Engineering and Design*, 241(2), 498–508.

[Cheng & Müller, 2003] Cheng, X. & Müller, U. (2003). *REVIEW ON CRITICAL HEAT FLUX IN WATER COOLED REACTORS: ISSN 0947-8620*. Scientific report FZKA 6825, Institut für Kern- und Energietechnik, Forschungszentrum Karslruhe GmbH, Germany.

[Cheng & Schulenberg, 2001] Cheng, X. & Schulenberg, T. (2001). *Heat Transfer at Supercritical Pressures: Literature Review and Application to an HPLWR*. Scientific report FZKA 6609, Institut für Kern- und Energietechnik, Forschungszentrum Karlsruhe GmbH, Germany.

[Cheng et al., 2009a] Cheng, X., Yang, Y., & Huang, S. (2009a). A simple heat transfer correlation for sc fluid flow in circular tubes. In *The 13th International Topical Meeting on Nuclear Reactor Thermal Hydraulics (NURETH-13)*, volume N13P1047 (pp. 1–11). Kanazawa City, Ishikawa Prefecture, Japan. September 27-October 2, 2009.

[Cheng et al., 2009b] Cheng, X., Yang, Y., & Huang, S. (2009b). A simplified method for heat transfer prediction of supercritical fluids in circular tubes. *Annals of Nuclear Energy*, 36(8), 1120–1128.

[Cheng et al., 2019] Cheng, X., Zhao, M., Feuerstein, F., & Liu, X. J. (2019). Prediction of heat transfer to supercritical water at different boundary conditions. *International Journal of Heat and Mass Transfer*, 131, 527–536.

[Chu & Laurien, 2016] Chu, X. & Laurien, E. (2016). Investigation of convective heat transfer to supercritical carbon dioxide with direct numerical simulation. In E. W. Nagel, H. D. Kröner, & M. M. Resch (Eds.), *High Performance Computing in Science and Engineering 15: Transactions of the High Performance Computing Center, Stuttgart (HLRS) 2015* (pp. 315–331). Cham: Springer International Publishing.

[Chun et al., 2007a] Chun, S.-Y., Hong, S.-D., Cho, Y.-S., & Baek, W.-P. (2007a). Comparison of the CHF data for water and refrigerant HFC-134a by using the fluid-to-fluid modeling methods. *International Journal of Heat and Mass Transfer*, 50(21–22), 4446–4456.

[Chun et al., 2007b] Chun, S.-Y., Hong, S.-D., KIKURA, H., & ARITOMI, M. (2007b). Critical heat flux in a heater rod bundle cooled by R-134a fluid near the critical pressure. *Journal of Nuclear Science and Technology*, 44(9), 1189–1198.

[Churkin et al., 2015] Churkin, A., Deev, V., & Kharitonov, V. (2015). A new correlation of a heat transfer coefficient in supercritical water. In VTT Technical Research Centre of Finland Ltd (Ed.), *The 7th International Symposium on Supercritical Water-Cooled Reactors*, volume ISSCWR7-2020 (pp. 1–17). Helsinki, Finland. 15-18 March.

[Coelho Silva, 2015] Coelho Silva, A. (2015). *Versuche zum Wärmeübergang mit überkritischem R134a an der KIMOF*. Master thesis, Karlsruher Institut für Technologie, Germany. Supervisor: Cheng, X.; Co-supervisor: Feuerstein, F.

[Cui & Wang, 2017] Cui, Y.-L. & Wang, H.-X. (2017). Experimental study on convection heat transfer of R134a at supercritical pressures in a vertical tube for upward and downward flows. *Applied Thermal Engineering*, 129, 1414–1425.

[Dai et al., 2016] Dai, X., Shi, L., An, Q., & Qian, W. (2016). Screening of hydrocarbons as supercritical ORCs working fluids by thermal stability. *Energy Conversion and Management*, 126(Supplement C), 632–637.

[Dai et al., 2018] Dai, X., Shi, L., An, Q., & Qian, W. (2018). Thermal stability of some hydrofluorocarbons as supercritical ORCs working fluids. *Applied Thermal Engineering*, 128(Supplement C), 1095–1101.

[DeBortoli et al., 1958] DeBortoli, R., Green, S. J., LeTourneau, B. W., Troy, M., & Weiss, A. (1958). *Forced-convection heat transfer burnout studies for water in rectangular channels and round tubes at pressures above 500 psia*. Technical Report WAPD-188 (pp. 1-173), Westinghouse Electric Corp. Bettis Plant, Pittsburgh.

[Deev et al., 2016] Deev, V. I., Rachkov, V. I., Kharitonov, V. S., & Churkin, A. N. (2016). Analysis of relations for calculating normal heat transfer to supercritical pressure water flow in vertical tubes. *Atomic Energy*, 119(3), 169–176.

[Dhanuskodi et al., 2015] Dhanuskodi, R., Kaliappan, R., Suresh, S., Anantharaman, N., Arunagiri, A., & Krishnaiah, J. (2015). Artificial neural networks model for predicting wall temperature of supercritical boilers. *Applied Thermal Engineering*, 90, 749–753.

[Dickinson & Welch, 1958] Dickinson, N. L. & Welch, C. P. (1958). Heat transfer to supercritical water. *Trans. Am. Soc. Mech. Engrs.*, Vol: 80, 746–752.

[Dittus & Boelter, 1985] Dittus, F. W. & Boelter, L. (1985). Heat transfer in automobile radiators of the tubular type. *International Communications in Heat and Mass Transfer*, 12(1), 3–22.

[DoE, 2002] DoE, U. S., Ed. (2002). *A Technology Roadmap for Generation IV Nuclear Energy Systems*, Nuclear Energy Research Advisory Committee and the Generation IV International Forum; Technical Roadmap Report (pp. 1 - 163).

[Dongliang et al., 2018] Dongliang, M., Tao, Z., Bing, L., Ali Shahzad, M., & Yanping, H. (2018). An improved correlation on the onset of heat transfer deterioration in supercritical water. *Nuclear Engineering and Design*, 326, 290–300.

[Doroshchuk et al., 1975] Doroshchuk, V. E., Levitan, L. L., & Lantsman, F. P. (1975). Recommendations for calculating burnout in a round tube with uniform heat release. *Thermal Engineering*, 22(12), 66–70.

[Dubey et al., 1998] Dubey, B. P., Pilkhwal, D. S., & Vijayan, P. K. (1998). Reliable prediction of complex thermal hydraulic parameters by ANN. *Annals of Nuclear Energy*, 25(13), 1069–1078.

[Duffey & Pioro, 2005] Duffey, R. B. & Pioro, I. L. (2005). Experimental heat transfer of supercritical carbon dioxide flowing inside channels (survey). *Nuclear Engineering and Design*, 235(8), 913–924.

[Eter et al., 2017a] Eter, A., Groeneveld, D., & Tavoularis, S. (2017a). Convective heat transfer at high subcritical pressures in tubes with and without flow obstacles. *Nuclear Engineering and Design*, 318, 1–23.

[Eter et al., 2017b] Eter, A., Groeneveld, D., & Tavoularis, S. (2017b). Convective heat transfer in supercritical flows of CO2 in tubes with and without flow obstacles. *Nuclear Engineering and Design*, 313, 162–176.

[Fewster, 1976] Fewster, J. (01.01.1976). *Mixed forced and free convective heat transfer to supercritical pressure fluids flowing in vertical pipes*. Ph.d. thesis, The University of Manchester.

[Fewster & Jackson, 2004] Fewster, J. & Jackson, J. D. (2004). Experiments on supercritical pressure convective heat transfer having relevance to spwr. In *Proceedings of ICAPP'04*, volume Paper 4342 Pittsburgh, PA USA. June 13-17.

[FINKE MINERALÖLWERK GMBH, 2017] FINKE MINERALÖLWERK GMBH (2017). *Sicherheitsdatenblatt gemäß Verordnung (EG) Nr. 1907/2006: AVIATICON HLP-D 46*. Technical Report (pp. 1 - 9).

[Gao, 2017] Gao, Y. (2017). *Messfehlerberechnung für Wärmeübergangsversuche mit überkritischen R134a an der KIMOF*. Bachelor thesis, Karlsruher Institut für Technologie, Germany. Supervisor: Cheng, X.; Co-supervisor: Feuerstein, F.

[Gnielinski, 1975] Gnielinski, V. (1975). Neue Gleichungen für den Wärme- und den Stoffübergang in turbulent durchströmten Rohren und Kanälen. *Forschung im Ingenieurwesen A*, 41(1), 8–16.

[Goldmann, 1961] Goldmann, K. (1961). Heat transfer to supercritical water at 5000 psi flowing at high mass flow rates through round tubes. *International Developments in Heat Transfer, Part III, ASME, New York*, (pp. 561–568).

[Gorban et al., 1990] Gorban, L. M., Pomet'ko, R. S., & Khryaschev, O. A. (1990). *Modeling of water heat transfer with Freon of supercritical pressure: (In Russian)*. 19. Obninsk in Russia: Institute of Physics and Power Engineering.

[Grass et al., 1971] Grass, G., Herkenrath, H., & Hufschmidt, W. (1971). Anwendung des Prandtlschen Grenzschichtmodells auf den Wärmeübergang an Flüssigkeiten mit stark temperaturabhängigen Stoffeigenschaften bei erzwungener Strömung. *Heat and Mass Transfer*, 4(2), 113–119.

[Griem, 1996] Griem, H. (1996). A new procedure for the prediction of forced convection heat transfer at near- and supercritical pressure. *Heat and Mass Transfer*, 31(5), 301–305.

[Groeneveld, 2011] Groeneveld, D. C. (2011). Anomalies and other concerns related to the critical heat flux. *Nuclear Engineering and Design*, 241(11), 4604–4611.

[Groeneveld et al., 1997] Groeneveld, D. C., Doerffer, S., Tain, R. M., Hammouda, N., & CHENG, S. C. (1997). Fluid-to-fluid modelling of crtical heat flux and post-dryout heat transfer. *Experimental Heat Transfer, Fluid Mechanics and Thermodynacmics 1997*, 34(48), 859–867.

[Groeneveld et al., 2003] Groeneveld, D. C., Leung, L., Vasic', A. Z., Guo, Y. J., & CHENG, S. C. (2003). A look-up table for fully developed film-boiling heat transfer. *Nuclear Engineering and Design*, 225(1), 83–97.

[Groeneveld et al., 2007] Groeneveld, D. C., Shan, J. Q., Vasić, A. Z., Leung, L., Durmayaz, A., Yang, J., CHENG, S. C., & Tanase, A. (2007). The 2006 CHF look-up table. *Nuclear Engineering and Design*, 237(15-17), 1909–1922.

[Groeneveld & Snoek, 1986] Groeneveld, D. C. & Snoek, C. W. (1986). A comprehensive examination of heat transfer correlations suitable for reactor safety analysis. *Multiphase Science and Technology*, 2(1-4).

[Gupta et al., 2013] Gupta, S., Saltanov, E., Mokry, S. J., Pioro, I., Trevani, L., & McGillivray, D. (2013). Developing empirical heat-transfer correlations for supercritical CO2 flowing in vertical bare tubes. *Nuclear Engineering and Design*, 261, 116–131.

[Haas, 2012] Haas, C. (2012). *Critical Heat Flux for Flow Boiling of Water at Low Pressure on Smooth and Micro-Structured Zircaloy Tube Surfaces*. Dissertation, KIT scientific reports 7627, Karlsruher Institut für Technologie, Germany.

[Hall & Mudawar, 2000a] Hall, D. D. & Mudawar, I. (2000a). Critical heat flux (CHF) for water flow in tubes—II. subcooled chf correlations. *International Journal of Heat and Mass Transfer*, 43(14), 2605–2640.

[Hall & Mudawar, 2000b] Hall, D. D. & Mudawar, I. (2000b). Critical heat flux (CHF) for water flow in tubes-I. compilation and assessment of world CHF data. *International Journal of Heat and Mass Transfer*, 43(14), 2573–2604.

[Hall & Jackson, 1969] Hall, W. B. & Jackson, J. D., Eds. (1969). *Laminarization of a turbulent pipe flow by buoyancy forces*, volume 11. ASME-AMER soc mechanical eng 345 E 47TH ST, New York, 10017.

[Hall et al., 1967] Hall, W. B., Jackson, J. D., & Watson, A. (1967). A review of forced convection heat transfer to fluids at supercritical pressures: Paper 3. *Proceedings of the Institution of Mechanical Engineers, Conference Proceedings*, 182(9), 10–22.

[He et al., 2016] He, S., He, K., & Seddighi, M. (2016). Laminarisation of flow at low reynolds number due to streamwise body force. *Journal of Fluid Mechanics*, 809, 31–71.

[He et al., 2008] He, S., Kim, W., & Bae, J. (2008). Assessment of performance of turbulence models in predicting supercritical pressure heat transfer in a vertical tube. *International Journal of Heat and Mass Transfer*, 51(19-20), 4659–4675.

[Hendricks et al., 1970] Hendricks, R. C., Simoneau, R. J., & Smith, R. V. (November 1970). *Survey of heat transfer to near-critical fluids*. Technical Report NASA TN D-5886 (pp. 1-116), National Aeronautic and Space Administration, Washington, D. C.

[Herkenrath et al., 1967] Herkenrath, H., Mork-Morkenstein, P., Jung, U., & Weckermann, F. J. (1967). *Heat transfer in water with forced circulation in the pressure range from 140–250 bar*. EUR 3658d. Ispra, Italiy: Joint Research Nuclear Research Centre.

[Hess & Kunz, 1965] Hess, H. L. & Kunz, H. R. (1965). A study of forced convection heat transfer to supercritical hydrogen. *Journal of Heat Transfer*, 87(1), 41–46.

[Ho & Chu, 1977] Ho, C. Y. & Chu, T. K. (1977). *Electrical resistivity and thermal conductivity of nine selected AISI stainless steels*. Technical Report CINDAS Report 45 (pp. 1 -53), Thermophysical and Electronic Properties Information Analysis Center, LaFayette.

[Hong et al., 2004] Hong, S.-D., Chun, S.-Y., Kim, S.-Y., & Baek, W.-P. (2004). Heat transfer characteristics of an internally-heated annulus cooled with R-134a near the critical pressure. *Journal of the Korean Nuclear Society*, 36(5), 403–414.

[Hong et al., 2003] Hong, S. D., Chun, S. Y., Yoon, Y. J., & Baek, W. P. (2003). Heat transfer characteristics of R-134a fluid during the pressure transient from supercritical pressure to subcritical pressure. In *The 10th International Topical Meeting on Nuclear Reactor Thermal Hydraulics (NURETH-10)*, volume 36 (pp. 1–12). Seoul, Korea. October 5 - 11, 2003.

[Huang & Li, 2018] Huang, D. & Li, W. (2018). A brief review on the buoyancy criteria for supercritical fluids. *Applied Thermal Engineering*, 131, 977–987.

[Inasaka & Nariai, 1996] Inasaka, F. & Nariai, H. (1996). Evaluation of subcooled critical heat flux correlations for tubes with and without internal twisted tapes. *Nuclear Engineering and Design*, 163(1), 225–239.

[International Atomic Energy Agency, 2014] International Atomic Energy Agency (2014). *Heat Transfer Behaviour and Thermohydraulics Code Testing for Supercritical Water Cooled Reactors (SCWRs)*, volume 1746 of *IAEA TECDOC Series*. Vienna, Austria.

[International Atomic Energy Agency, 2017] International Atomic Energy Agency (2017). *Nuclear Power Reactors in the World*, volume 2 of *Reference Data Series*. Vienna, Austria.

[Jackson, 2008] Jackson, J. D. (2008). A semi-empirical model of turbulent convective heat transfer to fluids at supercritical pressure. In *16th International Conference on Nuclear Engineering*, volume ICONE16-48914 (pp. 1–11). Orlando, Florida, USA. May 11-15.

[Jackson, 2011] Jackson, J. D. (2011). A model of developing mixed convection heat transfer in vertical tubes to fluids at supercritical pressure. In *The 5th Int. Symp. SCWR's*, volume P104 (pp. 1–16). Vancouver, British Columbia, Canada. March 13 - 16.

[Jackson, 2013a] Jackson, J. D. (2013a). Fluid flow and convective heat transfer to fluids at supercritical pressure. *Nuclear Engineering and Design*, 264, 24–40.

[Jackson, 2013b] Jackson, J. D. (2013b). On the deterioration of forced convection heat transfer in tubes to fluids at supercritical pressure due to bulk flow acceleration. In *The 6th International Symposium on Supercritical Water-Cooled Reactors*, volume ISSCWR6-098 (pp. 1–17). Shenzhen, Guangdong, China. March 03-07.

[Jackson, 2017] Jackson, J. D. (2017). Models of heat transfer to fluids at supercritical pressure with influences of buoyancy and acceleration. *Applied Thermal Engineering*, 124, 1481–1491.

[Jackson et al., 1989] Jackson, J. D., Cotton, M. A., & Axcell, B. P. (1989). Studies of mixed convection in vertical tubes. *International Journal of Heat and Fluid Flow*, 10(1), 2–15.

[Jackson & Fewster, 1975] Jackson, J. D. & Fewster, J. (1975). *Forced convection data for supercritical pressure fluids*. Technical Report Report No. HTFS, 21540 (pp. 1 - 65), The University of Manchester.

[Jackson & Hall, 1979] Jackson, J. D. & Hall, W. B. (1979). Influences of buoyancy on heat transfer to fluids flowing in vertical tubes under turbulent conditions. *Turbulent forced convection in channels and bundles*, 2, 613–640.

[Jäger et al., 2011] Jäger, W., Sánchez Espinoza, Victor Hugo, & Hurtado, A. (2011). Review and proposal for heat transfer predictions at supercritical water conditions using existing correlations and experiments. *Nuclear Engineering and Design*, 241(6), 2184–2203.

[J.D. Jackson, W. B. Hall, 1979] J.D. Jackson, W. B. Hall (1979). Forced convection heat transfer to fluids at supercritial pressures. *Hemisphere Publishing Corp.*, 2, 563–661.

[Jiang, 2015] Jiang, K. (2015). *An Experimental Facility for Studying Heat Transfer in Supercritical Fluids*. Master thesis, University of Ottawa, Ottawa, Canada.

[Kang & Chang, 2009] Kang, K.-H. & Chang, S.-H. (2009). Experimental study on the heat transfer characteristics during the pressure transients under supercritical pressures. *International Journal of Heat and Mass Transfer*, 52(21-22), 4946–4955.

[Kang et al., 2009] Kang, K.-H., Moon, S.-K., Chun, S.-Y., Song, C.-H., & Baek, W.-P. (2009). Experimental study on the chf and the heat transfer characteristics under supercritical pressures. In *The 13th International Topical Meeting on Nuclear Reactor Thermal Hydraulics (NURETH-13)*, volume N13P1239 (pp. 1–13). Kanazawa City, Ishikawa Prefecture, Japan. September 27-October 2, 2009.

[Kariya et al., 2013] Kariya, K., Yoshizumi, K., Mori, H., Mawatari, T., Ohno, M., & Hamamoto, Y. (2013). Correlation for critical heat flux at near - critical pressure in tubes. In *The 6th International Symposium on Supercritical Water-Cooled Reactors*, volume ISSCWR6-028 (pp. 1–12). Shenzhen, Guangdong, China. March 03-07.

[Katto, 1978] Katto, Y. (1978). A generalized correlation of critical heat flux for the forced convection boiling in vertical uniformly heated round tubes. *International Journal of Heat and Mass Transfer*, 21(12), 1527–1542.

[Katto & Ohno, 1984] Katto, Y. & Ohno, H. (1984). An improved version of the generalized correlation of critical heat flux for the forced convective boiling in uniformly heated vertical tubes. *International Journal of Heat and Mass Transfer*, 27(9), 1641–1648.

[Kays & Crawford, 1980] Kays, W. M. & Crawford, M. E. (1980). *Convective Heat and Mass Transfer*. New York, USA: Tata McGraw-Hill Education.

[Kenning et al., 1973] Kenning, D. B., Poon, J. Y., & Shock, R. A. (1973). *Local Reductions in Heat Transfer Due to Bouyancy Effects in Upward Turbulent Flow*. Harwell, Great Britain: Atomic Energy Research Establishment.

[Kim & Chang, 2005] Kim, C. H. & Chang, S. H. (2005). CHF characteristics of R-134a flowing upward in uniformly heated vertical tube. *International Journal of Heat and Mass Transfer*, 48(11), 2242–2249.

[Kim & Kim, 2011a] Kim, D. E. & Kim, M.-H. (2011a). Experimental investigation of heat transfer in vertical upward and downward supercritical CO2 flow in a circular tube. *International Journal of Heat and Fluid Flow*, 32(1), 176–191.

[Kim & Kim, 2011b] Kim, D. E. & Kim, M. H. (2011b). Two layer heat transfer model for supercritical fluid flow in a vertical tube. *The Journal of Supercritical Fluids*, 58(1), 15–25.

[Kim et al., 2008] Kim, H., Kim, H. Y., Song, J. H., & Bae, Y. Y. (2008). Heat transfer to supercritical pressure carbon dioxide flowing upward through tubes and a narrow annulus passage. *Progress in Nuclear Energy*, 50(2–6), 518–525.

[Kim et al., 2006] Kim, H., Song, J. H., Bae, Y. Y., & Kim, H. Y. (2006). Assessment of heat transfer correlations on supercritical pressure flows for an upward flow of CO2 in a circular tube. In *Fifth Korea-Japan Symposium on Nuclear Thermal Hydraulics and Safety*, volume NTHAS5-D101 (pp. 1–7). Jeju, Korea. November 26- 29.

[Kim et al., 2007a] Kim, H. Y., Kim Hyungrae, Song, J. H., Cho, B. H., & Bae, Y. Y. (2007a). Heat transfer test in a vertical tube using CO2 at supercritical pressures. *Journal of Nuclear Science and Technology*, 44(3), 285–293.

[Kim et al., 2007b] Kim, J. K., Jeon, H. K., & Lee, J. S. (2007b). Wall temperature measurement and heat transfer correlation of turbulent supercritical carbon dioxide flow in vertical circular/non-circular tubes. *Nuclear Engineering and Design*, 237(15), 1795–1802.

[Kim et al., 2004] Kim, S. H., Kim, Y. I., Bae, Y., & Cho, B. (2004). Numerical simulation of the vertical upward flow of water in a heated tube at supercritical pressure. In *Proceedings of the 2004 international congress on advances in nuclear power plants-ICAPP'04*, volume 35 (pp. 1–13). Pittsburgh, USA. 13.-17. Juni, 2004.

[Kirillov & Grabezhnaia, 2006] Kirillov, P. & Grabezhnaia, V. (July 17–20, 2006). Heat transfer at supercritical pressures and the onset of deterioration. In *14th International Conference on Nuclear Engineering*, volume ICONE14-89274 (pp. 1–7). Miami, USA. July 17–20, 2006.

[Kirillov, 2000] Kirillov, P. L. (2000). Heat and mass transfer at supercritical parameters. the short review of researches in russia. theory and experiments. In *Proceedings of the first international symposium on supercritical water-cooled reactors, design and technology*, volume 105 (pp. 58–71). Tokyo University. 6-9 November.

[Kline, 2017] Kline, N. (2017). *An Experimental Study of Heat Transfer Deterioration at Supercritical Pressures*. Master thesis, University of Ottawa, Ottawa, Canada.

[Kline et al., 2018] Kline, N., Feuerstein, F., & Tavoularis, S. (2018). Onset of heat transfer deterioration in vertical pipe flows of at supercritical pressures. *International Journal of Heat and Mass Transfer*, 118, 1056–1068.

[Komita et al., 2003] Komita, H., Morooka, S., Yoshida, S., & Mori, H. (2003). Study on the heat transfer to the supercritical pressure fluid for supercritical water cooled power reactor development. In *The 10th International Topical Meeting on Nuclear Reactor Thermal Hydraulics*, volume 36 (pp. 1–12). Seoul, Korea. October 5-11.

[Kondratev, 1969] Kondratev, N. S. (1969). Heat transfer and hydraulic resistance with supercritical water flowing in tubes. *Thermal Engineering*, 16(8), 73–77.

[Kon'Kov, 1965] Kon'Kov, A. S. (1965). Experimental study of the conditions under which heat exchange deteriorates when a steam-water mixture flows in heated tubes. *Teploenergetika*, 13(12), 77.

[Koshizuka et al., 1995] Koshizuka, S., Takano, N., & Oka, Y. (1995). Numerical analysis of deterioration phenomena in heat transfer to supercritical water. *International Journal of Heat and Mass Transfer*, 38(16), 3077–3084.

[Krasnoshchekov et al., 1964] Krasnoshchekov, E. A., Protopopov, V. S., Van, F., & Kuraeva, I. V., Eds. (1964). *Experimental investigation of heat transfer for carbon dioxide in the supercritical region: Proceedings of the 2nd All-Soviet Union Conference on Heat and Mass Transfer (pp. 26 - 35), Minsk, Belarus.*

[Kuang et al., 2008] Kuang, B., Zhang, Y., & Cheng, X. (2008). A new, wide-ranged heat transfer correlation of water at supercritical pressures in vertical upward ducts. In *The 7th International Topical Meeting on Nuclear Reactor Thermal Hydraulics, Operation and Safety* Seoul, Korea. October 5-9.

[Kunik, 2012] Kunik, C. (2012). *CFD-Simulationen turbulenter konvektiver Strömungen bei überkritischen Drücken*. Dissertation, Karlsruher Institut für Technologie, Germany.

[Kurganov & Kaptil'ny, 1992] Kurganov, V. A. & Kaptil'ny, A. G. (1992). Velocity and enthalpy fields and eddy diffusivities in a heated supercritical fluid flow. *Experimental Thermal and Fluid Science*, 5(4), 465–478.

[Kurganov et al., 2013] Kurganov, V. A., Zeigarnik, Y. A., & Maslakova, I. V. (2013). Heat transfer and hydraulic resistance of supercritical pressure coolants. part III: Generalized description of scp fluids normal heat transfer, empirical calculating correlations, integral method of theoretical calculations. *International Journal of Heat and Mass Transfer*, 67(0), 535–547.

[Kurganov et al., 2014] Kurganov, V. A., Zeigarnik, Y. A., & Maslakova, I. V. (2014). Heat transfer and hydraulic resistance of supercritical pressure coolants. part IV: Problems of generalized heat transfer description, methods of predicting deteriorated heat transfer; empirical correlations; deteriorated heat transfer enhancement; dissolved gas effects. *International Journal of Heat and Mass Transfer*, 77(0), 1197–1212.

[Ledinegg, 1938] Ledinegg, M. (1938). Instabilität der Strömung bei Natürlichen und Zwangumlauf. *die Wärme: Forschung u. Praxis d. Wärme-, Kälte- u. Verfahrenstechnik*, 61(48), 891–898.

[Lee et al., 2008] Lee, K. L., Bang, I. C., & Chang, S. H. (2008). The characteristics and visualization of critical heat flux of R-134a flowing in a vertical annular geometry with spacer grids. *International Journal of Heat and Mass Transfer*, 51(1-2), 91–103.

[Lee & Haller, 1974] Lee, R. & Haller, K., Eds. (1974). *Supercritical water heat transfer developments and applications: Proceedings of the 5th International Heat Transfer Conference*, Boiling (pp. 335-339), Tokyo, Japan. 3-7 September 1974.

[Lei et al., 2016] Lei, X., Li, H., Zhang, W., Dinh, N. T., Guo, Y., & Yu, S. (2016). Experimental study on the difference of heat transfer characteristics between vertical and horizontal flows of supercritical pressure water. *Applied Thermal Engineering*, 113, 609–620.

[Lemmon et al., 2007] Lemmon, E. W., Huber, M. L., & McLinden, M. O. (2007). NIST standard reference database 23: Reference fluid thermodynamic and transport properties-REFPROP, version 8.0: Standard reference data program.

[Li et al., 2017] Li, Y., Yin, Y., & Cheng, X. (2017). Experimental study on supercritical heat transfer in a downward flowing circular tube with freon R134a. In Xi'an Jiao Tong University (Ed.), *17th International Topical Meeting on Nuclear Reactor Thermal Hydraulics*, volume Paper 21257 (pp. 1–11). Xi'an, China. Sept. 3-8, 2017.

[Li et al., 2014] Li, Z., Wu, Y., Lu, J., Zhang, D., & Zhang, H. (2014). Heat transfer to supercritical water in circular tubes with circumferentially non-uniform heating. *Applied Thermal Engineering*, 70(1), 190–200.

[Lietzke & Mullins, 1981] Lietzke, M. H. & Mullins, C. (1981). The thermal decomposition of carbon dioxide. *Journal of Inorganic and Nuclear Chemistry*, 43(8), 1769–1771.

[Liu et al., 2016] Liu, W., Wang, S., & Shan, J. (2016). Parametric trends analysis of the chf based on vertical round tube and 5×5 rod bundle databases. In *The 11th International Topical Meeting on Nuclear Reactor Thermal Hydraulics, Operation and Safety*, volume N11P0326 (pp. 1–11). Gyeongju, Korea. October 9-13.

[Lombardi, 1995] Lombardi, C. (1995). A formal approach for the prediction of the critical heat flux in subcooled water. In American Nuclear Society (Ed.), *Proceedings of the 7th International Meeting on Nuclear Reactor Thermal-Hydraulics* (pp. 2506–2518). Saratoga Springs, New York, USA. September 10-15.

[Löwenberg, 2007] Löwenberg, M. F. (2007). *Wämeuebergang von Wasser in vertikalen Rohrströmungen bei überkritischem Druck*. Dissertation, Universität Stuttgart, Germany.

[Ma et al., 2017] Ma, D., Zhou, T., Chen, J., Qi, S., Ali Shahzad, M., & Xiao, Z. (2017). Supercritical water heat transfer coefficient prediction analysis based on bp neural network. *Nuclear Engineering and Design*, 320, 400–408.

[Mayinger & Scheldt, 1984] Mayinger, F. & Scheldt, M. (1984). Heat transfer in the supercritical region with vertical upflow. *Wärme - und Stoffübertragung*, 18(4), 207–214.

[McEligot & Laurien, 2015] McEligot, D. M. & Laurien, E. (2015). Insight from simple heat transfer models. In *The 7th International Symposium on Supercritical Water-Cooled Reactors (ISSCWR-7)*, volume ISSCWR7-2023 (pp. 1–10). Helsinki, Finland. March 15-18.

[Miropolskii & Shitsman, 1957] Miropolskii, L. & Shitsman, M. E. (1957). Heat transfer to water and steam at variable specific heat (in near-critical region). *Soviet Physics-Technical Physics*, 2(10), 2196–2208.

[Miropolsky et al., 1966] Miropolsky, Z. L., Picus, V. J., & Shitsman, M. E. (1966). Regimes of deteriorated heat transfer at forced flow of fluids in curvilinear channels. In *International Heat Transfer Conference 3* (pp. 95–105). Chicago, USA. August 7-12.

[Mohammed Shah, 1987] Mohammed Shah, M. (1987). Improved general correlation for critical heat flux during upflow in uniformly heated vertical tubes. *International Journal of Heat and Fluid Flow*, 8(4), 326–335.

[Mokry et al., 2009] Mokry, S., Pioro, I., & Duffey, R. (2009). Experimental heat transfer to supercritical CO2 flowing upward in a bare vertical tube. In *SCCO2 Power Cycle Symposium* (pp. 1–15). RPI, Troy, NY, USA. April 29-30.

[Mokry et al., 2011] Mokry, S., Pioro, I., Farah, A., King, K., Gupta, S., Peiman, W., & Kirillov, P. (2011). Development of supercritical water heat-transfer correlation for vertical bare tubes. *Nuclear Engineering and Design*, 241(4), 1126–1136.

[Moon et al., 1996] Moon, S. K., Baek, W.-P., & Chang, S. H. (1996). Parametric trends analysis of the critical heat flux based on artificial neural networks. *Nuclear Engineering and Design*, 163(1), 29–49.

[Nishikawa et al., 1982] Nishikawa, K., Yoshida, S., Yamada, A., & Ohno, M. (1982). Experimental investigation of critical heat flux in forced convection boiling of freon in a tube at high subcritical pressure. In *7th International Heat Transfer Conference* (pp. 321–326). München, Germany. September 6-10.

[Noel, 1966] Noel, M. B. (1966). *Experimental investigation of the forced- convection and nucleate-boiling heat-transfer characteristics of liquid ammonia(Forced convection and nucleate boiling heat transfer characteristics of liquid ammonia)*. Technical report No. 32-125 (pp. 1-19), NASA, Washington, DC, United States.

[Nukiyama, 1966] Nukiyama, S. (1966). The maximum and minimum values of the heat Q transmitted from metal to boiling water under atmospheric pressure. *International Journal of Heat and Mass Transfer*, 9(12), 1419–1433.

[Oka et al., 2010] Oka, Y., Koshizuka, S., Ishiwatari, Y., & Yamaji, A. (2010). *Super Light Water Reactors and Super Fast Reactors*. New York, USA: Springer Science+Business Media, LLC.

[Olivier et al., 2017] Olivier, J. G., Schure, K. M., & Peters, J. (2017). Trends in global CO2 and total greenhouse gas emissions. *Summary of the 2017 Report. PBL Netherlands Environmental Assessment Agency. The Hague*.

[Ornatskiy et al., 1972] Ornatskiy, A. P., Glushchenko, L. F., & Gandzyuk, O. F. (1972). An experimental study of heat transfer in externally-heated annuli at supercritical pressures. *Heat Transfer-Sov. Res*, 4, 1–25.

[Pandey & Laurien, 2015] Pandey, S. & Laurien, E. (2015). Heat transfer analysis at supercritical pressure using two layer theory. *The Journal of Supercritical Fluids*, 109, 80–86.

[Pandey et al., 2017] Pandey, S., Laurien, E., & Chu, X. (2017). A modified convective heat transfer model for heated pipe flow of supercritical carbon dioxide. *International Journal of Thermal Sciences*, 117, 227–238.

[Petukhov, 1961] Petukhov, B. S. (1961). An investigation of heat transfer to fluids flowing in pipes under supercritical conditions. In The American Society of Mechanical Engineers (Ed.), *Proceedings of 2nd Int. Heat Transfer Conference* (pp. 1–12). University of Colorado, Boulder, Colorado USA. August 28-September 1.

[Petukhov, 1970] Petukhov, B. S. (1970). Heat transfer and friction in turbulent pipe flow with variable physical properties. In J. P. Hartnett & T. F. Irvine (Eds.), *Advances in Heat Transfer*, volume 6 (pp. 503–564). Elsevier.

[Petukov et al., 1988] Petukov, B. S., Poljakov, A. F., & Launder, B. E., Eds. (1988). *Heat transfer in turbulent mixed convection*. New York, USA: Hemisphere Publ. Corp.

[Pioro et al., 2002] Pioro, I., Groeneveld, D., Leung, L., Doerffer, S., Cheng, S., Antoshko, Y., Guo, Y., & Vasić, A. (2002). Comparison of CHF measurements in horizontal and vertical tubes cooled with R-134a. *International Journal of Heat and Mass Transfer*, 45(22), 4435–4450.

[Pioro & Duffey, 2005] Pioro, I. L. & Duffey, R. B. (2005). Experimental heat transfer in supercritical water flowing inside channels (survey). *Nuclear Engineering and Design*, 235(22), 2407–2430.

[Pioro & Duffey, 2007] Pioro, I. L. & Duffey, R. B. (2007). *Heat transfer and hydraulic resistance at supercritical pressures in power engineering applications*. New York, USA: ASME Press.

[Pioro et al., 2004a] Pioro, I. L., Duffey, R. B., & Dumouchel, T. J. (2004a). Hydraulic resistance of fluids flowing in channels at supercritical pressures (survey). *Nuclear Engineering and Design*, 231(2), 187–197.

[Pioro et al., 2001] Pioro, I. L., Groeneveld, D. C., CHENG, S. C., Doerffer, S., Vasić, A. Ž., & Antoshko, Y. V. (2001). Comparison of chf measurements in R-134a cooled tubes and the water chf look-up table. *International Journal of Heat and Mass Transfer*, 44(1), 73–88.

[Pioro et al., 2004b] Pioro, I. L., Khartabil, H. F., & Duffey, R. B. (2004b). Heat transfer to supercritical fluids flowing in channels—empirical correlations (survey). *Nuclear Engineering and Design*, 230(1–3), 69–91.

[Pitla et al., 1998] Pitla, S. S., Robinson, D. M., Groll, E. A., & Ramadhyani, S. (1998). Heat transfer from supercritical carbon dioxide in tube flow: A critical review. *HVAC&R Research*, 4(3), 281–301.

[Polyakov, 1991] Polyakov, A. F. (1991). Heat transfer under supercritical pressures. *Advances in heat transfer*, 21, 1–53.

[Preda et al., 2012] Preda, T., Saltanov, E., Pioro, I., & Gabriel, K. S. (2012). Development of a heat transfer correlation for supercritical CO2 based on multiple data sets. In ASME (Ed.), *20th International Conference on Nuclear Engineering and the ASME 2012 Power Conference, ICONE 2012-POWER 2012*, volume 5 (pp. 211–217). Anaheim, California, USA. July 30–August 3, 2012.

[Pucciarelli et al., 2015] Pucciarelli, A., Borroni, I., Sharabi, M., & Ambrosini, W. (2015). Results of 4-equation turbulence models in the prediction of heat transfer to supercritical pressure fluids. *Nuclear Engineering and Design*, 281(0), 5–14.

[Pucciarelli et al., 2016] Pucciarelli, A., Sharabi, M., & Ambrosini, W. (2016). Prediction of heat transfer to supercritical fluids by the use of algebraic heat flux models. *Nuclear Engineering and Design*, 297, 257–266.

[Rahman et al., 2016] Rahman, M. M., Dongxu, J., Beni, M. S., Hei, H. C., He, W., & Zhao, J. (2016). Supercritical water heat transfer for nuclear reactor applications: A review. *Annals of Nuclear Energy*, 97, 53–65.

[Rayleigh, 1892] Rayleigh (1892). VIII. on the question of the stability of the flow of fluids. *The London, Edinburgh, and Dublin Philosophical Magazine and Journal of Science*, 34(206), 59–70.

[Razumovskiy et al., 1990] Razumovskiy, V. G., Ornatskiy, A. P., & Mayevskiy, Y. E. (1990). Local heat transfer and hydraulic behavior in turbulent channel flow of water at supercritical pressure. *Heat Transfer-Soviet Research;(USA)*, 22(1).

[Richard A. Perkins et al., 2000] Richard A. Perkins, Arno R. Laesecke, J. Howley, M L. Ramires, & A N. Gurova, L -. Cusco (2000). *Experimental Thermal Conductivity Values for the Iupac Round-Robin Sample 1,1,1,2-Tetrafluoroethane (R134a)*. Technical Report 6605 (pp. 1 - 153), Physical and Chemical Properties Division Chemical Science and Technology Laboratory National Institute of Standards and Technology, Boulder, Colorado.

[Saltanov et al., 2015] Saltanov, E., Pioro, I., Mann, D., Gupta, S., Mokry, S., & Harvel, G. (2015). Study on specifics of forced-convective heat transfer in supercritical carbon dioxide. *Journal of Nuclear Engineering and Radiation Science*, 1(1), 011008–1–011008–8.

[Sarrade et al., 2017] Sarrade, S., Féron, D., Rouillard, F., Perrin, S., Robin, R., Ruiz, J.-C., & Turc, H.-A. (2017). Overview on corrosion in supercritical fluids. *The Journal of Supercritical Fluids*, 120(Part 2), 335–344.

[Scalabrin & Piazza, 2003] Scalabrin, G. & Piazza, L. (2003). Analysis of forced convection heat transfer to supercritical carbon dioxide inside tubes using neural networks. *International Journal of Heat and Mass Transfer*, 46(7), 1139–1154.

[Schatte et al., 2016] Schatte, G. A., Kohlhepp, A., Wieland, C., & Spliethoff, H. (2016). Development of a new empirical correlation for the prediction of the onset of the deterioration of heat transfer to supercritical water in vertical tubes. *International Journal of Heat and Mass Transfer*, 102, 133–141.

[Schindler, 2016] Schindler, P. (2016). *Versuche für kritische Wärmestromdichte (CHF) an der KIMOF*. Bachelor thesis, Karlsruher Institut für Technologie, Germany. Supervisor: Cheng, X.; Co-supervisor: Feuerstein, F.

[Schmidt et al., 1946] Schmidt, E., Eckert, E., Grigull, U., & Command, U. S. A. F. A. M. (1946). *Heat Transfer by Liquids Near the Critical State*. 527. USA: Wright Field, Air Materiel Command.

[Schulenberg & Starflinger, 2012] Schulenberg, T. & Starflinger, J. (2012). *High performance light water reactor: design and analyses*. Karlsruhe, Germany: KIT Scientific Publishing.

[Sharma et al., 2014] Sharma, M., Vijayan, P. K., Pilkhwal, D. S., & Asako, Y. (2014). Natural convective flow and heat transfer studies for supercritical water in a rectangular circulation loop. *Nuclear Engineering and Design*, 273, 304–320.

[Shen et al., 2017] Shen, Z., Yang, D., Wang, S., Wang, W., & Li, Y. (2017). Experimental and numerical analysis of heat transfer to water at supercritical pressures. *International Journal of Heat and Mass Transfer*, 108, Part B, 1676–1688.

[Shen et al., 2016] Shen, Z., Yang, D., Xie, H., Nie, X., Liu, W., & Wang, S. (2016). Flow and heat transfer characteristics of high-pressure water flowing in a vertical upward smooth tube at low mass flux conditions. *Applied Thermal Engineering*, 102, 391–401.

[Shim & Lee, 2006] Shim, W. & Lee, J.-S. (2006). Prediction of CHF in vertical round tubes with uniform heat flux for water. *Journal of Industrial and Engineering Chemistry*, 12(1), 127–133.

[Shiralkar & Griffith, 1970] Shiralkar, B. & Griffith, P. (1970). The effect of swirl, inlet conditions, flow direction, and tube diameter on the heat transfer to fluids at supercritical pressure. *Journal of Heat Transfer*, 92(3), 465–471.

[Shiralkar & Griffith, 1968] Shiralkar, B. S. & Griffith, P. (1968). *The deterioration in heat transfer to fluids at supercritical pressure and high heat fluxes*. Report No. DSR 70332-55. Department of Mechanical Engineering, Massachusetts Instiutute of Technology.

[Shitsman, 1963] Shitsman, M. E. (1963). Impairment of the heat transmission at supercritical pressures(heat transfer process examined during forced motion of water at supercritical pressures). *High temperature*, 1, 237–244.

[Shitsman, 1967] Shitsman, M. E. (1967). Paper 6: Natural convection effect on heat transfer to a turbulent water flow in intensively heated tubes at supercritical pressures. *Proceedings of the Institution of Mechanical Engineers*, 182(9), 36–41.

[Sieder & Tate, 1936] Sieder, E. N. & Tate, G. E. (1936). s. *Industrial & Engineering Chemistry*, 28(12), 1429–1435.

[Song et al., 2008] Song, J., Kim, H., Kim, H., & Bae, Y. (2008). Heat transfer characteristics of a supercritical fluid flow in a vertical pipe. *The Journal of Supercritical Fluids*, 44(2), 164–171.

[Span & Wagner, 1996] Span, R. & Wagner, W. (1996). A new equation of state for carbon dioxide covering the fluid region from the triple–point temperature to 1100 K at pressures up to 800 MPa. *Journal of Physical and Chemical Reference Data*, 25(6), 1509–1596.

[Swenson et al., 1965] Swenson, H. S., Carver, J. R., & Kakarala, C. R. (1965). Heat transfer to supercritical water in smooth-bore tubes. *Journal of Heat Transfer*, 87(4), 477–483.

[Tang et al., 2016] Tang, G., Shi, H., Wu, Y., Lu, J., Li, Z., Liu, Q., & Zhang, H. (2016). A variable turbulent prandtl number model for simulating supercritical pressure CO2 heat transfer. *International Journal of Heat and Mass Transfer*, 102, 1082–1092.

[Tian et al., 2018] Tian, R., Feuerstein, F., Dai, X., & Shi, L. (2018). Fluid–to–fluid scaling of heat transfer to mixed convection flow of supercritical pressure fluids. *International Journal of Energy Research*, 42(10), 3361–3377.

[Tillner-Roth & Baehr, 1994] Tillner-Roth, R. & Baehr, H. D. (1994). An international standard formulation for the thermodynamic properties of 1,1,1,2–tetrafluoroethane (HFC–134a) for temperatures from 170 K to 455 k and pressures up to 70 MPa. *Journal of Physical and Chemical Reference Data*, 23(5), 657–729.

[Tong & Tang, 1997] Tong, L. S. & Tang, Y. S. (1997). *Boiling heat transfer and two-phase flow*. Washington, D.C., USA: Taylor & Francis.

[Verein Deutscher Ingenieure, 2013] Verein Deutscher Ingenieure (2013). *VDI-Wärmeatlas*. VDI-Buch. Berlin, Germany: Springer Vieweg, 11. edition.

[Vesovic et al., 1990] Vesovic, V., Wakeham, W. A., Olchowy, G. A., Sengers, J. V., Watson, J. T., & Millat, J. (1990). The transport properties of carbon dioxide. *Journal of Physical and Chemical Reference Data*, 19(3), 763–808.

[Vijayarangan et al., 2006] Vijayarangan, B. R., Jayanti, S., & Balakrishnan, A. R. (2006). Studies on critical heat flux in flow boiling at near critical pressures. *International Journal of Heat and Mass Transfer*, 49(1–2), 259–268.

[Vikhrev et al., 1967] Vikhrev, Y. V., Barulin, Y. D., & Kon'Kov, A. S. (1967). A study of heat transfer in vertical tubes at supercritical pressures. *Thermal Engineering*, 14(9), 116–119.

[Wang & Li, 2013] Wang, C. & Li, H. (2013). Evaluation of the heat transfer correlations for supercritical pressure water in vertical tubes. *Heat Transfer Engineering*, 35, 685–692.

[Wang et al., 2011] Wang, J., Li, H., Yu, S., & Chen, T. (2011). Investigation on the characteristics and mechanisms of unusual heat transfer of supercritical pressure water in vertically-upward tubes. *International Journal of Heat and Mass Transfer*, 54(9–10), 1950–1958.

[Wang & He, 2015] Wang, W. & He, S. (2015). Direct numerical simulation of fluid flow at supercritical pressure in a vertical channel. In American Nuclear Society (Ed.), *NURETH-16* (pp. 2334–2347). Chicago. August 30-September 4.

[Watts & Chou, 1982] Watts, M. J. & Chou, C. T. (1982). Mixed convection heat transfer to supercritical pressure water. In *7th International Heat Transfer Conference*, volume 3 (pp. 495–500). München, Germany. September 6-10.

[WESTWATER, 1963] WESTWATER, J. W. (1963). Things we don't know about boiling heat transfer. In *Theory and Fundamental Research in Heat Transfer* (pp. 61–73). Elsevier.

[Wirbser, 1995] Wirbser, H. (1995). *Hochdruck-Strömungskalorimetrie: spezifische Wärmekapazität Cp und differentieller Joule-Thomson-Koeffizient halogenierter Kohlenwasserstoffe*. Dissertation, Universität Karlsruhe, Germany.

[Wood & Smith, 1964] Wood, R. D. & Smith, J. M. (1964). Heat transfer in the critical region— temperature and velocity profiles in turbulent flow. *AIChE Journal*, 10(2), 180–186.

[Xiong et al., 2017] Xiong, Z., Gu, H., Zhang, S., & Chen, J. (2017). Effect of intermittent heating on the heat transfer performance of supercritical R134a flowing in a pipe. *Experimental Thermal and Fluid Science*, 88, 434–443.

[Yamagata et al., 1972] Yamagata, K., Nishikawa, K., Hasegawa, S., Fujii, T., & Yoshida, S. (1972). Forced convective heat transfer to supercritical water flowing in tubes. *International Journal of Heat and Mass Transfer*, 15(12), 2575–2593.

[Yamashita et al., 2003] Yamashita, T., Yoshida, S., Mori, H., Morooka, S., Komita, H., & Nishida, K. (2003). Heat transfer study under supercritical pressure conditions. In *Proceedings of the international conference on global environment and advanced nuclear power plants*, volume Paper 1119 (pp. 1–8). Kyoto, Japan. Sep. 15-19.

[Yang et al., 2017] Yang, B.-W., Liu, X., & Mao, H. (2017). Review of chf mechanisms models. In Xi'an Jiao Tong University (Ed.), *17th International Topical Meeting on Nuclear Reactor Thermal Hydraulics*, volume Paper 19535 (pp. 1–15). Xi'an, China. Sept. 3-8, 2017.

[Yeroshenko & Yaskin, 1981] Yeroshenko, V. M. & Yaskin, L. A. (1981). Applicability of various correlations for the prediction of turbulent heat transfer of supercritical helium. *Cryogenics*, 21(2), 94–96.

[Yi et al., 2004] Yi, T. T., KOSHIZUKA, S., & Oka, Y. (2004). A linear stability analysis of supercritical water reactors, (II): Coupled neutronic thermal-hydraulic stability. *Journal of Nuclear Science and Technology*, 41(12), 1176–1186.

[Yildiz & Groeneveld, 2014] Yildiz, S. & Groeneveld, D. C. (2014). Diameter effect on supercritical heat transfer. *International Communications in Heat and Mass Transfer*, 54, 27–32.

[Yoo, 2013] Yoo, J. Y. (2013). The turbulent flows of supercritical fluids with heat transfer. *Annual Review of Fluid Mechanics*, 45(1), 495–525.

[Zahlan, 2015] Zahlan, H. (2015). *Derivation of a look-up table for trans-critical heat transfer in water-cooled tubes*. Ph.d. thesis, University of Ottawa, Canada.

[Zahlan et al., 2015a] Zahlan, H., Groeneveld, D., & Tavoularis, S. (2015a). Measurements of convective heat transfer to vertical upward flows of CO2 in circular tubes at near-critical and supercritical pressures. *Nuclear Engineering and Design*, 289, 92–107.

[Zahlan et al., 2014] Zahlan, H., Groeneveld, D. C., & Tavoularis, S. (2014). Fluid-to-fluid scaling for convective heat transfer in tubes at supercritical and high subcritical pressures. *International Journal of Heat and Mass Transfer*, 73, 274–283.

[Zahlan et al., 2011] Zahlan, H., Groeneveld, D. C., Tavoularis, S., Mokry, S., & Pioro, I. (2011). Assessment of supercritical heat transfer prediction methods. In *The 5th Int. Symp. SCWR's*, volume P008 (pp. 1–20). Vancouver, British Columbia, Canada. March 13 - 16.

[Zahlan & Leung, 2018] Zahlan, H. & Leung, L. K. (2018). Critical heat flux in tubes near the critical point: presentation at SCWR information exchange meeting, IEM-12, Montreal, Canada, March 19-20.

[Zahlan et al., 2015b] Zahlan, H., Tavoularis, S., & Groeneveld, D. C. (2015b). A look-up table for trans-critical heat transfer in water-cooled tubes. *Nuclear Engineering and Design*, 285, 109–125.

[Zhang et al., 2018] Zhang, Q., Li, H., Kong, X., Liu, J., & Lei, X. (2018). Special heat transfer characteristics of supercritical CO2 flowing in a vertically-upward tube with low mass flux. *International Journal of Heat and Mass Transfer*, 122, 469–482.

[Zhang et al., 2015a] Zhang, Q., Li, H., Zhang, W., Li, L., & Lei, X. (2015a). Experimental study on heat transfer to the supercritical water upward flow in a vertical tube with internal helical ribs. *International Journal of Heat and Mass Transfer*, 89, 1044–1053.

[Zhang et al., 2015b] Zhang, S., Gu, H., & Cheng, X. (2015b). Prediction of heat transfer of supercritical freon flowing upward in vertical tubes. In VTT Technical Research Centre of

Finland Ltd (Ed.), *The 7th International Symposium on Supercritical Water-Cooled Reactors*, volume ISSCWR7-2063 (pp. 1–12). Helsinki, Finland. 15-18 March.

[Zhang et al., 2014] Zhang, S., Gu, H., Cheng, X., & Xiong, Z. (2014). Experimental study on heat transfer of supercritical freon flowing upward in a circular tube. *Nuclear Engineering and Design*, 280, 305–315.

[Zhao et al., 2017] Zhao, M., Badea, A. F., Feuerstein, F., & Cheng, X. (2017). Assessment of experimental data of heat transfer of supercritical water in tubes. In Xi'an Jiao Tong University (Ed.), *17th International Topical Meeting on Nuclear Reactor Thermal Hydraulics*, volume Paper 21004 (pp. 1–14). Xi'an, China. Sept. 3-8, 2017.

[Zhao et al., 2014] Zhao, M., Gu, H. Y., & Cheng, X. (2014). Experimental study on heat transfer of supercritical water flowing downward in circular tubes. *Annals of Nuclear Energy*, 63, 339–349.

[Zhou, 2014] Zhou, F. (2014). *CFD study of convective heat transfer to carbon dioxide and water at supercritical pressures in vertical circular pipes*. Master thesis, Mc Master University, Hamilton, Ontario, Canada.

[Zhu et al., 2009] Zhu, X., Bi, Q., Yang, D., & Chen, T. (2009). An investigation on heat transfer characteristics of different pressure steam-water in vertical upward tube. *Nuclear Engineering and Design*, 239(2), 381–388.

[Zierep, 1972] Zierep, J. (1972). *Ähnlichkeitsgesetze und Modellregeln der Strömungslehre*. Karlsruhe: Braun.

[Zwolinski et al., 2011] Zwolinski, S., Anderson, M., Corradini, M., & Licht, J. (2011). Evaluation of fluid-to-fluid scaling method for water and carbon dioxide at supercritical pressure. In *The 5th Int. Symp. SCWR's*, volume P001 (pp. 1–11). Vancouver, British Columbia, Canada. March 13 - 16.

Own publications

[Badea et al., 2018] Badea, A. F., Zhao, M., Cheng, X., Feuerstein, F., & Liu, X. (2018). Consistency considerations on a large databank and wide range heat transfer prediction for supercritical water in circular tubes. *Nuclear Engineering and Design*, 335, 178–185.

[Cheng et al., 2019] Cheng, X., Zhao, M., Feuerstein, F., & Liu, X. J. (2019). Prediction of heat transfer to supercritical water at different boundary conditions. *International Journal of Heat and Mass Transfer*, 131, 527–536.

[Kline et al., 2018] Kline, N., Feuerstein, F., & Tavoularis, S. (2018). Onset of heat transfer deterioration in vertical pipe flows of at supercritical pressures. *International Journal of Heat and Mass Transfer*, 118, 1056–1068.

[Tian et al., 2018] Tian, R., Feuerstein, F., Dai, X., & Shi, L. (2018). Fluid–to–fluid scaling of heat transfer to mixed convection flow of supercritical pressure fluids. *International Journal of Energy Research*, 42(10), 3361–3377.

[Zhao et al., 2017] Zhao, M., Badea, A. F., Feuerstein, F., & Cheng, X. (2017). Assessment of experimental data of heat transfer of supercritical water in tubes. In Xi'an Jiao Tong University (Ed.), *17th International Topical Meeting on Nuclear Reactor Thermal Hydraulics*, volume Paper 21004 (pp. 1–14). Xi'an, China. Sept. 3-8, 2017.

Supervised theses

[Coelho Silva, 2015] Coelho Silva, A. (2015). *Versuche zum Wärmeübergang mit überkritischem R134a an der KIMOF*. Master thesis, Karlsruher Institut für Technologie, Germany. Supervisor: Cheng, X.; Co-supervisor: Feuerstein, F.

[Gao, 2017] Gao, Y. (2017). *Messfehlerberechnung für Wärmeübergangsversuche mit überkritischen R134a an der KIMOF*. Bachelor thesis, Karlsruher Institut für Technologie, Germany. Supervisor: Cheng, X.; Co-supervisor: Feuerstein, F.

[Schindler, 2016] Schindler, P. (2016). *Versuche für kritische Wärmestromdichte (CHF) an der KIMOF*. Bachelor thesis, Karlsruher Institut für Technologie, Germany. Supervisor: Cheng, X.; Co-supervisor: Feuerstein, F.

Appendix

All fluid properties in the equations in the appendix are at local bulk temperature if not defined differently. Same definitions are only given once.

A. Correlations for heat transfer at supercritical conditions

A.1. Badea

$$Nu_b = \alpha_1 \, Re_b^{\alpha_2} \, Pr_b^{\alpha_3} \, Pr_w^{\alpha_4} \left(\frac{\rho_w}{\rho_b}\right)^{\alpha_5} \left(\frac{\lambda_w}{\lambda_b}\right)^{\alpha_6} \left(\frac{\eta_w}{\eta_b}\right)^{\alpha_7} \left(\frac{c_{p,w}}{c_{p,b}}\right)^{\alpha_8} \left(\frac{\pi_A}{\pi_{A,pc}}\right)^{\alpha_9} \tag{A.1}$$

no HTD

$$
\begin{aligned}
\alpha_1 &= \quad 1.464 \ 10^{-2} \\
\alpha_2 &= \quad 8.695 \ 10^{-1} \\
\alpha_3 &= \quad 4.995 \ 10^{-1} \\
\alpha_4 &= \quad 1.278 \ 10^{-1} \\
\alpha_5 &= \quad 1.243 \ 10^{0} \\
\alpha_6 &= \quad 3.267 \ 10^{-1} \\
\alpha_7 &= \quad 4.329 \ 10^{-2} \\
\alpha_8 &= \quad 1.608 \ 10^{-1} \\
\alpha_9 &= \quad 2.217 \ 10^{-1}
\end{aligned}
$$

HTD

$$
\begin{aligned}
\alpha_1 &= \quad 5.864 \ 10^{-3} \\
\alpha_2 &= \quad 9.158 \ 10^{-1} \\
\alpha_3 &= \quad -1.189 \ 10^{-1} \\
\alpha_4 &= \quad -9.812 \ 10^{-3} \\
\alpha_5 &= \quad 1.004 \ 10^{0} \\
\alpha_6 &= \quad 2.644 \ 10^{-2} \\
\alpha_7 &= \quad 2.869 \ 10^{0} \\
\alpha_8 &= \quad 5.746 \ 10^{-2} \\
\alpha_9 &= \quad 1.529 \ 10^{0}
\end{aligned}
$$

Detailed information can be found in [Badea et al., 2018].

A.2. Bae

$$Nu_b = 0.021 \, Re_b^{0.8} \, \overline{Pr_b}^{0.55} \left(\frac{\rho_w}{\rho_b}\right)^{0.35} \cdot \phi \tag{A.2}$$

$$Bu = \frac{\overline{Gr_b}}{Re_b^{2.7}}$$

$$\phi = \left\{ \begin{array}{lll} (1 - 8000\ Bu)^{0.5} & ; & Bu < 10^{-4} \\ 15\ Bu^{0.38} & ; & Bu > 10^{-4} \end{array} \right\}$$

$$\overline{Pr_b} = \frac{\eta_b\ \overline{c_p}}{\lambda_b}$$

$$\overline{c_p} = \frac{h_w - h_b}{T_w - T_b}$$

$\overline{Gr_b}$ from equation 2.11.

Detailed information can be found in [Bae, 2011].

A.3. Bae and Kim

$$Nu_b = 0.021\ Re_b^{0.8}\ \overline{Pr_b}^{-0.55} \left(\frac{\rho_w}{\rho_b}\right)^{0.35} \left(\frac{\overline{c_p}}{c_{p,b}}\right)^n \cdot \phi \tag{A.3}$$

n same as Krasnoshchekov A.27

$$Bu = \frac{\overline{Gr_b}}{Re_b^{2.7}\ \overline{Pr_b}^{-0.5}}$$

$$\phi = \left\{ \begin{array}{lll} \left(1 + 1 \cdot 10^8\ Bu\right)^{-0.032} & ; & 5 \cdot 10^{-8} < Bu < 7 \cdot 10^{-7} \\ 0.0185\ Bu^{-0.43465} & ; & 7 \cdot 10^{-7} < Bu < 1 \cdot 10^{-6} \\ 0.75 & ; & 1 \cdot 10^{-6} < Bu < 1 \cdot 10^{-5} \\ 0.0119\ Bu^{-0.36} & ; & 1 \cdot 10^{-5} < Bu < 3 \cdot 10^{-5} \\ 32.4\ Bu^{0.4} & ; & 3 \cdot 10^{-5} < Bu < 1 \cdot 10^{-4} \end{array} \right\}$$

Detailed information can be found in [Bae & Kim, 2009].

A.4. Bishop

$$Nu_b = 0.0069\ Re_b^{0.9}\ \overline{Pr_b}^{-0.66} \left(\frac{\rho_w}{\rho_b}\right)^{0.43} \tag{A.4}$$

Detailed information can be found in [Bishop et al., 1965].

A.5. Bogachev

$$Nu_b = 0.0243\ Re_b^{0.8}\ Pr_b^{0.4} \left(\frac{\overline{c_p}}{c_{p,b}}\right)^{0.35} \tag{A.5}$$

Detailed information can be found in [Bogachev et al., 1983].

A.6. Bringer and Smith

$$Nu_b = 0.0375\,Re_x^{0.77}\,Pr_w^{0.55} \tag{A.6}$$

$$x = \begin{cases} b & ; & \frac{T_{pc}-T_b}{T_w-T_b} < 0 \\ pc & ; & 0 \leq \frac{T_{pc}-T_b}{T_w-T_b} \leq 1 \\ w & ; & \frac{T_{pc}-T_b}{T_w-T_b} > 1 \end{cases}$$

Detailed information can be found in [Bringer & Smith, 1957].

A.7. Chen and Fang

$$Nu_b = 0.46\,Re_b^{0.16}\left(\frac{Pr_w}{Pr_b}\right)^{0.1}\left(\frac{\eta_w}{\eta_b}\right)^{-0.55}\left(\frac{\overline{c_p}}{c_{p,b}}\right)^{0.88}\left(\frac{Gr_b}{Gr_m}\right)^{0.81} \tag{A.7}$$

$$Gr_m = \left(\frac{\rho_b - \rho_w}{\rho_b}\right)\frac{gd^3}{\eta_b{}^2}$$

Detailed information can be found in [Chen & Fang, 2014].

A.8. Cheng

$$Nu = 0.023\,Re_b^{0.8}\,Pr_b^{1/3}\cdot F \tag{A.8}$$

$$F = min(F_1, F_2)$$
$$F_1 = 0.85\ +\ 0.776\left(\pi_A \cdot 10^3\right)^{2.4}$$

$$F_2 = \frac{0.48}{\left(\pi_{A,pc} \cdot 10^3\right)^{1.55}}\ +\ 1.21\cdot\left(1 - \frac{\pi_A}{\pi_{A,pc}}\right)$$

with $\pi_A = \frac{\beta}{c_p}\frac{q}{G}$ and $\pi_{A,pc} = \frac{\beta_{pc}}{c_{p,pc}}\frac{q}{G}$

Detailed information can be found in [Cheng et al., 2009b].

A.9. Cheng - q

$$Nu = 0.023\,Re_b^{0.8}\,Pr_b^{1/3}\cdot F_1 \cdot F_2 \tag{A.9}$$

$$F_1 = \begin{cases} 0.98 & ; \pi_A < 1.75 \cdot 10^{-4} \\ 0.85 + 0.056\cdot\left(10^4 \cdot \pi_A\right)^{1.5} & ; 1.75 \cdot 10^{-4} \leq \pi_A \leq 3.75 \cdot 10^{-4} \\ \frac{13.1}{4.5+\left(10^4\cdot\pi_A\right)^{1.35}} & ; 3.75 \cdot 10^{-4} < \pi_A \end{cases}$$

$$F_2 = \begin{cases} 0.93 Pr^{0.265} & ; Pr \le 2.5 \\ 1.61 Pr^{-0.333} & ; Pr > 2.5 \end{cases}$$

with $\pi_A = \frac{\beta}{c_p} \frac{q}{G}$

Detailed information can be found in [Cheng et al., 2019].

A.10. Cheng - T

$$Nu = 0.023 \, Re_b^{0.8} \, Pr_b^{1/3} \cdot F_3 \cdot F_4 \cdot F_5 \tag{A.10}$$

$$F_3 = \frac{2.1}{1.4 + \pi_C^{0.93}}$$

$$F_4 = \begin{cases} 1 & ; Pr \le 6 \\ 0.764 Pr^{0.167} & ; Pr > 6 \end{cases}$$

$$F_5 = \begin{cases} 1.5\pi_\rho - 0.5 & ; \frac{\rho_b}{\rho_w} \le 1.3 \\ 1.65\pi_\rho - 0.49 & ; \frac{\rho_b}{\rho_w} > 1.3 \end{cases}$$

with $\pi_C = \frac{c_{p,b}}{c_p}$ and $\pi_\rho = \frac{\rho_b}{\rho_w}$

Detailed information can be found in [Cheng et al., 2019].

A.11. Cui and Wang

upward flow

$$Nu_b = 0.029 \, Re_b^{0.762} \, \overline{Pr_b}^{-0.706} \left(\frac{\rho_w}{\rho_b} \right)^{0.353} (100000 \cdot Bu)^{-0.0046} \tag{A.11}$$

downward flow

$$Nu_b = 0.0189 \, Re_b^{0.812} \, \overline{Pr_b}^{-0.685} \left(\frac{\rho_w}{\rho_b} \right)^{0.394} (100000 \cdot Bu)^{0.0176}$$

$$Bu = \overline{Gr_b} \, Re_b^{-2.7}$$

Detailed information can be found in [Cui & Wang, 2017].

A.12. Deev

$$Nu_b = 0.023\, Re_b^{0.8}\, Pr_b^{0.4} \left(\frac{\rho_w}{\rho_b}\right)^{0.25} \left(\frac{\overline{c_p}}{c_{p,b}}\right)^n \tag{A.12}$$

$$n = \begin{Bmatrix} 0.4 & ; & \dfrac{\overline{c_p}}{c_{p,b}} \geq 1 \\[2ex] 0.6 & ; & \dfrac{\overline{c_p}}{c_{p,b}} < 1 \end{Bmatrix}$$

Detailed information can be found in [Deev et al., 2016].

A.13. Dittus-Boelter

$$Nu_b = 0.023\, Re_b^{0.8}\, Pr_b^{0.4} \quad \cdot \left[\left[1 + \left(\frac{d}{L}\right)^{2/3}\right] K\right] \tag{A.13}$$

$K = \left(\frac{Pr_b}{Pr_w}\right)^{0.11}$

Detailed information can be found in [Dittus & Boelter, 1985].

A.14. Gnielinski

$$Nu_b = \frac{(f/8)\,(Re_b - 1000)\, Pr_b}{1 + 12.7\,\sqrt{f/8}\left(Pr_b^{2/3} - 1\right)} \left[1 + \left(\frac{d}{L}\right)^{2/3}\right] K \tag{A.14}$$

with $f = (1.8 \log(Re_b) - 1.5)^{-2}$
and $K = \left(\frac{Pr_b}{Pr_w}\right)^{0.11}$

Detailed information can be found in [Gnielinski, 1975].

A.15. Gorban

$$Nu_b = 0.0059\, Re_b^{0.9}\, Pr_b^{-0.12} \tag{A.15}$$

Detailed information can be found in [Gorban et al., 1990].

A.16. Gorban-R12

$$Nu_b = 0.0094\, Re_b^{0.86}\, Pr_b^{-0.15} \tag{A.16}$$

Detailed information can be found in [Gorban et al., 1990].

A.17. Grass

$$Nu_b = \frac{(f/8)\, Re_b\, Pr_b}{1.07 + 12.7\, \sqrt{f/8}\left(Pr_G^{2/3}\, \frac{c_{p,b}}{c_{pG}} - 1\right)} \tag{A.17}$$

$$f = (1.82 \log(Re_b) - 1.64)^{-2}$$

$$Pr_G = \left\{ \begin{array}{lll} Pr_b & ; & Pr_b < 0.5\, Pr_w \\ Pr_w & ; & Pr_b > 0.5\, Pr_w \end{array} \right\}$$

$$c_{pG} = \left\{ \begin{array}{lll} c_{p,b} & ; & Pr_b < 0.5\, Pr_w \\ c_{p,w} & ; & Pr_b > 0.5\, Pr_w \end{array} \right\}$$

Detailed information can be found in [Grass et al., 1971].

A.18. Griem

$$\hat{Nu} = 0.0169\, Re_b^{0.8356}\, \hat{Pr}^{0.432} \phi \tag{A.18}$$

$$\hat{Nu} = \frac{\alpha\, d}{\overline{\lambda}} \qquad\qquad \hat{Pr} = \frac{c_{p,sel}\, \eta_b}{\overline{\lambda}} \qquad\qquad \overline{\lambda} = \frac{1}{2}\, (\lambda_b + \lambda_w)$$

$$c_{p,sel} = \frac{1}{3} \left\{ \sum_{i=1}^{5} c_p(T_i) - c_{p,max} - c_{p,2,max} \right\}$$

$$T_i = \left\{ T_w, \frac{1.5 T_w + T_b}{2}, \frac{T_w + T_b}{2}, \frac{T_w + 1.5 T_b}{2}, T_b \right\}$$

$$\phi = \left\{ \begin{array}{lll} 0.82 & ; & h_b \leq 1540 kJ/kg \\ 0.82 + \frac{0.18}{200}\, (h_b - 1540) & ; & 1540 kJ/kg < h_b \leq 1740 kJ/kg \\ 1 & ; & h_b > 1740 kJ/kg \end{array} \right\}$$

Detailed information can be found in [Griem, 1996].

A.19. Gupta

$$Nu_w = 0.004\, Re_w^{0.923}\, \overline{Pr_w}^{-0.773} \left(\frac{\eta_w}{\eta_b}\right)^{0.366} \left(\frac{\rho_w}{\rho_b}\right)^{0.186} ; \tag{A.19}$$

Detailed information can be found in [Gupta et al., 2013].

A.20. Jackson and Hall

$$Nu_b = 0.0183 \, Re_b^{0.82} \, Pr_b^{0.5} \left(\frac{\rho_w}{\rho_b}\right)^{0.3} \left(\frac{\overline{c_p}}{c_{p,b}}\right)^n \tag{A.20}$$

$$n = \begin{cases} 0.4 & ; \quad T_b < T_w \leq T_{pc} \quad \text{or} \quad 1.2T_{pc} \leq T_b < T_w \\ 0.4 + 0.2\left[\left(\frac{T_w}{T_{pc}}\right) - 1\right] & ; \quad T_b \leq T_{pc} < T_w \\ 0.4 + 0.2\left[\left(\frac{T_w}{T_{pc}}\right) - 1\right]\left\{1 - 5\left[\left(\frac{T_b}{T_{pc}}\right) - 1\right]\right\} & ; \quad T_{pc} \leq T_b \leq 1.2T_{pc} \quad \text{and} \quad T_b < T_w \end{cases}$$

Detailed information can be found in [J.D. Jackson, W. B. Hall, 1979].

A.21. Jackson and Fewster

$$Nu_b = 0.0183 \, Re_b^{0.82} \, \overline{Pr_b}^{-0.5} \left(\frac{\rho_w}{\rho_b}\right)^{0.3} \tag{A.21}$$

Detailed information can be found in [Jackson & Fewster, 1975].

A.22. Kim

$$Nu_b = Nu_0 \left(\frac{\xi_m}{\xi_f}\right) \left(\frac{\overline{c_p}}{c_{p,b}}\right)^{0.6} \left(\frac{\rho_w}{\rho_b}\right)^n \tag{A.22}$$

$$Nu_0 = 0.0243 \, Re_b^{0.8} \, Pr_b^{0.4}$$

$$\xi_m = \frac{8\tau_w}{\rho_b u_b^2}$$

$$\tau_w = \rho_w u_\tau^2$$

$$\frac{u_b}{u_\tau} = \frac{1}{0.41} \ln\left(\frac{yu_\tau}{\eta_b}\right) + 5$$

$$\xi_f = (1.8\log(Re_b) - 1.5)^{-2}$$

$$n = 0.955 - 0.0087\left(\frac{q}{G}\right) + 1.3 \cdot 10^{-5}\left(\frac{q}{G}\right)^2$$

Detailed information can be found in [Kim et al., 2007b].

A.23. Kim and Kim

$$Nu_b = 0.226 \, Re_b^{1.174} \, Pr_b^{1.057} \left(\frac{\rho_b}{\rho_w}\right)^{0.571} \left(\frac{\overline{c_p}}{c_{p,b}}\right)^{1.032} Ac_K^{0.489} \, Bu_K^{0.0021} \tag{A.23}$$

$$Ac_K = \frac{\pi_A}{Re_b^{0.625}} \left(\frac{\eta_w}{\eta_b}\right) \left(\frac{\rho_b}{\rho_w}\right)^{0.5}$$

$$Bu_K = \frac{Gr_b}{Re_b^{3.425} Pr_b^{0.8}} \left(\frac{\eta_w}{\eta_b}\right) \left(\frac{\rho_b}{\rho_w}\right)^{0.5}$$

Detailed information can be found in [Kim & Kim, 2011a].

A.24. Kirillov

$$\begin{aligned}
Nu_b &= Nu_0 \left(\frac{\overline{c_p}}{c_{p,b}}\right)^n \left(\frac{\rho_w}{\rho_b}\right)^m & k^* < 0.01 \\
Nu_b &= Nu_0 \left(\frac{\overline{c_p}}{c_{p,b}}\right)^n \left(\frac{\rho_w}{\rho_b}\right)^m \cdot \phi(k^*) & k^* \geq 0.01
\end{aligned} \tag{A.24}$$

$$Nu_0 = 0.023 \, Re_b^{0.8} \, \overline{Pr_b}^{0.4} \cdot C_t$$

$$C_t = \left(\frac{\eta_w}{\eta_b}\right)^{0.11}$$

0.11 heating; 0.25 cooling

$$Gr = g \left(1 - \frac{\rho_w}{\rho_b}\right) D^3 / \eta_b^2$$

$$k^* = \left(1 - \frac{\rho_w}{\rho_b}\right) \frac{Gr}{Re^2};$$

$m = 0.3$ upward flow, $m = 0.4$ downward flow

$$n = \begin{cases} 0.7 & & \left(\frac{\overline{c_p}}{c_{p,b}}\right) \geq 1 \\[2mm] \begin{cases} 0.4 & ; \ \frac{T_w}{T_{pc}} < 1 \ \& \ \frac{T_b}{T_{pc}} > 1.2 \\[2mm] 0.22 + 0.18\left(\frac{T_w}{T_{pc}}\right) & ; \ \frac{T_w}{T_{pc}} > 1 \ \& \ \frac{T_b}{T_{pc}} < 1 \\[2mm] 0.9\left(\frac{T_b}{T_{pc}}\right)\left(1 - \left(\frac{T_w}{T_{pc}}\right)\right) + 1.08\left(\frac{T_w}{T_{pc}}\right) - 0.68 & ; \ \frac{T_w}{T_{pc}} > 1 \ \& \ 1 < \frac{T_b}{T_{pc}} < 1.2 \end{cases} & \left(\frac{\overline{c_p}}{c_{p,b}}\right) < 1 \end{cases}$$

$$\phi(k^*) = \begin{cases} \begin{aligned} &0.79782686 - 1.6459037 \ln(k^*) - 2.7547316 \ (\ln(k^*))^2 \\ &-1.7422714 \ (\ln(k^*))^3 - 0.54805506 \ (\ln(k^*))^4 \\ &-0.086914323 \ (\ln(k^*))^5 - 0.0055187343 \ (\ln(k^*))^6 \end{aligned} & ; \ k^* \leq 0.4 \\[3mm] 1.4 \ (k^*)^{0.37} & ; \ k^* > 0.4 \end{cases}$$

Detailed information can be found in [Kirillov, 2000].

A.25. Komita

$$Nu_b = 0.021 \, Re_b^{0.8} \, \overline{Pr_b}^{0.55} \left(\frac{\rho_w}{\rho_b}\right)^{0.35} \cdot \phi \tag{A.25}$$

$$Bu = \frac{\overline{Gr_b}}{Re_b^{2.7} \, \overline{Pr_b}^{0.5}}$$

$$\phi = \begin{cases} (0.84 - 19500 \, Bu)^{0.7} & ; \ Bu < 2.7 \cdot 10^{-4} \\ (5141 \, Bu)^{0.41} & ; \ Bu \geq 2.7 \cdot 10^{-4} \end{cases}$$

Detailed information can be found in [Komita et al., 2003].

A.26. Kondratev

$$Nu_b = 0.02 \, Re_b^{0.8} \tag{A.26}$$

Detailed information can be found in [Kondratev, 1969].

A.27. Krasnoshchekov

$$Nu_b = Nu_0 \left(\frac{\rho_w}{\rho_b}\right)^{0.3} \left(\frac{\overline{c_p}}{c_{p,b}}\right)^n \tag{A.27}$$

$$Nu_0 = \frac{(f/8)\, Re_b \overline{Pr_b}}{1.07 + 12.7\, \sqrt{f/8} \left(\overline{Pr_b}^{2/3} - 1\right)}$$

$$n_1 = 0.22 + 0.18\frac{T_w}{T_{pc}}$$

$$n = \begin{cases} 0.4 & ; \quad \frac{T_w}{T_{pc}} < 1 \quad \text{or} \quad \frac{T_b}{T_{pc}} \geq 1.2 \\ n_1 & ; \quad 1 \leq \frac{T_w}{T_{pc}} \leq 2.5 \\ n_1 + (5n_1 - 2)\left(1 - \frac{T_b}{T_{pc}}\right) & ; \quad 1 \leq \frac{T_b}{T_{pc}} \leq 1.2 \end{cases}$$

f is the same as from Gnielinski A.14.

Detailed information can be found in [Krasnoshchekov et al., 1964].

A.28. Kuang

$$Nu_b = 0.0239\, Re_b^{0.959}\, \overline{Pr_b}^{-0.833} \left(\frac{\lambda_w}{\lambda_b}\right)^{0.0863} \left(\frac{\eta_w}{\eta_b}\right)^{0.832} \left(\frac{\rho_w}{\rho_b}\right)^{0.31} Gr_b^{0.014}\, (q^+)^{-0.021} \tag{A.28}$$

$$q^+ = \frac{q \cdot \beta}{G \cdot c_p}$$

Detailed information can be found in [Kuang et al., 2008].

A.29. Kurganov

$$Nu_b = \frac{(f_n/8)\, Re_b Pr_b}{1 + (900/Re_b) + 12.7\, \sqrt{f_n/8} \left(\left[\overline{Pr}_{b-w} \left(\frac{\overline{c_p}}{c_{p,b}}\right)^n\right]^{2/3} - 1\right)} \tag{A.29}$$

$$f_n = f \left(\frac{\rho_w}{\rho_b}\right)^{0.35} \left(\frac{\eta_w}{\eta_b}\right)^{n_\eta}$$

$$n_\eta = 0.2 + \frac{70}{Re_b^{2/3}}$$

f is the same as from Gnielinski A.14.

Detailed information can be found in [Kurganov et al., 2013].

A.30. Mayinger and Scheldt

$$Ec = \frac{T_{pc} - T_b}{T_w - T_b} \tag{A.30}$$

$$Ra_b = Gr_b \cdot Pr_b \tag{A.31}$$

$$Nu_b = \begin{cases} C_1 \cdot Re_b^{0.85} \cdot Pr_b^{0.33} \cdot \left(\frac{\rho_w}{\rho_b}\right)^{0.2} & ; \quad Ec > 1 \quad \text{and} \quad T_b < T_w < T_{pc} \\ C_2 \cdot Re_b^{0.87} \cdot Pr_b^{0.56} \cdot \left(\frac{\rho_w}{\rho_b}\right)^{0.21} \cdot \left(\frac{\overline{c_p}}{c_{p,b}}\right)^{0.57} \cdot Ra_b^{0.06} & ; \quad 0 \leq Ec \leq 1 \quad \text{and} \quad T_b \leq T_{pc} \leq T_w \\ C_3 \cdot Re_b^{0.85} \cdot Pr_b^{0.62} \cdot \left(\frac{\rho_w}{\rho_b}\right)^{0.155} & ; \quad Ec < 0 \quad \text{and} \quad T_{pc} < T_b < T_w \\ C_4 \cdot Re_b^{0.87} \cdot Pr_b^{0.61} \cdot \left(\frac{\rho_w}{\rho_b}\right)^{0.18} \cdot \left(\frac{\overline{c_p}}{c_{p,b}}\right)^{0.28} \cdot Ra_b^{0.12} & ; \quad \text{for deteriorated conditions} \end{cases}$$

C	Wasser	R12
C_1	0.0102	0.0128
C_2	0.00166	0.00207
C_3	0.0094	0.0115
C_4	0.00038	0.00024

Detailed information can be found in [Mayinger & Scheldt, 1984]

A.31. Miropolskii and Shitsman

$$Nu_b = 0.023 \, Re_b^{0.8} Pr_x^{0.8} \tag{A.32}$$
$$Pr_x = min(Pr_b, Pr_w)$$

Detailed information can be found in [Miropolskii & Shitsman, 1957].

A.32. Mokry

$$Nu_b = 0.0061 \, Re_b^{0.904} \, \overline{Pr_b}^{0.684} \left(\frac{\rho_w}{\rho_b}\right)^{0.564} \tag{A.33}$$

Detailed information can be found in [Mokry et al., 2011].

A.33. Mokry-CO$_2$

$$Nu_b = 0.0121 \, Re_b^{0.86} \, \overline{Pr_b}^{0.23} \left(\frac{\rho_w}{\rho_b}\right)^{0.59} \tag{A.34}$$

Detailed information can be found in [Mokry et al., 2009].

A.34. Nicholas

$$Nu_b = 0.0074 \, Re_b^{0.878} \, \overline{Pr_b}^{0.668} \left(\frac{\eta_w}{\eta_b}\right)^{0.337} \left(\frac{\rho_w}{\rho_b}\right)^{0.105} \tag{A.35}$$

Correlation is taken from [Cui & Wang, 2017].

A.35. Ornatsky

$$Nu_b = 0.023 \, Re_b^{0.8} \, Pr_x^{0.8} \left(\frac{\rho_w}{\rho_b}\right)^{0.3} \tag{A.36}$$

$$Pr_x = min(Pr_b, Pr_w)$$

Detailed information can be found in [Ornatskiy et al., 1972].

A.36. Petukhov

$$Nu_b = Nu_0 \left(\frac{\eta_b}{\eta_w}\right)^{0.11} \left(\frac{\lambda_b}{\lambda_w}\right)^{-0.33} \left(\frac{\overline{c_p}}{c_{p,b}}\right)^{0.35} ; \tag{A.37}$$

$$Nu_0 = \frac{(f/8) \, Re_b \overline{Pr_b}}{1.07 + 12.7 \sqrt{f/8} \left(\overline{Pr_b}^{2/3} - 1\right)}$$

Detailed information can be found in [Petukhov, 1961].

A.37. Pitla

$$Nu = \left(\frac{Nu_w + Nu_b}{2}\right) \frac{\lambda_w}{\lambda_b} \tag{A.38}$$

Nu from Gnielinski.

Detailed information can be found in [Pitla et al., 1998].

A.38. Preda

$$Nu_b = 0.0015 \, Re_w^{1.03} \, Pr_w^{0.76} \left(\frac{\eta_w}{\eta_b}\right)^{0.53} \left(\frac{\rho_w}{\rho_b}\right)^{0.46} \left(\frac{\lambda_w}{\lambda_b}\right)^{-0.43} \tag{A.39}$$

Detailed information can be found in [Preda et al., 2012].

A.39. Razumovskiy

$$Nu_b = \frac{\left(f_{fr}/8\right) Re_b \, \overline{Pr_b}}{1.07 + 12.7 \sqrt{f_{fr}/8} \left(\overline{Pr_b}^{2/3} - 1\right)} \left(\frac{\overline{c_p}}{c_{p,b}}\right)^{0.65} \tag{A.40}$$

$$f_{fr} = f_0 \left(\frac{\eta_w}{\eta_b} \frac{\rho_w}{\rho_b}\right)^{0.18}$$

$$f_0 = \left(1.82 \log\left(\frac{Re_b}{8}\right)\right)^{-2}$$

Detailed information can be found in [Razumovskiy et al., 1990].

A.40. Saltanov

$$Nu_b = 0.0164 \, Re_b^{0.823} \, \overline{Pr_b}^{-0.195} \left(\frac{\rho_w}{\rho_b}\right)^{0.374} \tag{A.41}$$

Detailed information can be found in [Saltanov et al., 2015].

A.41. Swenson

$$Nu_w = 0.00459 \, Re_w^{0.923} \, \overline{Pr_w}^{-0.613} \left(\frac{\rho_w}{\rho_b}\right)^{0.231}$$

(A.42)

Detailed information can be found in [Swenson et al., 1965].

A.42. Watts and Chou

$$Nu_b = 0.021 \, Re_b^{0.8} \, \overline{Pr_b}^{-0.55} \left(\frac{\rho_w}{\rho_b}\right)^{0.35} \cdot \phi$$

(A.43)

$$\phi = \begin{cases} 1 & ; & \left(\frac{\overline{Gr_b}}{Re_b^{2.7} \, \overline{Pr_b}^{-0.5}}\right) < 10^{-5} \\[4mm] \left[1 - 3000 \, \frac{\overline{Gr_b}}{Re_b^{2.7} \, \overline{Pr_b}^{-0.5}}\right]^{0.295} & ; & 10^{-5} < \left(\frac{\overline{Gr_b}}{Re_b^{2.7} \, \overline{Pr_b}^{-0.5}}\right) \le 10^{-4} \\[4mm] \left[7000 \, \frac{\overline{Gr_b}}{Re_b^{2.7} \, \overline{Pr_b}^{-0.5}}\right]^{0.295} & ; & \left(\frac{\overline{Gr_b}}{Re_b^{2.7} \, \overline{Pr_b}^{-0.5}}\right) > 10^{-4} \end{cases}$$

Detailed information can be found in [Watts & Chou, 1982].

A.43. Yamagata

$$Nu_b = 0.0135 \, Re_b^{0.85} \, Pr_b^{0.8} \cdot F_c$$

(A.44)

$$E = \frac{T_{pc} - T_b}{T_w - T_b}$$

$$F_c = \begin{cases} 1 & ; & E > 1 \\ 0.67 \, Pr_{pc}^{-0.05} \left(\frac{\overline{c_p}}{c_{p,b}}\right)^{n_1} & ; & 0 \le E \le 1 \qquad n_1 = -0.77\left(1 + \frac{1}{Pr_{pc}}\right) + 1.49 \\ \left(\frac{\overline{c_p}}{c_{p,b}}\right)^{n_2} & ; & E < 0 \qquad n_2 = 1.44\left(1 + \frac{1}{Pr_{pc}}\right) - 0.53 \end{cases}$$

Detailed information can be found in [Yamagata et al., 1972].

A.44. Yeroshenko and Yaskin

$$Nu_b = 0.023 \, Re_b^{0.8} \, Pr_b^{0.4} \cdot \phi$$

(A.45)

$$\phi = \left(\frac{2}{(0.8 \, \psi + 0.2)^{0.5} + 1}\right)^2 \cdot F$$

$$\psi = 1 + \beta_b \, (T_w - T_b)$$

$$\begin{cases} F = \left(\frac{\overline{c_p}}{c_{p,b}}\right)^{0.28} & \overline{c_p} > c_{p,b} \\ F = 1 & \overline{c_p} \le c_{p,b} \end{cases}$$

Detailed information can be found in [Yeroshenko & Yaskin, 1981].

A.45. Zhang

$$Nu_b = 0.023 \, Re_b^{0.8} \, Pr_b^{0.4} \cdot F \tag{A.46}$$

$$F = min(F_1, F_2)$$

$$F_1 = 1 + 1936 \cdot \pi_A^{1.059}$$

$$F_2 = -5.19 - 0.817 \cdot \ln \pi_A$$

Detailed information can be found in [Zhang et al., 2014].

A.46. Zhu

$$Nu_b = 0.0068 \, Re_b^{0.9} \, \overline{Pr_b}^{-0.63} \left(\frac{\rho_w}{\rho_b}\right)^{0.17} \left(\frac{\lambda_w}{\lambda_b}\right)^{0.29}; \tag{A.47}$$

Detailed information can be found in [Zhu et al., 2009].

B. Fluid-to-fluid scaling models for heat transfer at supercritical conditions

B.1. Ambrosini

$$\left(Pr_{pc}(P)\right)_A = \left(Pr_{pc}(P)\right)_B \tag{B.48}$$

$$\left(\left(h_{pc} - h_{in}\right)\frac{\beta_{pc}}{c_{p,pc}}\right)_A = \left(\left(h_{pc} - h_{in}\right)\frac{\beta_{pc}}{c_{p,pc}}\right)_B \tag{B.49}$$

$$\left(\frac{u_{in}^2}{gd}\right)_A = \left(\frac{u_{in}^2}{gd}\right)_B \tag{B.50}$$

$$\left(\frac{\rho_{pc}u_{in}d}{\mu}\right)_A = \left(\frac{\rho_{pc}u_{in}d}{\mu}\right)_B \tag{B.51}$$

$$\left(\frac{\rho_{pc}c_p u_{in}d}{\lambda}\right)_A = \left(\frac{\rho_{pc}c_p u_{in}d}{\lambda}\right)_B \tag{B.52}$$

$$\left(\frac{\dot{Q}}{W}\frac{\beta_{pc}}{c_{p,pc}}\right)_A = \left(\frac{\dot{Q}}{W}\frac{\beta_{pc}}{c_{p,pc}}\right)_B \tag{B.53}$$

$$\left(\left(h_{pc} - h_b\right)\frac{\beta_{pc}}{c_{p,pc}}\right)_A = \left(\left(h_{pc} - h_b\right)\frac{\beta_{pc}}{c_{p,pc}}\right)_B \tag{B.54}$$

$$\left(\frac{\alpha d}{\lambda_b}\right)_A = \left(\frac{\alpha d}{\lambda_b}\right)_B \tag{B.55}$$

Detailed information can be found in [Ambrosini, 2011a].

B.2. Azih and Yaras

$$\left(\frac{P_{in}}{P_c}\right)_A = \left(\frac{P_{in}}{P_c}\right)_B \tag{B.56}$$

$$\left(\frac{\beta_{pc}}{c_{p,pc}}\left(h_{in} - h_{pc}\right)\right)_A = \left(\frac{\beta_{pc}}{c_{p,pc}}\left(h_{in} - h_{pc}\right)\right)_B \tag{B.57}$$

$$\left(\frac{Gd}{\mu_{in}}\right)_A = \left(\frac{Gd}{\mu_{in}}\right)_B \tag{B.58}$$

$$\left(\frac{\rho_{in}^2 g d^2}{G^2}\frac{\beta_{in}q^2}{\lambda_{in}}\right)_A = \left(\frac{\rho_{in}^2 g d^2}{G^2}\frac{\beta_{in}q^2}{\lambda_{in}}\right)_B \tag{B.59}$$

$$\left(\frac{q\beta_{pc}}{Gc_{p,pc}}\right)_A = \left(\frac{q\beta_{pc}}{Gc_{p,pc}}\right)_B \tag{B.60}$$

$$\left(\frac{\beta_{pc}}{c_{p,pc}}\left(h_b - h_{pc}\right)\right)_A = \left(\frac{\beta_{pc}}{c_{p,pc}}\left(h_b - h_{pc}\right)\right)_B \tag{B.61}$$

$$\left(\frac{\alpha d}{\lambda_b}\right)_A = \left(\frac{\alpha d}{\lambda_b}\right)_B \tag{B.62}$$

Detailed information can be found in [Azih & Yaras, 2017].

B.3. Cheng et al.

$$(d)_A = (d)_B \tag{B.63}$$

$$\left(\frac{P}{P_c}\right)_A = \left(\frac{P}{P_c}\right)_B \tag{B.64}$$

$$\theta_A = \left(\frac{T_b - T_{pc}}{T_{pc} - T_c}\right)_A = \left(\frac{T_b - T_{pc}}{T_{pc} - T_c}\right)_B = \theta_B \tag{B.65}$$

$$\left(\frac{qd}{\lambda_b\left(T_{pc} - T_c\right)}\right)_A = \left(\frac{qd}{\lambda_b\left(T_{pc} - T_c\right)}\right)_B \tag{B.66}$$

$$\left(\frac{GPr_b^{\frac{5}{12}}d}{\mu_b}\right)_A = \left(\frac{GPr_b^{\frac{5}{12}}d}{\mu_b}\right)_B \tag{B.67}$$

$$\left(\frac{\alpha d}{\lambda_b}\right)_A = \left(\frac{\alpha d}{\lambda_b}\right)_B \tag{B.68}$$

Detailed information can be found in [Cheng et al., 2011].

B.4. Cheng modified by Zahlan

The model is similar except the power coefficient in equation B.67:

$$\left(\frac{GPr_b^{0.63}d}{\mu_b}\right)_A = \left(\frac{GPr_b^{0.63}d}{\mu_b}\right)_B \tag{B.69}$$

Detailed information can be found in [Zahlan, 2015, Zahlan et al., 2014].

B.5. Jackson and Hall

$$(f(R))_A = (f(R))_B \qquad \text{(Entry condition)} \qquad \text{(B.70)}$$

$$\left(\frac{qd}{\lambda_b T_b}\right)_A = \left(\frac{qd}{\lambda_b T_b}\right)_B \qquad \text{(Flux parameter, later thermal loading number)} \qquad \text{(B.71)}$$

$$\left(\frac{\rho_b u_b d}{\mu_b}\right)_A = \left(\frac{\rho_b u_b d}{\mu_b}\right)_B \qquad \text{(Reynolds number)} \qquad \text{(B.72)}$$

$$\left(\frac{\mu_b c_{p,b}}{\lambda_b}\right)_A = \left(\frac{\mu_b c_{p,b}}{\lambda_b}\right)_B \qquad \text{(Prandtl number)} \qquad \text{(B.73)}$$

$$\left(\frac{u_b^2 \beta_b}{c_{p,b}}\right)_A = \left(\frac{u_b^2 \beta_b}{c_{p,b}}\right)_B \qquad \text{(Compressibility group)} \qquad \text{(B.74)}$$

$$\left(\frac{\mu_b u_b}{\rho_b c_{p,b} T_b d}\right)_A = \left(\frac{\mu_b u_b}{\rho_b c_{p,b} T_b d}\right)_B \qquad \text{(Dissipation group)} \qquad \text{(B.75)}$$

$$\left(\frac{u_b^2}{gd}\right)_A = \left(\frac{u_b^2}{gd}\right)_B \qquad \text{(Froude number)} \qquad \text{(B.76)}$$

$$(\rho^*(\theta))_A = (\rho^*(\theta))_B \qquad \text{(Property function)} \qquad \text{(B.77)}$$

Detailed information can be found in [J.D. Jackson, W. B. Hall, 1979, Jackson, 2008]

B.6. Pioro and Duffey

$$\left(\frac{l}{d}\right)_A = \left(\frac{l}{d}\right)_B \qquad \text{(B.78)}$$

$$\left(\frac{P}{P_c}\right)_A = \left(\frac{P}{P_c}\right)_B \qquad \text{(B.79)}$$

$$\left(\frac{T_b}{T_c}\right)_A = \left(\frac{T_b}{T_c}\right)_B \qquad \text{(B.80)}$$

$$\left(\frac{qd}{\lambda_b T_b}\right)_A = \left(\frac{qd}{\lambda_b T_b}\right)_B \qquad \text{(For heat flux controlled system)} \qquad \text{(B.81)}$$

$$\left(\frac{T_w - T_b}{T_c}\right)_A = \left(\frac{T_w - T_b}{T_c}\right)_A \qquad \text{(For wall temperature controlled system)} \qquad \text{(B.82)}$$

$$\left(\frac{Gd}{\mu_b}\right)_A = \left(\frac{Gd}{\mu_b}\right)_B \qquad \text{(B.83)}$$

$$(Nu)_A = (Nu)_B \qquad \text{(B.84)}$$

An alternative to equation B.79:

$$\left(\frac{\rho_b}{\rho_c}\right)_A = \left(\frac{\rho_b}{\rho_c}\right)_B \tag{B.85}$$

Detailed information can be found in [Pioro & Duffey, 2007].

B.7. Tian et al.

$$\left(\frac{P}{P_c}\right)_A = \left(\frac{P}{P_c}\right)_B \tag{B.86}$$

$$\left(\frac{\beta_{pc}}{c_{p,pc}}\left(h - h_{pc}\right)\right)_A = \left(\frac{\beta_{pc}}{c_{p,pc}}\left(h - h_{pc}\right)\right)_B \tag{B.87}$$

$$\left(\frac{qd}{\lambda_b\left(T_{pc} - T_c\right)}\right)_A = \left(\frac{qd}{\lambda_b\left(T_{pc} - T_c\right)}\right)_B \tag{B.88}$$

$$\left(Re^{-0.9}\pi_{A,pc}\right)_A = \left(Re^{-0.9}\pi_{A,pc}\right)_B \tag{B.89}$$

$$(Nu)_A = (Nu)_B \tag{B.90}$$

With π_A as in Cheng (A.8). Detailed information can be found in [Tian et al., 2018].

B.8. Zahlan et al.

$$(d)_A = (d)_B \tag{B.91}$$

$$\left(\frac{P}{P_c}\right)_A = \left(\frac{P}{P_c}\right)_B \tag{B.92}$$

$$\left(\frac{T_b}{T_{pc}}\right)_A = \left(\frac{T_b}{T_{pc}}\right)_B \tag{B.93}$$

$$\left(\frac{qd}{\lambda_b T_{pc}}\right)_A = \left(\frac{qd}{\lambda_b T_{pc}}\right)_B \tag{B.94}$$

$$\left(\frac{GPr_b^{0.66}d}{\mu_b}\right)_A = \left(\frac{GPr_b^{0.66}d}{\mu_b}\right)_B \tag{B.95}$$

$$\left(\frac{\alpha d}{\lambda_b}\right)_A = \left(\frac{\alpha d}{\lambda_b}\right)_B \tag{B.96}$$

Detailed information can be found in [Zahlan, 2015, Zahlan et al., 2014].

B.9. Zwolinski

$$\left(\frac{l}{d}\right)_A = \left(\frac{l}{d}\right)_B \tag{B.97}$$

$$\left(\frac{P}{P_c}\right)_A = \left(\frac{P}{P_c}\right)_B \tag{B.98}$$

$$\left(\frac{T_b}{T_{pc}}\right)_A = \left(\frac{T_b}{T_{pc}}\right)_B \tag{B.99}$$

$$\left(\frac{qd}{\lambda_b T_b}\right)_A = \left(\frac{qd}{\lambda_b T_b}\right)_B \tag{B.100}$$

$$\left(\frac{Gd}{\mu_b}\right)_A = \left(\frac{Gd}{\mu_b}\right)_B \tag{B.101}$$

$$\left(\frac{\alpha d}{\lambda_b}\right)_A = \left(\frac{\alpha d}{\lambda_b}\right)_B \tag{B.102}$$

Detailed information can be found in [Zwolinski et al., 2011].

C. Correlations for CHF

C.1. Chen old

$$q_{chf} = c \cdot \frac{q_s}{1000} \tag{C.103}$$

$$q_s = \Delta h_{sub} \cdot G \cdot \frac{d}{4 \cdot l}$$

$$c = min\left(\frac{2350 \cdot d \cdot (1 - 0.0307 \cdot P)}{(G \cdot \Delta h_{sub} \cdot d/0.008)^{0.35}}, 1.0\right)$$

More information are found in [Chen et al., 2015b].

C.2. Chen new

$$q_{chf} = c \cdot \frac{q_0}{1000} \tag{C.104}$$

$$q_0 = (1 - x_o) \cdot \Delta h_{vap} \cdot G \cdot \frac{d}{4 \cdot l}$$

$$c = 1 - 0.00216 \cdot (G \cdot \Delta h_{vap})^{0.25}$$

More information are found in [Chen et al., 2017].

C.3. Katto and Ohno

$$q_{chf} = q_{c_0} \cdot (1 - K \cdot x_{in}) \tag{C.105}$$

$$x_{in} = \frac{h_{in} - h'}{\Delta h_{vap}}$$

$$l_s = \frac{L}{d}$$

$$\sigma^* = \frac{\sigma \cdot \rho_l}{G^2 \cdot L}$$

$$\rho^* = \frac{\rho_g}{\rho_L}$$

$$C = \left\{ \begin{array}{lll} 0.25 & ; & l_s < 50 \\ 0.25 + 9 \cdot 10^{-4} \cdot (l_s - 50) & ; & 50 \leq l_s \leq 150 \\ 0.34 & ; & l_s > 150 \end{array} \right\}$$

$$K_1 = \frac{1.043}{4 \cdot C \cdot \sigma^{*0.043}}$$

$$K_2 = \frac{5}{6} \cdot \frac{0.0124 + 1/l_s}{\rho^{*0.133} \cdot \sigma^{*1/3}}$$

$$K_3 = 1.12 \cdot \frac{1.52 \cdot \sigma^{*0.233} + 1/l_s}{\rho^{*0.6} \cdot \sigma^{*0.173}}$$

$$q_1^* = C \cdot \sigma^{*0.043} \cdot 1/l_s$$

$$q_2^* = 0.1 \cdot \rho^{*0.133} \cdot \sigma^{*1/3} \cdot \frac{1}{1 + 0.0031 \cdot l_s}$$

$$q_3^* = 0.098 \cdot \rho^{*0.133} \cdot \sigma^{*0.433} \cdot \frac{l_s^{0.27}}{1 + 0.0031 \cdot l_s}$$

$$q_4^* = 0.234 \cdot \rho^{*0.513} \cdot \sigma^{*0.433} \cdot \frac{l_s^{0.27}}{1 + 0.0031 \cdot l_s}$$

$$q_5^* = 0.0384 \cdot \rho^{*0.6} \cdot \sigma^{*0.173} \cdot \frac{1}{1 + 0.28 \cdot \sigma^{*0.233} \cdot l_s}$$

$$\rho^* \leq 0.15:$$

$$\rho^* > 0.15:$$

$$q^* = \begin{cases} q_1^* & ; & q_1^* \leq q_2^* \\ q_2^* & ; & q_1^* > q_2^* \quad \text{and} \quad q_2^* \leq q_3^* \\ q_3^* & ; & q_1^* > q_2^* \quad \text{and} \quad q_2^* > q_3^* \end{cases}$$

$$q^* = \begin{cases} q_1^* & ; & q_1^* \leq q_4^* \\ q_4^* & ; & q_1^* > q_4^* \quad \text{and} \quad q_4^* \leq q_5^* \\ q_5^* & ; & q_1^* > q_4^* \quad \text{and} \quad q_4^* > q_5^* \end{cases}$$

$$K = \begin{cases} K_1 & ; & K_1 \geq K_2 \\ K_2 & ; & K_1 < K_2 \end{cases}$$

$$K = \begin{cases} K_1 & ; & K_1 \geq K_2 \\ K_2 & ; & K_1 < K_2 \quad \text{and} \quad K_2 \leq K_3 \\ K_3 & ; & K_1 < K_2 \quad \text{and} \quad K_2 > K_3 \end{cases}$$

More information are found in [Katto & Ohno, 1984].

C.4. Kariya

$$q_{chf} = \begin{cases} q_{c,F1} & ; & Bo_{F2} < Bo_{F1} \\ q_{c,F2} & ; & Bo_{F1} \leq Bo_{F2} \quad \text{and} \quad Bo_{D1} \leq Bo_{F2} \quad \text{and} \quad Bo_{F2} < Bo_{D2} \\ q_{c,D1} & ; & Bo_{F1} \leq Bo_{F2} \quad \text{and} \quad Bo_{F2} < Bo_{D1} \quad \text{and} \quad Bo_{D1} < Bo_{D2} \\ q_{c,D2} & ; & Bo_{F1} \leq Bo_{F2} \quad \text{and} \quad Bo_{D1} \leq Bo_{F2} \quad \text{and} \quad Bo_{D2} \leq Bo_{F2} \\ q_{c,D2} & ; & Bo_{F1} \leq Bo_{F2} \quad \text{and} \quad Bo_{F2} < Bo_{D1} \quad \text{and} \quad Bo_{D2} \leq Bo_{D1} \end{cases} \quad \text{(C.106)}$$

$$q_{c,F1} = G \cdot \Delta h_{vap} \cdot 10^{-4} \cdot \begin{cases} (-10.6) \cdot (x - 0.1) & ; & \text{for HCFC22 and HFC134a} \\ (-18.1) \cdot (x - 0.1) & ; & \text{for water} \end{cases}$$

$$q_{c,F2} = G \cdot \Delta h_{vap} \cdot 10^{-4} \cdot$$

$$\left(-5.43 \cdot \left(\frac{\rho_g}{\rho_l} \right)^{-0.47} \cdot \left(\frac{\rho_l \cdot \sigma}{G^2 \cdot d} \right)^{0.082} \cdot \left(\frac{G \cdot d}{\mu_l} \right)^{0.08} \cdot x + 5.17 \cdot \left(\frac{\rho_g}{\rho_l} \right)^{-1.08} \cdot \left(\frac{\rho_l \cdot \sigma}{G^2 \cdot d} \right)^{0.35} \cdot \left(\frac{G \cdot d}{\mu_l} \right)^{0.3} \right)$$

$$q_{c,D1} = G \cdot \Delta h_{vap} \cdot 10^{-4} \cdot \left(-1.62 \cdot x + 5.13 \cdot \left(\frac{\rho_g}{\rho_l} \right)^{-0.64} \cdot \left(\frac{\rho_l \cdot \sigma}{G^2 \cdot d} \right)^{0.39} \cdot \left(\frac{G \cdot d}{\mu_l} \right)^{0.36} \right)$$

$$q_{c,D2} = G \cdot \Delta h_{vap} \cdot 10^{-4} \cdot 4.74 \cdot \left(\frac{\rho_g}{\rho_l} \right)^{0.83} \cdot x \cdot \left(\frac{1}{x} - 1 \right)^{2.5}$$

$$Bo_{F1} = \frac{q_{c,F1}}{G \cdot \Delta h_{vap}}$$

$$Bo_{F2} = \frac{q_{c,F2}}{G \cdot \Delta h_{vap}}$$

$$Bo_{D1} = \frac{q_{c,D1}}{G \cdot \Delta h_{vap}}$$

$$Bo_{D2} = \frac{q_{c,D2}}{G \cdot \Delta h_{vap}}$$

More information are found in [Kariya et al., 2013].

C.5. Lombardi

$$q_{chf} = \frac{G \cdot \Delta h_{sub}}{4 \cdot (\frac{L}{d} + k \cdot (0.5 \cdot G^2/\rho_l)^{0.5} \cdot d^{0.4})} \tag{C.107}$$

$$k = 2$$

More information are found in [Lombardi, 1995].

C.6. Shah

C.6.1. Local condition correlation (LCC)

$$q_{chf} = G \cdot \Delta h_{vap} \cdot Bo \tag{C.108}$$

$$Bo = F_E \cdot F_x \cdot Bo_0$$

$$F_E = \left\{ \begin{array}{lll} 1.54 - 0.032 \cdot l_s & ; & 1.54 - 0.032 \cdot l_s > 1 \\ 1 & ; & 1.54 - 0.032 \cdot l_s \le 1 \end{array} \right\}$$

$$l_s = \frac{L}{d}$$

$$Pe = G \cdot d \cdot \frac{c_p}{\lambda_l}$$

$$Y_{Shah} = Pe \cdot F_E^{0.4} \cdot \left(\frac{\mu_l}{\mu_g}\right)^{0.6}$$

$$P_r = \frac{P}{P_c}$$

$$Bo_0 = max \left\{ \begin{array}{l} 15 \cdot Y_{Shah}^{-0.612} \\ 0.082 \cdot Y_{Shah}^{-0.3} \cdot (1 + 1.45 \cdot P_r^{4.03}) \\ 0.0024 \cdot Y_{Shah}^{-0.105} \cdot (1 + 1.15 \cdot P_r^{3.39}) \end{array} \right\}$$

for $x_{chf} > 0$:

$$c = \left\{ \begin{array}{lll} 0 & ; & P_r \le 0.6 \\ 1 & ; & P_r > 0.6 \end{array} \right\}$$

$$F_3 = \left(\frac{1.25 \cdot 10^5}{Y_{Shah}}\right)^{0.833} \cdot x_{chf}$$

$$F_x = F_3 \cdot \left(1 + (F_3^{-0.29} - 1) \cdot \frac{P_r - 0.6}{0.35}\right)^c$$

for $x_{chf} \le 0$:

$$b = \left\{ \begin{array}{lll} 0 & ; & P_r \le 0.6 \\ 1 & ; & P_r > 0.6 \end{array} \right\}$$

$$F_1 = \left\{ \begin{array}{lll} 1 + 0.0052 \cdot (-x_{chf}^{0.88}) \cdot Y_{Shah}^{0.41} & ; & Y_{Shah} \le 1.4 \cdot 10^7 \\ 1 + 0.0052 \cdot (-x_{chf}^{0.88}) \cdot Y_{Shah,1}^{0.41} & ; & Y_{Shah} > 1.4 \cdot 10^7 \end{array} \right\}$$

$$Y_{Shah,1} = 1.4 \cdot 10^7$$

$$F_2 = \left\{ \begin{array}{lll} F_1^{-0.42} & ; & F_1 \le 4 \\ 0.55 & ; & F_1 > 4 \end{array} \right\}$$

$$F_x = F_1 \cdot \left(1 - \frac{(1 - F_2) \cdot (P_r - 0.6)}{0.35} \right)^b$$

C.6.2. Upstream condition correlation (UCC)

$$q_{chf} = G \cdot \Delta h_{vap} \cdot 0.124 \cdot l_s^{-0.89} \cdot \left(\frac{10^4}{Y_{Shah}} \right)^n \cdot (1 - x_{in}) \qquad \text{(C.109)}$$

$$F_E = \left\{ \begin{array}{lll} 1.54 - 0.032 \cdot l_s & ; & 1.54 - 0.032 \cdot l_s > 1 \\ 1 & ; & 1.54 - 0.032 \cdot l_s \le 1 \end{array} \right\}$$

$$l_s = \frac{L}{d}$$

$$Pe = G \cdot d \cdot \frac{c_p}{\lambda_l}$$

$$Y_{Shah} = Pe \cdot F_E^{0.4} \cdot \left(\frac{\mu_l}{\mu_g} \right)^{0.6}$$

$$n = \left\{ \begin{array}{lll} 0 & ; & Y_{Shah} < 10^4 \\ l_s^{-0.54} & ; & Y_{Shah} \le 10^6 \\ 0.12/(1 - x_E)^{0.5} & ; & Y_{Shah} > 10^6 \end{array} \right\}$$

Correlations are cut down for tubes which are boiling at the whole length. More information can be found in [Mohammed Shah, 1987].

C.7. Vijayarangan

The set of correlations of Katto and Ohno described in section C.3 is used, except the second equation of q_2^*, which is expressed instead as:

$$q_{2,Vij}^* = 0.0051 \cdot \rho^{*0.133} \cdot \sigma^{*1/3} \cdot \frac{1}{1 + 0.0031 \cdot l_s} P_r^{0.147} Re_l^{0.25}$$

with

$$P_r = \frac{P}{P_c}$$

More information can be found in [Vijayarangan et al., 2006].

D. Uncertainty of R134a properties from REFPROP of NIST

D.1. Uncertainty of critical values

Table D.1.: Critical temperature, density, pressure from [Tillner-Roth & Baehr, 1994]

Source	Year	Purity [%]	T_c [K]	p_c [MPa]	ρ_c [kg/m^3]
Basu and Wilson	1989	99.95	374.22 ± 0.15	4.067 ± 0.027	512.2 ± 5
McLinden	1989	99.94	374.18 ± 0.01	4.056 ± 0.01	515.3 ± 1
Bier	1990	99.9	374.10 ± 0.05	4.050 ± 0.06	514.0 ± 10
Fukushima	1991	99.99	374.16 ± 0.02	4.067 ± 0.02	507.0 ± 5
Morrison and Ward	1991	99.95	374.23 ± 0.01	4.068 ± 0.01	512.2 ± 2
Yamashita	1989	99.9	374.24 ± 0.05	4.065 ± 0.005	-

D.2. Uncertainty of temperature and density

Table D.2.: Temperature and pressure of the phases from [Tillner-Roth & Baehr, 1994]

Phase	T	p	T_u	ρ_u
gas	T < 385 K	p < 3.7278 MPa	0.18 K	< 0.05 %
liquid	T < 385 K	p > 4.7679 MPa	0.18 K	< 0.05 %
trans-critical	370 K < T < 385 K	3.7278 MPa < p < 4.7679 MPa	0.18 K	< 1.6 %
super-critical	T > 385 K	-	0.18 K	< 0.05 %

D.3. Uncertainty of specific heat

Table D.3.: Measurement range and uncertainty of measurement of heat capacity from [Tillner-Roth & Baehr, 1994, Wirbser, 1995]

Source	T [K]	p [MPa]	T_u [K]	p_u	$C_{p,u}$
Wirbser	273-535	0.5-30	0.005	0.0002 p	(0.001-0.1) C_p
Gürtner	253-423	0-0.5	0.005	0.0001 p	0.002 C_p
Nakagawa	273-356	0.5-3	0.01	3 kPa	0.003 C_p
Saitob	275-356	1-3	0.01	3 kPa	0.003 C_p

Table D.4.: Measurement range and uncertainty of heat capacity from [Wirbser, 1995]

Uncertainty	A	B	C
0.15 %	-	-	-
0.20 %	$363 \leq T < 374$ $3.0 \leq p < 3.5$	$374 \leq T < 375$ $5.0 \leq p < 6.0$	$393 \leq T < 398$ $4.0 \leq p < 4.5$
	$403 \leq T < 413$ $5.0 \leq p < 6.0$	$423 \leq T < 435$ $6.0 \leq p < 12.0$	
0.30 %	$363 \leq T < 374$ $3.0 \leq p < 3.5$	$374 \leq T < 393$ $3.5 \leq p < 3.8$	$398 \leq T < 403$ $5.0 \leq p < 6.0$
	$393 \leq T < 398$ $5.5 \leq p < 6.0$	$393 \leq T < 398$ $7.0 \leq p < 8.0$	
0.40 %	$383 \leq T < 393$ $5.0 \leq p < 5.5$	$383 \leq T < 393$ $6.0 \leq p < 7.0$	$398 \leq T < 413$ $6.0 \leq p < 7.0$
0.50 %	$374 \leq T < 375$ $4.5 \leq p < 5.0$	$375 \leq T < 383$ $3.8 \leq p < 3.9$	$393 \leq T < 398$ $6.0 \leq p < 7.0$
1.00 %	$373 \leq T < 374$ $5.0 \leq p < 5.5$		
1.50 %	$373 \leq T < 375$ $4.2 \leq p < 5.0$		
2.50 %	$374 \leq T < 375$ $3.8 \leq p < 4.0$	$375 \leq T < 383$ $3.9 \leq p < 4.0$	
3.50 %	$373 \leq T < 374$ $3.8 \leq p < 4.0$	$374 \leq T < 375$ $4.0 \leq p < 4.5$	$373 \leq T < 374$ $4.1 \leq p < 4.2$
	$375 \leq T < 383$ $4.0 \leq p < 5.5$		
7.00 %	$373 \leq T < 374$ $4.0 \leq p < 4.1$		

E. Tables for assessment of correlations

Table E.6.: Mean and standard deviation of correlations split into mass fluxes for CO_2 - I in % for 200–500 kg/m^{2}s

Correlation	200		300		400		500	
	MD	STD	MD	STD	MD	STD	MD	STD
Badea et al. A.1	83.9	61	72.7	64	41.3	65.7	39	52.3
Bae A.2	22.7	23.1	-9.5	17.7	-8.2	16	-8.9	15.6
Bae & Kim A.3	46	64.8	-2.5	52.4	-24	39.3	-44	29.9
Bishop et al.A.4	111	59.3	45.7	34.6	26.1	25.5	9.7	19.4
Bogachev et al. A.5	120	52.6	107	49.4	71.5	65.5	77	66.5
Bringer & Smith A.6	304	288	172	125	113	123	106	108
Chen & Fang A.7	8.9	9.3	-1.1	7.5	-5.3	7.1	-8.4	5.6
Cheng et al. A.8	50.4	74.3	38.8	40.8	25.2	58.2	20.9	61
Cheng-q A.9	62.4	54.6	39.3	54.6	18.5	73.9	4.9	75.2
Cheng-T A.10	72.5	54.6	22.8	29.3	2.2	29.7	-9.1	26.2
Cui& Wang A.11	160	79.8	74.7	47.2	44.7	34.7	21.2	26.6
Deev et al. A.12	72.7	48.5	28.4	35.8	5.3	38.9	-4.3	36.6
Dittus-Boelter A.13	124	159	153	178	110	146	158	172
Gnielinski A.14	143	182	185	211	142	176	203	212
Gorban et al. water A.15	-29.1	28.9	-25.2	29.5	-38.5	35.6	-26.8	40.9
Gorban et al. R12 A.16	-28.2	28.6	-26.3	28	-40.3	34.9	-29.8	39.8
Grass et al. A.17	95.3	57.6	60.5	42.2	31.4	55.2	33.1	61.9
Griem A.18	59.6	75.7	8.7	38.1	-13.5	37.2	-16.5	35.9
Gupta et al. A.19	156	92.4	180	76.1	147	71.5	139	58.7
Jackson A.20	98.5	44.3	54.2	26.9	30.7	34	25.9	31.1
Jackson & Fewster A.21	103	49	52.6	30.5	27.5	33.4	18.4	29.6
Kim et al. A.22	98.1	87.6	7	32.7	-7.9	24.7	-2.4	29.4
Kim & Kim A.23	149	153	303	138	259	144	291	174
Kirillov et al. A.24	81.8	97.2	-0.6	63.7	-31.8	37.3	-50.1	25.1
Komita et al. A.25	-94.9	74.9	-105	67.9	-46.3	39.9	-40.4	29.8
Kondratev A.26	2.2	42.4	5.5	43.7	-15.1	48.2	-0.5	53.8
Krasnoshchekov et al. A.27	121	101	46.4	78.7	18.3	62.4	-9.3	53
Kuang et al. A.28	999	541	939	279	836	134	689	159
Kurganov et al. A.29	192	490	273	595	215	455	354	582
Mayinger & Scheidt A.30	84.7	142	85.7	151	66.1	135	89.1	173
Miropolskii & Shitsman A.31	134	58.4	61.4	35.8	32.8	39.7	30.9	44.6
Mokry et al. water A.32	88.6	54.6	19.8	30.5	4	19.1	-12.1	13.4
Mokry et al. CO_2 A.33	16.1	36.4	-20.8	19.8	-33.7	21.9	-33	22.8
Nicholas A.34	81.4	44.6	33.2	24.9	14.7	24.3	4.5	22.3
Ornatsky et al. A.35	103	61.3	15.5	28.9	-4.7	26.4	-10.1	29.4
Petukhov et al. A.36	149	127	73.4	91.9	40.3	78.2	12.1	70.9
Pitla et al. A.37	114	129	21.1	52.6	-2.1	47.1	-5	41.3
Preda et al. A.38	172	175	82.8	76.2	60.8	72.9	57.1	54.6
Razumovskiy et al. A.39	161	152	69.1	115	34.4	89.7	-5	72.2
Saltanov et al. A.40	13.9	34	-11.6	22.7	-27.2	27.3	-24.1	27.8
Swenson et al. A.41	178	101	246	116	198	115	197	105
Watts & Chou A.42	92.8	48.2	36.9	28.4	16.3	26.9	5.1	22.7
Yamagata et al. A.43	157	61.5	95.4	45.9	65.8	44.7	50	41.9
Yeroshenko & Yaskin A.44	74.6	44	39.8	39.9	16.8	43.1	8.2	43.8
Zhang et al. A.45	98.8	103	49.4	96	36.5	79.4	2	99.2
Zhu et al. A.46	108	66.9	43.2	35.4	22.6	31.1	7.7	26.6

Table E.7.: Mean and standard deviation of correlations split into mass fluxes for CO_2 - I in % for 1000–1500 kg/m^{2}s

Correlation	600		1000		1200		1500	
	MD	STD	MD	STD	MD	STD	MD	STD
Badea et al. A.1	45.9	36.8	38.7	25.8	25.5	18.4	9.8	18.7
Bae A.2	-1.7	20.2	9.5	18.3	13.1	15.9	8.2	17.7
Bae & Kim A.3	-43.7	28.9	-28.9	98.3	-41.5	77.9	-17	94.8
Bishop et al.A.4	9.8	16.3	12.3	15.6	15.1	13.5	11.3	14.7
Bogachev et al. A.5	75.1	56.3	132	59.6	154.5	57.1	149	67.7
Bringer & Smith A.6	94.7	66.6	142	54.7	152	59.3	142	74.1
Chen & Fang A.7	-7.9	4.4	-7.4	6.1	-4.8	5	-1.1	5.7
Cheng et al. A.8	15.6	44.7	21.6	29.3	14.8	30.7	-9.6	30.7
Cheng-q A.9	-3.1	41.1	-8.4	21.9	-16.2	20.5	-26.9	18.4
Cheng-T A.10	-15.4	14.8	-25.9	10.8	-30.3	10.1	-28.9	10.3
Cui & Wang A.11	16.9	16.4	6.3	11.3	4.1	11.7	-1.8	12.2
Deev et al. A.12	-10.6	19.4	-14.6	12	-17.1	10.1	-16.3	11.9
Dittus-Boelter A.13	196	232	475	314	594	284	532	324
Gnielinski A.14	258	293	637	414	808	379	737	440
Gorban et al. water A.15	-25.5	38.2	29.1	45.1	52.3	40.6	58.7	50.7
Gorban et al. R12 A.16	-30.1	34.2	16.3	38.6	35.2	35.3	40.7	43.8
Grass et al. A.17	24.9	35.6	64	35.7	85.4	40.5	105	53.4
Griem A.18	-18	28.1	8.1	27.1	20.8	26.7	27.1	34.7
Gupta et al. A.19	147	52.4	168	52.9	168	55.6	137	50.9
Jackson A.20	28	37.3	48.2	30	52.3	21.8	37.6	18.4
Jackson & Fewster A.21	17.7	25.8	32.1	24	38.1	21.3	33	24.2
Kim et al. A.22	-1.9	26.2	38.2	29.6	53.6	28.8	70.8	32.5
Kim & Kim A.23	253	85.2	343	115	409	161	479	211
Kirillov et al. A.24	-51.6	20.3	-63.5	10.9	-68.8	6.2	-68.1	6.3
Komita et al. A.25	-20.8	17	-5.8	16.5	-1.5	13.8	-5.1	15.4
Kondratev A.26	1.8	54.9	72.5	64.7	102	57.6	100	69.7
Krasnoshchekov et al. A.27	-16.7	44.8	-53.3	29.6	-67.9	7.3	-67	7.2
Kuang et al. A.28	695	232	850	292	970	199	999	248
Kurganov et al. A.29	533	796	999	999	999	999	999	999
Mayinger & Scheidt A.30	126	243	326	384	404	399	347	383
Miropolskii & Shitsman A.31	34.1	54.1	85.4	60.4	107	51.9	98.3	61.1
Mokry et al. water A.32	-11.8	12.5	-12.6	12.6	-11.1	10.1	-15	10.1
Mokry et al. CO_2 A.33	-28.5	31.9	-0.4	32.2	10.3	23.6	4.4	25.1
Nicholas A.34	3.2	20.1	17.5	22.6	26.4	19.5	27.1	24.9
Ornatsky et al. A.35	-5.9	41	25.7	42.7	38.6	33.1	28.6	36.2
Petukhov et al. A.36	-0.7	54.4	-37.4	37.8	-52.5	12.5	-46.8	12.8
Pitla et al. A.37	-3.9	43.6	57.5	63.4	93.6	58.3	109	81.5
Preda et al. A.38	75.8	75.1	147	79.5	167	71.2	135	67.7
Razumovskiy et al. A.39	-13.2	66.5	-61.7	39.9	-79.1	7.6	-76.3	7.4
Saltanov et al. A.40	-20.6	34.5	13.3	35.6	26.3	27.9	21.2	31.3
Swenson et al. A.41	204	71.7	224	64.6	211	66.3	176	59
Watts & Chou A.42	4.8	19.8	10.9	17.6	13.7	15.9	8.5	17.7
Yamagata et al. A.43	43.7	24.9	43.6	28.1	45.4	34.9	43.7	39.3
Yeroshenko & Yaskin A.44	-1.8	24.1	-20.3	20.9	-32.9	12	-34	11
Zhang et al. A.45	4.2	56.5	-88.9	80.2	-159	87.9	-208	102
Zhu et al. A.46	4.5	16.3	10.8	15.8	17	16.1	21.3	21.1

Table E.5.: Mean and standard deviation of correlations split into mass fluxes for R134a - I in %

Correlation	300		500		750		1000		1500		2000	
	MD	STD	MD	STD	MD	STD	MD	STD	MD	STD	MD	STD
Badea A.1	52.7	35.7	70.8	73.3	50.1	31.4	91.1	38.9	71.4	33.3	78.7	35.6
Bae A.2	-17.1	24.3	-8.1	15.4	-6.2	13	0.6	10.9	20.6	6.9	24.9	9
Bae & Kim A.3	-6.4	34.5	-18.5	21.1	-10.4	16.7	-16.4	24.7	50.1	145	-64.1	2
Bishop et al.A.4	33.2	41.3	26.2	22.2	13.2	14.6	15	10.8	36.2	7	43.4	9.1
Bogachev A.5	59.8	33.6	60.2	50.3	31.9	33.6	69.6	28.4	130	18.2	145	24.5
Bringer A.6	177	176	144	104	96.6	80.1	120	45.2	97.4	17.6	109	22.9
Chen A.7	75.9	41.9	59.6	37	56.9	33.5	28.1	16.6	40	7.2	43.1	6.8
Cheng A.8	1.8	29.9	11.5	43.9	-10.8	25.4	16	17.6	20.7	12.8	30.4	12.5
Cheng-q A.9	21.9	48.6	36.4	65.1	14.4	43.1	42.4	41.3	-12.7	9.2	-5.7	10.1
Cheng-T A.10	24.3	44.8	12.5	22.9	-10	14.7	-8.8	9.3	-16.2	5	-16.1	5.1
Cui A.11	60.3	52	44	29.7	23.3	17.8	22.4	10.9	19.3	5	21.1	7.1
Deev. A.12	21.8	36.6	14.4	29.1	-5.3	18.1	3	12.8	-13.8	5.4	-11.2	6.8
DB A.13	51.1	53.7	45.7	52.9	11.7	55.2	82.8	126	431	64.8	484	76.9
Gnielinski A.14	65.2	64.6	63	62.6	27.5	70.4	118	173	622	90.9	713	109
Gorban H_2O A.15	-42	15.4	-41.2	19.8	-53.3	14.6	-31.9	19.6	17.3	16.8	30.1	19
Gorban R12 A.16	-41.7	15.1	-42	19.7	-54.7	14	-35.1	16.4	2.3	14.6	12.1	16.3
Grass A.17	93.9	58.6	95.7	65.9	62.4	45.2	103	30.7	136	21.6	163	30.9
Griem A.18	17.1	39.2	11.6	32.7	-6.6	22.5	10.4	19.7	23.4	12.2	34.2	15.8
Gupta . A.19	54.7	32.9	68.5	51.4	56.8	33.5	92.4	23.5	146	12.9	162	15.8
Jackson A.20	34	36.7	24.3	25.9	2.9	19.6	18.1	22	71.4	10.9	78.3	13.1
Jack. & Few. A.21	35.7	38.4	26.3	27.2	6.9	18.1	17.4	13.8	43	9	49.5	11.8
Kim A.22	28.9	72	-2.6	39	-24.1	16.8	-28.7	15	-6.5	14.2	-4.6	12.5
Kim & Kim A.23	109	106	162	132	136	84.3	240	67.2	346	61	388	72.9
Kirillov A.24	4.1	41.4	-22.7	24.2	-32.7	11.8	-39.7	10.7	-61.6	2.8	-61.9	2.6
Komita A.25	-112.1	54.9	-43.4	28.6	-21.4	9.2	-15.2	9.5	5.9	6.1	10.1	8
Kondratev A.26	-20.9	20.5	-23.6	25.5	-41.8	19	-15.5	27.2	51.6	19.4	64.2	22.4
Krasnosh. A.27	40.9	53	34.5	39.8	25.3	25.2	19.9	32.5	-55.2	3	-55.6	2.5
Kuang et al. A.28	883	447	726	160	586	99.2	525	227	999	122	999	132
Kurganov A.29	41.3	146	17.7	117	-12.8	157	135	422	999	251	999	264
Mayinger A.30	16.7	47.8	17.5	46.4	10.6	47.7	54.1	125	334	241	363	268
Miropolskii A.31	58.9	72.5	28.2	32.5	1.5	27.6	3.8	27.9	72.3	18.9	83.4	21.8
Mokry H_2O A.32	15.4	40.7	5.3	17.2	-6.1	11	-9.8	9.2	9.3	6	14.2	7
Mokry CO_2 A.33	-21.1	30.5	-33.5	13	-47.6	10.4	-41.6	19.1	6.8	12.6	12.6	13
Nicholas A.34	9.4	29	4.6	19.1	-9.2	13.8	-1.9	13.4	32.2	8.3	40.8	11.5
Ornatsky A.35	32	74.4	-2.7	34.2	-26.6	22.2	-32.6	22.6	22	14.8	27.6	15.5
Petukhov A.36	70.7	60.9	75.5	63.2	65	39.6	71.7	48.7	-38	5.5	-36.4	5.8
Pitla et al. A.37	51.6	66.4	35.6	36.9	11.9	32.9	24.4	34.5	118	23.8	144	32
Preda . A.38	61.4	97.1	48.9	55.7	30.7	44.4	39.4	37.5	150	26.2	176	28.3
Razumov. A.39	50.3	62.9	46.3	51.5	44.1	33.7	33	45.3	-73.3	2.8	-73.7	2.2
Saltanov A.40	-19.7	25.6	-29.1	15.1	-44.2	12.1	-33.1	18.9	13.9	12.5	20.4	13.7
Swenson A.41	110	58.6	146	104	132	61.4	208	44.6	204	16.3	226	20.4
Watts A.42	23.9	38.1	15.9	22.8	-0.1	15.5	5.6	10.9	20.9	6.8	25.1	9
Yamagata A.43	76.3	55.4	70.5	42.8	40.7	29.7	65	19.3	66.3	26.5	76.7	31
Yeroshenko A.44	27.2	34.6	23.5	37	3.6	23.7	18	23.6	-30.1	5.1	-33	3.6
Zhang A.45	27	65.5	48	66.4	23.9	45.2	39.5	50.7	-27.8	38.6	-21	26.6
Zhu A.46	36.8	37.6	35.2	28.8	21.9	18.7	28.8	10.7	40.9	7.7	51	11.6